



Provided by the author(s) and University of Galway in accordance with publisher policies. Please cite the published version when available.

Title	Development of computationally efficient nested hydrodynamic models
Author(s)	O'Brien, Noreen
Publication Date	2014-04-25
Item record	<a href="http://hdl.handle.net/10379/4373">http://hdl.handle.net/10379/4373</a>

Downloaded 2024-04-26T18:03:45Z

Some rights reserved. For more information, please see the item record link above.



# **Development of computationally efficient nested hydrodynamic models**

**By**

**Noreen O'Brien**



**Dissertation submitted to NUI, Galway in partial fulfilment of the  
requirements for the degree of PhD**

Department of Civil engineering

College of Engineering and Informatics

2014

## **DECLARATION**

I declare that this dissertation, in whole or in part, has not been submitted to any University as an exercise for a degree. I further declare that, except where references are given, the work is entirely my own.

Signed:

---

Noreen O'Brien

## ABSTRACT

Hydrodynamic numerical modelling of coastal zones typically requires a high level of horizontal spatial resolution to improve the realism of its solution, particularly in areas of complex bathymetry. These high resolution models result in high computational costs. One solution to this spatial resolution problem are nested models, which reduce computational needs by embedding a high resolution grid into a low resolution grid, that covers the entire model domain and the two grids interact with each other.

A one-way nesting technique in the numerical model DIVAST was expanded by introducing two novel approaches to further reduce its computational effort and to increase the applicability and flexibility of the model. These features included the generation of irregular geometry boundaries and the transformation of the nested domain into a rotational coordinate system to allow the orientation of the model to be modified.

A two-way nested modelling technique was developed to simulate tidal hydraulics in coastal zones. This technique enabled high resolution data in the nested domain to be transmitted to the low resolution domain. To the Author's knowledge this is the first two-way nested model that incorporates ghost cells that enables the formulation of the nested grid open boundaries as internal boundaries. Tidal turbine farms of different array configurations were incorporated into the two-way nested model, and possible changes in the tidal regime were identified with the use of the Linear Momentum Actuator Disc Theory. To the Author's knowledge this the first type of two-way nested modelling procedure that simulated the effects of tidal turbines.

The model was extensively tested in a real coastal system. Results showed the two-way nested model can produce an accurate high resolution solution in areas of interest, and improve the realism of the solution in the low resolution coarse domain for a much lower computational effort than the standard single grid high resolution model. Applications of such a technique are applicable in sediment transport modelling, wave modelling, flood modelling and identifying possible environmental impacts of tidal turbine farms.



## **ACKNOWLEDGMENT**

The author wishes to thank her family, friends and colleagues for all the help, support and encouragement throughout this research. Without them I would not have enjoyed my time in Galway as much as I did.

I would like to thank Professor O'Donoghue for providing me with the opportunity to conduct this research at NUI, Galway.

A special thanks to my supervisor Prof. Michael Hartnett and my co-supervisor Dr. Stephen Nash for all their encouragement and technical advice throughout this research.

Finally, I would like to thank my parents Paddy and Carmel for their endless support. To my brother, Frank, for his constant encouragement to follow by ambitions, and my Nan-Nan and Matt for all their love.

# **TABLE OF CONTENTS**

Abstract.....	iii
Acknowledgment.....	v
<b>CHAPTER 1: Introduction.....</b>	<b>1</b>
1.1 Tidal power industry.....	1
1.2 Numerical modelling.....	2
1.3 Aims and objectives.....	3
1.4 Thesis layout and content.....	4
<b>CHAPTER 2: Literature Review.....</b>	<b>5</b>
2.1 Introduction.....	5
2.2 Hydrodynamic model resolution.....	6
2.3 Temporal resolution and the Courant Condition.....	6
2.4 Computational grids and spatial resolution.....	7
2.4.1 Finite difference grids.....	7
2.4.2 Finite element grids.....	10
2.4.3 Finite volume grids.....	13
2.5 Advanced computational grids.....	15
2.5.1 Hybrid grid.....	15
2.5.2 Quadtree grids.....	17
2.5.3 Adaptive grid system.....	18
2.6 Nested models.....	20
2.6.1 One-way nested modelling.....	22
2.6.2 Two-way nested modelling.....	24
2.7 Two-way nested modelling techniques.....	26
2.7.1 Formulation of nesting technique.....	26
2.7.2 Data transmission problem.....	27
2.9 Summary and Conclusion.....	37
<b>CHAPTER 3: Description of the numerical model DIVAST.....</b>	<b>40</b>
3.1 Introduction.....	40
3.2 Model Description.....	40
3.3 Governing equations of motion.....	42

3.4 Finite difference formulation.....	45
3.5 Hydrodynamic solution scheme .....	48
3.6 Model accuracy and stability.....	52
<b>Chapter 4: Advanced one-way nested model .....</b>	<b>54</b>
4.1 Introduction .....	54
4.2 Description of one-way nested model in DIVAST .....	55
4.3 Description of Rotated Nested Model .....	58
4.4 Design of Rotated Nested Model .....	60
4.5 Implementation of Rotated Nested Model.....	63
4.5.1 Rotated domain formulation .....	66
4.6 Results.....	69
4.7 Description of Irregular Geometry Boundaries .....	74
4.7.1 Identification of new domain .....	76
4.7.2 Boundary reconstruction .....	77
4.8 Results.....	78
4.9 Summary and Conclusion.....	81
<b>Chapter 5:.....</b>	<b>83</b>
<b>Two-way nested model design and development, Phase I.....</b>	<b>83</b>
5.1 Overview.....	83
5.2 Nesting methodology .....	84
5.2.1 Details on nesting approach.....	86
5.3 Design of basic two-way nested model.....	88
5.4 Modification of model code.....	91
5.5 Case study of the Shannon estuary .....	96
5.5.1 Error analysis and model performance .....	99
5.6 Feedback prescriptions .....	101
5.6.1 BTWNM_I.....	102
5.6.2 BTWNM_II.....	105
5.6.3 BTWNM_III .....	107
5.6.4 BTWNM_IV .....	109
5.7 Summary and Conclusion.....	118
<b>Chapter 6: Two-way nested model design and development, Phase II.....</b>	<b>121</b>

<b>6.1 Introduction</b> .....	121
<b>6.2 Feedback conditions</b> .....	121
<b>6.2.1 Momentum relaxation scheme</b> .....	124
<b>6.2.2 Kinetic relaxation scheme</b> .....	140
<b>6.3 Interpolation/ update schemes</b> .....	154
<b>6.3.1 BTWNM_COPY</b> .....	155
<b>6.3.2 BTWNM_SHAP</b> .....	162
<b>6.3.3 BTWNM_FULLW</b> .....	169
<b>6.4 Summary and Conclusions</b> .....	176
<b>Chapter 7: Development of TTWNM</b> .....	179
<b>7.1 Introduction</b> .....	179
<b>7.2 Turbine representation</b> .....	179
<b>7.3 Implementation</b> .....	182
<b>7.4 Results</b> .....	185
<b>7.5 Summary and conclusion</b> .....	198
<b>Chapter 8: Summary and Conclusions</b> .....	200
<b>8.1 Summary</b> .....	200
<b>8.2 Conclusion</b> .....	202
<b>8.3 Future work</b> .....	204
<b>References</b> .....	205
<b>Appendix A</b> .....	219
<b>Appendix B</b> .....	224

## Table of Figures

Figure 2: 1(a) Structured uniform grid (b) Structured rectangular grid.....	8
Figure 2: 2 (a) Physical grid system with coordinate system (x,y) (b) Computational grid system with coordinate system ( $\xi,\eta$ ) (Yu 2013).....	9
Figure 2: 3 Orthogonal grid                      Figure 2: 4 Non-Orthogonal grid (Hong 2000).....	10
Figure 2: 5 Finite element domain generated by GPGEN (Group 2013) .....	11
Figure 2: 6 TELEMAC-2D mesh of coastal domain (Denot 2012) .....	12
Figure 2: 7 Unstructured Finite Volume mesh (Shore 2009).....	13
Figure 2: 8 Control volumes (Bakker 2008).....	14
Figure 2: 9 Hybrid grid (Xinghua 2012).....	15
Figure 2: 10 Finite Element hybrid mesh of the River Danube (Berkhahn 2005) .....	16
Figure 2: 11 Hybrid grid of pipe with ball valve (Wang 2006).....	16
Figure 2: 12 Simple quadratic grid and its tree representation (Park 2006).....	17
Figure 2: 13 Adaptive mesh refinement.....	19
Figure 2: 14 (a) Static nested domain (b) Adaptive nested domain.....	20
Figure 2: 15 Coarse and fine/nested grids.....	22
Figure 2: 16 Coarse domain $\Omega_c$ embedded with a nested domain $\Omega_n$ .....	27
Figure 2: 17 Seamlessly embedded nested domain .....	32
Figure 2: 18 Schematic of overlapping grid configuration.....	33
Figure 2: 19 Copy interpolation scheme .....	34
Figure 2: 20 Average interpolation scheme.....	35
Figure 2: 21 Shapiro interpolation scheme .....	36
Figure 2: 22 Fully weighted averaging interpolation scheme.....	37
Figure 3: 1 Uniform rectilinear grid (Wanga 2004).....	41
Figure 3: 2 The space staggered grid system (Layeka 2007).....	42

Figure 3: 3 A shallow well mixed water body ( $\zeta$ = water elevation above or below MWL, $h$ =water depth below MWL).....	43
Figure 3: 4 Principle of the two dimensional model (Fowler 2012).....	44
Figure 3: 5 Illustration of model grid and integration section (Nash 2010).....	50
Figure 4: 1 Nested grid configuration showing boundary interface of nested grid incorporating internal boundary $\Gamma$ and adjacent exterior ghost cells $\Gamma^*$ . ....	58
Figure 4: 2 Rotated nested domain $\Omega Rn$ .....	59
Figure 4: 3 Flowchart of rotated nested model (OBC's=Open Boundary Conditions).....	62
Figure 4: 4 Flow chart of nested model structure, with red identifying the subroutines used in the nesting procedure and green identify the subroutines that were modified for the RNM. ....	65
Figure 4: 5 Illustrations of the non-rotated domain and the rotated domain.....	66
Figure 4: 6 Rotated nested boundary.....	68
Figure 4: 7(a1) Plan view of rectangular harbour (a2) view of bathymetry in harbour (depths in meters).....	70
Figure 4: 8 RNM in low resolution domain with points A, B, and C specified in the nested domain and the four open boundaries (OB).....	71
Figure 4: 9 Graph of velocity vs. time at point A in a high resolution standard model and in the RNM.....	72
Figure 4: 10 Graph of velocity vs. time at point B in a high resolution standard model and in the RNM.....	72
Figure 4: 11 Graph of velocity vs. time at point C in a high resolution standard model and in the RNM.....	72
Figure 4: 12 $RE_T$ in velocities for RNMs nested domain.....	73
Figure 4: 13 Irregular geometry boundary domains.....	74
Figure 4: 14 Flowchart of one-way nested procedure with irregular boundary geometry (with OBC's = open boundary conditions). ....	75
Figure 4: 15 Nested domain showing sections 1-5.....	76
Figure 4: 16 Open boundary identification.....	77
Figure 4: 17 Gently sloped rectangular harbour .....	78

Figure 4: 18 Rectangular harbour nested with (a) original rectangular nested grid and (b) IRG nested grid, specified with red shading and all boundaries identified. ....	78
Figure 4: 19 $RE_T$ for velocities between regular nested model and high resolution model. ....	79
Figure 4: 20 $RE_T$ for velocities between IGB model and high resolution model in the nested domain.....	79
Figure 4: 21 Time history locations .....	80
Figure 4: 22 Time history at point B.....	80
Figure 4: 23 Time history at point E.....	80
Figure 5: 1 Schematic of a nested model of an estuary.....	86
Figure 5: 2 Nested grid configuration showing nested domain (green grid lines) and coarse domain (black grid lines), with points of feedback to one coarse grid highlighted with purple arrows and circles.....	87
Figure 5: 3 Flowchart of proposed basic two-way nested model.....	90
Figure 5: 4 Flowchart of Coarse model.....	92
Figure 5: 5 Flow chart of one-way nested model structure(Nash 2010) .....	93
Figure 5: 6 Flow chart of TWNM structure .....	95
Figure 5: 7 Illustration of the Shannon Estuary.....	96
Figure 5: 8 Illustration of the Shannon Estuary bathymetry.....	97
Figure 5: 9 Locations of measured data for tidal amplitudes (T1- T6) and tidal current velocities (C1) used to validate the model (Dabrowski 2005) .....	97
Figure 5: 10 Comparison of measured data against the predicted model data (Dabrowski 2005).....	98
Figure 5: 11 $RE_T$ in velocities for the low resolution coarse model without nesting.....	100
Figure 5: 12 Momentum fluxes across the boundary for BTWNM_I.....	102
Figure 5: 13 Nested grid momentum fluxes across the boundary cells and cells adjacent to the boundary for BTWNM_I.....	104
Figure 5: 14 Momentum fluxes across the boundary for BTWNM_II.....	105
Figure 5: 15 Nested grid momentum fluxes across the boundary cells and cells adjacent to the boundary for BTWNM_II.....	106

Figure 5: 16 Momentum fluxes across the boundary for BTWNM_III.....	107
Figure 5: 17 Nested grid momentum fluxes across the boundary cells and cells adjacent to the boundary for BTWNM_III.....	108
Figure 5: 18 Momentum fluxes across the boundary for BTWNM_IV.....	109
Figure 5: 19 Nested grid momentum fluxes across the boundary cells and cells adjacent to the boundary for BTWNM_IV.....	110
Figure 5: 20 $RE_T$ in full model domain for (a) BTWNM_IV and (b) non-updated coarse model, with black square highlighting area of feedback.....	111
Figure 5: 21 Time history analysis at Point A for BTWNM_IV model.....	112
Figure 5: 22 Time history analysis at Point B for BTWNM_IV model.....	113
Figure 5: 23 Time history analysis at Point C for BTWNM_IV model.....	114
Figure 5: 24 Time history analysis at Point D for BTWNM_IV model.....	115
Figure 5: 25 $RE_T$ for velocities in nested domain for (a) BTWNM_IV and (b) non-nested low resolution coarse model.....	116
Figure 5: 26 Time history analysis of Point E for BTWNM_IV model.....	117
Figure 6: 1 Sponge layer.....	122
Figure 6: 2 Momentum fluxes across the boundary for BTWNM_MOM (V+E).....	124
Figure 6: 3 Nested grid momentum fluxes across the boundary cells and cells adjacent to the boundary for BTWNM_MOM (V+E).....	126
Figure 6: 4 Illustration showing time history points A-D.....	127
Figure 6: 5 Time history analysis of point A.....	127
Figure 6: 6 Time history analysis of point B.....	128
Figure 6: 7 Time history analysis of point C.....	129
Figure 6: 8 Time history analysis of point D.....	130
Figure 6: 9 Illustration of nested domain with point E used in the time history analysis.....	131
Figure 6: 10 Time history analysis of point E.....	132
Figure 6: 11 Momentum fluxes across the boundary for BTWNM_MOM (Q (ALL)).....	133

Figure 6: 12 Nested grid momentum fluxes across the boundary cells and cells adjacent to the boundary for BTWNM_MOM (Q (ALL)).....	134
Figure 6: 13 Time history analysis of point A for BTWNM_MOM (Q (ALL)).....	135
Figure 6: 14 Time history analysis of point B for BTWNM_MOM (Q (ALL)).....	136
Figure 6: 15 Time history analysis of point C for BTWNM_MOM (Q (ALL)).....	137
Figure 6: 16 Time history analysis of point D for BTWNM_MOM (Q (ALL)).....	138
Figure 6: 17 Time history analysis of point E for BTWNM_MOM (Q (ALL)).....	139
Figure 6: 18 Momentum fluxes across the boundary for BTWNM_KIN (V+E).....	140
Figure 6: 19 Nested grid momentum fluxes across the boundary cells and cells adjacent to the boundary for BTWNM_KIN (V+E).....	141
Figure 6: 20 Time history analysis of point A for BTWNM_KIN (V+E).....	142
Figure 6: 21 Time history analysis of point B for BTWNM_KIN (V+E).....	143
Figure 6: 22 Time history analysis of point C for BTWNM_KIN (V+E).....	144
Figure 6: 23 Time history analysis of point D for BTWNM_KIN (V+E). .....	145
Figure 6: 24 Time history analysis of point E for BTWNM_KIN (V+E).....	146
Figure 6: 25 Momentum fluxes across the boundary for BTWNM_KIN (Q (ALL)).....	147
Figure 6: 26 Nested grid momentum fluxes across the boundary cells and cells adjacent to the boundary for BTWNM_KIN (Q (ALL)).....	148
Figure 6: 27 Time history analysis of point A for BTWNM_KIN (Q (ALL)).....	149
Figure 6: 28 Time history analysis of point B for BTWNM_KIN (Q (ALL)).....	150
Figure 6: 29 Time history analysis of point C for BTWNM_KIN (Q (ALL)).....	151
Figure 6: 30 Time history analysis of point D for BTWNM_KIN (Q (ALL)).....	152
Figure 6: 31 Time history analysis of point E for BTWNM_KIN (Q (ALL)).....	153
Figure 6: 32 Momentum fluxes across the boundary for BTWNM_COPY .....	155
Figure 6: 33 Nested grid momentum fluxes across the boundary cells and cells adjacent to the boundary for BTWNM_COPY .....	156
Figure 6: 34 Time history analysis of point A for BTWNM_COPY. ....	157
Figure 6: 35 Time history analysis of point B for BTWNM_COPY. ....	158
Figure 6: 36 Time history analysis of point C for BTWNM_COPY.....	159

Figure 6: 37 Time history analysis of point D for BTWNNM_COPY.....	160
Figure 6: 38 Time history analysis of point E for BTWNNM_COPY.....	161
Figure 6: 39 Momentum fluxes across the boundary for BTWNNM_SHAP .....	162
Figure 6: 40 Nested grid momentum fluxes across the boundary cells and cells adjacent to the boundary for BTWNNM_SHAP .....	163
Figure 6: 41 Time history analysis of point A for BTWNNM_SHAP.....	164
Figure 6: 42 Time history analysis of point B for BTWNNM_SHAP.....	165
Figure 6: 43 Time history analysis of point C for BTWNNM_SHAP.....	166
Figure 6: 44 Time history analysis of point D for BTWNNM_SHAP.....	167
Figure 6: 45 Time history analysis of point E for BTWNNM_SHAP.....	168
Figure 6: 46 Momentum fluxes across the boundary for BTWNNM_FULLLW .....	169
Figure 6: 47 Nested grid momentum fluxes across the boundary cells and cells adjacent to the boundary for BTWNNM_FULLLW .....	170
Figure 6: 48 Time history analysis of point A for BTWNNM_FULLLW.....	171
Figure 6: 49 Time history analysis of point B for BTWNNM_FULLLW.....	172
Figure 6: 50 Time history analysis of point C for BTWNNM_FULLLW.....	173
Figure 6: 51 Time history analysis of point D for BTWNNM_FULLLW.....	174
Figure 6: 52 Time history analysis of point E for BTWNNM_FULLLW.....	175
Figure 7: 1 Linear Momentum Actuator Disc Theory in an open channel flow.....	180
Figure 7: 2 Flow chart of TTWNNM with new and modified subroutine highlighted in yellow .....	184
Figure 7: 3 Maximum available power (MW per grid cell) for the Shannon Estuary.....	185
Figure 7: 4 The Shannon Estuary with the extent of the turbine farm highlighted in red and the nested grid position highlighted by the black square.....	186
Figure 7: 5 Comparisons of velocities at point 1 outside the turbine farm for 0.5 rotor spacing .....	187
Figure 7: 6 Comparisons of velocities at point 2 inside the turbine farm for 0.5 rotor spacing .....	188

Figure 7: 7 Comparisons of velocities at point 3 upstream of the turbine farm for 0.5 rotor spacing.....	189
Figure 7: 8 Relative percentage changes in velocities with the inclusion of 0.5 rotor spaced turbine farm.....	190
Figure 7: 9 Comparisons of velocities at point 1 outside the turbine farm for 2 rotor spacing .....	191
Figure 7: 10 Comparisons of velocities at point 2 inside the turbine farm for 2 rotor spacing .....	192
Figure 7: 11 Comparison of velocities at point 3 upstream of the turbine farm for 2 rotor spacing .....	193
Figure 7: 12 Relative change in velocities in the two-way nested model with the inclusion of turbine farm with 2 rotor spaced turbines .....	194
Figure 7: 13 Comparison of velocities at point 1 outside the turbine farm for 5 rotor spacing .....	195
Figure 7: 14 Comparison of velocities at point 2 inside the turbine farm for 5 rotor spacing .....	196
Figure 7: 15 Comparison of velocities at point 3 upstream of the turbine farm for 5 rotor spacing .....	197
Figure 7: 16 Relative change in velocities in the two-way nested model with the inclusion of turbine farm with 2 rotor diameter spaced turbines .....	198

## **Table of Tables**

Table 4: 1 Modifications of the source code to allow the rotation of the nested domain.....	64
Table 5: 1 List of two-way nested models used in development.....	84
Table 5: 2 Sections of source code incorporated to allow two-way nesting.....	94
Table 5: 3 Low resolution single grid parameters.....	98
Table 5: 4 High resolution single grid parameters.....	99
Table 5: 5 Models for feedback prescription.....	101
Table 5: 6 Peak ebb and peak flood momentum fluxes across the nested boundary for BTWNM_I.....	103
Table 5: 7 Peak ebb and peak flood momentum fluxes across the boundary cells and cells adjacent to the boundary for BTWNM_I.....	104
Table 5: 8 Peak ebb and peak flood momentum fluxes across the nested boundary for BTWNM_II.....	106
Table 5: 9 Peak ebb and peak flood momentum fluxes across the boundary cells and cells adjacent to the boundary for BTWNM_II.....	107
Table 5: 10 Peak ebb and peak flood momentum fluxes across the nested boundary for BTWNM_III.....	108
Table 5: 11 Peak ebb and peak flood momentum fluxes across the boundary cells and cells adjacent to the boundary for BTWNM_III.....	109
Table 5: 12 Peak ebb and peak flood momentum fluxes across the nested boundary for BTWNM_IV.....	110
Table 5: 13 Peak ebb and peak flood momentum fluxes across the boundary cells and cells adjacent to the boundary for BTWNM_IV.....	111
Table 5: 14 Peak ebb and peak flood velocities at point A.....	113
Table 5: 15 Peak ebb and peak flood velocities at point B.....	114
Table 5: 16 Peak ebb and peak flood velocities at point C.....	115
Table 5: 17 Peak ebb and peak flood velocities at point D.....	116
Table 5: 18 Results of the time history analysis for point E.....	118

Table 6: 1 Feedback condition models .....	123
Table 6: 2 Peak ebb and peak flood momentum flux across the nested boundary for BTWNM_MOM (V+E).....	125
Table 6: 3 Peak ebb and peak flood momentum for the propagation into the nested domain for BTWNM_MOM (V+E).....	126
Table 6: 4 Peak flood and peak ebb velocities of point A.....	128
Table 6: 5 Peak flood and peak ebb velocities of point B.....	129
Table 6: 6 Peak flood and peak ebb velocities of point C .....	130
Table 6: 7 Peak flood and peak ebb velocities of point D.....	130
Table 6: 8 Peak flood and peak ebb velocities of point E .....	132
Table 6: 9 Peak ebb and peak flood momentum fluxes across the nested boundary for BTWNM_MOM Q (ALL).....	133
Table 6: 10 Peak ebb and peak flood momentum for the propagation into the nested domain for BTWNM_MOM (Q (ALL)). .....	134
Table 6: 11 Peak flood and peak ebb velocities of point A for BTWNM_MOM (Q (ALL)). .....	135
Table 6: 12 Peak flood and peak ebb velocities of point B for BTWNM_MOM (Q (ALL)). .....	136
Table 6: 13 Peak flood and peak ebb velocities of point C for BTWNM_MOM (Q (ALL)). .....	137
Table 6: 14 Peak flood and peak ebb velocities of point D for BTWNM_MOM (Q (ALL)). .....	138
Table 6: 15 Peak flood and peak ebb velocities of point E for BTWNM_MOM (Q (ALL)). .....	139
Table 6: 16 Peak ebb and peak flood momentum fluxes across the nested boundary for BTWNM_KIN (V+E).....	140
Table 6: 17 Peak ebb and peak flood momentum fluxes across the nested boundary cells and cells adjacent to the boundary for BTWNM_KIN (V+E) .....	141
Table 6: 18 Peak flood and peak ebb velocities of point A for BTWNM_KIN (V+E).....	142
Table 6: 19 Peak flood and peak ebb velocities of point B for BTWNM_KIN (V+E).....	143
Table 6: 20 Peak flood and peak ebb velocities of point C for BTWNM_KIN (V+E).....	144
Table 6: 21 Peak flood and peak ebb velocities of point D for BTWNM_KIN (V+E).....	145

Table 6: 22 Peak flood and peak ebb velocities of point E for BTWNM_ KIN (V+E).....	146
Table 6: 23 Peak ebb and peak flood momentum flux across the nested boundary for BTWNM_KIN Q (ALL)).....	147
Table 6: 24 Peak ebb and peak flood momentum for the propagation into the nested domain for BTWNM_KIN (Q (ALL)).....	148
Table 6: 25 Peak flood and peak ebb velocities of point A for BTWNM_ KIN (Q (ALL)..	149
Table 6: 26 Peak flood and peak ebb velocities of point B for BTWNM_ KIN (Q (ALL)..	150
Table 6: 27 Peak flood and peak ebb velocities of point C for BTWNM_ KIN (Q (ALL)..	151
Table 6: 28 Peak flood and peak ebb velocities of point D for BTWNM_ KIN ((Q (ALL)).	152
Table 6: 29 Peak flood and peak ebb velocities of point E for BTWNM_ KIN ((Q (ALL)).	153
Table 6: 30 Interpolation models.....	154
Table 6: 31 Peak ebb and peak flood momentum flux across the nested boundary for BTWNM_COPY .....	155
Table 6: 32 Peak ebb and peak flood momentum fluxes across the boundary cells and cells adjacent to the boundary for BTWNM_COPY.....	156
Table 6: 33 Peak flood and peak ebb velocities of point A for BTWNM_ COPY. ....	157
Table 6: 34 Peak flood and peak ebb velocities of point B for BTWNM_ COPY. ....	158
Table 6: 35 Peak flood and peak ebb velocities of point C for BTWNM_ COPY.....	159
Table 6: 36 Peak flood and peak ebb velocities of point D for BTWNM_ COPY. ....	160
Table 6: 37 Peak flood and peak ebb velocities of point E for BTWNM_ COPY.....	161
Table 6: 38 Peak ebb and peak flood momentum flux across the nested boundary for BTWNM_SHAP .....	162
Table 6: 39 Peak ebb and peak flood momentum for the propagation into the nested domain for BTWNM_SHAP.....	163
Table 6: 40 Peak flood and peak ebb velocities of point A for BTWNM_ SHAP. ....	164
Table 6: 41 Peak flood and peak ebb velocities of point B for BTWNM_ SHAP. ....	165
Table 6: 42 Peak flood and peak ebb velocities of point C for BTWNM_ SHAP.....	166
Table 6: 43 Peak flood and peak ebb velocities of point D for BTWNM_ SHAP. ....	167
Table 6: 44 Peak flood and peak ebb velocities of point E for BTWNM_ SHAP.....	168

Table 6: 45 Peak ebb and peak flood momentum flux across the nested boundary for BTWNM_FULLLW .....	169
Table 6: 46 Peak ebb and peak flood momentum for the propagation into the nested domain for BTWNM_FULLLW.....	170
Table 6: 47 Peak flood and peak ebb velocities of point A for BTWNM_FULLLW. ....	171
Table 6: 48 Peak flood and peak ebb velocities of point B for BTWNM_FULLLW.....	172
Table 6: 49 Peak flood and peak ebb velocities of point C for BTWNM_FULLLW.....	173
Table 6: 50 Peak flood and peak ebb velocities of point D for BTWNM_FULLLW. ....	174
Table 6: 51 Peak flood and peak ebb velocities of point E for BTWNM_FULLLW.....	175
Table 7. 1 Sections of code added to BTWNM to enable the introduction of tidal turbines .....	182
Table 7. 2 Percentage change in peak ebb and peak flood velocities at point 1 for 0.5 rotor spacing.....	187
Table 7. 3: Percentage change in peak ebb and peak flood velocities at point 2 for 0.5 rotor spacing.....	188
Table 7. 4 : Percentage change in peak ebb and peak flood velocities at point 3 for 0.5 rotor spacing.....	189
Table 7. 5 : Percentage change in peak ebb and peak flood velocities at point 1 for 2 rotor spacing. ....	191
Table 7. 6 Percentage change in peak ebb and peak flood velocities at point 2 for 2 rotor spacing. ....	192
Table 7. 7 Percentage change in peak ebb and peak flood velocities at point 3 for 2 rotor spacing. ....	193
Table 7. 8 Percentage change in peak ebb and peak flood velocities at point 1 for 5 rotor spacing. ....	195
Table 7. 9 Percentage change in peak ebb and peak flood velocities at point 2 for 5 rotor spacing. ....	196
Table 7. 10 Percentage change in peak ebb and peak flood velocities at point 3 for 5 rotor spacing.....	197

## Mathematical notations

$A$	Exact solution to the continuous partial differential equation
$AE_T$	tidally-averaged absolute error
$A_n$	Solution generated from a finite difference scheme
$C$	Chezy bed roughness coefficient
$c$	Coarse grid/ parent grid
$C_n$	Courant number
$C^*$	Air-water interface coefficient
$C_w$	Speed of a gravitational wave
$f$	Coriolis parameter
$f_{c/n}$	Coarse/nested model forcing
$g$	gravity
$h$	water depth below datum
$H$	total water depth ( $h+\eta$ )
$I, J$	x and y coordinate direction of coarse grid cells on computational grid
$i, j$	x and y coordinate direction of nested grid cells on computational grid
$n$	time step level
$n$	Nested grid/ child grid
$N$	Normal vector to an open boundary
$OB$	Open boundary operator
$p_{c/n}$	Coarse/nested grid partial differential method
$q_x, q_y$	depth integrated volumetric flux in the x,y directions ( $q_x=UH, q_y=VH$ )
$R$	Updating operator
$RE_T$	tidally-averaged relative error
$Rn$	Rotated nested grid
$r_s$	Nesting ratio

$t$	time
$U, V$	depth integrated velocity components in the x,y directions
$u, v, w$	velocities in the x, y, and z direction respectively
$W_x, W_y,$	Wind velocity in x and y direction
$w$	Coefficient of proportionality
$x,y,z$	Coordinate directions in the three-dimensional Cartesian plane
$\xi,\eta$	Coordinate directions in two-dimensional rotated plane
$\varepsilon$	Depth mean eddy viscosity
$\Gamma$	boundary
$\Gamma^*$	Ghost cell
$\alpha$	Relaxation factor
$\beta$	momentum correction factor for non-uniform vertical velocity profile
$\Delta x$	x-direction grid spacing
$\Delta y$	y- direction grid spacing
$\Delta \xi$	$\xi$ - direction grid spacing
$\Delta \eta$	$\eta$ - direction grid spacing
$\Delta t$	model time step
$\theta$	Angle of rotation
$\zeta$	water elevation above or below datum
$\phi$	State variables
$\rho$	fluid density
$\rho_a$	density of air
$\nu_t$	depth integrated mean eddy viscosity
$\Omega$	domain

# CHAPTER 1: INTRODUCTION

## 1.1 TIDAL POWER INDUSTRY

The increase in global warming and the reduction in the sources of fossil fuels have led to a focus on renewable forms of energy. Many forms of renewable energy are coming to the forefront as possible leading technologies in this growing industry. One such form of renewable energy is tidal power. Tidal power has the advantage over other forms of energy sources due to its predictable nature. Hence, it is a very attractive renewable energy source to take advantage of (SEI 2009).

Large strides have occurred in the tidal power industry in relation to the design and development of tidal turbine devices to optimise the energy extraction from tides. However, considerably little research has been undertaken in relation to the possible environmental impacts that could occur with the extraction of energy from a tidal regime.

This is of considerable importance as the optimum location for energy extraction from tides is in coastal zones. Coastal zones are home to a large number of environmentally important eco systems, as well as being home to a large percentage of the world's population. Changes to the tidal regime in coastal zones could affect: environmentally protected habitats, the shipping industry, tourism, flooding and pollutant transportation (Dacre 2007). A major challenge for the tidal power industry is to minimise adverse environmental impacts that could occur with the extraction of energy from tides. Understanding the changes that could possibly occur with the introduction of tidal farms is crucial for the development of the tidal power industry. Hence, the European Union is keen to make it a focus of research projects internationally. One such EU funded project was the MAREN project (MAREN 2013).

The installation of tidal farms with minimal environmental impacts is impossible without understanding the hydrodynamic processes in a coastal zone and how these processes will respond to changes within the environment. Two of the main ways to

gain knowledge of hydrodynamic systems are: 1) measured data and 2) modelling. Measuring possible environmental impacts on site is extremely expensive and also unrealistic. Therefore, numerical modelling can be used to simulate a tidal farm and identify possible changes in the tidal regime.

## **1.2 NUMERICAL MODELLING**

Numerical models of coastal zones have been continually changing and evolving to “correctly” represent the complex hydrodynamic processes involved in these areas. Numerical modelling allows a means of simulating adverse changes in the hydrodynamics, such as energy extraction by tidal turbines, and identifying how these changes can affect the system as a whole. Therefore, accurate hydrodynamic modelling of tidal farms has potentially great value in the area of research and in industrial management and development.

Hydrodynamic models, in a management context, ideally make predictions in a sufficient time frame with determined confidence limits so they can be used in decision-making processes. These models are generally of a simple form to allow them to be used repeatedly. However, in the context of scientific research simplistic models can hinder the value of the information being sought, when the aim of the hydrodynamic model is to gain insight into the role of small scale processes in the whole hydrodynamic system.

In an industrial and research setting the control of cost is one of the main parameters in the use of certain hydrodynamic models. Simulation times in hydrodynamic models are directly linked to the cost of modelling. In order to reduce cost a reduction in the computational effort needs to be achieved, and hence allowing a reduction in simulation time. In addition, models with a low simulation time are essential in a management context to enable them to be used in decision making processes.

### 1.3 AIMS AND OBJECTIVES

The primary objective of the research was to reduce the computational needs of a widely used hydrodynamic model. Model resolution is one of the main determinants of computational needs. High resolution models can have great computational costs; however, they produce a higher level of accuracy in comparison to low resolution models that have lower computational effort but have a lower level of accuracy. To try and incorporate the positive benefits of both models different techniques can be introduced into the model. One such technique is nesting, which allows a high resolution in areas of interest and a lower resolution in the rest of the model domain, hence reducing the computational effort.

The hydrodynamic model used in this research, DIVAST (depth integrated velocity and solute transport) is a two-dimensional, depth integrated, finite difference model which is applicable to well mixed shallow water bodies such as coastal zones.

The first aim of the research was to modify an existing one-way nested modelling technique in DIVAST to increase the applicability and flexibility of the nested domain and further reduce the computational needs of the model. These modifications were carried out in two ways: 1) the development of irregular geometry boundaries, 2) the transformation of the nested domain into a rotational coordinate system.

The second aim of the project was to develop an effective two-way nested model. This development involved a number of stages to identify the optimum two-way nesting technique, which allows the maximum transfer of data from the nested domain while insuring the conservation of properties. The following elements were examined to identify their effects on the performance of the model: the prescription of variables at the feedback interface, the technique used for the interpolation of the high resolution nested domains data and the type of feedback conditions used at the feedback interface.

The third aim of the research was to use the two-way nested model to identify changes in hydrodynamics that can occur with the introduction of tidal turbine farms of different array configurations. This was achieved by manipulating the governing momentum equations with the use of the Linear Momentum Actuator Disc Theory (LMADT) (Houlsby 2008) to simulate the extraction of energy that occurs with the deployment of tidal turbine farms.

Through these techniques numerical finite difference models can be used as desktop management tools in the area of research and industry without incurring large computational cost.

## **1.4 THESIS LAYOUT AND CONTENT**

The following is the layout and content of this thesis:

A literature review of techniques used to try and accurately model coastal zones are presented in Chapter 2. The resolution of models and their relationship with computational costs are outlined initially. Different grid structures are outlined in relation to their spatial resolution. Nesting modelling techniques are introduced and their advantages and disadvantages discussed. The two-way nested modelling technique is explained in detail in relation to its mathematical formulation and common approaches are reviewed. The strategy for the research is presented based on the literature review, along with the unique aspects of the research.

The theory for the numerical model, DIVAST, is presented in Chapter 3. The governing equations, solution scheme and finite difference method are all outlined.

Chapter 4 outlines the development of the addition features introduced into the existing one-way nested model, which include a unique feature of irregular geometry boundaries and a rotational coordinate system.

Chapter 5 outlines the initial phase for the development of the basic two-way nested model (BTWNM). This phase involves the design and construction of the initial version of the BTWNM. The model was then used to identify the optimum variable prescription at the updating/feedback interface. Chapter 6 looks into the optimum feedback condition and interpolation technique to maximise the feedback of information and to insure the conservation of properties.

Chapter 7 presents the development of a two-way nested model with the introduction of tidal turbines. The simulations of the tidal turbine farms with different array configurations are described. The performance and accuracy of the model are tested and results are presented.

A summary of the research and the final conclusions are presented in Chapter 8 along with future possible methods to progress the research.

# CHAPTER 2: LITERATURE REVIEW

## 2.1 INTRODUCTION

An increase in horizontal resolution in a numerical model without an excessive increase in computational needs is one of the key points required in the improvement of numerical modelling in coastal zones. Computational needs are directly linked to the spatial and temporal resolution of a numerical model (Debreu 2008).

The bathymetries of coastal zones are very complex, due to erosion and sedimentation constantly occurring by tides, wind and wave movement in the areas. High resolution modelling is required in such areas to correctly simulate the complex hydrodynamic processes, the transport of solutes and also to take into account the influence of coastal boundaries.

The location of open boundaries is another problem for coastal modelling. Boundaries must be positioned in locations that do not negatively affect the model predictions of variables in an area of interest. This positioning can lead to the requirement of a large computational domain with the area of interest occupying only a small portion of the model domain. If the area of interest requires a high level of resolution, this typically requires a high resolution must be used across the full model domain, which leads to large computational costs.

One such solution to the spatial resolution problem involves the use of a nesting technique. Nesting allows areas of interest to be modelled with a high level of resolution without increasing the resolution of the entire domain, hence allowing for a reduction in the computational needs without adversely affecting the model solution.

## 2.2 HYDRODYNAMIC MODEL RESOLUTION

Hydrodynamic modelling involves transforming the governing equations that represent flow fields in a water body from a differential form to an algebraic differential form. The algebraic difference equations can then be solved to generate a solution to variables at points in time and space. There are a number of different methods used by hydrodynamic models to generate these algebraic equations, such as the finite difference method (Falconer 2001), the finite volume method (DHI 2013) and the finite element method (Denot 2012). These methods involve dividing space and time into intervals to allow an approximation of the solution to the governing equation to occur. This segmentation processes is known as the resolution of the hydrodynamic model.

The computational needs of a numerical model are governed by the resolution of the model, as the governing equations need to be solved at each discrete point in space and time. The main criteria for an optimal numerical model are convergence, accuracy and stability. These aspects are directly linked to the resolution of the model domain with respect to both space and time. The Courant Condition governs the relationship between the time and space resolution. The spatial resolution is usually selected first, which dictates the models temporal resolution.

## 2.3 TEMPORAL RESOLUTION AND THE COURANT CONDITION

Model resolutions in time and space are linked and one influences the other in generating a stable and accurate solution (Debreu 2005). This link between the resolutions of space and time is governed by the Courant Condition. The Courant number is a measure of how fast a water particle will move through a segment in one time step, and the condition is often expressed in terms of this number. Equation 2.1 represents the Courant number ( $C_n$ )(Sheng 2005):

$$C_n = C_w \frac{\Delta t}{\Delta x} \quad (2.1)$$

where  $C_w$  represents the speed of a wave,  $\Delta t$  and  $\Delta x$  represent the time step and the grid spacing size respectively. The constraint placed on numerical models in relation to the Courant condition differs in explicit and implicit numerical solution

schemes. Explicit methods are required to meet the Courant stability criteria. Intrinsically stable implicit models choose their time step with respect to the Courant condition to reduce numerical dispersion (Adcroft 2004).

This accuracy requirement is less demanding on computational needs, however, this is still a requirement that generates a greater leave of computational effort. The accuracy requirement of the Courant condition for an implicit scheme involves the  $C_n$  value being less than a constant that has a value greater than 1 (Beevers 2009).

## **2.4 COMPUTATIONAL GRIDS AND SPATIAL RESOLUTION**

Water bodies are divided into spatial segments so they can be used as computational grids. There are three main types of domain segmentation: finite difference, finite element and finite volume. Computational grids can be of a structured or unstructured form. Structured grids consist of regularly spaced grid points, unlike unstructured grids that allow a variation in the spacing between grid points.

### **2.4.1 FINITE DIFFERENCE GRIDS**

Finite difference is the oldest computation fluid dynamic (CFD) technique and has been seen in publications as early as 1928 with the fundamental theoretical paper by Courant, Friedrichs and Lewy (1928). The initiation of computational experimentation was generated with the utilization of the finite difference approach (Thomé 2001).

Finite difference is used to calculate an approximation to a partial differential solution scheme. The differential forms of the governing equations are discretised into algebraic form and a Taylor series expansion method is used to calculate the first and second order derivatives. The resulting equations are solved in a simultaneous or iterative form.

The method requires that the computation grid be of a structured form. This structured form of the physical domain can be directly imposed or can be transformed to allow the computation domain to be of a structured form e.g. from cylindrical to rectangular.

There are many different finite difference models in the area of hydrodynamics such as DIVAST (Falconer 2001), ECOMSED and EFDC. According to Bakker (2008), the main advantage of finite difference is its ease of implementation; therefore, allowing it to be one of the most popular forms of solution schemes.

The most common grid system in a finite difference model is a structured uniform rectilinear grid (see Figure 2.1(a)). These models are constructed from equally spaced grid cells in two mutually orthogonal axes. The structured grid can also be of a rectangular type (see Figure 2.1(b)) that has a variation in the grid spacing in relation to the x and y direction. Structured uniform rectilinear grid systems have been successively applied to many water bodies around the island of Ireland, such as Galway Bay and Cork Harbour, with the employment of the finite difference model DIVAST (Nash 2010, Hartnett 2004).

Structured finite difference modelling domains, according to Rodenhuis (1994), are usually applied to water bodies that have relatively uniform characteristics i.e. open oceans and domains of uniform geometry. The main disadvantage in structured domains is the decrease in accuracy, mainly in relation to current velocities, with an increase in the complexity of a domain particularly in the presence of irregular boundaries (Rodenhuis 1994). The solution to such a problem involves increasing the number of grid points and decreasing the grid spacing. These large numbers of grid points increase the computation procedures, which in turn greatly increase the computation needs of a model.

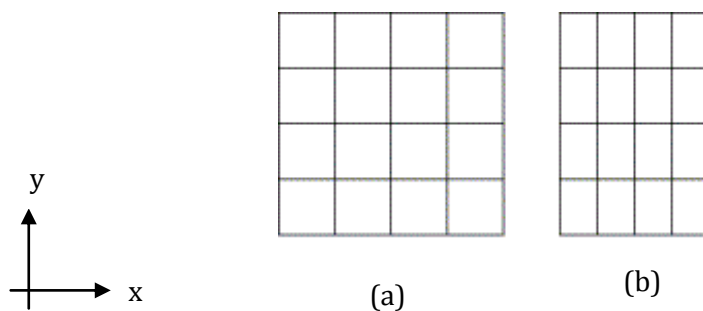


Figure 2: 1(a) Structured uniform grid (b) Structured rectangular grid

(Laramee 2003)

Stretched grid finite different meshes are one of the methods used to reduce the stringent limitations that are put on the grid spacing in relation to a structured grid system. This involves changing the grid spacing in the x and y-directions, to achieve

higher resolution in areas of interest (Martin 1999). Figure 2.2 shows an illustration of the stretched grid system represented in the physical domain and the domain that is read by the computer. The method involves the transformation of the physical domain to the computational domain; therefore, allowing the grid to be solved on a pseudo structured rectangular form. This allows the regular use of the finite difference method (Yu 2013).

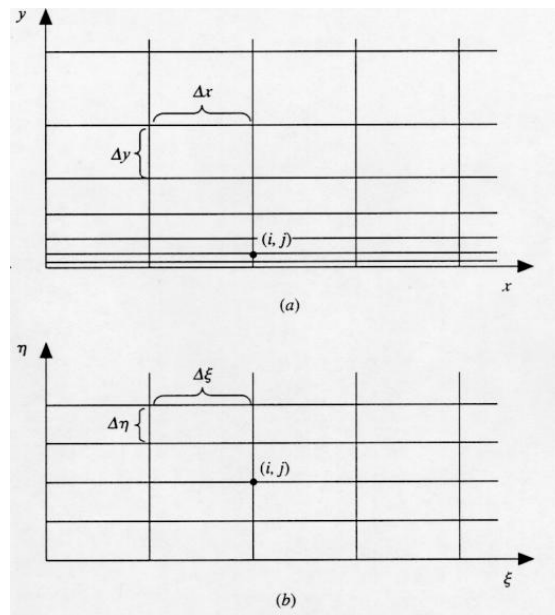


Figure 2: 2 (a) Physical grid system with coordinate system  $(x,y)$  (b) Computational grid system with coordinate system  $(\xi,\eta)$  (Yu 2013).

This method involves the introduction of transformation techniques to allow the spacing in both the  $x$  and  $y$  directions to vary in an exponential manner, however, Martin (1999) states this increases computational requirements of a hydrodynamic model and errors can arise when stretching between regions does not occur smoothly.

Boundary fitted grids or curvilinear grids are another type of finite difference method that has been used by Sheng (1988) in water bodies such as Lake Okeechobee, James River and Chesapeake Bay. This finite difference method allows the placing of grid points in a more flexible nature. It involves transforming the physical Cartesian domain onto a computational domain that is structured and rectangular in relation to a curvilinear coordinate system. The domain is constructed so that one of the curvilinear coordinates always follows the boundary, which allows for a high

level of resolution along the boundaries and a lower resolution in the rest of the domain (Yu 2013).

These systems are attractive due to their ability to better represent the boundaries of water bodies. There are two main types of curvilinear grid systems: orthogonal and non-orthogonal. An orthogonal scheme requires that all grid lines intersect close to perpendicular. This is not a requirement in the non-orthogonal grid; however, the movement away from orthogonality increases the risk of large error generation. An orthogonal mesh is illustrated in Figure 2.3 with a non-orthogonal shown in Figure 2.4.

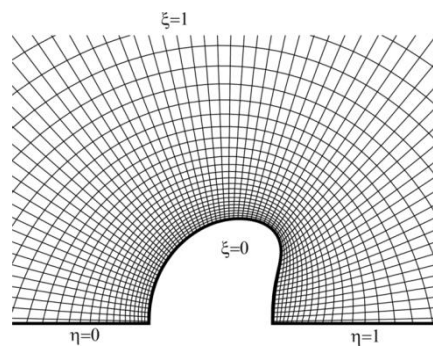
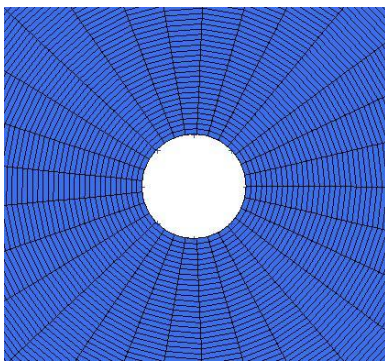


Figure 2: 3 Orthogonal grid

Figure 2: 4 Non-Orthogonal grid (Hong 2000)

This method involves additional transformation terms to be introduced into the numerical scheme, hence eliminating any computational saving from the reduction in the number of grid points. Other disadvantages associated with such schemes have been identified by Smith (1997) as: the generation of such a scheme is difficult and expensive, numerical dispersion is increased and conservation is not always guaranteed in the advective terms.

#### 2.4.2 FINITE ELEMENT GRIDS

Finite element was first used by Courant in 1943 in relation to torsion problem solving, with the use of approximate piecewise linear functions and a triangular mesh representing the geometry of the domain (Thomé 2001). The method was refined greatly for use in structural mechanics with the work of Clough and Zienkiewicz (Thomé 2001). The field of fluid dynamics incorporated finite element schemes with the work of Gray and Lynch and Foreman (Bakker 2008).

The method allows the computational domain to be of a structured or unstructured form. This, unlike the finite difference method, allows the algebraic form of the governing equations to be calculated directly in the physical plane on a non-uniform grid.

The finite element method has become quite competitive relative to the finite difference scheme due to the introduction of advanced methods by Gray and Lynch, which involved using their 'wave equation' scheme. This scheme transforms the continuity equation to a second order partial differential form and solves the system of equations with a Galerkin finite element method, piecewise linear basic functions and central time stepping (Thomé 2001). There are a number of finite element models used in the area of hydrodynamics, such as TABS and TELEMAC.

The U.S Army Cooperation of Waterway Experimental Hydraulic Group developed the finite element hydrodynamic model TABS. The model is a vertically average, fully implicit, two dimensional finite element model. This model consists of a subprogram called GFGEN (geometry file generation program), which provides a system for the development of the finite element mesh generation. The mesh can fill the model domain with triangular grids, quad lateral grids ( see Figure 2.5) and grids generated by an underlying function that is calculated in relation to density (Mcarthur 1996).

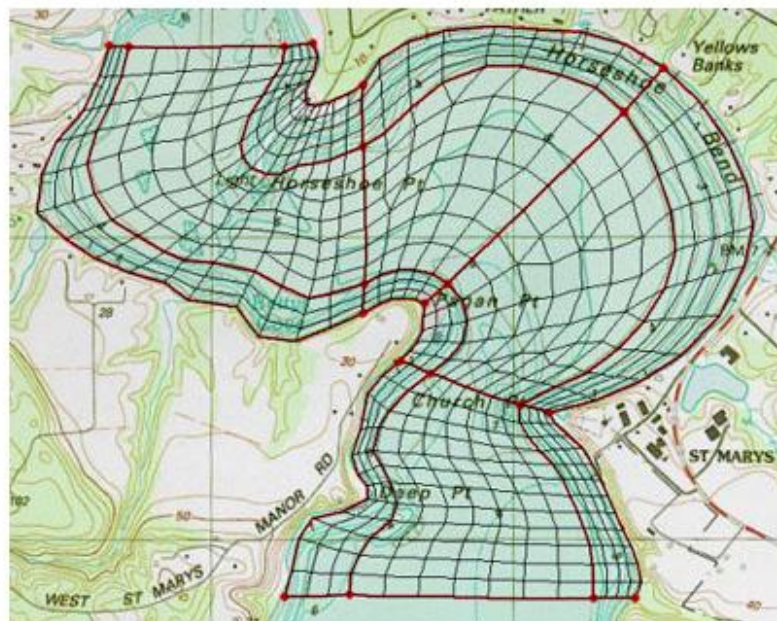


Figure 2: 5 Finite element domain generated by GPGEN (Group 2013)

This model has been applied to many estuaries and water bodies for the modelling of hydrodynamic, salinity and sediment transport, such as Laguna Madre and Galveston Bay in the Gulf of Mexico. It was also applied in Florida Bay to study the effects of alternating freshwater release on the circulation and salinity distribution in the bay (Kim 2004).

A finite element scheme has also been used by Lam (2004) for a watershed management study on Lake Seymour in Canada. The model used was TELEMAC-2d, which was developed in France by the Laboratoire National d'hydraulique et Electricite. This model generates a triangular unstructured grid to provide two dimensional simulation of current, elevations and solute transport to be performed (Lam 2004). TELEMAC-2d was also used in the La Rance estuary for the forecasting of sediment transport. Figure 2.6 shows the mesh of the coastal domain for the hydrodynamic model (Denot 2012).

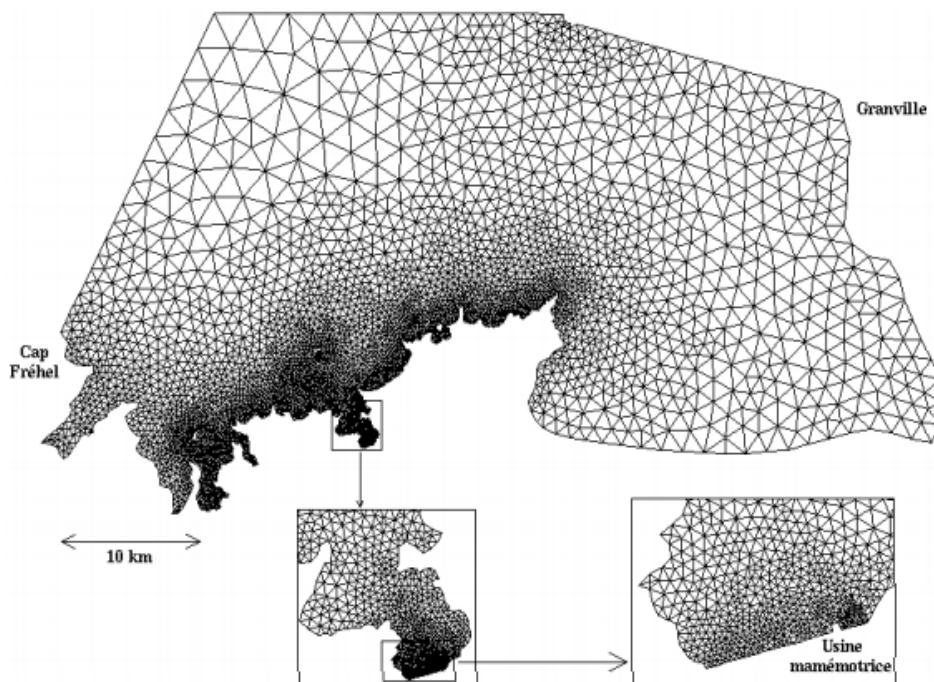


Figure 2: 6 TELEMAC-2D mesh of coastal domain (Denot 2012)

The advantage of finite element schemes are their ability to be geographically flexible i.e. the elements in the domain can readily change shape to follow complex boundaries and geographical features (Kantha 2000). This advantage can lead to a

more accurate bathymetry representation which may result in a better representation of flow.

Disadvantages associated with the method are the extensive runtimes required to solve large problems. There is a possibility of noise generation due to wave reflection and other errors occurring if grid points are not ordered in a regular sequence, hence a careful ordering of the elements is essential to the accuracy of the model (Mcarthur 1996; Nash 2010).

### 2.4.3 FINITE VOLUME GRIDS

Finite volume is another method for evaluating partial differential equations. This method was first introduced in 1957 by Evans and Harlow at Los Alamos (Bakker 2008). The method involves generating a solution for the variables at each grid point in a model domain. The main difference in relation to a finite difference scheme is the inclusion of a diversion coefficient with respect to a finite volume. This allows for a more accurate representation of an irregular boundary domain in comparison to a finite difference model. However, this method is more time consuming and more sensitive to error generation. Figure 2.7 shows an unstructured finite volume mesh with control volumes in a triangle shape.

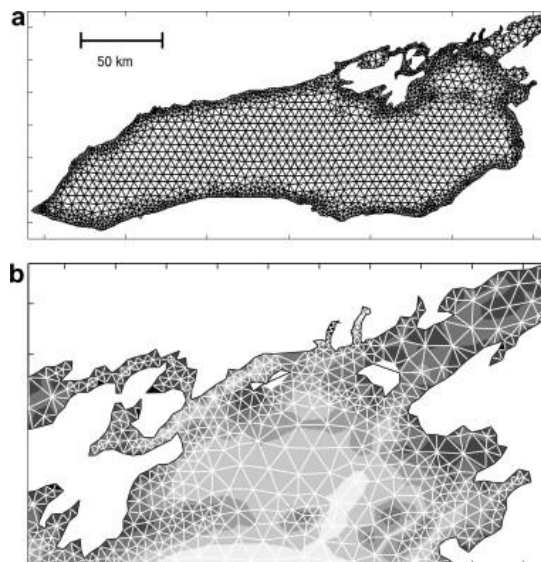


Figure 2: 7 Unstructured Finite Volume mesh (Shore 2009)

The procedure involves the domain been divided up into control volumes (see Figure 2.8). The differential equations are integrated over the control volume incorporating the divergence theorem. The values at the faces of the control volume are re-

quired for the evaluation of the derivative terms, along with an assumption to how much the values will vary. This method results in a set of equations for each control volume, which are solved in sequence or simultaneously (Daoud 2008).

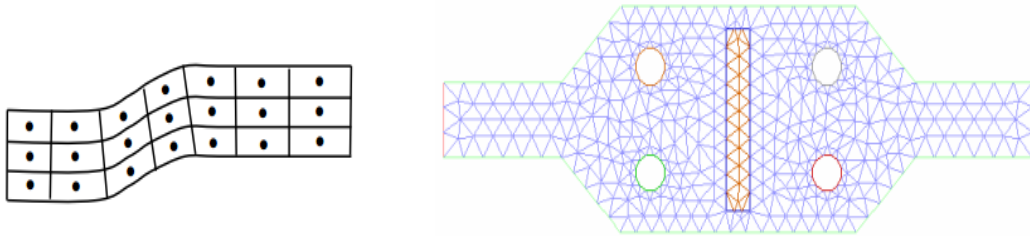


Figure 2: 8 Control volumes (Bakker 2008)

There are a number of different types of finite volume scheme in hydrodynamics and these can be classified in relation to the type of flows that are being simulated.

Schemes simulating superficial flows, discontinuous flows and capturing bore waves like the model employed by Mingham (1998) to allow the simulation of dam breaking phenomena employ schemes that include flux splitting, flux limiters and Riemann solvers.

Finite volume models have also been used in rivers, estuaries and harbours for the modelling of tidal and wind induced currents. Olsen (1995) used a finite volume scheme for the modelling of Norwegian river Sokna to calculate the interaction between porous and non-porous areas. The method was also used by Demirdzic (1990) for the representation of flow in a channel with a moving indentation. The SIMPLE algorithm is employed by both these models for the coupling of pressure and velocity.

Advantages of the finite volume method are the unlimited shape of the cells; hence, it can easily describe irregular boundaries. Also the method exhibits good conservation of properties on low resolution domains.

The disadvantages that can occur are the introduction of false diffusion error with simple numerics. The computational needs of the scheme in coastal zones and estuaries are greater than the finite difference method, however, less demanding than the finite element scheme (Petrila 2005).

## 2.5 ADVANCED COMPUTATIONAL GRIDS

### 2.5.1 HYBRID GRID

Hybrid schemes involve the incorporation of different types of grid systems for the representation of the model domain. These methods allow the use of different spatial interpolation techniques in a single model at different sections of the physical domain. Figure 2.9 shows an illustration of a physical domain that contains a structured grid system, unstructured finite element system and a boundary fitted grid system. This mesh configuration was used by Xinghua (2012), for the modelling of a fish swimming in a thunniform mode, to further understand the influence of Reynolds stresses and turbulence on the movement and also characteristics of the wake formation from the fish during locomotion.

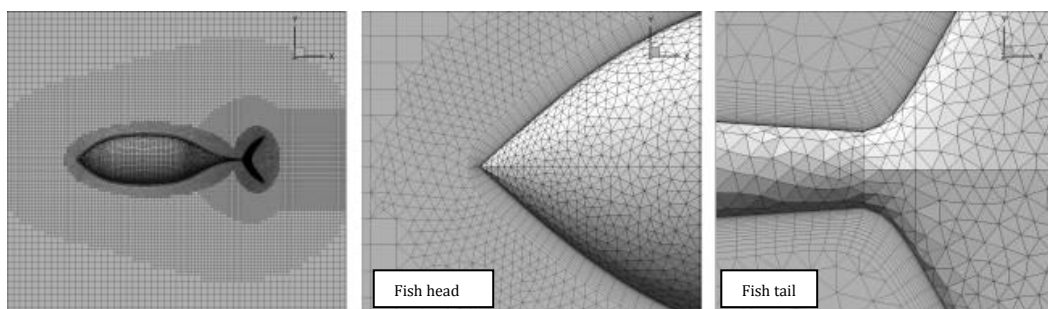


Figure 2: 9 Hybrid grid (Xinghua 2012)

A hybrid meshing scheme was used in a hydrodynamic study of tributaries in the River Elba and the River Danube, which were undertaken by Berkahn (2005). The study used a finite element hybrid system that contained structured and unstructured features. The model involved generating a mesh with regular elements for the river bed and area of significant terrain slope but allowing floodplains to be represented as irregular triangular meshes. Figure 2.10 shows an illustration of the hybrid mesh used in the River Danube for the study.

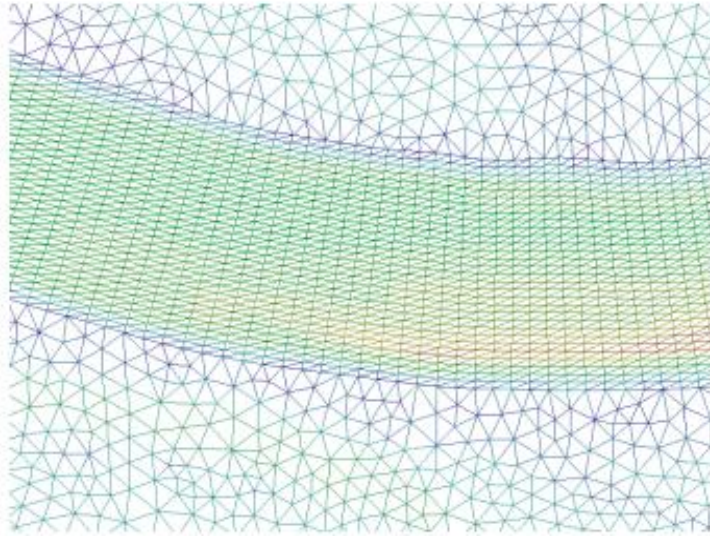


Figure 2: 10 Finite Element hybrid mesh of the River Danube (Berkhahn 2005)

Wang (2006) presented an approach for the generation of unstructured hybrid systems that contained prismatic and tetrahedral elements for the computation of viscous flow through a pipe section with a ball valve. Figure 2.11 shows an illustration of the hybrid mesh, which consists of a triangular surface mesh, prismatic elements at the boundaries and a tetrahedral grid on the rest of the domain.

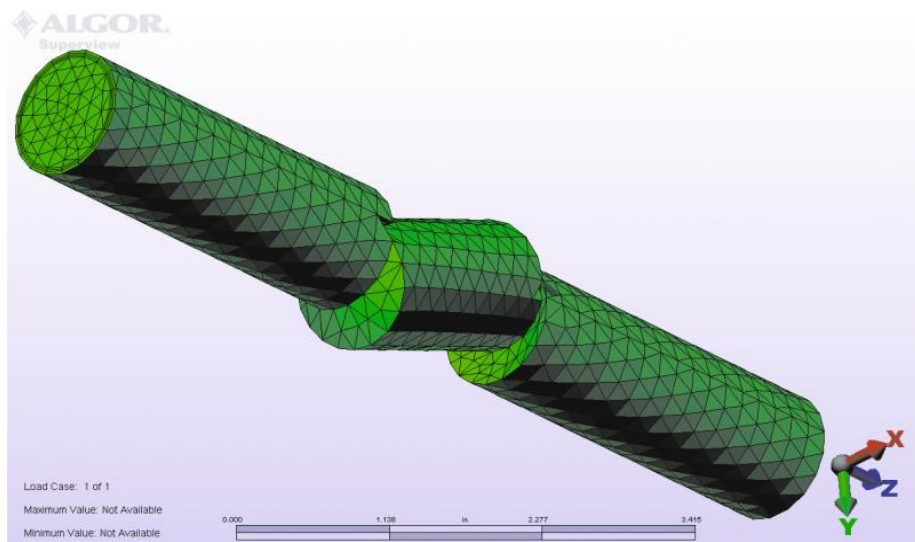


Figure 2: 11 Hybrid grid of pipe with ball valve (Wang 2006)

Hybrid meshes are attractive due to their ability to incorporate the positive features of different types of meshes into one model domain. However, the introduction of different types of interpolation schemes requires a large number of integration sequences to be included, which leads to a large strain on the computational needs of the model. These forms of grid structure are also more difficult to implement in comparison to a nesting modelling technique.

### 2.5.2 QUADTREE GRIDS

Quadtree is a grid generation technique that can adapt itself to a sufficient level of refinement until an accurate solution is generated. This method involves generating a domain in a Quadtree structure. This hierarchy method involves dividing grid cells into four equal smaller cells. These sub-cells are further divided and the process repeated until a sufficient level of resolution refinement is achieved. Figure 2.12 shows an illustration of a simple grid and its Quadtree representation.

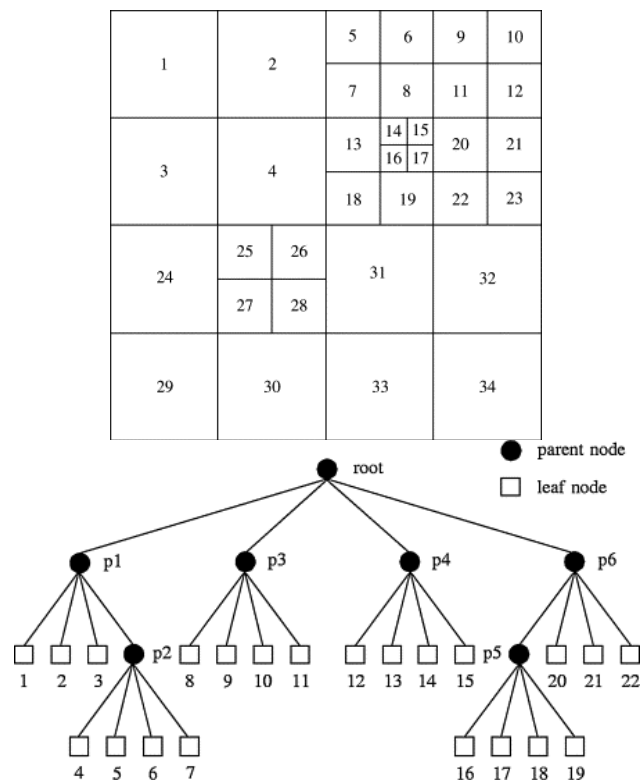


Figure 2: 12 Simple quadratic grid and its tree representation (Park 2006)

One of the earliest uses of this method was for the reduction in computational space required for computer images by spatial decomposition (Samet 1990). Borthwick used a Quadtree adaptive grid to solve the depth-averaged, shallow water equations for the approximation of flow in large complex shallow water domains, while focusing on localized small scale processes/features. The method was used to model Laminar jet-forced flow in a circular basin (Borthwick 2001), with flow pattern results complying with alternative models (e.g. (Borthwick 1993)). Borthwick (2000) also used this method for a pollutant transport model of the Sepetibe Bay in Brazil. The model allowed the representation of a complex domain and showed the dissipation of a pollutant from a continuous discharge point. Wave-current interaction in a complex coastal environment was modelled by Park and Borthwick using this technique, with model results coinciding adequately with laboratory based results (Park 2006).

Flood inundation was modelling by Liang (2008) using a Quadtree grid. The model used was applied to a realistic scenario of flooding, by the River Thames in the UK, over 36 km<sup>2</sup> of urban area. Results generated were comparable to predictions made by the commercially available software TUFLOW.

The initial problem encountered with such a technique includes storing and receiving information for the grid, caused by the recurring tree type structure. This large storage space hinders the efficiency of a computational model and requires a computer to run the model with a large amount of storage space, which is not the case for a nested modelling technique. Hanging nodes, which are adjacent cells of different size that are generated during refinement, are also a problem. Interpolation techniques are also required across the cell interface to ensure conservation. These interpolation techniques can offset some of the computational savings.

### **2.5.3 ADAPTIVE GRID SYSTEM**

This method allows for a change in the grid system in relation to time. The grid domain moves during a model simulation and adapts its resolution to allow for higher degrees of resolution at different stages of the model simulation time. The physical model can move in relation to the solution to the flow field properties. This non-static grid domain is attractive for coastal models that highlight a process during a

flow regime i.e. discharges from industries and water treatment facilities or a propagation of a wave front.

Adaptive grid domains have been used extensively in the area of meteorology particularly in hurricane modelling. The adaptive nest procedure allows for the high resolution domain to be approximately the size of the hurricane itself. In contrast, static models require a high resolution domain in the full region of the hurricane movement, which incurs high computation costs (Bender 2007).

The ground breaking work of Berger and Olinger (1984) paved the way for adaptive mesh refinement schemes in ocean modelling. This scheme involves a set of algorithms that are uniform in space and time, with areas of interest containing fine grids overlapping coarse i.e. nested domains. The scheme uses a Cauchy type coordinate and grids system that generates a solution in a particular time frame at a particular resolution (Berger 1984).

The purpose of the method is to gain certain level of accuracy for the minimum amount of work. The method used a truncation error established by the Richardson method generated at regular intervals of time, to identify areas that require higher level of nesting where and when necessary. The method is recursive; therefore, the finer grids may themselves contain even finer grids. Figure 2.13 shows an illustration of the hierarchy of the solution grid.

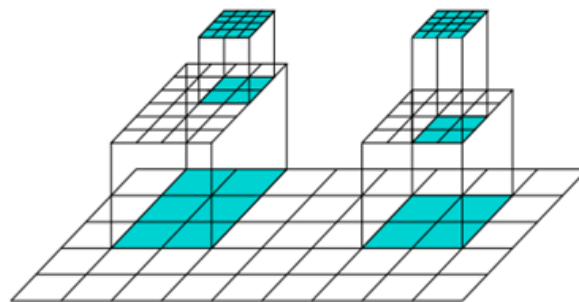


Figure 2: 13 Adaptive mesh refinement

Blayo (1999) used this method and applied it to a case with two levels of nesting with a ratio of 4. The truncation error was calculated every 10 coarse time steps and movement/re-gridding was performed if necessary. Figure 2.14 shows an illustration of the static nested domain, used in the research, and the adaptive nested do-

main and their movement with time. The results generated showed a 20% decrease in error in the adaptive nested model.

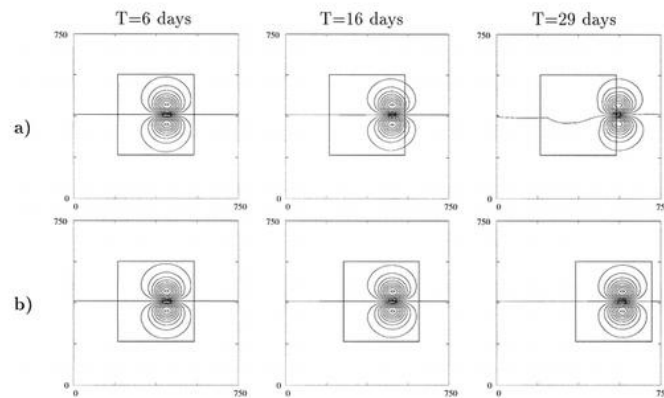


Figure 2: 14 (a) Static nested domain (b) Adaptive nested domain

(Blayo 1999)

Rowley (1999) compiled a simpler method for adaptive modelling by allowing the nested domain to move during a model simulation; however, the structure and configuration of the nested domain remains constant throughout the modelling procedure. Movement of the nested domain can be specified by the user at the start of the simulation if the movements of the features of interest are pre-determined. The model can also induce the movement of the domain during the course of the simulation by using some pre-determined rules (Rowley 1999).

There are a number of problems encountered with such a scheme: the time integration in the nested domain needs to be at the same level as the parent/coarse domain the conservation of properties is essential as the nested domain moves position.

The Rowley method was used as a basis for the development of an adaptive mesh model in the finite difference model DIVAST by Nash (2010). The model allowed the predetermined or automatic movement of the nested domain and the size and the shape of the domain to be altered at any time during the model simulation.

## 2.6 NESTED MODELS

An increase in resolution of a numerical model improves the realism of the model solution in areas of interest that contain small scale features. This increase in resolution is not generally required throughout the full model domain, especially in areas

of low gradient/less complex bathymetry where a lower resolution is sufficient. However, open boundaries must be located in areas such that their conditions do not adversely affect the model solution in an area of interest, this can lead to a requirement of a large computational domain, which the area of interest representing only a small proportion. This high resolution across a large domain can lead to high computational costs.

Nesting methods have been implemented into numerical hydrodynamic models to locally refine features of a domain. This allows a more accurate solution to the hydrodynamic model to be achieved in areas of interest, without a large increase in computational time. The method involves the embedding of a higher resolution grid into a lower resolution grid, which covers the full model domain. There are two main types of nesting procedures, they are the one-way/passive method (Anthes 1974) and two-way/interactive method (Zhang 1986). One-way nested model allow interaction between the two domains through the coarse grid providing boundary conditions for the nested grid, while two-way nesting allows additional interaction between the two domains by using the high resolution nested grid solution to update the coarse domain solution.

In the area of metrology, nesting is a well-established numerical technique for reducing the computational needs of numerical models. The first area in metrology to use this method was in the prediction of hurricanes and their movement patterns with the work of Birchfield (1960). Further work by Harrison (1973) and Ookochi (1972) allowed nested modelling to be a well known numerical technique in the area by the late 1970s.

Nesting techniques were initially used in the area of hydrodynamics by Holland (1990) for the generation of a nested high resolution model of the California current region embedded in a low resolution North pacific model. The area of ocean hydrodynamics does not contain a large number of nested domain models. The main contributor to this decrease in growth is lack of global ocean forecasting models in comparison with atmospheric models that are routinely run in many numerical weather prediction centres around the world (Bleck 2002).

## 2.6.1 ONE-WAY NESTED MODELLING

One-way nesting is applied to models to generate a higher level of resolution in an area of interest. The nested domain is positioned so it is overlapping the coarse domain (see Figure 2.15). This allows the models to run almost completely separately to compute the area of interest in both levels of resolution. Interaction between the domains occurs in the area of the boundary of the nested domain. The boundary conditions for the nested domain are generated from the coarse domains data that are interpolated in space and time. The coarse domain is initially integrated in time and the data required for the nested domains boundary conditions is preserved and modified to collaborate with the fine domains resolution. The fine domain hydrodynamic solution is then performed using the boundary data with the fine domain time step.

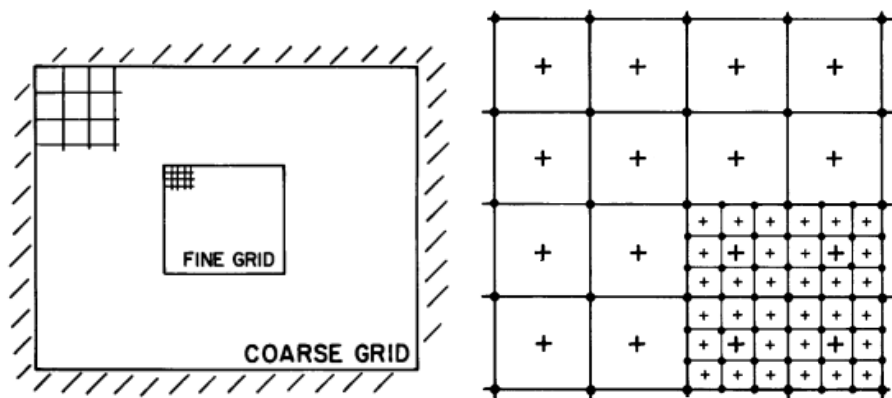


Figure 2: 15 Coarse and fine/nested grids

One-way nested models are used in operational forecasting in the area of meteorological, such as the Washington WRF model and the Oklahoma ARPS/wx model. Colle (2005) applied a one-way nested version of the Pennsylvania University's meteorological mesoscale model (MM5) to areas over and upstream of the Wasatch Mountains. The model developed consisted of 4 levels of one-way nesting. The nested model allowed accurate representation of kinematic flow and precipitation evolution in the central region of the mountains that required a high level of resolution, without the need for a high resolution model of the full domain (Colle 2005).

Spall and Robinson (1989) were the first to use the one-way nesting technique in hydrodynamics for the simulation of a mesoscale eddy field, and it has since been applied to many studies of oceans and coastal waters. For example, Penven (2006)

developed and applied a one-way nested model of the central California upwelling system. The method involved the integration of a nested grid into the Regional Oceanic Modelling System (ROMS). The model was applied to a domain that spanned the continental Pacific coast of the United States and nested an area that covers the central upwelling region of California around Monterey Bay. The model showed good results for the representation of the upwelling system with a considerable decrease in the CPU cost (Penven 2006). One-way nested grids have also been used by Korres (2003) to represent eddy fields in the Aegean and Levantine basins located in the Mediterranean Sea, which had never been captured by a numerical model in the same region previously.

Hydrodynamics and sediment movement in the German Bight area have been modelled by Staneva (2009) with the use of one-way nesting modelling procedures. The model consisted of three levels of nesting: a coarse model of the North Sea - Baltic Sea (about 5km resolution), inner fine model of the German Bight with horizontal resolution of around 0.8km and an even finer resolution model of the Wadden Sea region with a resolution of 200m. This model was compared with modern satellite observations and showed similar results for the flow regime and sediment movements (Staneva 2009).

There are two main schemes for the running of a one-way nesting technique. The initial scheme involves the complete separation of the coarse and fine models with respect to simulation time. In this method the coarse model is fully run for the model simulation time. The data required for the boundary conditions are stored in a data file to be used for the fine domain model that is then fully run for the simulation time. This method is known as an uncoupled modelling procedure and has been used for the modelling of the Adriatic Sea (Zavatarelli 2003).

The coupled modelling procedure is more attractive than the uncoupled, as it does not require large amounts of storage. In this method the parent model is run for one time step and data required for the nested domains boundary conditions are assigned, allowing the nested model to proceed to a time step equal to the coarse domains. The coarse domain only proceeds to the next time step when the fine domain has been integrated. The shelf and slope flow surrounding Cape Mendocino in Northern California was modelled by Pullen (2001) using a coupled one-way nested model.

The DIVAST model is nested with a one-way nesting procedure. The formulation of the nesting procedure involved a coupled model that does not require high quantities of data storage. The boundary operator involves the use of a linear interpolation procedure and a Dirichlet boundary condition, with the use of ghost cells to enable the formulation of the nested grid boundaries as internal boundaries. A nesting ratio of 9:1 was achieved and results found to give excellent agreement with a corresponding high resolution model. This scheme has been successfully deployed to estuaries and coastal areas around the island of Ireland (Nash 2010).

A common problem in the modelling of water bodies with the use of one-way nested grids is the positioning of the nested domains boundaries. They must be located in areas where the low resolution domain conditions will not negatively affect the model solution in the nested domain. This leads to a possible increase in the size of the nested domain grid, which increase the computational requirements. Research is required to track this issue to increase the attractiveness of the one-way nested technique.

## **2.6.2 TWO-WAY NESTED MODELLING**

Two-way nesting is an advanced nesting technique due to the increase in the interaction between the domains of different resolution i.e. the coarse domain and the nested domain. The interaction is expanded through a updating/feedback procedure that uses the high resolution nested grid solution to update the coarse domain solution in a common area.

Spall and Holland (1991) were among the first to apply a two-way nesting routine to a model for oceanographic applications. This was applied to two types of test cases in artificial domains that are relevant to oceanic phenomena – a barotropic modon and a baroclinic vortex. The nested domain was contained entirely in a low resolution coarse domain. Interaction between the two domains occurred through: the interpolation of the coarse grid data at the interface between the two domains to provide boundary conditions for the nested domain, the high resolution nested domain solution was used to update the coarse solution in the zone where the two domains overlap. Results indicated that the model performed well at nesting grid ratios of 3:1 and 5:1 (Spall 1991).

Fox (1995) adapted the Spall and Holland method to investigate problems that may arise when fronts and other oceanic features intersect the boundaries between the domains, and also the performance of the model when topographical features are present. Results of the model showed that including a Newtonian damping effect into the model reduced the wave reflection generated at the interface with the introduction of topographical features.

Oey (1992) used a two-way nested model in the Norwegian Coast to simulate meanders and eddies in the coastal currents. The model used the coarse grid solution to drive the nested domain, with the use of a flow relaxation scheme, around the nest's boundary. The fine grid influenced the coarse grid through averaging procedures in the overlapping region. The results of the model were compared with observed hydrographics and showed good correlation with observations.

The two-way nested model used by Ginis (1997) to model the tropical Pacific Ocean employed a two-way interactive method initially proposed by Kurihara (1979) for the application in hurricane prediction modelling. The method differs from the previously mentioned two-way nested models in relation to the interface where the two domains interact with each other. The interaction between the two domains occurring in an area called the dynamic interface located near the nested domain boundary. Results presented showed that the interaction at the dynamic interface improved the conservation of properties between the two domains.

Features of the Ligurian Sea were modelled by Barth (2005), with the use of a two-way nested model. The model consisted of a coarse resolution model of the Mediterranean Sea of a  $1/4^\circ$  resolution. This domain was embedded with a  $1/20^\circ$  resolution model of the Liguro-Provencal basin and Northern part of the Tyrrhenian Sea. A final level of nesting was embedded in the previous domain with a resolution of  $1/60^\circ$  and represents the dynamics of the Ligurian Sea. The nesting procedure used was similar to those employed by Oey (1992) and Spall (1991), with feedback being performed over the entire volume of the nested domain. The model was used to investigate the characteristics of the Eastern and Western Corsican currents and the Northern currents. Results showed the two-way method was effective and robust and generated a better representation of currents in comparison to a coarse resolution model and one-way nested model (Barth 2005).

A tide-surge prediction model with two-way nesting features was applied in the Taiwan strait by Zhang (2007). The nested model used an overlapping technique and employed a radiation condition for the dissipation of noise. The model was compared with a similar one-way nested model of the domain and proved more accurate.

In the context of this research nesting was required to investigate effects of a tidal turbine farm in the area of deployment and the area outside deployment, at a low computational cost, therefore this requires that a two-way nesting modelling technique be used.

## 2.7 TWO-WAY NESTED MODELLING TECHNIQUES

The main differences between nesting techniques is in relation to the transfer of information from the coarse to the fine and the updating procedure from the fine to the coarse. The appeal of a two-way nested model lies in the exchange of information that can generate a more realistic model, especially if high levels of mesoscale disturbances are generated in the nested fine resolution domain (Zhang 1986).

### 2.7.1 FORMULATION OF NESTING TECHNIQUE

Nested modelling techniques are used with the aim of representing an area of interest in a numerical model as accurately as possible. The following equation represents the simulation of a nested domain  $\Omega_n$  over a time period of  $t=0$  to  $t=T$  (see Figure 2.16) (Blayo 2006).

$$p_n \phi_n = f_n \quad \text{in } \Omega_n \quad \text{from } t = 0 \dots T \quad (2.2)$$

where  $p_n$  represents the partial differential method,  $\phi_n$  represents the variables in the nested domain and  $f_n$  is the forcing in the domain. The initial conditions are prescribed at time  $t=0$ . The boundary conditions for the nested domain are fed in through a boundary that does not correspond to a solid wall. This boundary is an artificial interface between the low resolution coarse domain and the high resolution nested domain. The coarse domain  $\Omega_c$  can be represented symbolically as.

$$p_c \phi_c = f_c \quad \text{in } \Omega_c \quad \text{from } t = 0 \dots T \quad (2.3)$$

where  $p_c$  represents the partial differential method,  $\phi_c$  represents the variables in the coarse domain and  $f_c$  is the forcing in the coarse domain.

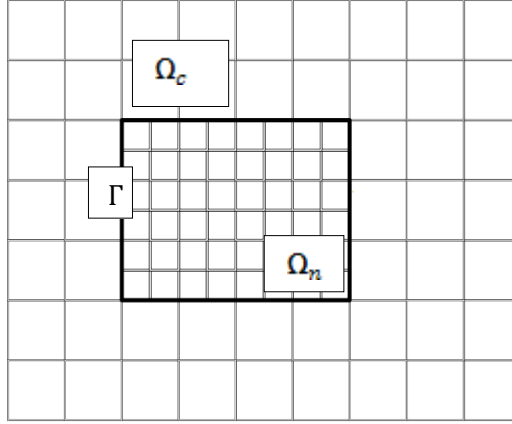


Figure 2: 16 Coarse domain  $\Omega_c$  embedded with a nested domain  $\Omega_n$

The adequate representation of  $\phi_n$  is directly linked to the interaction between the two domains in the ‘open boundary’ region  $\Gamma$ . An updating procedure increases the accuracy of the coarse domain, to allow the error between the two domains to decrease, to generate a more accurate solution to the full model domain (Debreu 2008).

### 2.7.2 DATA TRANSMISSION PROBLEM

Data is transmitted between the nested domain and the coarse domain in two ways. Initially, the coarse model simulates the hydrodynamics for the coarse domain. Data generated in the region of the nested domains boundary is used as the boundary conditions required for the simulation of the high resolution nested domain. The high resolution solution generated in the nested domain is then used to update the low resolution coarse domains solution. Equation 2.4 represents this procedure symbolically (Debreu 2008).

$$\begin{aligned}
 p_c \phi_c &= f_c && \text{in } \Omega_c \cup \Omega_n \text{ from } t = 0 \dots T \\
 \begin{cases}
 OB\phi_n = OB\phi_c \text{ on } \Gamma \\
 p_n \phi_n = f_n \text{ in } \Omega_n \\
 \phi_c = R\phi_n \text{ in } \Omega_n
 \end{cases} &&& (2.4)
 \end{aligned}$$

where the open boundary operators are denoted with  $OB$  and are used along the nested domains boundary ( $\Gamma$ ) to generate values for the nested domains variables ( $\phi_n$ ) along its boundary. The updating procedure is denoted with  $R$  and is used to update the solution of the coarse domain variables  $\phi_c$ . The accuracy of the nested domains solution is directly linked to the type of open boundary procedure and the accuracy of the hydrodynamic solution of the coarse domain along the nested domains boundary.

The optimum updating procedure maximises the information being transmitted into the coarse domain, conserves momentum and increases the accuracy of the coarse domain to allow a better nested domains solution to occur (Ginis 1997; Debreu 2008).

Boundary operator and updating procedures are required to reduce the error that can occur when domains of different resolutions are not blended correctly (Debreu 2008). Blending of the two domains is required to prevent wave reflection (noise) in the nested domain, due to incompatibility between the two domains resolutions and model physics.

Over-specification of the boundary data is another error that can be produced with inadequate data transmission (Kantha 2000). This involves using too much data from the coarse domain to blend the two domains. Two-way nested models can generate large wave reflection when over-specified, due to excessive data propagating out of the nested domain into the coarse domain.

Data transmission is arguably the main point in relation to all nested modelling applications. Methods have ranged from purely mathematical to modelling applications. Research in the area is extensive; some examples of literature include (Blayo 2005; Oddo 2008; Nash 2010). Two of the main data transmitting procedures, relaxation and radiation, will now be discussed.

### **2.7.2.1 Relaxation method**

This method attempts to introduce more consistency between the high resolution/nested and low resolution/coarse domains. This is done by trying to nudge the nested grid solution to the coarse grids solution. The most severe relaxation method

is known as the Dirichlet condition or the clamping condition. This boundary condition has been applied in one-way nested models such as (Spall 1991; Blayo 2005; Nash 2010) and two-way nested models (Barth 2005). Equation 2.5 represents the condition.

$$\phi_c = \phi_n \quad (2.5)$$

The equation shows that the coarse grid solution ( $\phi_c$ ) and nested grid solution ( $\phi_n$ ) are totally dependent on one another. This method has encountered some problem in relation to out flowing variables that reflect back inaccurate information into the nested domain, due to the independence of the internal solution (Oddo 2008).

The flow relaxation scheme allows a less dependent relationship to exist between the coarse and the nested domain. It was original proposed by Davies (1976). The method involves expanding the nested computational domain to allow for an additional domain called the sponge layer to be incorporated. This sponger layer now becomes the boundary ( $\Gamma$ ) interface for the nested domain. The method introduces a relaxation factor into the updating section to allow gradual dissipation of information to be passed into the coarse domain. The relaxation factor is applied to the grid points in the area of the boundary. This factor varies between one and zero depending on the distance from the boundary. Equation 2.6 represents the scheme, where the variables that are solved in the sponge layer  $\Omega_s$  are replaced in the following way at each time step (Davies 1976; Oey 1992).

$$\phi_s = (1 - \alpha)\phi_n + \alpha\phi_c \quad (2.6)$$

with  $\alpha$  representing the relaxation function that varies with respect to the distance from the boundary ( $\Gamma$ ),  $\phi_s$  represents the sponge layer variables,  $\phi_n$  the nested domain variables and  $\phi_c$  representing the coarse domain variables (Blayo 2005; Oddo 2008).

Disadvantages associated with such schemes involve an increase in the computational time due to the addition of the sponge layer. The empirical nature of the solution generated in the sponge layer is also a disadvantage. The main advantage associated which such schemes is the ease of implantation. The relaxation method in research undertaken appears to be a very agreeable data transferring method (Røed 1987; Palma 1998; Nycander 2003; Nash 2010).

### 2.7.2.2 Radiation methods

The radiation condition is the most widely used method for the dissipation of errors generated (Kantha 2000). The scheme involves the use of wave velocity or phase speed to establish a relationship between the nested and the coarse model. Equation 2.7 represents the Sommerfeld condition the radiation method is based on.

$$\frac{\partial \phi_n}{\partial t} + c_w \frac{\partial \phi_n}{\partial N} = 0 \quad (2.7)$$

The equation shows the transport of the variable  $\phi$  through the boundary  $\Gamma$ , with  $c_w$  representing the wave speed that transports the variable. The outgoing velocity vector that is normal to the boundary is represented by  $N$ .

The condition has the assumption that the variable  $\phi$  will pass through the boundary in a wave like motion freely. The equation states the temporal rate of change of a variable  $\phi$  is governed by the speed of propagation and the change in the variable with respect to distance from the boundary.

The model is usually set to a relaxation method, such as the following; if the wave speed is in an inward fashion i.e. the nested domains variables are dependent on the coarse domains solution at the nested domain boundary.

$$\phi_n = \phi_c \quad (2.8)$$

Or a more relaxed term is used as follows, where  $t_{in}$  is the short term relaxation time.

$$\frac{\partial \phi_n}{\partial t} = - \frac{\phi_n - \phi_c}{t_{in}} \quad (2.9)$$

If the wave speed is outwards the above radiation equation is applied, though sometimes the relaxation term is included as follows, with  $t_{out}$  being the long term radiation timescale:

$$\frac{\partial \phi_n}{\partial t} + c_w \frac{\partial \phi_n}{\partial t} = - \frac{\phi_n - \phi_c}{t_{out}} \quad (2.10)$$

The efficiency of such a scheme in relation to complex flow regimes is not fully determined. The use of the method in studies by (Røed 1987; Palma 1998; Nycander 2003) have produced poor results, however in comparison to (Marchesiello 2001; Treguier 2001) who have produced rather efficient results.

The main error generated from the radiation condition is the assumption that the wave equation in a domain has a constant phase speed (Blayo 2005). This is not the case in relation to ocean modelling. The change in time of wave direction is also a concern in relation to the generation of error (Oddo 2008).

### **2.7.2.3 Mesh structure**

The structure of a two-way nested mesh consists of two main types, the first is an overlapping method, and the second is a seamlessly embedded method that consists of two types: adjacent and separated.

The adjacent seamlessly embedded meshes were used in the early generation of two-way nested domains (Harrison 1973; Ley 1976). The procedure involves the time integration for the coarse and nested domain to proceed simultaneously. Boundary data from the coarse domain is interpolated onto the interface between the nested and coarse domains to allow the forcing of the nested domain. The feedback/updating data from the nested domain is transmitted through the same interface the boundary data is interpolated on.

Problems associated with such a technique include an over specification problem at the boundaries. This problem arises from interpolated nested domain boundary data that are generated from the coarse domain data points, which themselves have been generated from a previous forecasted nested domain values (Debreu 2008).

The separated embedded model, involves the separation of the nested and coarse domain by a mesh. This mesh, also known as a window frame, is shown in Figure 2.17 as domain 2. The frame consists of an overlapping of the two different resolution domains. The internal boundary of the coarse domain is the mesh interface and the fine domains external boundary, where the boundary conditions for the domain are generated, is the dynamic interface. The separation of the interfaces allows for only internally generated nested domain values being used in the feedback calculation.

The scheme involves initially the simulation of the coarse domain and the mesh/window frame domain (domains 1 and 2 in Figure 2.17). The second step involves the use of the data generated at the dynamic interface as boundary conditions

for the simulation over domain (2) and the nested grid in domain (3). Time interpolation is performed at the dynamic interface and spatial interpolation is performed at the mesh interface. This method allows two-way interaction due to domain 1 being influenced by domain 2 and the coarse domain influences the nested domain by providing the boundary conditions for the nested domain simulation. This method is a very common method in nested modelling and has been used in a large number of nesting schemes in both metrology and hydrology (Kurihara 1979; Ginis 1997; Zhang 2007).

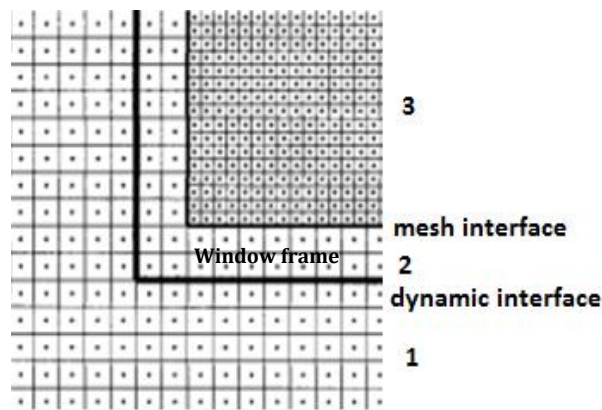


Figure 2: 17 Seamlessly embedded nested domain

The second type of two-way nested modelling procedure is an overlapping method that involves the extension of the coarse domain over the full nested domain. The overlapping method has been used in a number of applications (Spall 1991; Fox 1995 ; Barth 2005).

The procedure involves the coarse domain integrating for one time step and boundary data from the coarse domain are interpolated onto the dynamic interface (see Figure 2.18) between the nested and coarse domains. The nested domain is then integrated using the boundary data until the time step is equivalent to the coarse domains time step. The transfer of the high resolution nested domain data occurs at points where the coarse domain grid points coincide with the fine domain grid points and are updated using some interpolation method of the enclosed nested grid data .Figure 2.18 shows an illustration of the grid configuration for a nested ratio of 3:1.

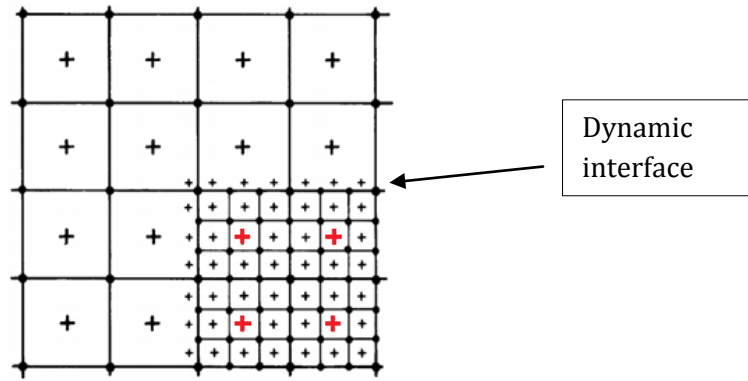


Figure 2: 18 Schematic of overlapping grid configuration

### 2.7.2.4 Interpolation

Interpolation techniques are required for effective data transmission, as data is transferred between domains of different spatial and temporal resolution. There are two main goals for an interpolation scheme to be optimum: (1) to maximize the information being transferred and (2) to minimize the generation of noise.

Interpolation techniques used in the transfer of information from the coarse domain to the nested domain are usually of a polynomial form or a linear/bilinear form. Problems can arise with the use of polynomial techniques in areas of sharp gradients due to the formation of surplus oscillation of the interpolation variables (Alapaty, 1998). Therefore, linear interpolation is more widely used for both spatial and temporal interpolation (Nash, 2010, Korres, 2003, Pullen, 2001).

There are four main updating interpolation procedures for the transfer of information from the fine domain into the coarse domain: (1) direct copy, (2) basic averaging procedure, (3) Shapiro and (4) fully weighted averaging procedure (Zhang 1986; Kosh 1987).

Direct copy is the most severe interpolation technique, with only the nested grid point that lies directly in the region of the coarse grid point being used in the procedure. Equation 2.11 represents this interpolation scheme, with Figure 2.19 showing an illustration of the scheme, with subscripts  $i, j$  representing the grid point locations in relation to the  $x$  and  $y$  direction in the nested domain and  $I, J$  representing the coarse domains grid point locations in relation to the  $x$  and  $y$  direction.

$$\phi_{I,J}^c = \phi_{i,j}^n \quad (2.11)$$

where  $\phi_{I,J}^c$  represents the coarse grid point and  $\phi_{i,j}^n$  represents the nested grid point that overlays the centre of the coarse grid cell.

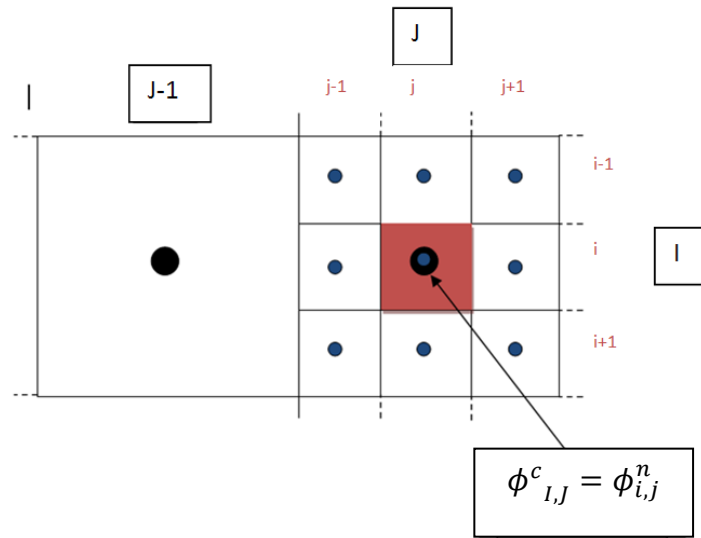


Figure 2: 19 Copy interpolation scheme

The average procedure takes into account all fine grid points that are enclosed in the coarse cell (Clark 1984). Equation 2.12 shows the formation of the average scheme for a mesh refinement factor of 3:

$$\phi_{I,J}^c = \frac{1}{9} (\phi_{i-1,j-1}^n + \phi_{i-1,j}^n + \phi_{i-1,j+1}^n + \phi_{i,j-1}^n + \phi_{i,j}^n + \phi_{i,j+1}^n + \phi_{i+1,j-1}^n + \phi_{i+1,j}^n + \phi_{i+1,j+1}^n) \quad (2.12)$$

with  $\phi^c$  representing the coarse point (black circles) that is being updated and  $\phi^n$  being the fine grid values in the same cell (blue circles). This scheme is based on the assumption that the fine grid variables over laying the one coarse grid cell have a uniform distribution of value. Figure 2.20 shows an illustration of this interpolation scheme.

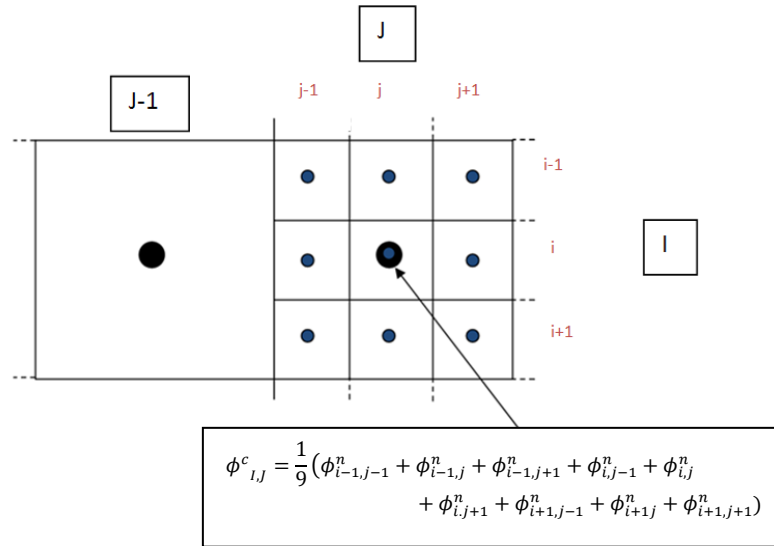


Figure 2: 20 Average interpolation scheme

The Shapiro interpolation scheme is based on the assumption that the nested grid point that lies in the central region of the coarse grid (blue square) is of equal importance to the sum of the other nested grid (red squares) points enclosed in the coarse grid cell (Zhang 1986). The following equation shows that mathematics of the scheme, with Figure 2.21 illustrating the process.

$$\phi_{I,J}^c = \frac{1}{16} (\phi_{i-1,j-1}^n + \phi_{i-1,j}^n + \phi_{i-1,j+1}^n + \phi_{i,j-1}^n + 8\phi_{i,j}^n + \phi_{i,j+1}^n + \phi_{i+1,j-1}^n + \phi_{i+1,j}^n + \phi_{i+1,j+1}^n)$$

(2.13)

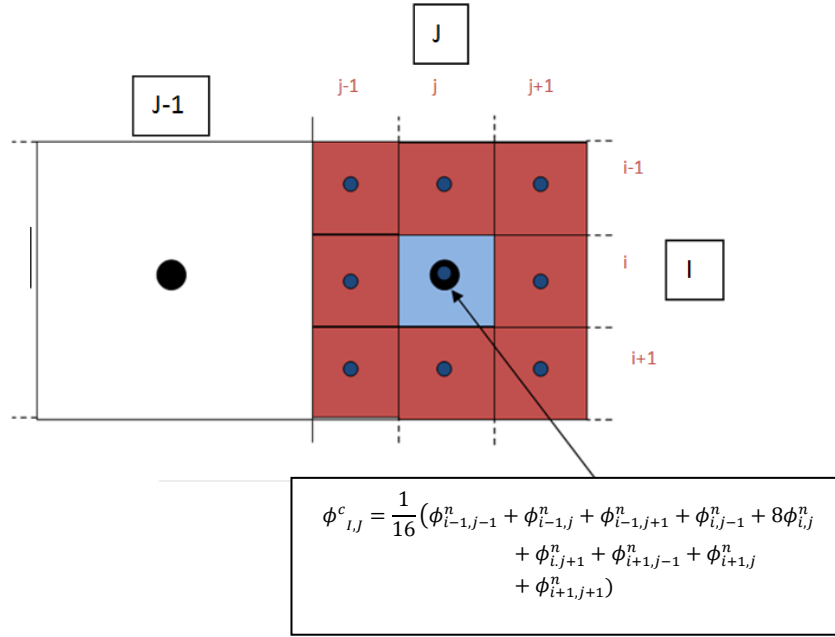


Figure 2: 21 Shapiro interpolation scheme

The final interpolation scheme is the full weighted averaging method and assumes that the interpolated value used for the updating procedure should be influenced mainly by nested grid points close to the centre of the coarse grid point being updated (green + blue squares) and less by the more distant points (red squares) (Hemker 2001; Debreu 2008). The following equation presents the fully weighted scheme for a nesting ratio of 3.

$$\phi_{I,J}^c = \frac{1}{20} (\phi_{i-1,j-1}^n + 2\phi_{i-1,j}^n + \phi_{i-1,j+1}^n + 2\phi_{i,j-1}^n + 8\phi_{i,j}^n + 2\phi_{i,j+1}^n + \phi_{i+1,j-1}^n + 2\phi_{i+1,j}^n + \phi_{i+1,j+1}^n)$$

(2.14)

Figure 2.22 shows an illustration of this interpolation scheme.

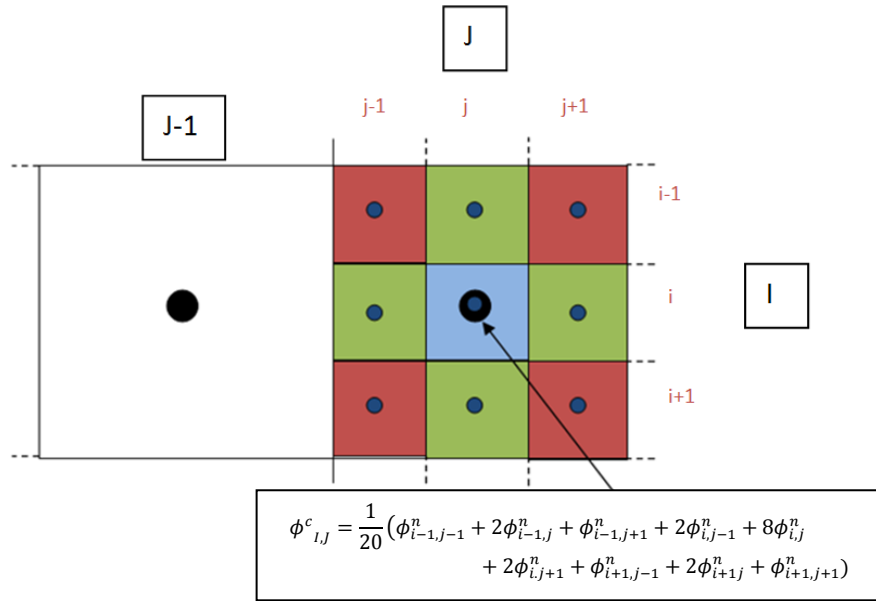


Figure 2: 22 Fully weighted averaging interpolation scheme

## 2.9 SUMMARY AND CONCLUSION

The ability of hydrodynamic models to model small scale processes accurately, without excessive computation needs, is one of the main areas that requires development. The introduction of nesting techniques to model areas of interest with a high level of resolution is one of the methods used to achieve this accuracy without employing a heavy weight on the computational needs or requiring a high level of computational memory. There are two main forms of nesting procedures; one-way nesting and two-way nesting.

One-way nesting modelling techniques have been successively implemented into the numerical model DIVAST, however, the location of the open boundaries of the nested domain are crucial to the accuracy of the model solution. Errors generated by the boundary are directly linked to the inaccuracies in the coarse domain along the nested domain boundary. Therefore, boundaries have to be located in areas of low coarse domain inaccuracies. Literature reported no method of tackling this problem without an increase in the nested domain and, hence, the computational needs.

Therefore, this research focused on a method to alleviate this problem. This was achieved by allowing boundaries to have an irregular shape to position them in areas of high coarse domain accuracy without an increase in the computational needs.

To the Author's knowledge this is the first application of such a technique to a one-way nested model.

Research has highlighted the possibility of incorporating two different types of coordinate systems into a single model domain to accurately represent the hydrodynamics of a water body (hybrid grid). A novel approach was generated by allowing the one-way nested domain to be generated in a rotated coordinate system to accurately represent areas of the computational domain i.e. rivers flowing into an estuary at an angle.

In the context of this research, nesting was required to investigate the effects of energy extraction by tidal turbines in an estuary. Two-way nesting is more beneficial for such applications as features modelled on the nested grid i.e. turbine farms, are capable of propagating out to the coarse domain, thus improving the coarse domains solution and allowing the identification of possible environmental impacts outside the nested tidal farm.

A two-way nested model was developed, which is a modified form of the one-way nesting procedure in DIVAST. The model is capable of simulating hydrodynamic processes at a high resolution and allowing the data to be fed back into the low resolution domain. The grid structure employed was an overlapping method, in comparison to an embedded grid due to large modification required in the solution scheme of the model. Literature identified that an effective data transmission method was crucial in maximising the transmission of data while preventing the generation of error. Therefore, a large section of the research was focused on this. Based on the literature three different forms of feedback conditions were assessed; a Dirichlet condition and two forms of the flow relaxation method. Different interpolation scheme were also tested: direct copy, average, Shapiro and fully weighted. The final version of the scheme allows two different forms of data transmission depending on the complexity of the domain, they were: (1) a Dirichlet feedback condition with an average interpolation scheme, and (2) a momentum flow relaxation feedback condition with an average interpolation scheme.

Two-way nested models reviewed in the literature exclude an open boundary formulation that incorporates ghost cells adjacent to the nested open boundary cells so the open boundary is considered an internal boundary. This technique was used in

the existing one-way nested model in DIVAST and incorporated into the two-way nested model.

Tidal turbines of different array configurations have not been incorporated into any nested model reviewed in the literature. The two-way nested model was developed to allow the effects of energy extraction by tidal turbine farms to be incorporated based on the Linear Momentum Actuator Disc Theory.

# **CHAPTER 3: DESCRIPTION OF THE NUMERICAL MODEL DIVAST**

## **3.1 INTRODUCTION**

The open source code used in this study was DIVAST, which was developed by Professor R.A Falconer, professor of environmental water management, and Prof. B. Lin both of Cardiff University. DIVAST is a two-dimensional hydrodynamic model that uses the programming language FORTRAN to simulate the distribution of currents, elevations of water surface and water quality parameters.

The basis of the numerical hydrodynamic model involves solving the Navier-Stokes equations. These equations are integrated over depths and take into account the effects of local and advective acceleration, the rotation of the earth, pressure gradients at barotropic and free surface levels, wind movement, resistance generated from the waterbed and turbulent mixing.

A finite difference scheme is used to solve the governing equations, along with an semi-implicit alternating direction (ADI) formulation scheme (Falconer 2001). The model has been calibrated using many field and laboratory experimental results. It has been used extensively in projects throughout Ireland and the UK and is considered a high standard hydrodynamic model within the industry (Hartnett 2004).

## **3.2 MODEL DESCRIPTION**

DIVAST is a versatile model for the prediction of water elevations and currents in water bodies dominated by horizontal, unsteady flows, which do not display significant vertical stratification. The governing equations are solved using a finite difference technique along with an alternation direction (ADI) method, which allows a stable semi-implicit scheme to be generated. The grid structure used in the model is a uniform rectilinear grid, shown in Figure 3.1, which is a very common structure in finite difference models. The structure involves equal spacing between grid points in both the x and y directions.

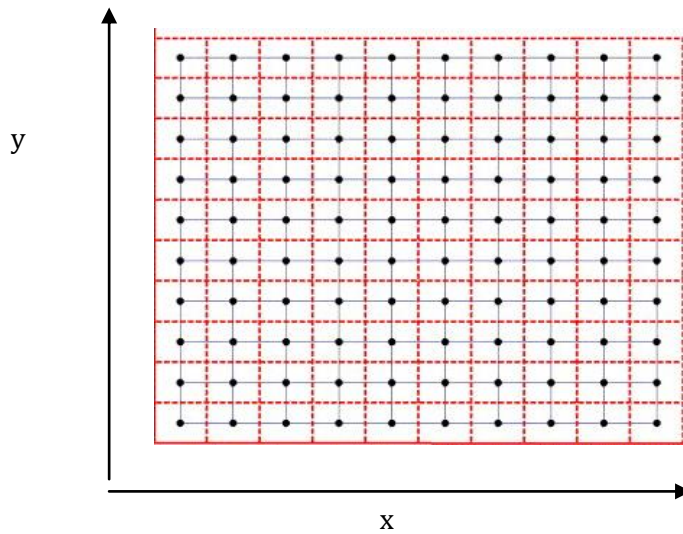


Figure 3: 1 Uniform rectilinear grid (Wanga 2004)

The ADI method involves the splitting of each time step in two. This allows a one dimensional matrix to be solved implicitly at each step instead of a more complex two dimensional matrix. Discretization of the model grid is performed on an I-J plane, with I and J axes corresponding to the x and y direction (Figure 3.2). During the first half time step the solution scheme proceeds in the x-direction and generates values for the water elevations  $\zeta$  and x-direction velocity components, with the use of a back substitution and Gaussian elimination method. The second half time step repeats the process in the y-direction and computes water elevations  $\zeta$  and y-direction velocity components.

Figure 3.2 represents the space staggered orthogonal grid system used in the model, that allows each variable operated on in time to have centrally located spatial derivatives for each of the other variables available. The method involves the discretisation of the water elevations ( $\zeta$ ) at the centre of the grid cells and the velocity variable in the x and the y direction at the centre of the cell sides.

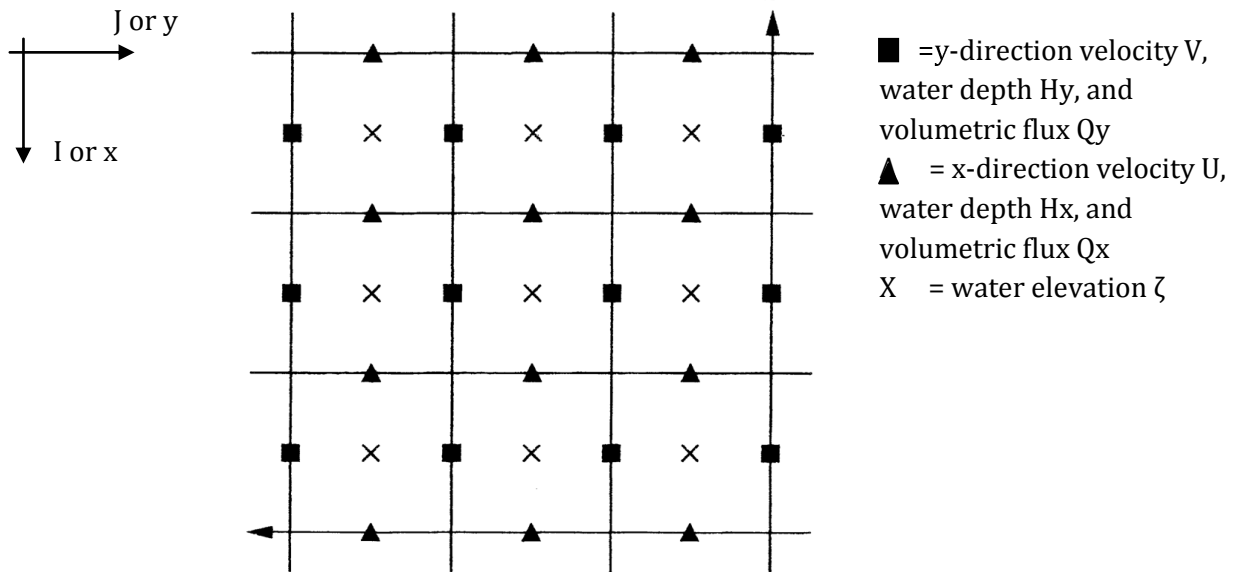


Figure 3: 2 The space staggered grid system (Layeka 2007).

DIVAST was chosen as the hydrodynamic model for the study as it has been used in a number of different studies around Ireland in relation to estuaries and water bodies. The model has been previously calibrated to a very high standard and seen as one of the leading finite difference models in the area of hydrodynamics (Falconer 2001).

The space staggered orthogonal grid system can become inaccurate in areas where complex geographical and topography features are present, therefore, they are best suited to open seas and harbours with a regular shape. The accuracy of such models can be increased with an increase in the number of grid cells, however, this leads to a greater stress on the computational needs of the model. Therefore, this type of model is ideally suited for the incorporation of a nested domain to reduce the computational needs of the finite difference model and to improve accuracy.

### 3.3 GOVERNING EQUATIONS OF MOTION

Governing equations of fluid motion, which are written with respect to the rotation of the earth's coordinate systems frame of reference, need to be solved in all hydrodynamic models. The governing equations involved in this hydrodynamic model are the Navier-Stokes equations - these equations are derived from Newton's second law of motion in relation to a particle of fluid (Drazin 2002).

The generation of a two dimension hydrodynamic model involves considering only the horizontal components and representing the less dominant vertical ( $w$ ) components in relation to the horizontal components ( $u,v$ ) (see Figure 3.3). This can be implemented into shallow well mixed water bodies, due to the vertical components being considerably small in relation to the horizontal components.

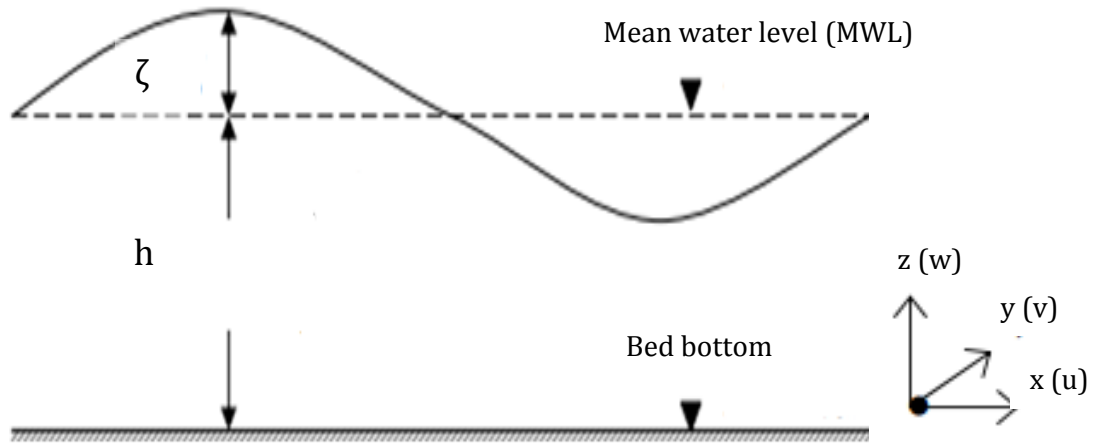


Figure 3: 3 A shallow well mixed water body ( $\zeta$  = water elevation above or below MWL,  $h$  =water depth below MWL)

The following equations represent the depth integrated velocity components that are used to transform the complex three dimensional parabolic velocity profiles:

$$U = \frac{1}{H} \int_{-h}^{\zeta} u dz \quad (3.1)$$

$$V = \frac{1}{H} \int_{-h}^{\zeta} v dz \quad (3.2)$$

where the horizontal velocity components are represented with  $u$  and  $v$ . The depth integrated velocity components are  $U$  and  $V$  and  $H=h+\zeta$ , is the total water depth;  $h$  is water depth below mean water level and  $\zeta$  is water depth above or below mean water level. These equations allow the model to transform into a less complex two dimensional form as shown in Figure 3.4.

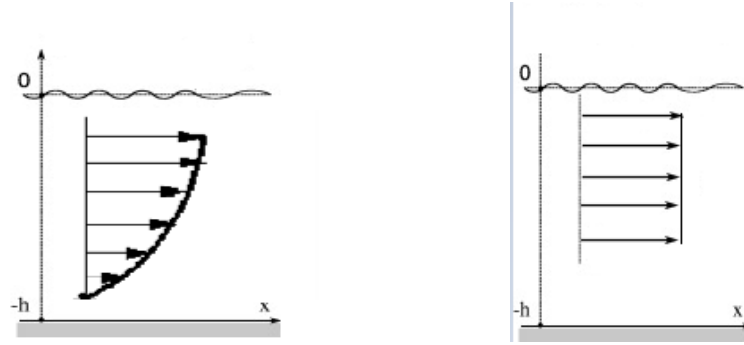


Figure 3: 4 Principle of the two dimensional model (Fowler 2012)

This integrated method, along with the assumption that vertical acceleration is negligible in comparison to gravity, can be used to express the governing equation in a two dimensional hydrodynamic model to calculate the depth integrated velocity components  $U, V$  and the water elevations  $\zeta$  (Falconer 1994). The following equations represent the governing equations in a two-dimensional form.

*Continuity equation:*

$$\frac{\partial \zeta}{\partial t} + \frac{\partial q_x}{\partial x} + \frac{\partial q_y}{\partial y} = 0 \quad (3.3)$$

*X-direction momentum equation:*

$$\begin{aligned} \frac{\partial q_x}{\partial t} + \beta \left[ \frac{\partial U q_x}{\partial x} + \frac{\partial U q_y}{\partial y} \right] = \\ f q_y - gH \frac{\partial \zeta}{\partial x} + \frac{\rho_a C^* W_x (W_x^2 + W_y^2)^{1/2}}{\rho} - \frac{gU(U^2 + V^2)^{1/2}}{c^2} 2 \frac{\partial}{\partial x} \left[ \varepsilon H \frac{\partial U}{\partial x} \right] + \frac{\partial}{\partial y} \left[ \varepsilon H \left[ \frac{\partial U}{\partial y} + \frac{\partial V}{\partial x} \right] \right] \end{aligned} \quad (3.4)$$

*Y-direction momentum equation:*

$$\begin{aligned} \frac{\partial q_y}{\partial t} + \beta \left[ \frac{\partial U q_x}{\partial x} + \frac{\partial V q_y}{\partial y} \right] = -f q_x - gH \frac{\partial \zeta}{\partial y} + \frac{\rho_a C^* W_y (W_x^2 + W_y^2)^{1/2}}{\rho} - \frac{gV(U^2 + V^2)^{1/2}}{c^2} + \\ 2 \frac{\partial}{\partial y} \left[ \varepsilon H \frac{\partial V}{\partial y} \right] + \frac{\partial}{\partial x} \left[ \varepsilon H \left[ \frac{\partial V}{\partial x} + \frac{\partial U}{\partial y} \right] \right] \end{aligned} \quad (3.5)$$

where,  $t$  =time

$\zeta$  = water elevation above or below the datum

$q_x, q_y$  = depth integrated volumetric flux in the x and y direction ( $q_x = UH, q_y = VH$ )

$\beta$  = momentum correction factor for non-uniform vertical velocity profile

$f$  = Coriolis parameter

$C$  = Chezy bed roughness coefficient

$\nu_t$  =depth-average mean eddy viscosity

$\rho_a$  = density of air (1.292 kg/m<sup>3</sup>)

$\rho$  = fluid density

$\varepsilon$  = depth mean eddy viscosity

$g$  = gravitational acceleration

$W_x, W_y$  = wind velocity in x and y direction

$C^*$  = air-water interface coefficient

The momentum equations shown in equations 3.4 - 3.5, consist of the local and advective acceleration terms on the left hand side of the equations. The right hand side of the momentum equation represents the forces and pressures that are being applied to the flow of water. The forces consist of Coriolis force, pressure gradient, wind shear force, bed shear resistance and turbulent induced shear force (see Appendix A.1).

### 3.4 FINITE DIFFERENCE FORMULATION

The governing equations are solved using a central difference, ADI, finite difference scheme to find approximations of the first derivatives. The following equation represents the first derivative of a function  $U(x)$ , which represents a velocity at point  $x$  in a one dimensional model, using the central difference method.

$$\frac{\partial U(x)}{\partial x} \approx \frac{(U_{(x+\Delta x)} - U_{(x-\Delta x)})}{2\Delta x} \quad (3.6)$$

Equation 3.6 shows that an approximation of the first derivative of  $U$  at point  $x$  can be generated by using the velocity values at point  $(x+\Delta x)$  and the velocity values at point  $(x-\Delta x)$ .

There are three different finite difference methods to generate an approximation of the first derivatives: forward difference, backward difference and central difference (Note: the three types of finite different methods are represented in Appendix A.2).

The central difference method is used along with an ADI scheme, which requires the time step be split in two, allowing the components in the x and y direction to be solved in separate time intervals. This requires the x-direction components to be expressed in an implicit form in the first half time step, with the y-direction components expressed in an explicit form. This is the opposite for the second half time step where the y-direction components are implicit and the x-direction components are explicit. Two iterations of the solution are performed in each half time step to allow all terms to be fully centred in time and space. The following equations represent the discretised form of the continuity equation and x-direction momentum equation using a uniform space staggered mesh as shown in Figure 3.2 (Falconer 1986).

*Continuity equation:*

$$\zeta_{i,j}^{n+\frac{1}{2}} - \zeta_{i,j}^n + \frac{\Delta t}{2\Delta x} \left[ q_x \Big|_{i+\frac{1}{2},j}^{n+\frac{1}{2}} - q_x \Big|_{i-\frac{1}{2},j}^{n+\frac{1}{2}} + q_y \Big|_{i,j+\frac{1}{2}}^n - q_y \Big|_{i,j-\frac{1}{2}}^n \right] = 0 \quad (3.7)$$

*Momentum equation in x-direction:*

$$q_x \Big|_{i+\frac{1}{2},j}^{n+\frac{1}{2}} = q_x \Big|_{i+\frac{1}{2},j}^{n-\frac{1}{2}} \quad (3.8)$$

$$- \frac{\beta \Delta t}{\Delta x} \left[ U' q_x \Big|_{i+1,j}^n - U' q_x \Big|_{i,j}^n + U' q_y \Big|_{i+\frac{1}{2},j+p}^n - U' q_y \Big|_{i+\frac{1}{2},j+q}^n \right]$$

$$+ \Delta t f q_y \Big|_{i+\frac{1}{2},j}^n - \frac{g \Delta t}{2\Delta x} H_{i+\frac{1}{2},j}^n \left[ \zeta_{i+1,j}^{n+\frac{1}{2}} + \zeta_{i+1,j}^{n-\frac{1}{2}} - \zeta_{i,j}^{n+\frac{1}{2}} - \zeta_{i,j}^{n-\frac{1}{2}} \right]$$

$$\begin{aligned}
& + \frac{\rho_a \Delta t C^* W_x (w_x^2 + w_y^2)^{\frac{1}{2}}}{\rho} - \frac{g \Delta t n^2 \left( U^{n+\frac{1}{2}} + U^{n-\frac{1}{2}} \right) (U'^2 + V^2)^{\frac{1}{2}}}{2C^2} \Bigg|_{i+\frac{1}{2},j}^n \\
& + \frac{\Delta t}{\Delta x^2} \varepsilon H_{i+\frac{1}{2},j}^n \left[ 2 \left( U'_{i+\frac{3}{2},j} + U'_{i-\frac{1}{2},j} \right) + U'_{i+\frac{1}{2},j+1} + U'_{i+\frac{1}{2},j-1} - 6U'_{i+\frac{1}{2},j} - V_{i,j+\frac{1}{2}} + V_{i,j-\frac{1}{2}} - \right. \\
& \left. V_{i+1,j-\frac{1}{2}} + V_{i+1,j+\frac{1}{2}} \right] \Bigg|_{i+\frac{1}{2},j}^n \tag{3.8}
\end{aligned}$$

where subscripts  $i, j$  represent the grid point location in the  $x$  and  $y$  direction and  $n$  represents the level at which the time step is at. With

$$p = (-V/2|V|)_{i+\frac{1}{2},j+\frac{1}{2}} \tag{3.9}$$

$$q = (-V/2|V|)_{i+\frac{1}{2},j-\frac{1}{2}} \tag{3.10}$$

The first half time step, from  $n$  to  $n+1/2$ , involves solving  $q_x$  and  $\zeta$  implicitly, during which the terms with the prime are expressed explicitly at  $n-1/2$  during the first iteration. For example, during equations 3.7 first iteration.

$$U'_{i+\frac{1}{2},j}^n = U_{i+\frac{1}{2},j}^{n-\frac{1}{2}} \tag{3.11}$$

The second iteration involves the terms with a prime being expressed at time step  $n$  using the average of the variables values computed at the end of the first iteration. Equation 3.12 shows an example of this.

$$U'_{i+\frac{1}{2},j}^n = \frac{1}{2} \left( U_{i+\frac{1}{2},j}^{n+\frac{1}{2}} + U_{i+\frac{1}{2},j}^{n-\frac{1}{2}} \right) \tag{3.12}$$

The  $y$ -direction momentum equation and continuity equation are solved in a similar way, but performed in the  $n+1/2$  to  $n+1$  time step level, to generate values for  $q_y$  and  $\zeta$ .

The accuracy of the hydrodynamic model is directly linked to the solution for the continuity and momentum equations; therefore a clear understanding of the scheme is essential to perform modifications and expansions to the existing model. The solution scheme is further explained in the following sections.

### 3.5 HYDRODYNAMIC SOLUTION SCHEME

The hydrodynamic solution scheme is a semi-implicit method, which as mentioned previously, involves the use of adjacent grid point of known and unknown values to calculate a variable at a particular grid point. Therefore, the governing equations cannot be solved directly to calculate a solution for  $U$ ,  $V$  and  $\zeta$  but must be solved in a simultaneous manner. Known terms are generally calculated at a previous time step, with unknown terms calculated at the current time step. The method of Gaussian elimination and back substitution (Falconer 1994) is applied to the hydrodynamic solution scheme in DIVAST to solve the governing equations in a tri-diagonal form.

The governing equations for the first half time step use the hydrodynamic solution scheme to calculate values for  $\zeta_{i,j}^{n+\frac{1}{2}}$  and  $q_x|_{i+\frac{1}{2},j}^{n+\frac{1}{2}}$ , which involves the use of known values at time  $n$  and unknown values at time  $n+\frac{1}{2}$ . The following equations show how the governing equations (3.7) and (3.8) are rearranged by bring all unknown terms to the left hand side of the equation and combining all known terms.

Continuity equation:

$$-\frac{\Delta t}{2\Delta x}q_x|_{i-\frac{1}{2},j}^{n+\frac{1}{2}} + \zeta_{i,j}^{n+\frac{1}{2}} + \frac{\Delta t}{2\Delta x}q_x|_{i+\frac{1}{2},j}^{n+\frac{1}{2}} = A_i^n \quad (3.13)$$

Replacing the know terms gives:

$$-d_i q_x|_{i-\frac{1}{2},j}^{n+\frac{1}{2}} + e_i \zeta_{i,j}^{n+\frac{1}{2}} + f_i q_x|_{i+\frac{1}{2},j}^{n+\frac{1}{2}} = A_i^n \quad (3.14)$$

where:

$$d_i = f_i = \frac{\Delta t}{2\Delta x} \quad e_i = 1$$

$$A_i^n = \zeta_{i,j}^n - \frac{\Delta t}{2\Delta x} \left[ q_y|_{i,j+\frac{1}{2}}^n - q_y|_{i,j-\frac{1}{2}}^n \right]$$

The momentum equation (3.8) terms are rearranged in a similar manner, with all known terms being positioned on the left hand side of the equation:

$$\left[ \frac{g\Delta t}{2\Delta x} H_{i+1/2,j}^n \right] \zeta_{i,j}^{n+1/2} + \left[ 1 + \frac{g\Delta t(q_x'^2 + q_y'^2)^{1/2}}{2(HC)^2} \right]_{i+1/2,j}^n q_x|_{i+1/2,j}^{n+1/2} + \left[ \frac{g\Delta t}{2\Delta x} H_{i+1/2,j}^n \right] \zeta_{i+1,j}^{n+1/2} = B_i^n \quad (3.15)$$

Replacing the know terms gives:

$$-a_i \zeta_{i,j}^{n+1/2} + b_i q_x|_{i+1/2,j}^{n+1/2} + c_i \zeta_{i+1,j}^{n+1/2} = B_i^n \quad (3.16)$$

where:

$$a_i = c_i = \frac{g\Delta t}{2\Delta x} H_{i+1/2,j}^n$$

$$b_i = 1 + \frac{g\Delta t(q_x'^2 + q_y'^2)^{1/2}}{2(HC)^2} \Big|_{i+1/2,j}^n$$

$$\begin{aligned} B_i^n = & q_x|_{i+1/2,j}^{n-1/2} - \frac{\beta\Delta t}{\Delta x} \left[ U' q_x'|_{i+1,j}^n - U' q_x'|_{i,j}^n + U' q_y|_{i+1/2,j+1/2}^n - U' q_y|_{i+1/2,j-1/2}^n \right] + \Delta t f q_y|_{i+1/2,j}^n \\ & - \frac{g\Delta t}{2\Delta x} H_{i+1/2,j}^n \left[ \zeta_{i+1,j}^{n-1/2} - \zeta_{i,j}^{n-1/2} \right] + \frac{\rho_a \Delta t C^* W_x (W_x^2 + W_y^2)^{1/2}}{\rho} \\ & - \frac{g\Delta t (q_x'^2 + q_y'^2)^{1/2}}{2(HC)^2} \Big|_{i+1/2,j}^n q_x^{n-1/2} \\ & + \frac{\Delta t}{\Delta x^2} \varepsilon H_{i+1/2,j}^n \left[ 2 \left( U'_{i+3/2,j} + U'_{i-1/2,j} \right) + U'_{i+1/2,j+1} + U'_{i+1/2,j-1} - 6U'_{i+1/2,j} \right. \\ & \left. - V_{i,j+1/2} + V_{i,j-1/2} - V_{i+1,j-1/2} + V_{i+1,j+1/2} \right]^n \end{aligned}$$

The known terms are represented by  $A_i^n$  in the continuity equation and  $B_i^n$  in the momentum equation, which are all at a time level  $n$ . The values  $a$ ,  $b$ ,  $c$ ,  $d$ ,  $e$  and  $f$  are all recursion coefficients. These equations are used to perform the Gaussian elimination and back substitution, along with water elevations or normal velocity conditions provided at the open boundary.

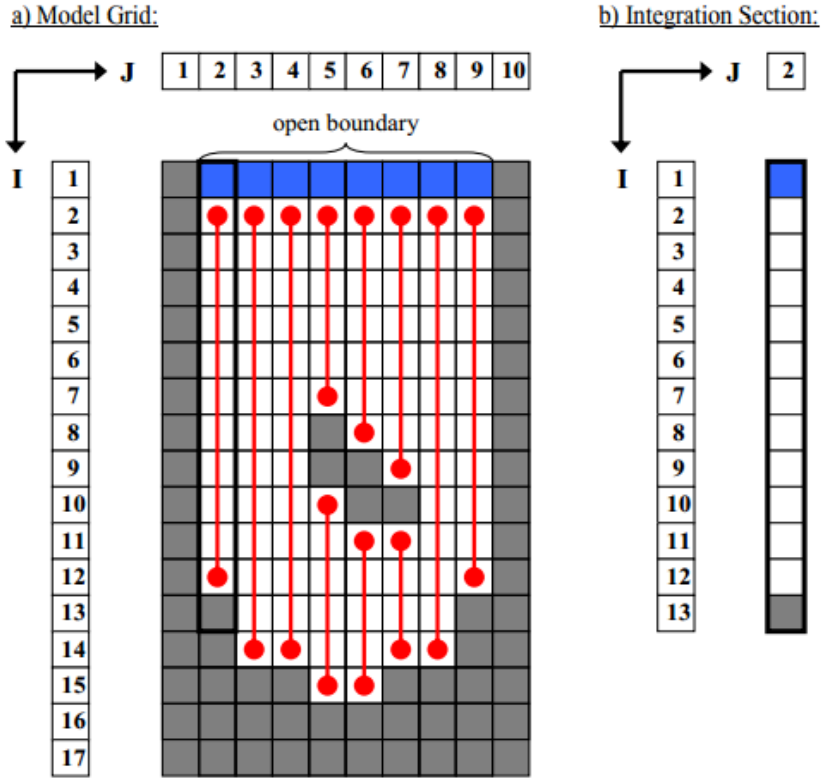


Figure 3: 5 Illustration of model grid and integration section (Nash 2010)

Figure 3.5 shows an illustration of a model grid, with Figure 3.5b showing section 2 in the domain, which will be used as an example to show the hydrodynamic solution technique performed in the x-direction for the first half time step. The section being computed contains a lower water elevation open boundary at (1, 2) and a closed boundary at (13, 2). The presence of the boundaries provide values for  $\zeta_{1,2}^{n+\frac{1}{2}}$  at the open boundary and the closed boundary will give a value of zero to  $q_x|_{12\frac{1}{2},2}^{n+\frac{1}{2}}$ .

The computation will start at the point where  $i=1$ , with the inclusion of the open boundary conditions i.e.  $\zeta_{1,2}^{n+\frac{1}{2}}$  is known, the following equation can be generated from the reconstructed momentum equation (3.16):

$$q_x|_{1\frac{1}{2},2}^{n+\frac{1}{2}} = -R_1\zeta_{2,2}^{n+\frac{1}{2}} + S_1 \quad (3.17)$$

The inclusion of the known boundary conditions allow for the recursion formula,  $R_I$  and  $S_I$  to be generated, which contains only known terms. An equation for  $\zeta_{2,2}^{n+\frac{1}{2}}$  can

be generated at  $i=2$  by introducing equation (3.17) into the continuity equation (3.14) and generates the following equation with new recursion formulae  $P$  and  $Q$ .

$$\zeta_{2,2}^{n+\frac{1}{2}} = -P_2 q_x \Big|_{2\frac{1}{2},2}^{n+\frac{1}{2}} + Q_2 \quad (3.18)$$

This equation can then be substituted back into equation (3.16) at  $i=2$  to eliminate  $\zeta_{2,2}^{n+\frac{1}{2}}$ . This procedure of Gaussian elimination continues until it reaches the closed boundary at  $i=12$  and allows a formulation of the continuity equation (3.14), which contains a known value of  $q_x \Big|_{12\frac{1}{2},2}^{n+\frac{1}{2}}$  equal to zero for the closed boundary condition, to be generated as follows:

$$\zeta_{12,2}^{n+\frac{1}{2}} = -P_{12} q_x \Big|_{12\frac{1}{2},2}^{n+\frac{1}{2}} + Q_{12} \quad (3.19)$$

This then allows back substitution to be performed after the Gaussian elimination to generate values for the unknown  $q_x \Big|_{i+\frac{1}{2},j}^{n+\frac{1}{2}}$  and  $\zeta_{i,j}^{n+\frac{1}{2}}$  at each grid cell in the integration section. The governing equations can now be written in their general recursive form:

$$\zeta_{i,j}^{n+\frac{1}{2}} = -P_i q_x \Big|_{i+\frac{1}{2},j}^{n+\frac{1}{2}} + Q_i \quad (3.20)$$

$$q_x \Big|_{i+\frac{1}{2},j}^{n+\frac{1}{2}} = -R_i \zeta_{i+1,j}^{n+\frac{1}{2}} + S_i \quad (3.21)$$

where  $P_i$ ,  $Q_i$ ,  $R_i$  and  $S_i$  are recursion terms computed as follows for  $i=1, \dots, i_{\max}$ :

$$P_i = \frac{c_i}{b_i + d_i R_{i-1}} \quad R_i = \frac{c_i}{b_i + a_i P_i}$$

$$Q_i = \frac{A_i^n + d_i S_{i-1}}{e_i + d_i R_{i-1}} \quad S_i = \frac{B_i^n + a_i Q_i}{b_i + a_i P_i}$$

The method of Gaussian elimination and back substitution is performed in both the  $x$  and  $y$  direction across the full model domain. The solution is stabilised by allowing a second iteration to be performed to centre all the terms in space and time.

The governing equation requires modification in the areas of open boundaries, due to the use of a central difference method used on a domain with a space staggered grid. The solution to such a problem involves the removal of the  $x$ -direction terms in

the momentum equation if the open boundary is in the x-direction and the removal of the y-direction terms with a boundary in the opposite direction. This will be explained in more depth in Chapter 4.

### 3.6 MODEL ACCURACY AND STABILITY

The ability of a hydrodynamic model to solve the governing equations is assessed by looking into the scheme in relation to its stability, accuracy and convergence. The resolution of a model and hence the computation needs of a model are directly linked to these assessment characteristics.

The partial differential form of the governing equations uses the finite difference method to generate an approximation of its solution in the DIVAST numerical model. This approximation is said to be convergent when the time step and distance step approach zero and the truncation error generated from the finite difference scheme is reduced to a negligible form. The following equations represent the convergent requirements (Thompson 1992).

$$|A - A_n| \rightarrow 0 \quad n \rightarrow \text{infinity} \quad (3.22)$$

where  $A$  represents the exact solution to the continuous partial differential equation and  $A_n$  is the solution generated from the finite difference scheme.

The stability of the model is linked to the round off error that is generated due to the calculation of finite difference equation. The inability of a model to generate a solution that goes to infinity results in the generation of a round off error. The error is generated with each individual calculation in the scheme and the model is said to be stable if this error is negligible in comparison to the true solution to the finite difference equation. The stability of the model is generally governed by the Courant condition and this condition is incorporated into the DIVAST model that will terminate a model before excessive error is generated. The Courant number is calculated by the following formula (Strikwerda 2004):

$$C_n = \sqrt{gH} \frac{\Delta t}{\Delta x} \quad (3.23)$$

with  $g$  representing gravity,  $H$  is average water depth below the mean water level,  $\Delta t$  and  $\Delta x$  are the time step and spatial resolution respectively.

The finite difference scheme used by the model is of an implicit form, which is inherently stable and does not have to comply with the Courant condition, however, the accuracy of a model can also be linked to such a condition (Falconer 1988). Research has shown that a Courant number greater than 8 leads to a decrease in the level of accuracy of the model solution. Therefore, the model imposes a restriction on the time step ( $\Delta t$ ) with respect to a certain grid spacing ( $\Delta x$ ). The following equations represent the time step restriction to prevent inaccuracy:

$$\Delta t_{max} \leq 8 \frac{\Delta x}{\sqrt{gH}} \quad (3.24)$$

The accuracy of a finite difference model is directly linked to the time step and the number of grid points. The most effective way of increasing accuracy is increasing the number of grid points, which also leads to an increase in the time step to coincide with the Courant condition. This, however, results in a large increase in the computational needs of the modelling procedure.

# CHAPTER 4: ADVANCED ONE-WAY NESTED MODEL

## 4.1 INTRODUCTION

The one-way nesting technique in the DIVAST model uses a Dirichlet boundary condition and a linear interpolation method to allow a nested domain of high resolution to be embedded in a coarse resolution grid. Results generated with this technique were shown to be highly compatible with a high resolution grid of the full domain (Nash 2010). However, the locations of the nested domains open boundaries are crucial to the accuracy of the model. Errors generated at the boundary of the nested domain are a result of inaccuracies in the coarse domain in the region of the nested boundary. Therefore, the nested boundaries should be positioned in an area of low coarse domain inaccuracies. Resulting in an increase in the number of grid points in the nested domain and increase the computational effort required for the model.

In the DIVAST one-way nested model the shape of the nested grid was restricted to a rectangular or square shape. The concept of a one-way nested model with the possibility of irregular geometry boundaries was proposed with the aim of allowing greater flexibility and applicability of the model. The irregular boundaries would allow ease of positioning for accurate boundary location, and also for an area of interest to be modelled with a reduction in the number of grid points required to produce a model solution of high accuracy and stability.

To further optimise the one-way nested model a novel approach was taken to modify the nested grid to allow the domain to be positioned at different orientations. In this manner, the size of the high resolution nested grid and the related computational needs can be reduced further.

This chapter presents a description of the DIVAST one-way nested model and modifications performed to allow the aforementioned advanced features to be introduced and results generated.

## 4.2 DESCRIPTION OF ONE-WAY NESTED MODEL IN DIVAST

DIVAST was extended with the introduction of a one-way nesting technique (Nash 2010). This technique involved the introduction of an additional higher resolution grid into an area of interest for a better representation of hydrodynamic processes.

The procedure for the one-way nested model involves a number of steps. Initially, the coarse domain is simulated for a full time step, at the end of which the open boundary information for the nested grid is allocated and interpolated from the coarse domain data with respect to space and time. The nested domain solution is then computed until the time level of the nested domain is equal to that of the coarse domain.

The majority of the code generated for the inclusion of a one-way nested grid has no interaction with the main code for the low resolution coarse grid, therefore the nested domain runs almost completely independently, excluding the interaction in a subroutine that allows information to be passed into the nested domain from the coarse domain to specify the boundary conditions (see Appendix B for flowchart of one-way nested procedure and description).

The accuracy of the nested model is governed mainly by the interaction between the coarse and nested grid through the boundary conditions. The generation of errors can result from the specification of incorrect boundary data, an inefficient boundary operator and also simplification of boundary formulation.

The boundary operator used in the one-way nesting procedure involves the use of the Dirichlet condition, where the characteristics of the coarse domain are directly imposed onto the boundary ( $\Gamma$ ) of the nested domain. Equation 4.1 represents the mathematics associated with the condition.

$$\phi_n|_{i,j} = \phi_c|_{i,j} \quad \text{On } \Gamma \quad (4.1)$$

where  $i, j$  are the nested grid coordinates. The coarse grid solution  $\phi_c|_{i,j}$  on  $\Gamma$  was obtained by interpolation in time and space to the resolution of the nested grid.

A linear method is used in relation to the spatial and time interpolation. Equation 4.2 represents the mathematics associated with this interpolation scheme:

$$\phi_k = \phi_{I-1} + w(\phi_I - \phi_{I-1}) \quad (4.2)$$

where:

$$w = \frac{2k+r_s-1}{2r_s} \quad \text{for } k=1\dots r_s$$

The equation shows the value of a scalar at the nested grid point  $k$ , in a horizontal row, is interpolated from the coarse domain points at  $I$  and  $I-1$  and a coefficient of proportionality  $w$ . This coefficient is calculated in relation to the distance the  $k$  point is from the  $I$  coarse point and the nesting ratio  $r_s$ .

The central finite difference, staggered grid scheme used in the DIVAST model presents a problem for the formulation of the finite difference approximations of the partial derivatives at the open boundary cells. The following equation represents the central finite difference method for the partial derivative of the x-direction depth integrated volumetric flux at point  $(i+\frac{1}{2}, j)$ .

$$\left. \frac{\partial q_x}{\partial x} \right|_{i+\frac{1}{2}, j}^n = \frac{q_x|_{i+1, j}^n - q_x|_{i, j}^n}{\Delta x} \quad (4.3)$$

The staggered grid method used introduces an extra calculation in the form of linear interpolation, as the values for  $q_x|_{i, j}^n$  and  $q_x|_{i+1, j}^n$  are not represented at the centre of the grids but at the sides of the grids (see Chapter 3, Figure 3.2). The following equations show the linear interpolation method used:

$$q_x|_{i, j}^n = \frac{q_x|_{i-\frac{1}{2}, j}^n + q_x|_{i+\frac{1}{2}, j}^n}{2} \quad (4.4)$$

$$q_x|_{i+1, j}^n = \frac{q_x|_{i+\frac{1}{2}, j}^n + q_x|_{i+1\frac{1}{2}, j}^n}{2} \quad (4.5)$$

The method requires the values for two adjacent grid points in both the positive and negative direction for the approximation of the unknown value. This method is appropriate for all internal boundaries, however, it requires alteration for open boundaries, as not all required known points are available.

DIVAST solves this problem by setting the boundary grid cells equation to zero. The following equations represent the alteration to the advective acceleration term in the x-direction momentum equation at an x-direction boundary:

Internal grid cell:

$$\beta \left[ \frac{\partial U q_x}{\partial x} + \frac{\partial U q_y}{\partial y} \right] \quad (4.6)$$

Boundary grid cell:

$$\beta \left[ \frac{\partial U q_y}{\partial y} \right] \quad (4.7)$$

A similar modification is made in the y-direction momentum equation for cells that lie on the y-boundary. This modification prevents the incorporation of a rate of change of momentum in the direction normal to the boundary cells. This can introduce errors in the area of boundaries.

Ghost cells are also incorporated into the one-way nested model to allow the boundary cells of the nested domain to be computed like internal boundaries in relation to the formulation of the governing equations.

Figure 4.1 shows an illustration of the boundary of the nested domain with the shaded region highlighting, where information from the coarse domain is interpolated and fed into the nested domain. The illustration also shows the location of the ghost cells, which are incorporated into the model to allow the boundary cells for the nested domain to be considered as internal boundaries, hence reducing the generation of error in the domain. The ghost cells are represented in Figure 4.1 with the symbol  $\Gamma^*$ .

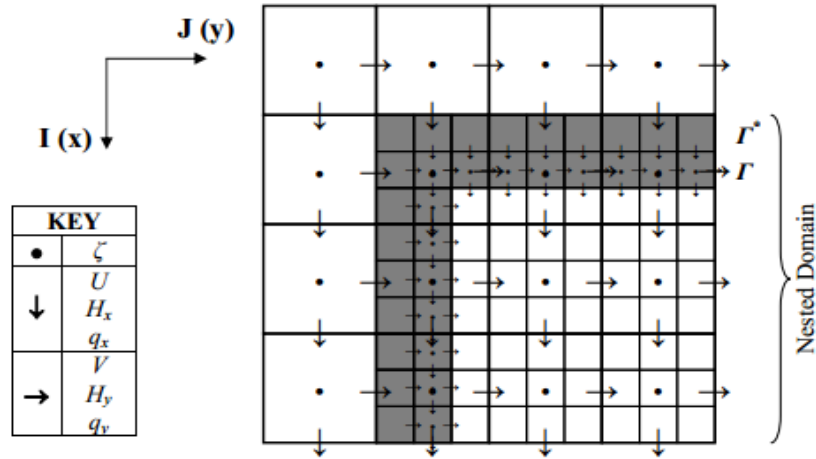


Figure 4: 1 Nested grid configuration showing boundary interface of nested grid incorporating internal boundary  $\Gamma$  and adjacent exterior ghost cells  $\Gamma^*$ .

Boundary data is assigned to both the nested domain boundary  $\Gamma$  and the ghost cells  $\Gamma^*$  from the coarse domain in a similar manner; however, only velocities and fluxes normal to the boundary are required for the ghost cells.

### 4.3 DESCRIPTION OF ROTATED NESTED MODEL

The RNM (Rotated Nested Model) was developed to allow a nested grid to be orientated at different angles in a low resolution coarse domain. This rotational ability provides an additional, optional, functionality to the features of the one-way nested model. Therefore, all the specifics covering the one-way nested model are applied to the rotated nested model. For a specified rotation, the angle of rotation and the orientation of the movement are defined by the user prior to the simulation of the model in an input data file.

The generation of the RNM required the transformation of the rotated nested grid in the original physical domain with a coordinate system of  $(x, y)$ , to a non-rotated grid in the computational domain with a coordinate system of  $(\xi, \eta)$ . Such a transformation is required to allow the conventional finite difference method to be used to solve the partial differential governing equations. Figure 4.2 represents the RNM grid in the physical domain, with the physical domains coordinate system and the computational domains coordinate system specified.

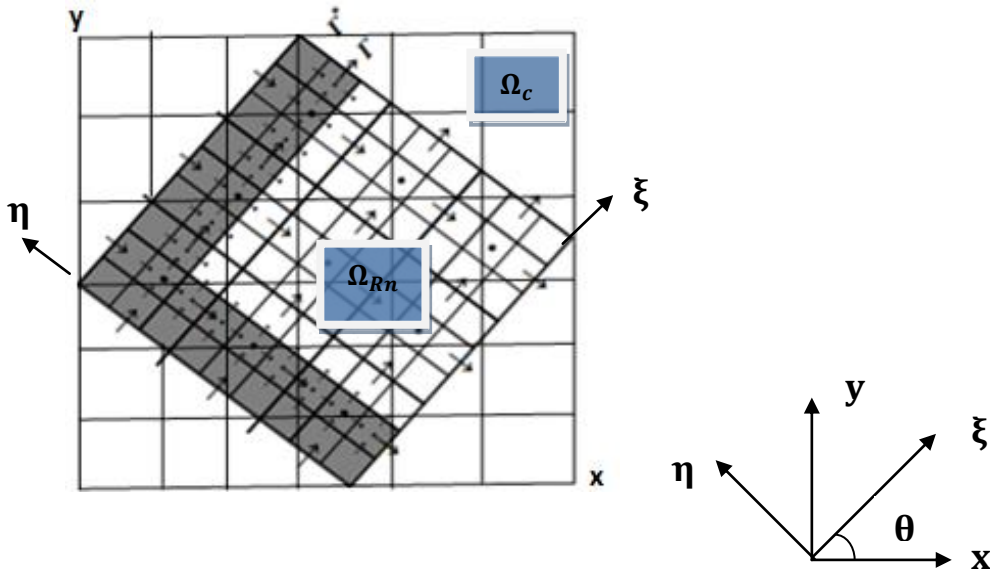


Figure 4: 2 Rotated nested domain  $\Omega_{Rn}$

The procedure requires a transformation scheme to establish a relationship of the following form between the physical domain and computational domain.

$$\eta = \eta(x, y) \quad (4.8)$$

$$\xi = \xi(x, y) \quad (4.9)$$

The initialisation files (see Appendix B) require this relationship to appropriately assign data to the grid cells in the rotated domain to identify initial depths and elevations.

The Dirichlet boundary condition and the linear interpolation procedures used in the non-rotated nested model were used in the rotated nested model to allow an accurate model to be generated. Modification of the interpolation procedure was performed to comply with the rotated nested boundaries.

The boundary conditions that are prescribed at the new boundaries were also transformed with respect to the rotated coordinate system. The hydrodynamic variables generated at the end of the simulation required an inverse transformation to allow the variables to be described in the non-rotated coordinate system.

## 4.4 DESIGN OF ROTATED NESTED MODEL

The RNM was proposed to expand the existing one-way model to allow the rotation of the nested grid. The one-way nested grid could then be placed into domains that are at an angle in the main model, examples include: rivers flowing into an estuary at an angle and meanders located along an estuary.

The following points represent the main design requirements for the rotated nested model:

- The user can specify the extent of the domain and the angle at which the domain will be rotated at.
- The model should be able to rotate at any angle in a clockwise or anticlockwise orientation.
- Boundary operators need to interpolate the data accurately from the coarse domain to the rotated nested domain.
- The governing equations need to be solved at every grid point in the nested domain to generate a solution to the unknown variables, with respect to the new coordinate system.
- There should be no significant reduction in the model accuracy.

Design requirements were taken into account and the following strategy was compiled:

- Read in the angle of rotation with the use of a new input file.
- Establish a relationship between physical domain and computational domain for the generation of matrices to be used in the governing equations.
- Transformation of the boundary conditions to the new rotated coordinate system.
- Solve the governing equation in the computational domain in a uniformly spaced rectangular grid.
- Perform a reverse transformation to identify the variables in the physical domain.

Figure 4.3 represents a flowchart of the proposed model program taking the design requirements into account. The majority of the code originates from the one-way nested scheme. The original DIVAST code is identified by the non-shaded regions in

the flow chart. The one-way nesting technique is identified by the blue shaded sections. The light blue shaded sections in the flowchart identify the sections where modifications were performed to allow for the rotation of the nested domain.



## 4.5 IMPLEMENTATION OF ROTATED NESTED MODEL

The RNM consists of a main program that calls a number of subroutines in sequence. Figure 4.4 illustrates the structure of the model in a flow chart form and gives a brief description of the different stages in the model. The model is of a similar form to the one-way nested model but includes modifications to some of the existing subroutines.

Input data, identification of the integration section and variable initialisation for the coarse domain are all performed in section 1-7 in the main program. The execution of subroutines 8-17 are performed at each time step during the model simulation, with subroutines 8-11 being performed in the first half time step to compute the hydrodynamic regime in the x-direction for the coarse domain, while the y-direction variables are computed in the second half time step in subroutine 12-15. The Chezy and Eddy viscosity are re-calculated in subroutines 16-17 at regular intervals at the end of a full time step. Specification of the nested domains integration section and variable initialisation are performed in subroutine A-C. Subroutine D oversees the calling of the subroutine that assigns the boundary data for the nested domain (D.1, D.5) and computation of the hydrodynamic subroutine in the nested domain for the x- direction (D.2-D.4) and y-direction (D.6-D.8). The re-calculation of the Eddy and Chezy variables for the nested domain are performed in subroutine E-F.

The implementation of the rotated nested domain was performed with the modification of the subroutines used in the one-way nesting procedure. The first of these modifications was performed in the FIND\_F (B) subroutine, with the incorporation of the coordinate transformation equations. This subroutine uses the information that is read into the model through the FIELD (A) subroutine to generate matrices that describe the characteristics of the modelling domain that are to be used in the hydrodynamic solution scheme. The relationship between the increments, or the grid spacing, is also incorporated in this subroutine to allow the correct information to be read into the matrix to correspond to the rotated nested domain. The modification of the code with respect to the boundary interpolation scheme and boundary conditions are generated in the FINEBND (D.1, D.5) subroutine. This subroutine generates the data required for the boundary conditions that are used in the recursion equation to generate a solution to the governing equations for the x-direction variable in the HYDMODX\_F (D.2) subroutine and the y-direction variable in the HYDMODY\_F (D.6) subroutine. This subroutine required that the new

boundary location be interpolated and generated with respect to the new coordinate system for the rotated domain- this was done by incorporating the boundary transformation procedure.

The initial variable transformation is performed at the nested open boundary and is undertaken in the same subroutine that performs the interpolation and boundary conditions procedure. This involves the transformation of the variables with respect to the angle and orientation of the rotated domain. The final stage of the code modification involves the inverse transformation of the variables after the hydrodynamic solution scheme has been performed. This is undertaken in the NEST subroutine at the end of the HYDMODX\_F and HYDMODY\_F. A full list of sections modified in the numerical model is presented in Table 4.1.

Table 4: 1 Modifications of the source code to allow the rotation of the nested domain

Program section	Function	Modification
Main Program	Reads input data	Read new input data
Main Program	Writes input data	Write input data from new data file
FIND_F	Establishes open boundaries in nested domain	Coordinate transformation and grid spacing calculation
FINEBND	Extracts, interpolates and assigns boundary data from coarse model	Rotated boundary identification, assignment of new boundary data in the rotated coordinates
HYDMODX_F	Solves hydrodynamics in x-direction	Solves hydrodynamics in $\xi$ -direction
HYMODY_F	Solves hydrodynamics in y-direction	Solves hydrodynamics in $\eta$ -direction
NEST	Main do loop in nested domain	Inverse transformation of variables



Figure 4: 4 Flow chart of nested model structure, with red identifying the subroutines used in the nesting procedure and green identify the subroutines that were modified for the RNM.

### 4.5.1 ROTATED DOMAIN FORMULATION

When a specific domain rotation is required, the first function of the new code in the FIND\_F subroutine is to determine the location of the new rotated nested domain in relation to the coarse domain. This is done by identifying the localised coordinates for each grid point, in the rotated domain, with respect to the coarse domain. Figure 4.5 illustrates the non-rotated domain (green) with corner coordinate points (a-d) and rotated domain (red) with corner coordinate points (A-D).

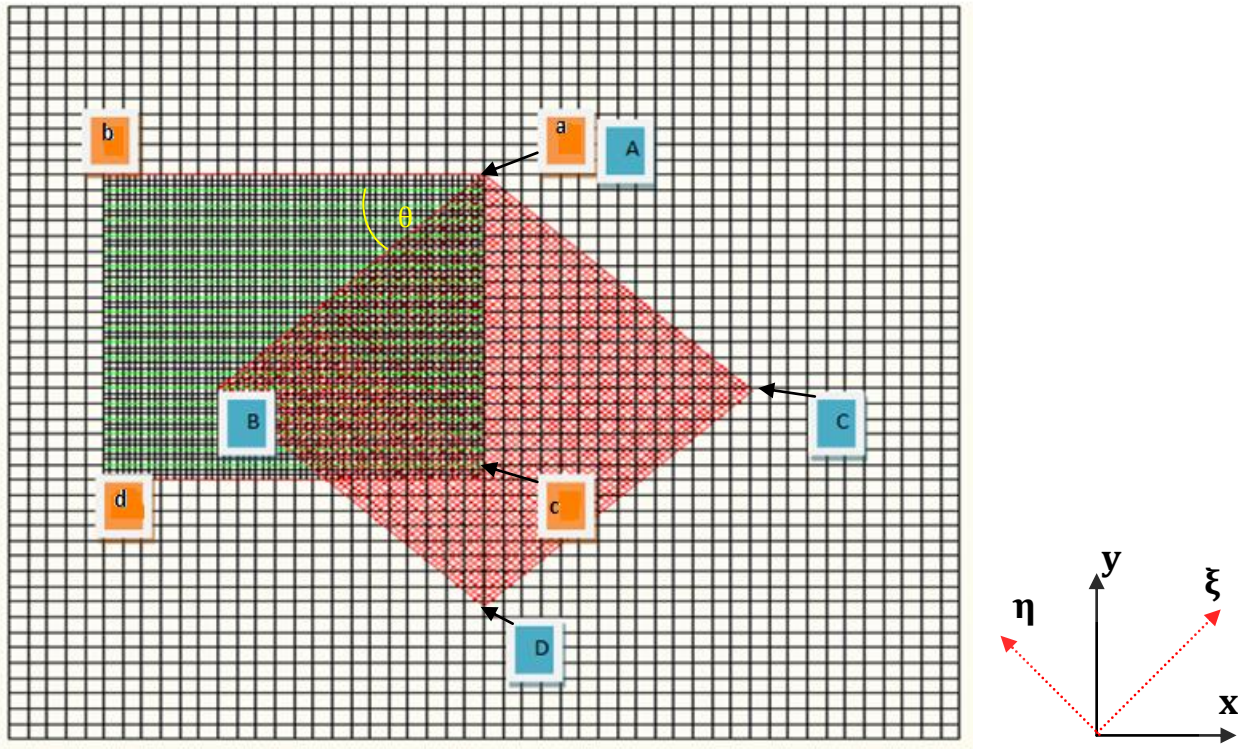


Figure 4: 5 Illustrations of the non-rotated domain and the rotated domain

The following equations represent the method used to identify A and B in relation to the coarse domain co-ordinate system.

$$A(\xi, \eta) = a(x, y) \quad (4.10)$$

$$|AB| = |x_a - x_b| + 1 \quad (4.11)$$

$$B_1 = |AB| \times \cos \theta \quad (4.12)$$

$$B_2 = |AB| \times \sin \theta \quad (4.13)$$

$$B_\xi = A_\xi - B_1 \quad (4.14)$$

$$B_\eta = A_\eta - B_2 \quad (4.15)$$

where  $\theta$  is the angle of rotation,  $x_a$  is the value of the x-coordinate point at  $a$  and  $x_b$  the value of the x-coordinate point at  $b$ .

Identifying the coordinates  $C (\xi, \eta)$  and  $D (\xi, \eta)$  required a similar calculation to the one used for the generation of the  $B (\xi, \eta)$  coordinates. In addition to the specification of the corner coordinates, the spacing between each point in the rotated nested domain is required. The following equations are used to calculate the spacing between points in the rotated nested grid:

$$\Delta\xi = INT_\xi \Delta x \quad (4.16)$$

$$\Delta\eta = INT_\eta \Delta y \quad (4.17)$$

with  $\Delta\xi$  representing the spacing in the  $\xi$  direction in the rotated nested grid and the spacing in the  $\eta$  direction is represented with  $\Delta\eta$ . These values are generated with respect to the original grid spacing values of  $\Delta x$  and  $\Delta y$  in the x and y directions respectively. The increment variation value is represents with the value INT and is calculated in the following manner:

$$Int_\xi = \frac{B_1}{|ab|} \quad (4.18)$$

$$Int_\eta = \frac{D_1}{|ad|} \quad (4.19)$$

where:

$$B_1 = |ab| \times \cos \theta$$

$$D_1 = |ad| \times \sin \theta$$

Through these methods a data mask can be generated over the new grid to allow the specification of land and sea. The cells in the grid that are sea and require assignment of data are specified as one, while the grid cells that are land do not require data, and are specified as zero. The

bathymetry data required for the nested domain can, also, now be carried forward from the FIELD\_F (see Figure 4.4) subroutine to represent the rotated nested domain.

The next step in the development of RNM involved the identification of the rotated nested grid boundary location with respect to the coarse domain, which was performed in the FIND\_F subroutine and FINEBND subroutine. This was required for open boundary conditions to be transfers to rotated boundary locations and to prevent error generation.

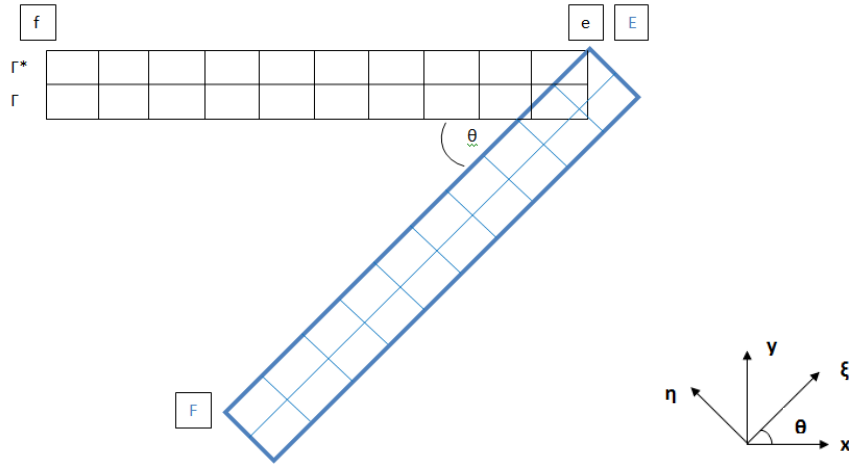


Figure 4: 6 Rotated nested boundary

Figure 4.6 shows an illustration of the non-rotated boundary ( $\Gamma$ ) and ghost cells ( $\Gamma^*$ ) with corner points  $e(x, y)$  and  $f(x, y)$ . The Figure also shows the rotated boundary and ghost cells (blue) with corner points  $E(\xi, \eta)$  and  $F(\xi, \eta)$ . The following equations represent the method used to identify the RNM boundaries.

$$E(\xi, \eta) = e(x, y) \quad (4.20)$$

$$|EF| = |x_e - x_f| + 1 \quad (4.21)$$

$$F_1 = |EF| \times \cos \theta \quad (4.22)$$

$$F_2 = |EF| \times \sin \theta \quad (4.23)$$

$$F_\xi = E_\xi - F_1 \quad (4.24)$$

$$F_\eta = E_\eta - F_2 \quad (4.25)$$

where  $\theta$  is the angle of rotation,  $x_e$  is the value of the x coordinate point at  $e$  and  $x_f$  value of the x coordinate point at  $f$ .

The next stage of the implementation procedure involved the modification of the FINEBND subroutine, in relation to the interpolated boundary conditions generated in the coarse domain. The boundary conditions require transformation into the new rotated domain coordinates to allow the accurate generation of variables in the model simulation, with respect to the computational domain. The following equations were used to transform the boundary conditions to the new computational rotated domain.

$$\begin{bmatrix} \phi_\xi \\ \phi_\eta \end{bmatrix} = \begin{bmatrix} \cos \theta & -\sin \theta \\ \sin \theta & \cos \theta \end{bmatrix} \begin{bmatrix} \phi_x \\ \phi_y \end{bmatrix} \quad (4.26)$$

where the boundary conditions in the computation domain, in the  $\xi$  and  $\eta$  direction, are represented with  $\phi_\xi$  and  $\phi_\eta$  and the boundary conditions in the physical domain are symbolised with  $\phi_x$  and  $\phi_y$  for the x and y directions. The angle of rotation is presented with  $\theta$ .

The variables in the computational domain need to be transformed back into the physical domain after the hydrodynamic solution scheme is performed. This is done in the reverse order, in the NEST subroutine, to the previous transformational method shown in equation 4.26.

## 4.6 RESULTS

The model used to test the performance of the rotated nested model was an idealised gently sloped harbour. This model was used to allow a high resolution RNM to be incorporated into a low resolution model to generate an area of interest with a higher degree of accuracy. Figure 4.7 shows an illustration of the harbour used in the development of the RNM.

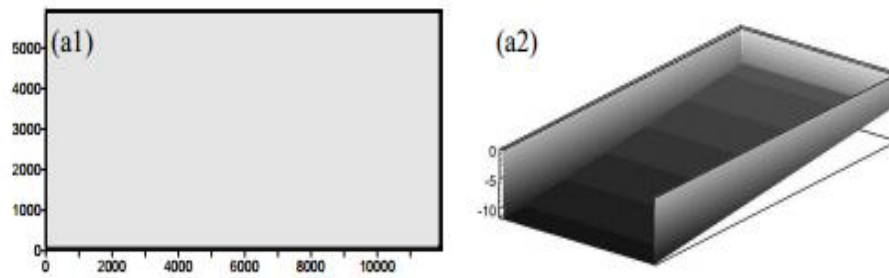


Figure 4: 7(a1) Plan view of rectangular harbour (a2) view of bathymetry in harbour (depths in meters)

The domain of the development model that was embedded with the RNM had dimensions of 12km x 6km. The nesting ratio between the low resolution coarse parent domain and the rotated nested domain was of a 3:1 scale. The grid spacing and time step associated with the coarse domain were 120 meters and 120 seconds respectively. The eddy viscosity and roughness of harbour bed were considered the same in both the coarse model and the rotated nested model. Problem areas that may occur in the model were easily identified by setting the degree of latitude to zero to reduce the Coriolis Effect on the hydrodynamic process, allowing all the flow patterns to be symmetric along the longitudinal axis. The tidal period associated with the model was a constant of 12.5hrs and had a range of 3 meters. The model was run for 50 hr, which consisted of 4 full tidal cycles.

The accuracy of the RNM was compared to a model that introduced a high resolution over the full domain. The dimension of the model was a 12km x 6km gently sloped harbour domain, however, the time step and the grid spacing associated with the domain were 40 seconds and 40 meters respectively. The model employed the same physical hydrodynamic parameters as the low resolution nested model. The external forcing associated with the model was also mirrored in relation to the nested model.

The model was initially run with a high resolution across the full harbour domain. The model was then run in a lower resolution and nested with a RNM. The position of the rotated nested grid is shown in Figure 4.8. This nested domain consisted of four open boundaries, which allowed for a severe test of the RNM. Error analysis and time history analysis were carried out on

the models to show the difference between the high resolution model of the full domain and the low resolution model with the incorporation of a RNM.

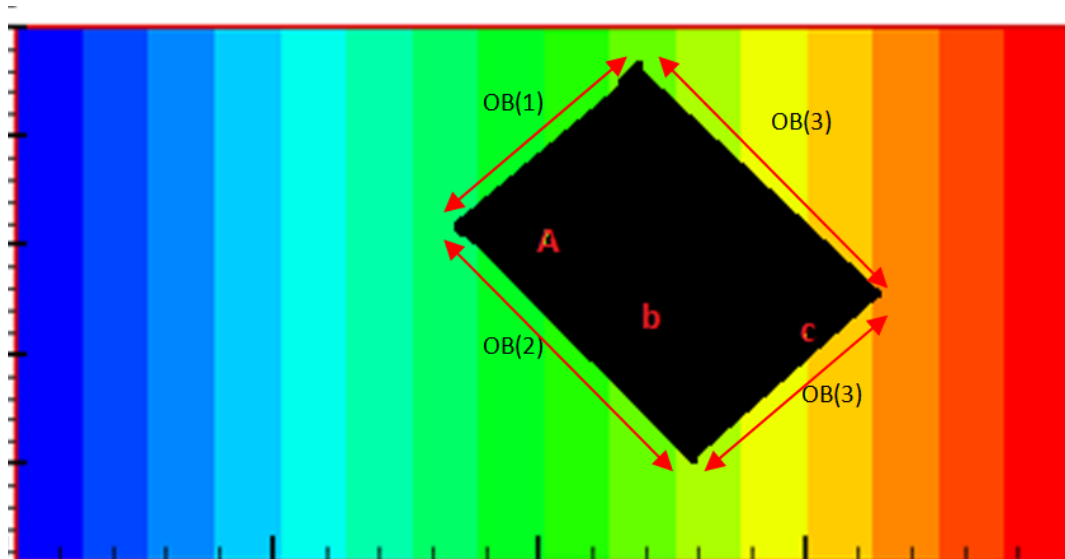


Figure 4: 8 RNM in low resolution domain with points A, B, and C specified in the nested domain and the four open boundaries (OB).

The first forms of outputs that are generated by the models are known as time series. Time series involve information being output, in relation to a particular grid point, over the course of a full model simulation at regular intervals. The information generated shows the variation of the output in relation to time not space. The RNM model performance is assessed using this method of analysis by comparing a point in the high resolution model domain with the same point in the RNM. Three points in the nested region were analysed in relation to the high resolution domain; these points are specified in Figure 4.8. The graphs shown in Figures 4.9-4.11 show the time series analysis of points A, B and C.

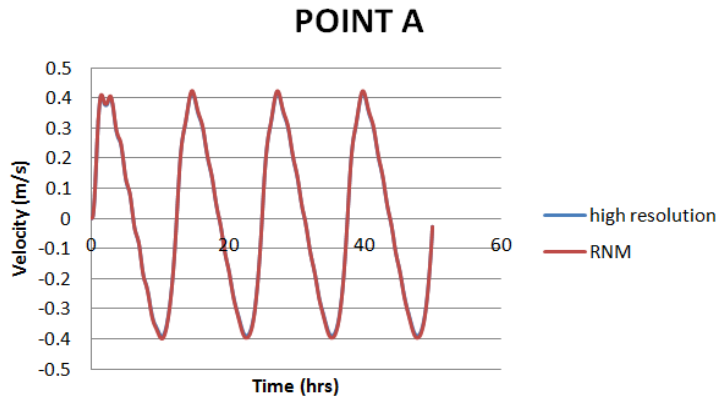


Figure 4: 9 Graph of velocity vs. time at point A in a high resolution standard model and in the RNM

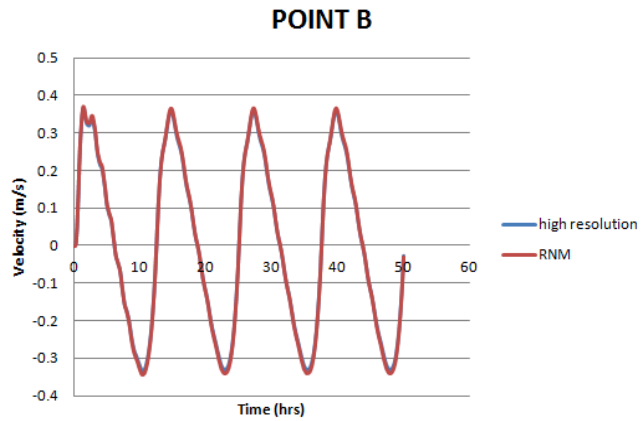


Figure 4: 10 Graph of velocity vs. time at point B in a high resolution standard model and in the RNM

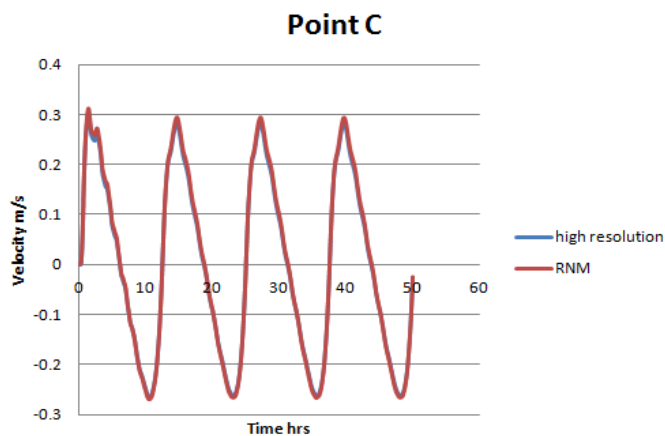


Figure 4: 11 Graph of velocity vs. time at point C in a high resolution standard model and in the RNM

The graphs show the rotated nested model generates a solution with a level of accuracy equivalent to the high resolution model with a reduction in the number of grid points.

The model was also assessed in relation to space and time. This was performed by generating snapshot files over a tidal cycle and calculating the tidally-averaged absolute error and relative error. Snapshot files contain model output values of model variables for all grid points at a particular instance of time. The following equation shows how the tidally-averaged relative error was calculated at a grid point (Nash 2010):

$$RE_{T|I,J} = \frac{\sum_{n=1}^N |\varphi_{i,j}^t - \phi_{i,j}^t|}{\sum_{n=1}^N |\varphi_{i,j}^n|} \times 100 \quad \text{for } i = 1, 2, \dots, i_{max} \quad j = 1, 2, \dots, j_{max} \quad (4.27)$$

with  $\varphi$  representing the nested domains variable and the high resolution single grid domain variables represented with  $\phi$ .  $N$  corresponds to the number of snapshots that are generated in one complete tidal cycle.

Figure 4.12 shows the relative error over a full tidal cycle in velocities for the RNMs nested region. The error analysis was completed in relation to the final tidal cycle in the model simulation. Results showed by inspection the relative error in the RNM nested domain is minimal.

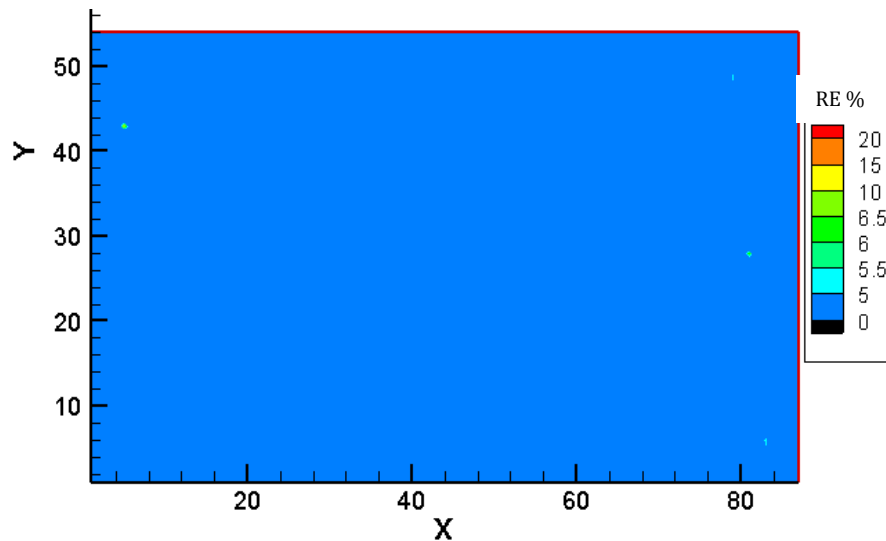


Figure 4: 12  $RE_T$  in velocities for RNMs nested domain

## 4.7 DESCRIPTION OF IRREGULAR GEOMETRY BOUNDARIES

The configuration of the nested grid in the one-way nesting technique in DIVAST has solely been of a rectangular form. The introduction of a technique to allow the nested domain to be of an irregular shape would increase the flexibility and applicability of the model. This irregular shape could also decrease the number of grid points required to model an area of interest to a high level of accuracy and stability. With this in mind, a nested grid with irregular geometry boundaries was developed. Figure 4.13 shows an illustration of possible domains and boundaries that can be developed with the new irregular geometry boundary (IGB) nested domain. The implementation of such a scheme involved using the existing one-way nesting technique with additional features added to the code.

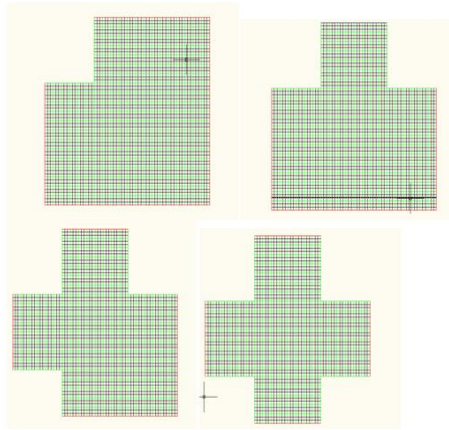


Figure 4: 13 Irregular geometry boundary domains

The first step involved the identification of the new shape of the nested domain with the reconstruction of the matrices that specific the characteristics of the nested domain. Secondly, boundaries that are generated from the new irregular shape required identification and boundary data from the coarse domain needed to be interpolated onto the new irregular geometry boundaries. The one-way nesting procedure with the inclusion of the IGB technique is illustrated in the flowchart in Figure 4.14, with the green shaded regions identifying the additional features added and the yellow shaded regions highlighting the routines in the one-way nesting technique.



#### 4.7.1 IDENTIFICATION OF NEW DOMAIN

Manipulation of the code that identifies the shape of the nested domain was required for the simulation of the model with a new nested irregular domain shape. Firstly, the matrices used to initialise the characteristics of the high resolution nested grid points require reconstruction to allow the integration of the solution scheme to be performed with respect to the new irregular nested domain.

Modification of the matrices requires a user to identify areas that are not involved in the integration procedure for the new irregular shapes i.e. are not part of the new nested domain. This required modification of existing code and the generation of new code to introduction the IGB model domain.

The initial changes to the code were undertaken in the subroutine FIND\_F (Figure 4.4). This subroutine processes the data from the FIELD\_F subroutine, which reads in information for cell characteristic in relation to depths of domain and what grid cells are wet and dry for a full high resolution model domain. The FIND\_F uses this data to generate matrices to identify the wet and dry cells in the nested domain and reads in the depths that are associated with the wet cells.

The generation of a domain with an irregular shape was constructed by specifying areas in the matrices that would not be taken into account in the hydrodynamic solution scheme of the nested domain. There are five sections in the code that can be specified as dry, these are shown in Figure 4.15.

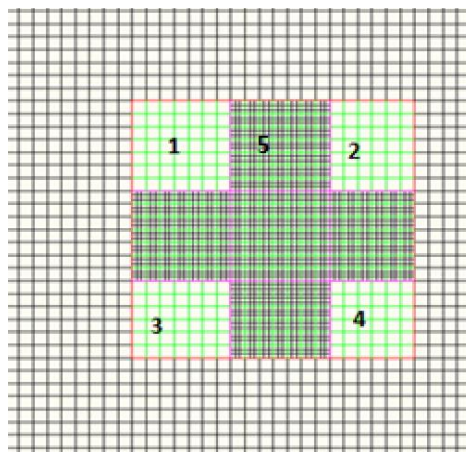


Figure 4: 15 Nested domain showing sections 1-5

## 4.7.2 BOUNDARY RECONSTRUCTION

The accuracy of the nested model, mentioned previously, is governed by the boundary conditions generated from the interaction between the fine and coarse domains. Large error can be generated if inaccurate boundary data is fed into the nested domain from the coarse model.

The new domain introduces irregular boundaries, which required identification by the nested model. The boundary formulation required modification for information to be transferred into the domain through irregular boundaries. The identification of the new boundaries is essential to allow linear interpolation and the Dirichlet boundary condition to be performed with respect to the new modified boundaries. The positioning of the ghost cells also required movement to allow the cells to be positioned in conjunction with the new irregular boundary.

Irregular boundaries were introduced into the model by breaking the boundaries up into multiples, which generated a number of new boundaries. Figure 4.16 shows all possible boundaries that can be introduced into the IGB model.

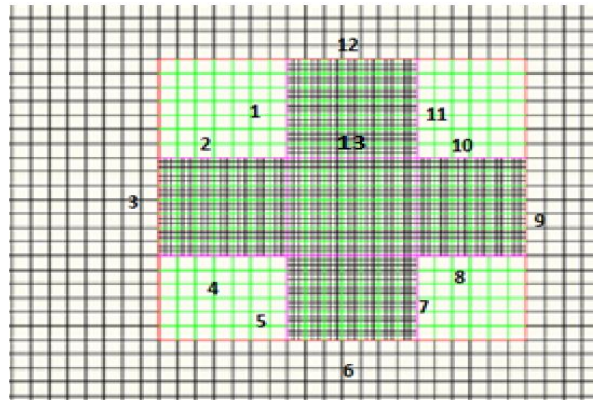


Figure 4: 16 Open boundary identification

The inclusion of the new open boundaries required the introduction of new code to allow data from the coarse domain to be assigned to all new open boundaries. This code was introduced in the FIND\_F subroutine, shown in the flowchart in Figure 4.4, where the data from a new input data file SHAPE is read. This data specifies the location, extent and type of the new boundaries required for the IGB model. The information from FIND\_F in relation to the boundaries is carried forward to the FINEBND (Figure 4.4) subroutine where the interpolation of the data from the coarse domain along the open boundaries is generated through linear interpolation and a

Dirichlet boundary operator. New code allowed this method to be performed on each of the new open boundaries generated with the inclusion of the new modified domain.

## 4.8 RESULTS

Testing of the model was carried out by applying it to a gently sloped harbour, shown in Figure 4.17. The harbour was initially nested with the original rectangular one-way nested model (Figure 4, 18(a)). The model was then nested with a nested domain containing irregular geometry boundaries, shown in Figure 4.18(b). Error analysis and time history analysis were carried out on the models to show the difference between the extensively tested original nested model (Nash 2010) and the IGB model.

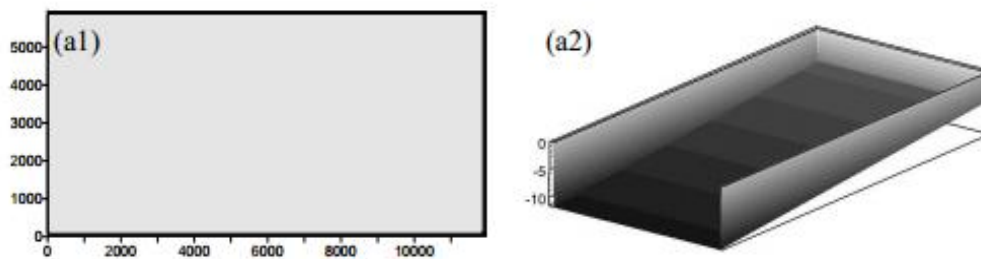


Figure 4: 17 Gently sloped rectangular harbour

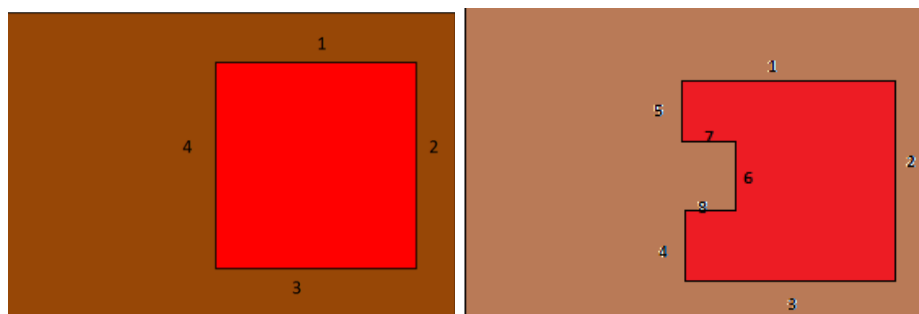


Figure 4: 18 Rectangular harbour nested with (a) original rectangular nested grid and (b) IRG nested grid, specified with red shading and all boundaries identified.

Figure 4.19 shows the tidally-averaged relative error for velocities in the nested domain, between the original rectangular one-way nested model and a high resolution model of the full domain. Results generated showed that the error is minimal and the accuracy of the one-way nested model of a high standard.

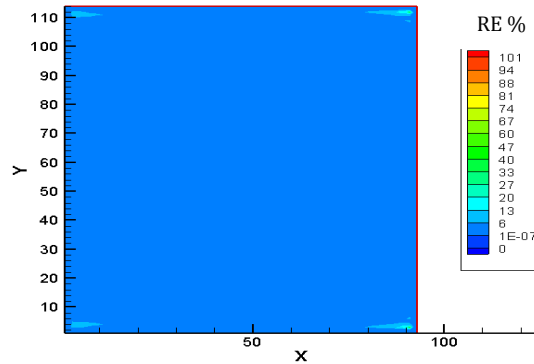


Figure 4: 19 RE<sub>T</sub> for velocities between regular nested model and high resolution model.

The rectangular harbour was nested with the u shaped IGB model, shown in Figure 4.18(b), and error analysis performed. Figure 4.20 shows the tidally-averaged relative error for velocities generated in the nested domain for the IGB model.

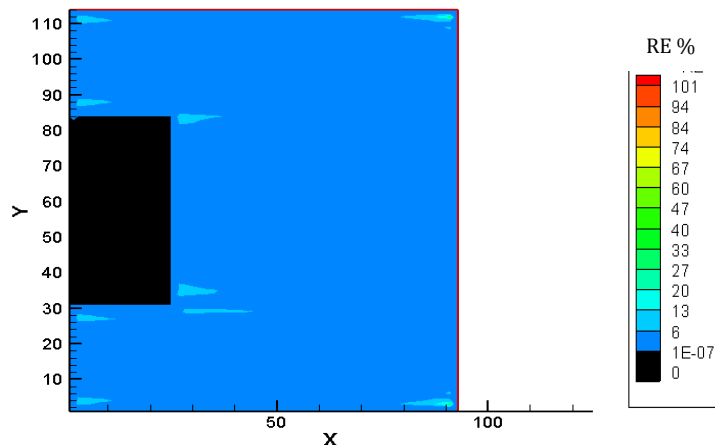


Figure 4: 20 RE<sub>T</sub> for velocities between IGB model and high resolution model in the nested domain.

Results showed the error generated is insignificant and the relative error is approximately the same as the original nested domain. Time history analysis was also performed, which show the output over the full run time of the model for a particular grid point. This is a very stringent analysis and can identify differences between the two models. The following graphs show time

history analysis for 2 points, which are specified in Figure 4.21, for both the regular boundary domain and the new irregular boundary domain.

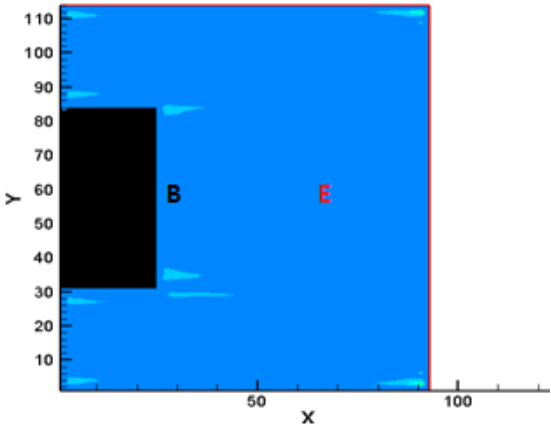


Figure 4: 21 Time history locations

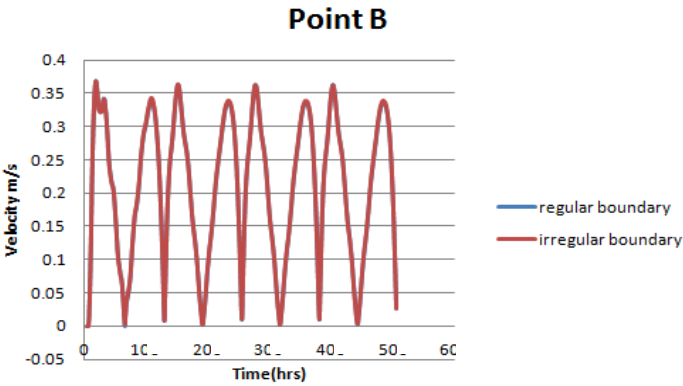


Figure 4: 22 Time history at point B

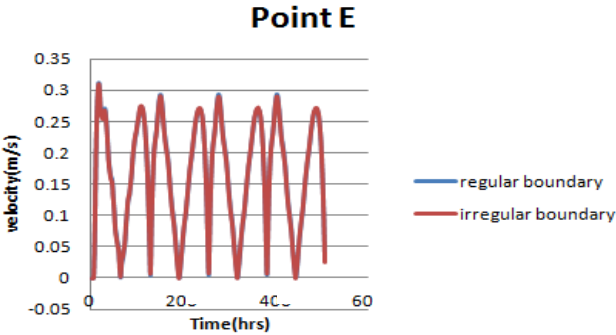


Figure 4: 23 Time history at point E

The graphs show that difference between the two models is negligible and the IGB nested model generates an accuracy equivalent to the original nested model with a reduction in the number of grid points.

## 4.9 SUMMARY AND CONCLUSION

This Chapter outlined the effective incorporation of additional feature added to a one-way nesting technique in the numerical model DIVAST to enable an increase in flexibility and applicability of a one-way nesting technique. Two features were successfully introduced: 1) the ability of the nested domain to be orientated at different angles, 2) Irregular geometry boundaries.

The extensively tested one-way nested model contains: a linear interpolation technique and a Dirichlet boundary condition. This one-way nesting model incorporates ghost cells into the formulation of the nested grid boundaries. This formulation enables the nested grid boundaries to be perceived as internal boundaries, and ensures a high level of conservation at the nested grid boundary.

The initial feature added to the one-way nested model, involved the incorporation of a technique that enables the nested domain to be orientated at different angles. This technique involved transforming the physical rotated nested domain onto a computational domain that is structured and non-rotated in relation to a rotated coordinated system. This enabled a structured grid scheme to perform the finite difference scheme in the computational rotated domain. Boundary conditions generated in the coarse domain required transformation to the rotated coordinate system to force the model simulation in the rotated nested domain. Transformation of variable values after the simulation of the high resolution nested domain hydrodynamic solution scheme was performed to describe the variables with respect to the physical non-rotated domain.

A rotated nested grid with four open boundaries was incorporated into a low resolution gently sloped harbour and its performance in the nested domain was compared to a single high resolution model of the full domain. The performance of the model was assessed with the use of time history analysis at three different locations in the nested grid. Results generated showed the RNM generated a solution with a level of accuracy equivalent to the high resolution single grid

with a reduction in the number of grid points. The model was also assessed in relation to space and time, with the generation of the tidally-averaged relative error and absolute error for velocities in the nested grid. Error analysis results by inspection showed the model solution in the rotated nested region is of a high order.

The one-way nested model was further extended by the incorporation of irregular geometry boundaries. The introduction of the IGB method enabled nested grids of different configurations to be incorporated into a low resolution grid. Resulting in a one-way nested model with greater flexibility, and a further reduction in the computational need of the hydrodynamic model.

Initially, reconstruction of matrices that identify the characteristics of the nested grid was carried out to allow integration of the model solution scheme to be performed with respect to the IGB model domain. The second modification required the identification of the IGB model boundaries. This was performed by breaking the boundaries up into individual sections to allow information to be fed through a number of different boundaries.

The performance of the model was tested in a gently sloped harbour and results generated were of high accuracy, with the relative error generated being approximately the same as the original nested domain, which contained a greater number of grid points. Therefore, the IRG scheme further reduces the computational needs of the nested model and, also, allow for a greater flexibility and applicability of the model.

One-way nesting techniques are adequate when higher resolution is required in a region to study small scale phenomena such as flow field interaction with local features. However, when using the nested model to study local processes that propagate out into the coarse grid one-way nesting techniques are inadequate. Two-way nesting techniques are required in such model and it was expected that further improvement in model accuracy could be achieved by incorporating such a technique into the DIVAST model.

# **CHAPTER 5:**

## **TWO-WAY NESTED MODEL DESIGN AND DEVELOPMENT, PHASE I**

### **5.1 OVERVIEW**

The development of the two-way nested model was accomplished in two stages. The initial stage involved the development of a basic two-way nested model (BTWNM). Once tested and validated, the second stage of development was carried out with the incorporation of tidal turbine devices (TTWNM). The assessment of the two-way nested model performance was undertaken by comparing its results with the results from a high resolution single grid model of the entire computational domain.

The development of the BTWNM was achieved in a number of different steps. The first step, which is described in this chapter, involves the development of the initial version of the BTWNM in the Shannon Estuary located on the west coast of Ireland. The BTWNM was then tested to identify the variable prescription at the feedback interface that conserves properties across the nested boundary and generated the most accurate model solution. Chapter 6 considers the issue of noise generation and the improvement of model accuracy in the nested/child domain and the lower resolution coarse/parent domain, with the identification of the optimum interpolation scheme and feedback condition. The development of a two-way nested model with the incorporation of tidal turbines is presented in Chapter 7. The effects of tidal turbines on the hydrodynamics were introduced into the model based on research undertaken by Houlsby (2008) on the Linear Momentum Actuator Disc Theory. Tidal farms of different array densities are simulated and their effects on hydrodynamics presented.

During the development of the BTWNM and the TTWNM a large number of models were used. For reference, Table 5.1 shows a list of all models used during the research and their roles in the development process.

Table 5: 1 List of two-way nested models used in development

<b>Model name</b>	<b>Development Role</b>
<b>BTWNM_I</b>	Test variable feedback prescription
<b>BTWNM_II</b>	Test variable feedback prescription
<b>BTWNM_III</b>	Test variable feedback prescription
<b>BTWNM_IV</b>	Test variable feedback prescription
<b>BTWNM_COPY</b>	Test interpolation technique
<b>BTWNM_SHAP</b>	Test interpolation technique
<b>BTWNM_FULLW</b>	Test interpolation technique
<b>BTWNM_MOM(V+E)</b>	Test feedback conditions
<b>BTWNM_MOMQ(ALL)</b>	Test feedback conditions
<b>BTWNM_KIN(V+E)</b>	Test feedback conditions
<b>BTWNM_KINQ(ALL)</b>	Test feedback conditions
<b>TTWNM_0.5</b>	Assess TTWNM performance + accuracy
<b>TTWNM_2</b>	Assess TTWNM performance + accuracy
<b>TTWNM_5</b>	Assess TTWNM performance + accuracy

## 5.2 NESTING METHODOLOGY

The development of a two-way nested model based on the one-way nesting technique in DIVAST was one of the primary objectives of the research. DIVAST is subjected to the spatial resolution problems, previously mentioned in Chapter 2, due to the use of a single rectilinear grid with fixed spacing. Based on the literature reviewed, a two-way nesting technique can be used to embed a

high resolution grid into a lower resolution grid of the entire domain, with interaction between the two domains occurring. Interaction between the two domains occurs by the coarse/parent grid providing boundary conditions for the nested/child domain and the high resolution nested/child grid solution is used to update the coarse/parent grid solution in a common area. Through this approach the computational cost of a hydrodynamic model can be reduced. Two-way nesting techniques enable local characteristics in an area of interest to be modelled with a high level of accuracy, as well as showing how these features propagate into and affects the surrounding domain in the low resolution area.

Figure 5.1 shows an illustration of the premise of a two-way nested model, where the nested grid ( $\Omega_n$ ) is a sub-domain of a larger, lower resolution grid ( $\Omega_c$ ). Therefore, the lower resolution coarse model solution can be used to force the nested grid model solution through the assignment of boundary conditions along the boundary ( $\Gamma$ ) of the nested domain (dashing red line). The overlapping of the two domains enables the computed variables in the high resolution nested domain to be fed back into the coarse domain through the updating of the low resolution variables at the points where the two-domains overlap (yellow circles). The following equations show the formulation of the method, which was originally presented in Chapter 2:

$$\begin{aligned}
 p_c v_c &= f_c && \text{in } \Omega_c \cup \Omega_n \\
 \left\{ \begin{array}{ll} p_n v_n = f_n & \text{in } \Omega_n \\ OB v_n = OB v_c & \text{on } \Gamma \\ v_c = R v_n & \text{in } \Omega_n \end{array} \right. &&& (5.1)
 \end{aligned}$$

The equations show that the accuracy of the scheme depends on: the boundary operator  $OB$ , the coarse/parent solution at the nested boundary  $v_c$ , the nested domain solution  $v_n$  and the choice of feedback operator  $R$ . Therefore, these are the main factors that need to be addressed when developing a two-way nested model.

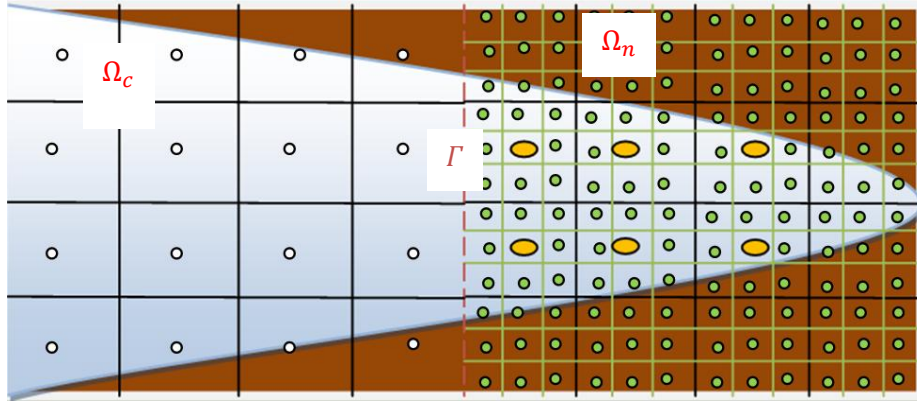


Figure 5: 1 Schematic of a nested model of an estuary

### 5.2.1 DETAILS ON NESTING APPROACH

The one-way nesting technique in DIVAST has been applied to many water bodies and results generated have been of a high accuracy. With this in mind, and through an extensive literature review, the procedure employed by this method to define the boundary operator was taken as an acceptable procedure to be used in the two-way nested model.

The one-way nested model is a dynamically linked, coupled model that enables data from the coarse domain to be transmitted, at the end of each coarse domain time step, along the boundary of the nested domain to drive the boundary operating procedure. This data is interpolated, due to the difference in resolution between the two domains, using a linear method. The boundary data is then applied to the nested domain using a Dirichlet boundary condition, allowing the nested model to be computed forward in time.

Therefore, the utmost importance for the introduction of a two-way nesting technique in the DIVAST model is the choice of feedback operator, which is used to blend the nested grid solution with the coarse grid solution. The operator consists of a suitable interpolation technique, variable prescription and feedback condition to enable data to be transmitted into the coarse/parent domain from the nested domain through overlapping grid points (see Figure 5.2) at the end of each full coarse domain time step.

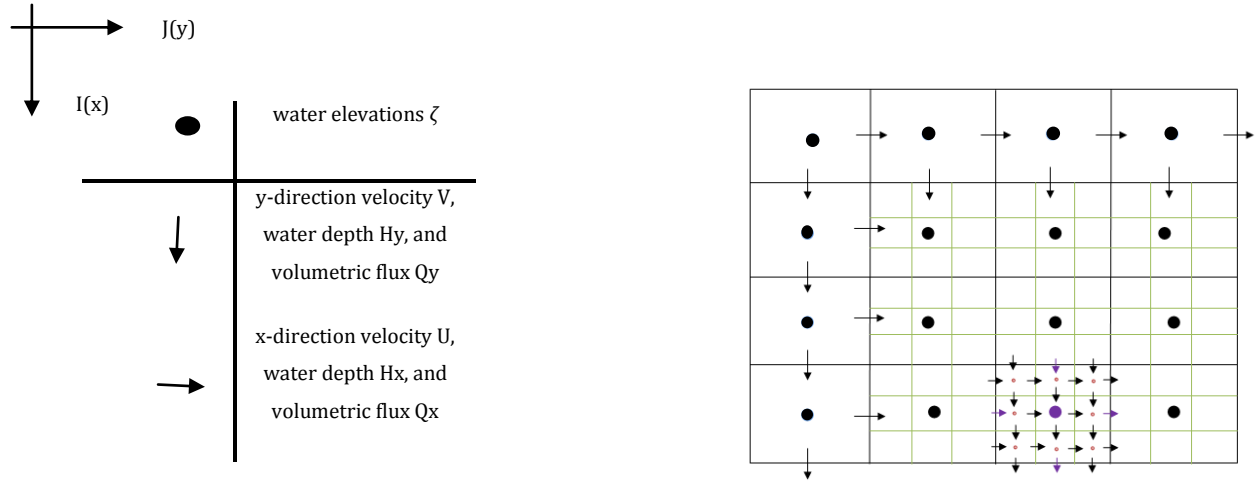


Figure 5: 2 Nested grid configuration showing nested domain (green grid lines) and coarse domain (black grid lines), with points of feedback to one coarse grid highlighted with purple arrows and circles.

### 5.2.2 Feedback operator and implementation

The accuracy of the two-way nested model is directly linked to the efficiency of the feedback operator. Feedback conditions, variable prescription and an interpolation technique are the main features of the feedback operator. Noise generation can occur with an inappropriate feedback condition as a result of reflection of waves. Literature has shown there has been a wide variety of different types of feedback conditions (Debreu 2008). One of these conditions is the Dirichlet and was initially used by the author in a two-way nested model. Two different forms of flow relaxation schemes were also later implemented into the model, and are introduced in Chapter 6.

The Dirichlet condition is one of the most severe conditions, with the nested grid conditions being directly imposed onto the coarse domain at the feedback interface. The following equation is used in the implementation of the condition and is performed at each point where the nested domain and the coarse domain points overlap:

$$\phi_c|_{I,J}^{n+\frac{1}{2}} = \phi_n|_{I,J}^{n+\frac{1}{2}} \quad (5.2)$$

where  $I$  and  $J$  are the coarse grid coordinates,  $\phi_c$  is the coarse grid variable and  $\phi_n$  are the fine grid variables. To generate a value for  $\phi_n|_{I,J}^{n+\frac{1}{2}}$  the nested grid solution was interpolated to the resolution of the coarse domain.

Suitable interpolation schemes enable the maximum amount of information to be transmitted and prevents the generation of inaccuracies and noise (Debreu 2008). In the development of the two-way nested model four types of interpolation techniques were assessed:

- Copy
- Average
- Shapiro
- Fully weighting

The averaging procedure was the most popular choice for the feedback operator in literature reviews and, therefore, was used as the interpolation technique in the initial phase of the development. This method involves replacing coarse grid values with an average of the nested grid values enclosed in the coarse grid cell. Equation 5.3 shows the averaging procedure for a model with a nested ratio of 3.

$$\phi_{I,J}^c = \frac{1}{9}(\phi_{i-1,j-1}^n + \phi_{i-1,j}^n + \phi_{i-1,j+1}^n + \phi_{i,j-1}^n + \phi_{i,j}^n + \phi_{i,j+1}^n + \phi_{i+1,j-1}^n + \phi_{i+1,j}^n + \phi_{i+1,j+1}^n) \quad (5.3)$$

where  $I$  and  $J$  are the coarse grid coordinates and  $i$  and  $j$  are the nested grid coordinates. Chapter 6 looks into the different forms of interpolation techniques and how they affect the model results.

Literature has shown a number of various combinations of component velocities and fluxes, surface elevations and density being used for the prescribed feedback variables (Zhang 2007). During the initial development of the model, various types of variable prescription at the feedback interface were tested and assessed to determine the most accurate model solution.

### 5.3 DESIGN OF BASIC TWO-WAY NESTED MODEL

It was proposed to develop the BTWNM as a nested hydrodynamic model that enables interaction between a higher resolution nested grid and a lower resolution coarse grid that occupies the full model domain. The initial interaction between the two domains would be achieved by the incorporation of the boundary operator used in the one-way nesting procedure in DIVAST. Secondly, interaction between the nested/child and coarse/parent domain should be achieved by the transfer of data from the nested domain to the coarse domain.

The main design requirements for the BTWNM are identified as the following:

- Boundary data for the nested domain should be provided by the coarse domain.
- The boundary operator employed should be equivalent to the one used in the one-way nesting technique.
- The nested domain should compute the variables by solving the governing equations in a similar nature to DIVAST.
- A feedback operator should enable two-way interaction between the grids.
- The feedback operator should consist of an interpolation procedure and a feedback condition.
- The model should generate a solution to the updated coarse domain and nested domain separately.

The design implementation is outlined with the help of a flow chart shown in Figure 5.3. The non-shaded region highlights the coarse model and the yellow shaded portion form the two-way nesting technique.

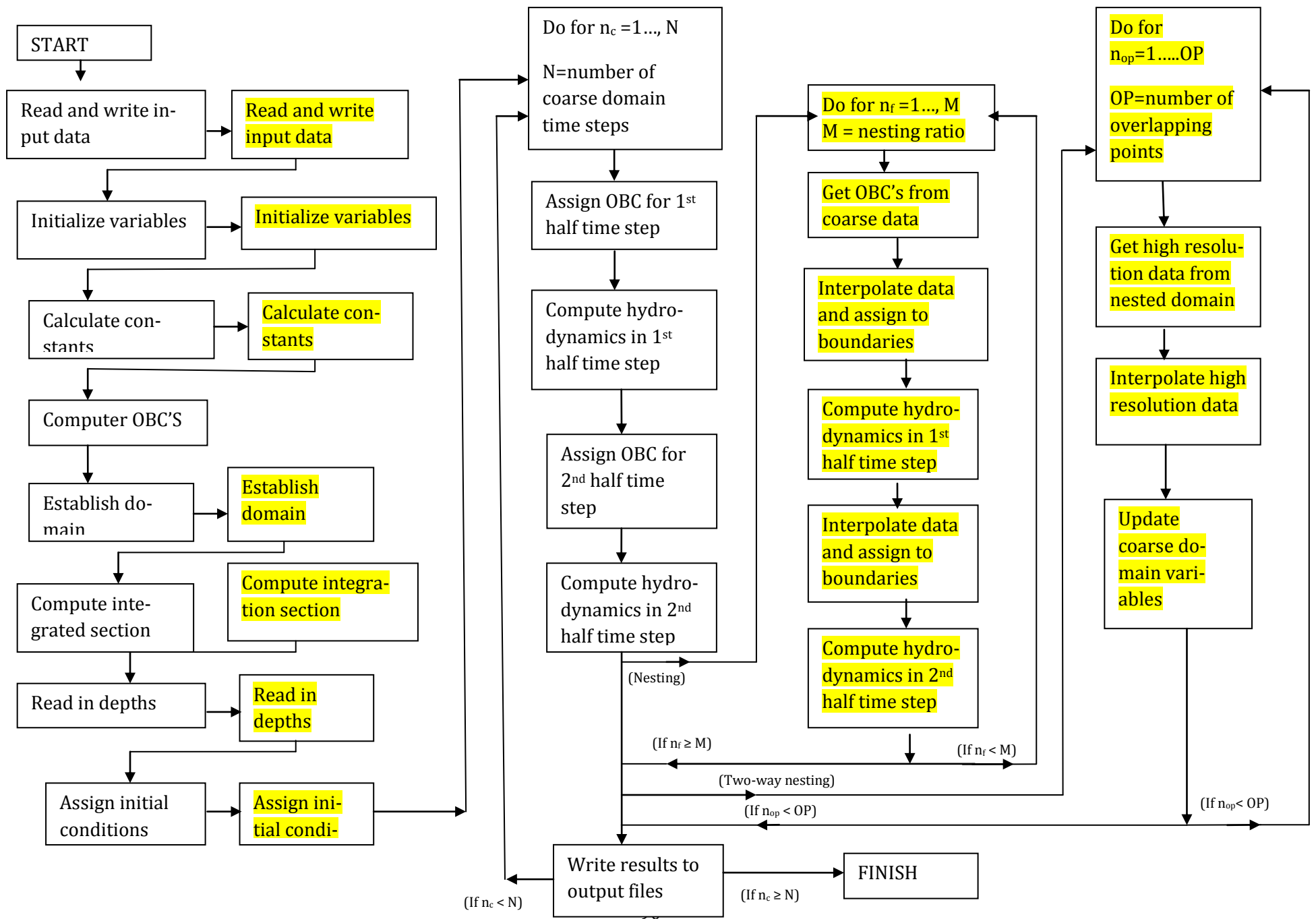


Figure 5: 3 Flowchart of proposed basic two-way nested model

## 5.4 MODIFICATION OF MODEL CODE

The incorporation of new code into the model required the generation of new matrices to store the information in relation to interpolated data and the updating data. The arrays that carried the matrices also required manipulation into different sizes to allow the 3-D nested domain matrices to be downsized to the coarse domain 2-D matrices. The new matrices that were generated are: TWSUMU, TWSUMV and TWSUME. These arrays are used to generate and store information in a two dimension format to be used in the interpolation of the high resolution data generated in the nested domain.

The two-way nested model consists of a coarse model that includes a number of subroutines, called in sequence in the main program. The flowchart in Figure 5.4 illustrates the coarse model structure and a brief description of the subroutines. The flowchart shows subroutines 1-7 that are used to read in the input data, establish the domain for integration and initialise the variables. The first half time step computes the hydrodynamics in the x-direction and this is performed in subroutines 8-11, with the second half time step computing the y-direction hydrodynamics in the 12-15 subroutines. The Chezy values and Eddy viscosity are calculated at regular intervals in the model simulation using subroutine 16 and 17 respectively.

The flowchart in Figure 5.5 shows the expansion of the model structure to enable one-way nesting to occur. The red shaded regions show the subroutines that are involved in the one-way nesting process. Modified versions of the coarse grid subroutines are required in the pre-computational stage of the model simulation to establish the input data, variable initialisation, delineation of boundaries, establishment of the integration sections and writing of model output data. The modified versions of the subroutines are shown as subroutines A-C in Figure 5.6. NEST is an addition subroutine added to the model structure, which oversees the computation of the nested domain. This subroutine is called at the end of each coarse grid time step. This subroutine calls FINEBND, which extracts data from the coarse domain to generate the boundary conditions, and uses them to perform the nested domains hydrodynamics in the x-direction with the use of subroutines D.2-D.4, in the nested domains first half time step. The y-direction hydrodynamics are performed in the nested domain with the use of subroutines D.5-D.8.

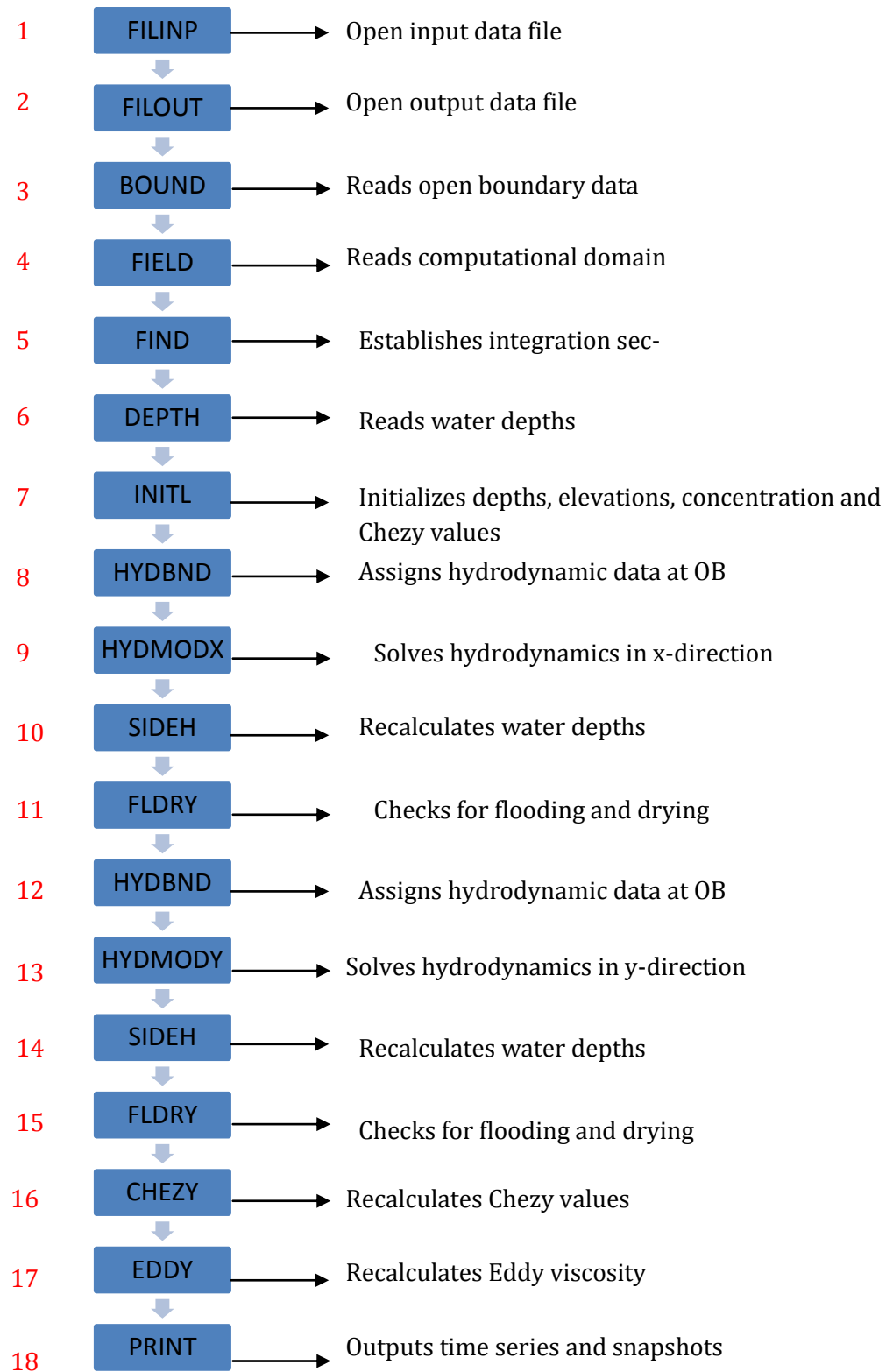


Figure 5: 4 Flowchart of Coarse model

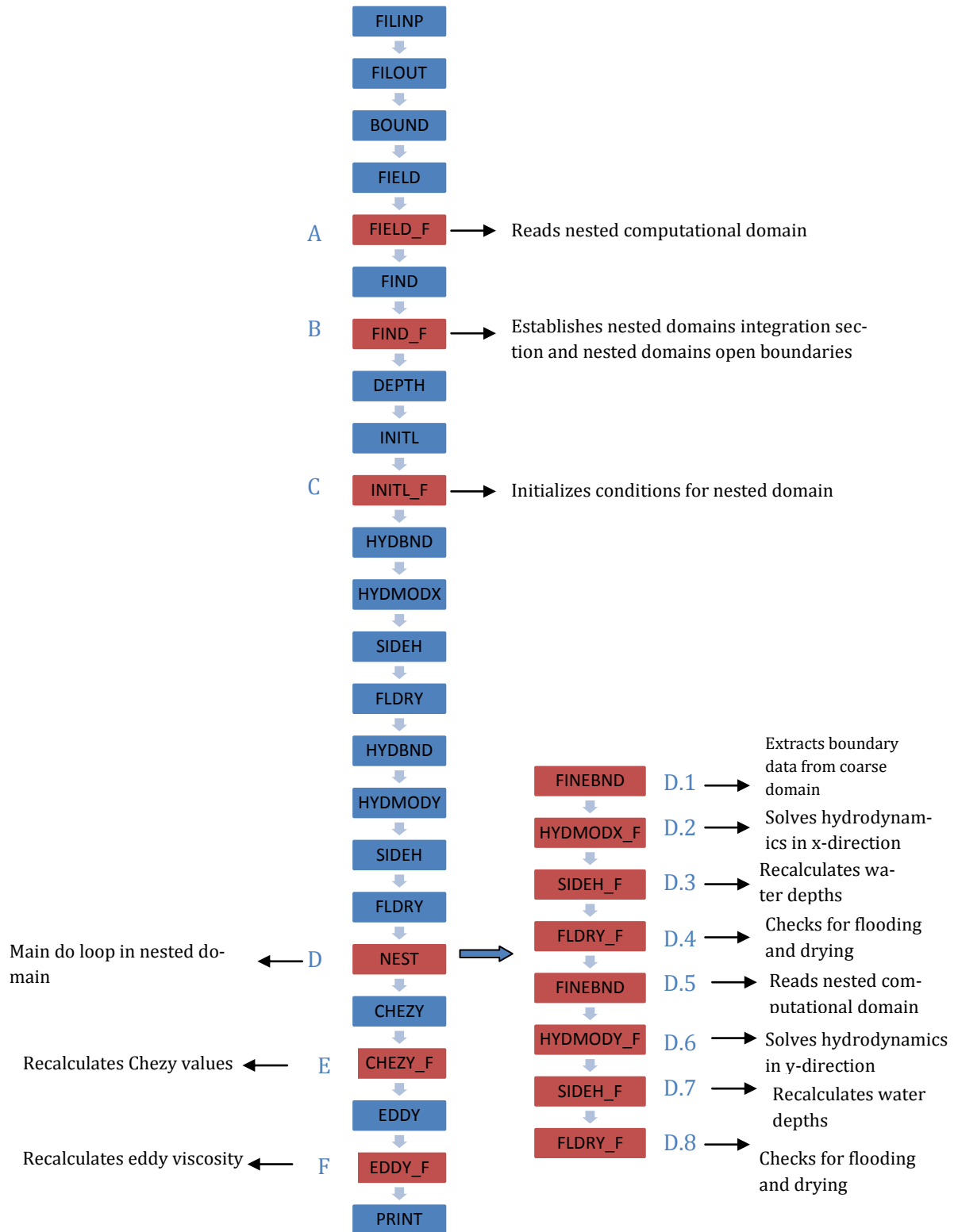


Figure 5: 5 Flow chart of one-way nested model structure(Nash 2010)

The implementation of the two-way nested procedure was carried out with the addition of a number of subroutines. The first of these subroutines is TWNM, which is used to oversee the computational procedure of the two-way nesting. This subroutine enables the coupling of the nested domain with the coarse domain by calling TWNM at the end of each nested domains full time step. The subroutine EXTRACT identifies the high resolution data used in the updating of the coarse domain. This data is then manipulated by the INTERPOLATION subroutine to ensure it is compatible with the coarse domains resolution. The model also includes the option of including a relaxation term, which is calculated with respect to momentum flux or kinetic energy in the RELAX subroutine; this is further explained in Chapter 6. The final new subroutine introduced into the two-way nested model is FEED, which transmits the data generated from the previous subroutines to the overlapping coarse domain. Table 5.2 lists the sections of code and their function added to the numerical model to allow two-way nesting to occur. Figure 5.7 shows a flow chart of the two-way nested model, with subroutines added for the implementation of two-way nesting highlighted in green.

Table 5: 2 Sections of source code incorporated to allow two-way nesting

Section in program	Function
Main program	Reads input data
Main program	Write input data
Main program	Open output data files
Main Do loop	Link nested/child model to coarse/parent model
TWNM	Main do loop in two-way nested model
EXTRACT	Extracts data from nested domains simulation
INTERPOLATE	Interpolates extracted data
RELAX	Calculation of relaxation factor
FEED	Transmits data from nested domain to overlapping coarse domain

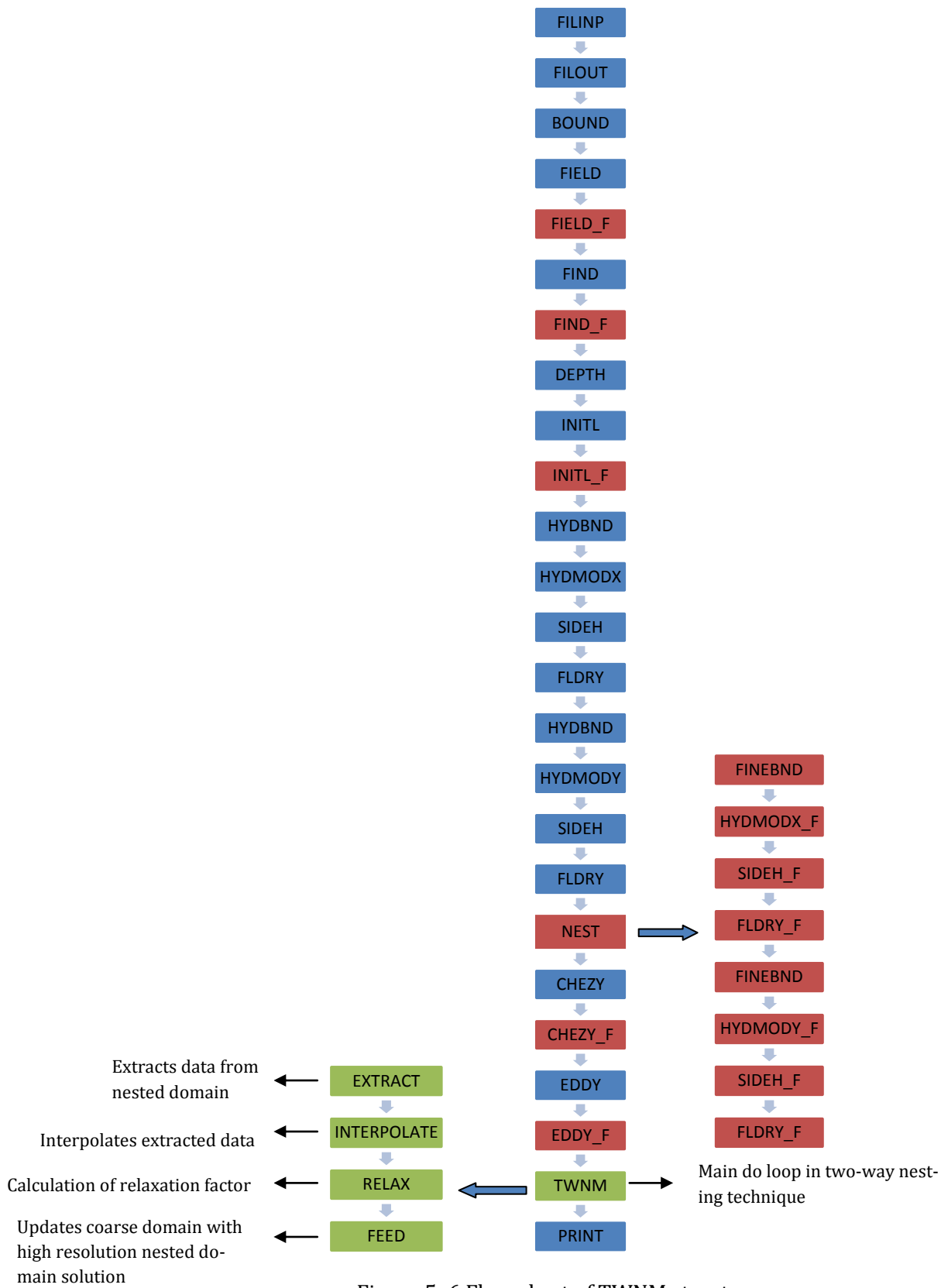


Figure 5: 6 Flow chart of TWNM structure

## 5.5 CASE STUDY OF THE SHANNON ESTUARY

The Shannon Estuary was used as the test site for the development of the two-way nested model. The estuary is located on the west coast of Ireland. It is a large estuary situated at the mouth of the Shannon River (Figure 5.7), where it flows into the Atlantic Ocean. The mouth of the estuary is located between  $52^{\circ} 25'$  and  $52^{\circ} 34'$  longitude and the head of the estuary lies just above Limerick City located at  $8^{\circ} 38' W$  and  $10^{\circ} W$ . The length of the estuary is approximately 87km, with a surface area of 500km<sup>2</sup>.

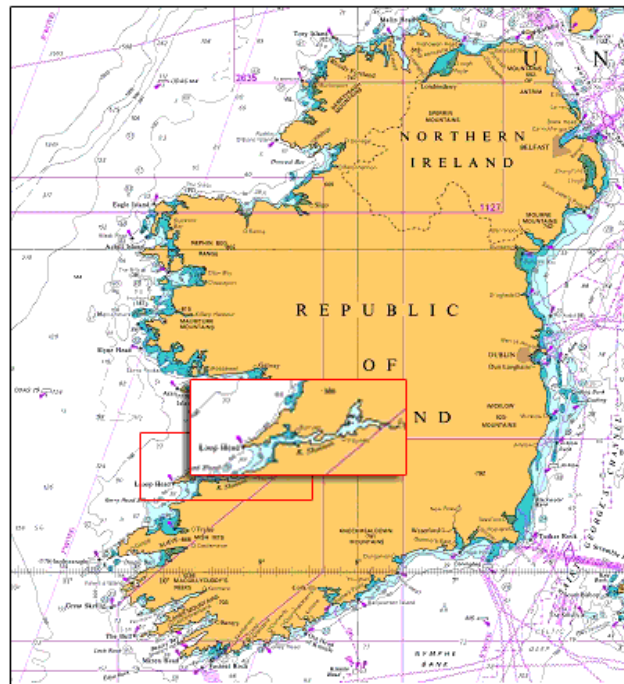


Figure 5: 7 Illustration of the Shannon Estuary

The bathymetry of the estuary varies considerably, with depths of approximately 5m at the head of the estuary and depths of up to 60 m at the mouth (see Figure 5.8). The annual average flow rate of the estuary is  $172.78 \text{ m}^3\text{s}^{-1}$  according to the Global River discharge database, which was compiled from monthly discharge data from 1973-1979 (Dabrowski 2005).

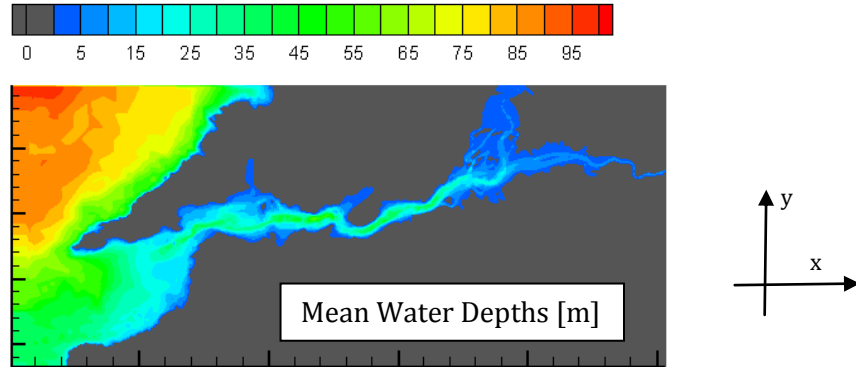


Figure 5: 8 Illustration of the Shannon Estuary bathymetry

Admiralty charts No. 1819, 1547, 1549 and 1540 were used to obtain bathymetry data. This data was interpolated onto two finite difference rectilinear grids, whose specifications are shown in Tables 5.3-5.4. The model was calibrated with the use of tidal elevation data at locations T1-T6 (see Figure 5.9) and tidal stream data located at C1. Figure 5.10 shows a comparison of modelled spring-neap tidal currents against measured data at C1. Flow data required for the specification of the discharge from the River Fergus and the River Shannon were acquired from the Office of Public Works (OPW 2011) and the Global River Discharge Database (Database. 2011) respectively.

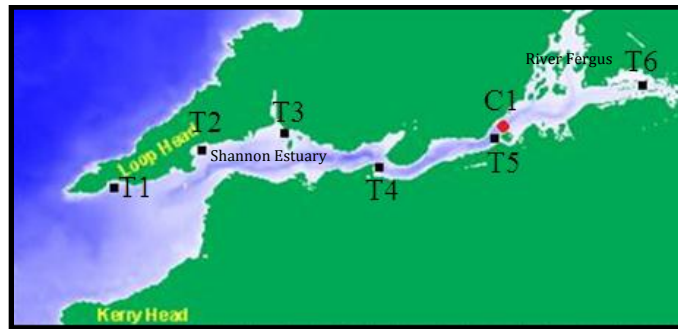


Figure 5: 9 Locations of measured data for tidal amplitudes (T1- T6) and tidal current velocities (C1) used to validate the model (Dabrowski 2005)

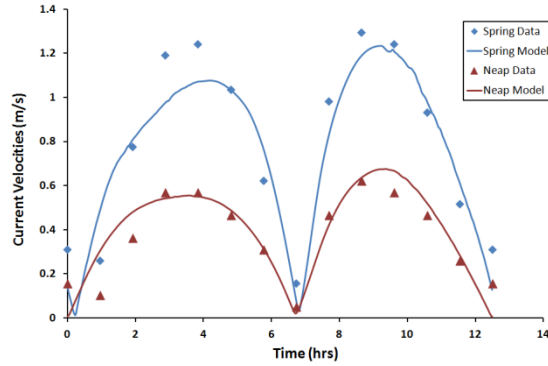


Figure 5: 10 Comparison of measured data against the predicted model data (Dabrowski 2005)

The site was chosen for the development study due to the complex bathymetry and flow regimes associated with it, to permit a stringent test of the two-way nesting procedure to be performed. The estuary has also been identified by a study undertaken by Sustainable Energy Ireland as a potential site for tidal farm deployment (SEI 2009).

Table 5: 3 Low resolution single grid parameters

Parameters	values	Units	Parameters	values	Units
No. of cells in x-direction	319	-	Half time step	12	s
No. of cells in y-direction	137	-	Roughness length	50	mm
Boundaries in x-direction	2	-	Coefficient of eddy viscosity	1	-
Boundaries in y-direction	3	-	Momentum correction coefficient	1.016	-
Grid spacing	300	m	Angle of latitude	52.58	degrees

Table 5: 4 High resolution single grid parameters

Parameters	values	Units	Parameters	values	Units
No. of cells in x-direction	957	-	Half time step	4	s
No. of cells in y-direction	411	-	Roughness length	50	mm
Boundaries in x-direction	2	-	Coefficient of eddy viscosity	1	-
Boundaries in y-direction	3	-	Momentum correction coefficient	1.016	-
Grid spacing	100	m	Angle of latitude	52.58	degrees

### 5.5.1 ERROR ANALYSIS AND MODEL PERFORMANCE

The performance of the two-way nested model was assessed with the use of a single grid high resolution model of the full domain (see Table 5.4). This model solution was assumed to be the ‘correct solution’ to the hydrodynamic model and was, therefore, used as a comparison for all other model solutions. The low resolution model (see Table 5.3) without nesting was initially compared with the high resolution solution, to determine the reduction in accuracy resulting from a lower resolution. The coarse model solution with the inclusion of the two-way nesting technique was then compared with the high resolution domain to calculate the increase in accuracy through the updating of the coarse model solution from the nested domain. The nested domain results were also compared with the high resolution results to determine the accuracy of the nested domain solution.

The assessment of the hydrodynamic model was performed by calculating the tidally-averaged relative error at all grid points in the model domain with the use of the following equation:

$$RE_T|_{I,J} = \frac{\sum_{n=1}^N |\phi_{I,J}^n - \phi_{I,J}^n|}{\sum_{n=1}^N |\phi_{I,J}^n|} \times 100 \quad (5.4)$$

where  $N$  is the number of snapshots,  $\Phi$  is the coarse grid variables and  $\phi$  is the single high resolution grid variables. The error data generated was represented graphically as spatial distributions for the model domain and used to show visually the level of improvement with the inclusion of the two-way nested model. Figure 5.11 shows the tidally-averaged relative error  $RE_T$  for current velocities in the coarse domain without the inclusion of two-way nesting.

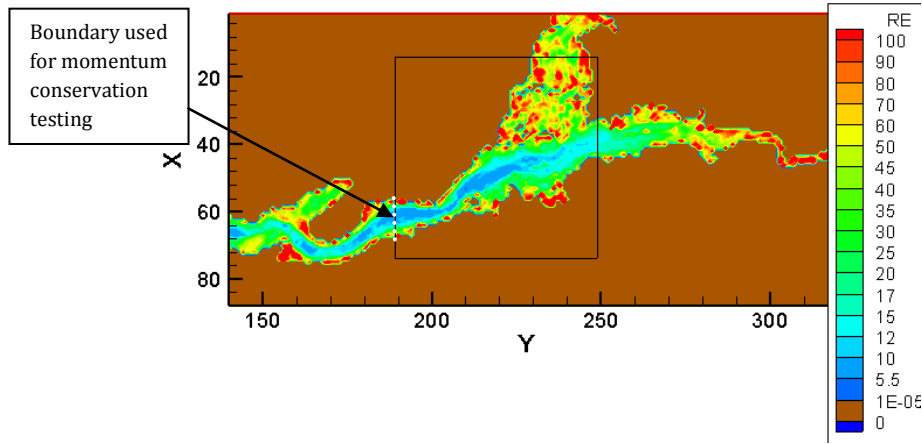


Figure 5: 11  $RE_T$  in velocities for the low resolution coarse model without nesting

The model was also assessed with use of time series, which output model variables at a particular grid point at regular intervals over a model simulation. Time series allowed detailed examination of problem areas in the model.

Conservation of properties is one of the main requirements for an effective nested model. The main conservation property of interest in this research is momentum. To quantify the performance of the model to conserve momentum, the momentum fluxes along the nested boundary interface were computed by the nested grid and compared with the corresponding fluxes computed by the coarse/parent grid and the high resolution single grid model. The following equation was used to calculate the momentum flux at time  $t$ :

$$M_{f,y}^t = \rho_w \Delta x \sum_{i=ib1}^{ibn} U^2 H_x |_{i,jb}^t \quad (5.5)$$

where the boundary is positioned on row  $jb$  and extends from grid points  $(ib1, jb)$  to  $(ibn, jb)$ . The fluxes were calculated in the same location in all three grids.

## 5.6 FEEDBACK PRESCRIPTIONS

The first version of the BTWNM was applied to the Shannon Estuary. The nested/child domain was positioned in an area highlighted in Figure 5.11 by a black square. In order to maximise the information being fed back to the coarse/parent domain from the nested domain and minimising the generation of noise, a number of different version of the BTWNM were developed and tested for different combinations of variables prescribed at the feedback interface. Table 5.5 lists the different versions of the model. The feedback operator used in all cases, is the Dirichlet boundary condition and an average interpolation technique.

Table 5: 5 Models for feedback prescription

Model	Variable prescribed
BTWNM_I	$\zeta, q_x, q_y$ -interpolated  $H_x, H_y, U, V$ - calculated
BTWNM_II	$\zeta, q_x, q_y$
BTWNM_III	$q_x, q_y$
BTWNM_IV	$\zeta, U, V$

### 5.6.1 BTWNM\_I

The initial feedback prescription involved the use of interpolated water elevation data and volumetric flux data, with water depths and velocities calculated using the interpolated data. This feedback prescription was initially used to meet one of the main criteria for optimum two-way nesting: maximising the information being fed back into the coarse domain.

Initially, the conservation of momentum was investigated, by calculating the momentum fluxes along the nested boundary highlighted in Figure 5.11 with a dashed line. Figure 5.12 shows a comparison of the nested domain of the BTWNM\_I model's momentum flux across the boundary (NB), with the corresponding fluxes in the updated coarse domain of the BTWNM\_I model (UC) and the high resolutions single grid model fluxes (HR). Table 5.6 tabulates the percentage difference in peak ebb and peak flood momentum fluxes across the nested boundary in the nested/child domain and the updated coarse/parent domain relative to the high resolution single grid model.

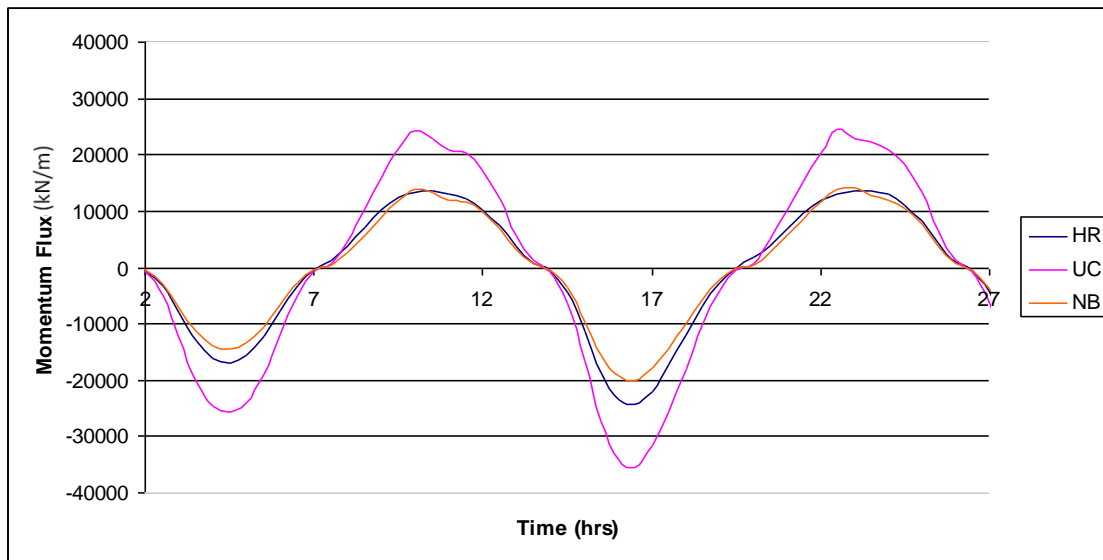


Figure 5: 12 Momentum fluxes across the boundary for BTWNM\_I.

Table 5: 6 Peak ebb and peak flood momentum fluxes across the nested boundary for BTWNM\_I

	Peak ebb momentum flux (kN/m)	% difference	Peak flood momentum flux (kN/m)	% difference
High resolution (HR)	-24277.2	-	13724.28	-
Nested boundary (NB)	-19977.6	-17.7%	14047.68	+2.3%
Updates Coarse (UC)	-35383.5	+45.7%	24585.61	+79.1%

Results showed a difference of 17.7% at peak ebb between HR and NB and a difference of 45.7% between the UC and HR. This is a difference of approximately 63% between NB and UC. Similarly, at peak flood a difference of approximately 77% between NB and UC was shown to exist. This large inconsistency between UC and NB suggests there is a low conservation of momentum across the boundary.

The propagation of the momentum from the nested boundary into the nested domain was also tested by comparing the momentum fluxes along the next column of interior nested cells adjacent to the boundary to momentum fluxes across the boundary (Figure 5.13).

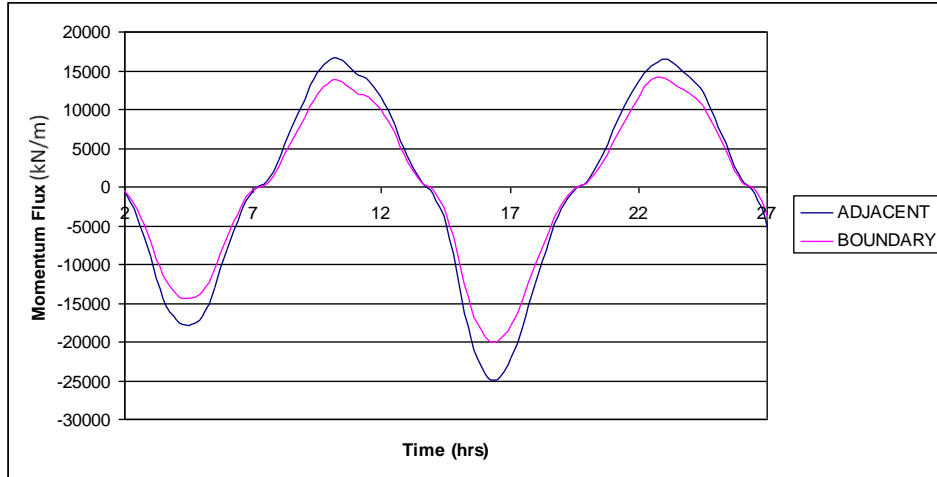


Figure 5: 13 Nested grid momentum fluxes across the boundary cells and cells adjacent to the boundary for BTWNM\_I

Table 5: 7 Peak ebb and peak flood momentum fluxes across the boundary cells and cells adjacent to the boundary for BTWNM\_I

	Peak ebb momentum flux (kN/m)	Peak flood momentum flux (kN/m)
Boundary	-19977.6	14047.68
Adjacent	-24839.3	16447.04

A slight difference in the fluxes should be expected, however, the diagram clearly shows that noise is generated between the first and second columns of nested grid cells. The average difference between the two columns is approximately 24% on the ebb and 17% on the flood.

These large inconsistencies between the two domains were deemed inadequate and no further investigation was undertaken with this variable prescription. Literature has shown the conservation of properties is one of the main determinants of a nested models accuracy (Nash 2010).

## 5.6.2 BTWNM\_II

In the BTWNM\_II model the information involved in the feedback prescription was reduced to the use of interpolated volumetric fluxes and water elevations. This was done to try and reduce the generation of noise that was seen in the BTWNM\_I model and to further increase the conservation of properties.

The momentum conservation in the region of the nested boundary was investigated and is shown in Figure 5.14, with results tabulated in Table 5.8. The results showed that a large difference between UC and NB exists with a difference of 66.3% on the ebb and 70% on flood. This is an increase of approximately 3% on the ebb, however a decrease of 7% on the flood in comparison to the previous model.

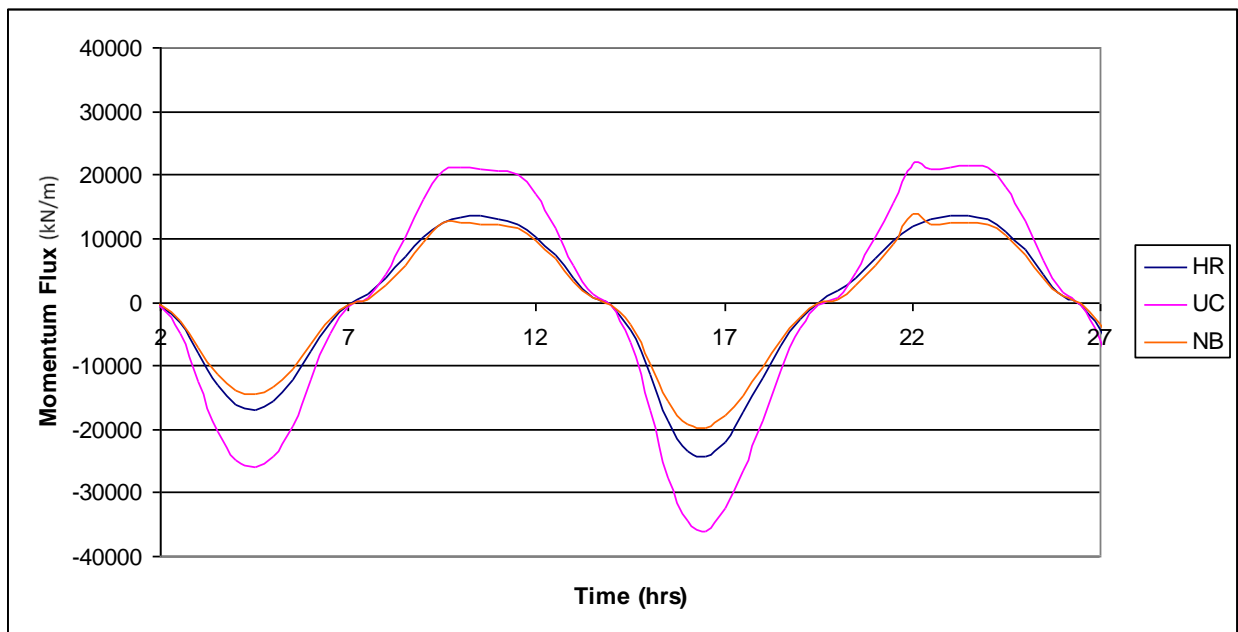


Figure 5: 14 Momentum fluxes across the boundary for BTWNM\_II

Table 5: 8 Peak ebb and peak flood momentum fluxes across the nested boundary for BTWNM\_II

	Peak ebb momentum flux (kN/m)	% difference	Peak flood momentum flux (kN/m)	% difference
High resolution (HR)	-24277.2	--	13724.28	-
Nested boundary (NB)	-19910.2	-17.98%	11797.54	-14%
Updates Coarse (UC)	-35967.2	+48.15%	21461.23	+56.37%

The propagation of momentum into nested domain was investigated and results shown in Figure 5.15 and a tabulated form of the results for peak flood and ebb momentum fluxes are shown in Table 5.9. The results show no change in the error that was experienced in the previous model on the ebb; however, a difference of 9% at peak flood was generated. The results showed no considerable increase in the conservation of properties, therefore, no further investigation was performed with this model.

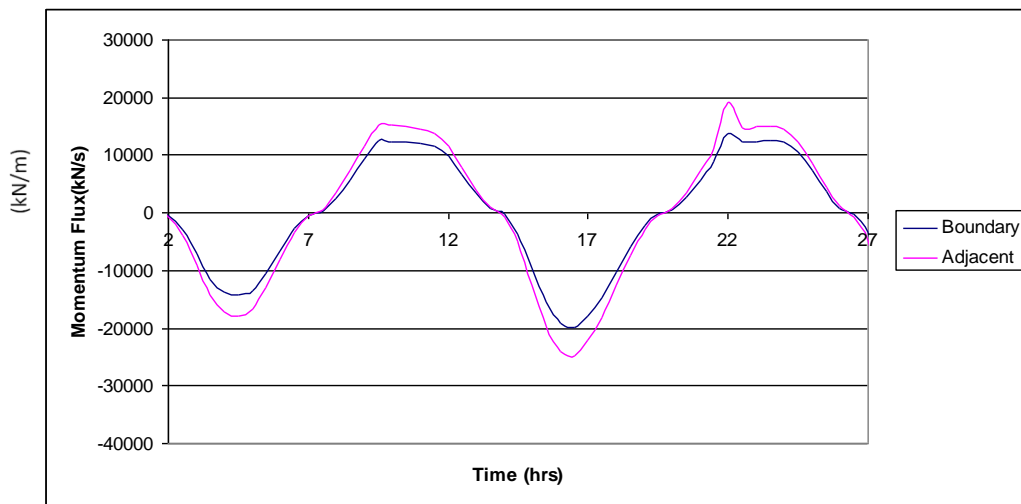


Figure 5: 15 Nested grid momentum fluxes across the boundary cells and cells adjacent to the boundary for BTWNM\_II

Table 5: 9 Peak ebb and peak flood momentum fluxes across the boundary cells and cells adjacent to the boundary for BTWNM\_II

	Peak ebb momentum flux (kN/s)	Peak flood momentum flux (kN/s)
Boundary	-19910.2	11797.54
Adjacent	-24802.8	12873.24

### 5.6.3 BTWNM\_III

The next version of the model was designated a flow feedback interface at which the volumetric fluxes were fed back into the coarse domain. Momentum conservation was investigated and Figure 5.16 shows the results. Table 5.10 tabulates the results for the percentage difference in the peak ebb and peak flood across the nested boundary for UC and NB relative to HR.

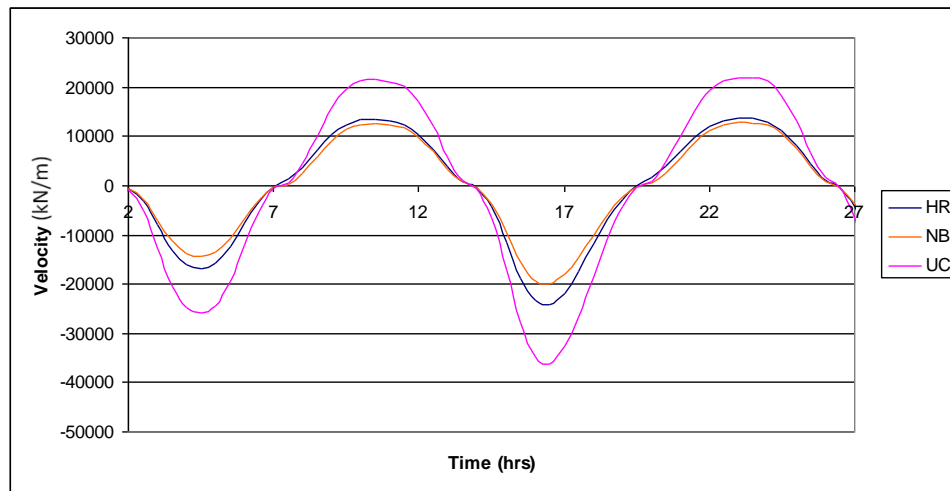


Figure 5: 16 Momentum fluxes across the boundary for BTWNM\_III.

Table 5: 10 Peak ebb and peak flood momentum fluxes across the nested boundary for BTWNM\_III

	Peak ebb momentum flux (kN/m)	% difference	Peak flood momentum flux (kN/m)	% difference
High resolution (HR)	-24277.2	-	13724.28	-
Nested boundary (NB)	-20044.9	-17.43%	12791.03	-6.79%
Updates Coarse (UC)	-36220.6	+49.19%	21964.61	+60.04%

Comparing the nested domain boundary fluxes with that of the adjacent interior grid cells (Figure 5.17), it can be seen a decrease in the propagation of momentum into the domain is experienced on the flood tide, however, an improvement is shown on the ebb tide. Results showed no considerable increase in the conservation of properties, therefore, no further research was undertaken.

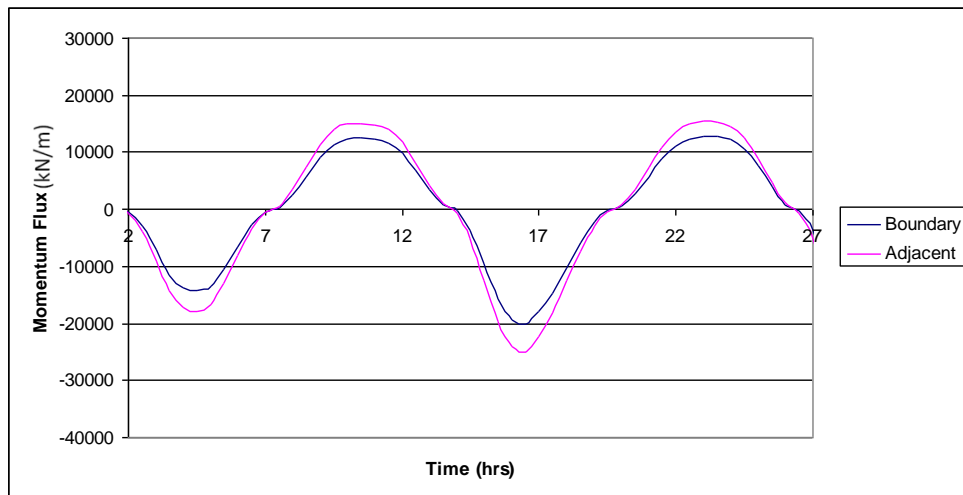


Figure 5: 17 Nested grid momentum fluxes across the boundary cells and cells adjacent to the boundary for BTWNM\_III

Table 5: 11 Peak ebb and peak flood momentum fluxes across the boundary cells and cells adjacent to the boundary for BTWNM\_III

	Peak ebb momentum flux (kN/s)	Peak flood momentum flux (Kn/s)
Boundary	-20044.9	12791.03
Adjacent	-24933.3	15404.8

### 5.6.4 BTWNM\_IV

The BTWNM\_IV version of the model used water elevations and current velocities as the variables prescribed at the feedback interface, with volumetric fluxes not being involved in the transfer of information. Figure 5.18 shows the momentum fluxes in the area of the nested boundary for the BTWNM\_IV model, with a tabulated form of the results shown in Table 5.12.

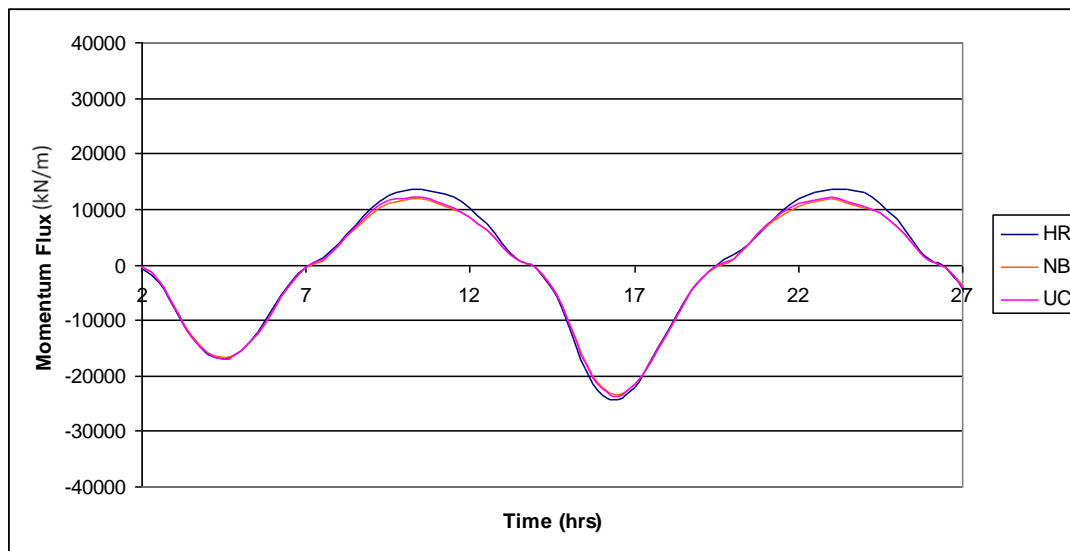


Figure 5: 18 Momentum fluxes across the boundary for BTWNM\_IV.

Table 5: 12 Peak ebb and peak flood momentum fluxes across the nested boundary for BTWNM\_IV

	Peak ebb momentum flux (kN/m)	% difference	Peak flood momentum flux (kN/m)	% difference
High resolution (HR)	-24277.2	-	13724.28	-
Nested boundary (NB)	-23594.3	-2.8%	12172.92	-11.3%
Updates Coarse (UC)	-23412.6	-3.5%	11797.54	-14.03%

The conservation of momentum at the boundary was increased, with results showing an average percentage difference at peak ebb between NB and HR of 2.8% and a difference of 3.5% between UC and HR, which is a difference of approximately 0.7% between UC and NB. Figure 5.18 shows a comparison of the nested domain boundary fluxes with the adjacent interior grid cells, it can be seen a significant improvement is experienced in the propagation of momentum into the nested domain.

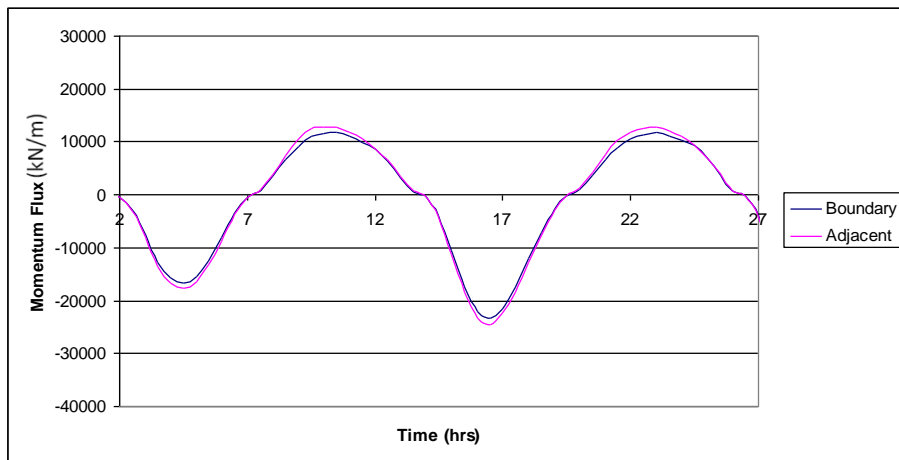


Figure 5: 19 Nested grid momentum fluxes across the boundary cells and cells adjacent to the boundary for BTWNM\_IV

Table 5: 13 Peak ebb and peak flood momentum fluxes across the boundary cells and cells adjacent to the boundary for BTWNNM\_IV

	Peak ebb momentum flux (kN/s)	Peak flood momentum flux (kN/s)
Boundary	-23594.3	12172.92
Adjacent	-24498.2	12873.24

This high level of conservation of momentum enabled further investigation to be performed on the model in relation to its ability to transfer information into the coarse/parent domain. The tidally-averaged relative errors for the updated coarse (UC) domain were calculated from snapshot data output during the final tidal cycle of the BTWNNM\_IV and HR simulations. Figure 5.20 shows an illustration of a comparison between the tidally-average relative errors ( $RE_T$ ) for current velocities in the UC domain to that of the non-updated low resolution coarse model.

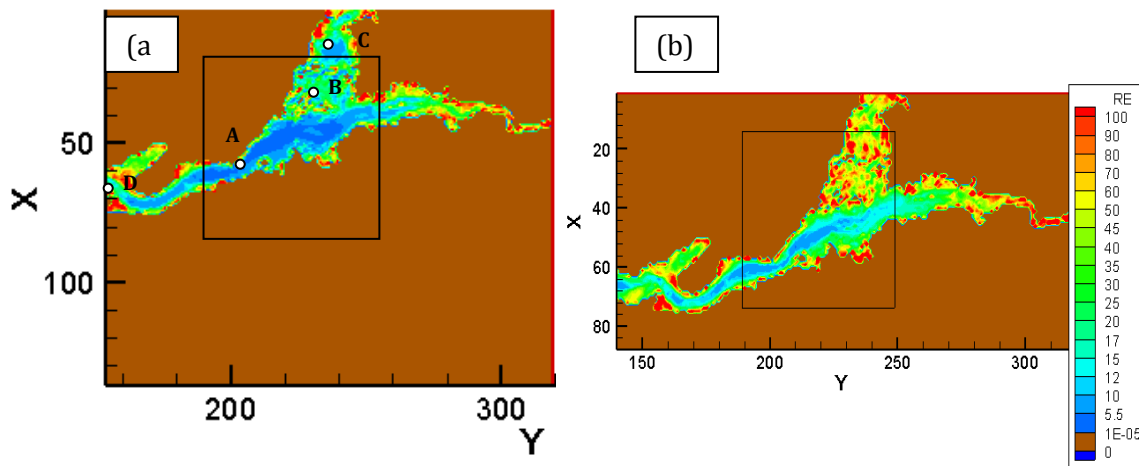


Figure 5: 20  $RE_T$  in full model domain for (a) BTWNNM\_IV and (b) non-updated coarse model, with black square highlighting area of feedback.

Figure 5.20 shows the relative error across the coarse domain has been considerable reduced, due to the transfer of data from the nested domain. The tendencies observed in the relative error plot were further exhibited with the time history analysis of points A-D shown in Figure 5.20(a).

Figures 5.21-5.22 show a comparison of the velocities at point A and B located in the region where data is transferred from the nested domain. The graphs show a comparison of the original coarse domain without nesting (LR), the updated coarse domain with two-way nesting (BTWNM) and the high resolution single grid domain (HR). Tables 5.14-5.15 tabulate the results for the percentage difference in the peak ebb and peak flood for the LR and the BTWNM relative to the HR model.

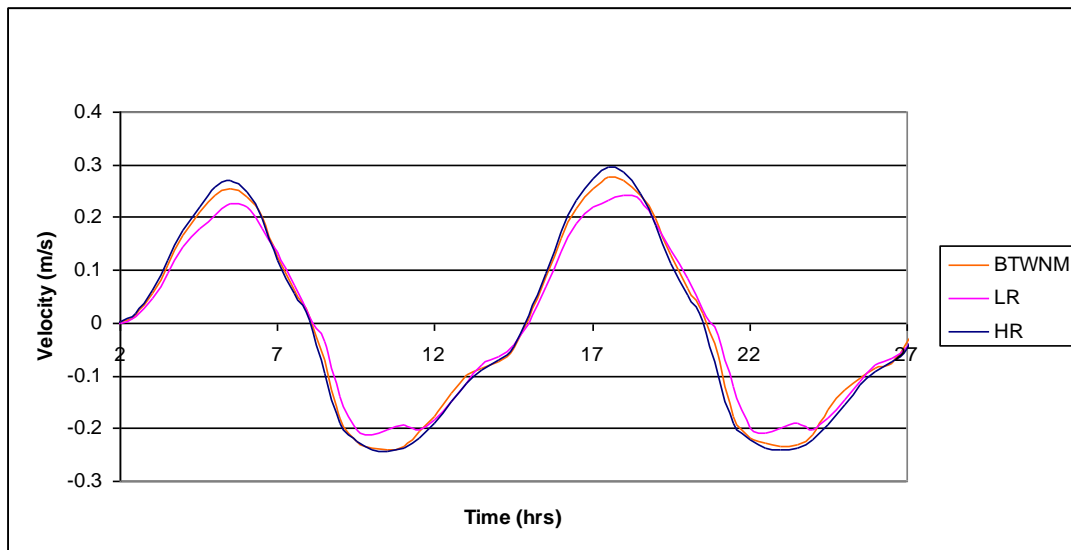


Figure 5: 21 Time history analysis at Point A for BTWNM\_IV model

Table 5: 14 Peak ebb and peak flood velocities at point A

Point A	Peak flood velocity (m/s)	% difference	Peak ebb velocity (m/s)	% difference
High resolution (HR)	0.297	-	-0.241	-
Low resolution (LR)	0.2338	-21.27%	-0.2017	+16.3%
BTWNM	0.2783	-6.26%	-0.2336	+3.07%

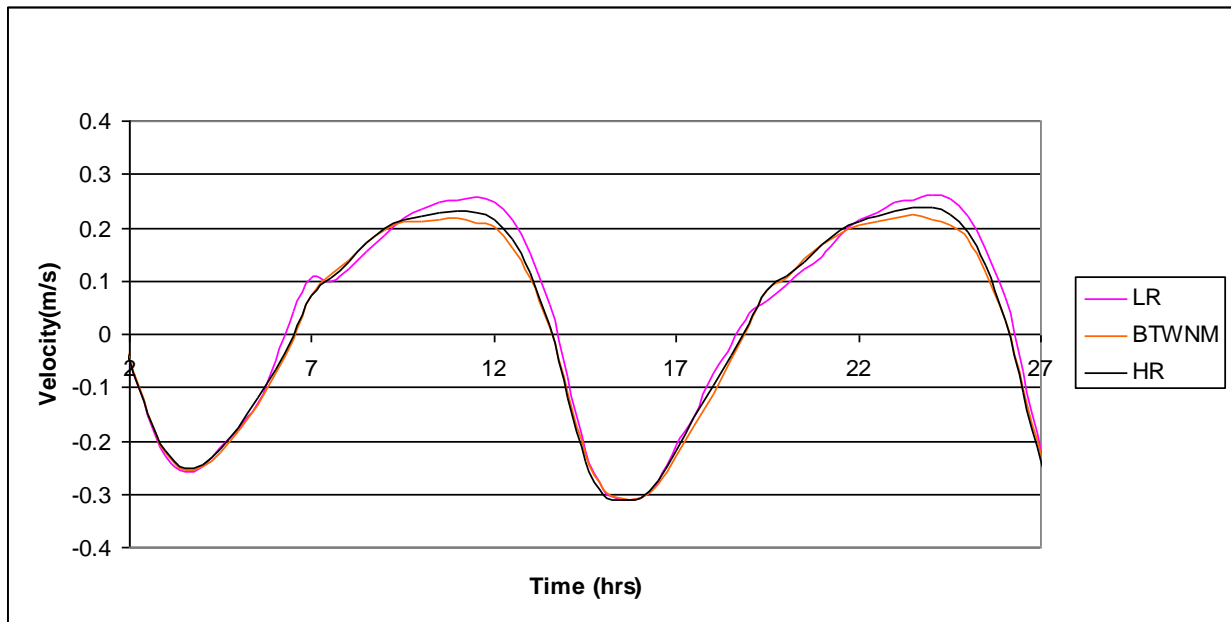


Figure 5: 22 Time history analysis at Point B for BTWNM\_IV model

Table 5: 15 Peak ebb and peak flood velocities at point B

Point B	Peak ebb velocity (m/s)	% difference	Peak flood velocity (m/s)	% difference
High resolution (HR)	-0.3101	-	0.2306	-
Low resolution (LR)	-0.3111	+0.323%	0.2563	+11.14%
BTWNM	-0.3096	-0.16%	0.2181	-5.4%

Results generated shows the BTWNM differs by 6.26% at A and 5.4% at B to the high resolution model at peak flood, and 3.07% at A and 0.26 % at B at peak ebb. Results generated exhibit an increase in accuracy in comparison to the low resolution model without nesting. Figures 5.23-5.24 show a comparison of the velocities at points C and D located outside the feedback area. The results are presented in a tabular form in Tables 5.16-5.17.

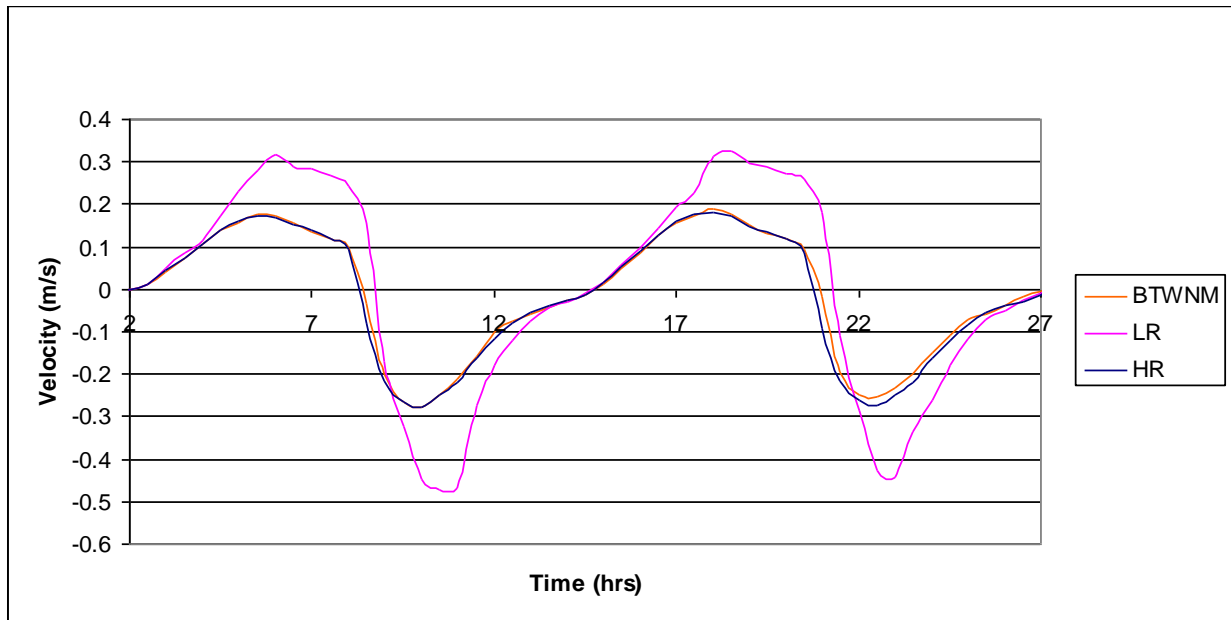


Figure 5: 23 Time history analysis at Point C for BTWNM\_IV model

Table 5: 16 Peak ebb and peak flood velocities at point C

Point C	Peak ebb velocity (m/s)	% difference	Peak flood velocity (m/s)	% difference
High resolution (HR)	-0.2786	-	0.1804	-
Low resolution (LR)	-0.4486	+61%	0.3263	+80.8%
BTWNM	-0.2788	+0.07%	0.1888	+4.6%

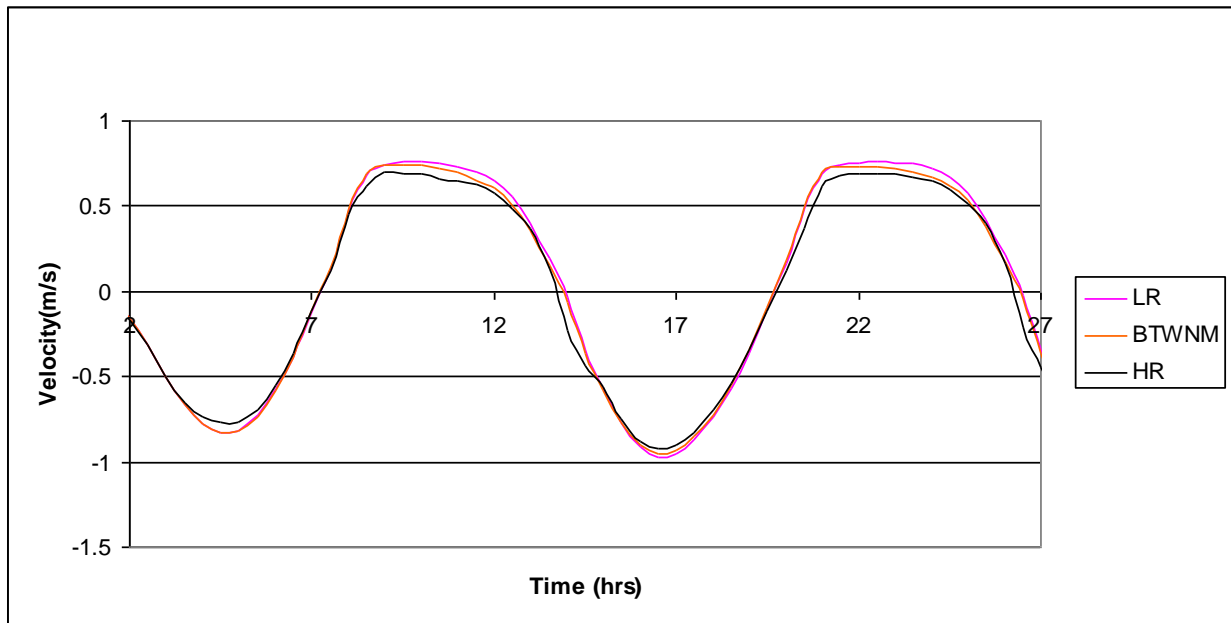


Figure 5: 24 Time history analysis at Point D for BTWNM\_IV model

Table 5: 17 Peak ebb and peak flood velocities at point D

Point D	Peak ebb velocity (m/s)	% difference	Peak flood velocity (m/s)	% difference
High resolution	-0.9172	-	0.6944	-
Low resolution	-0.9694	+5.69%	0.7578	+9.13%
BTWNM	-0.9477	+3.3%	0.7215	+3.9%

The results generated show there is a significant improvement in accuracy at point C located just outside the feedback region, with an increase of approximately 75% on the flood tide and 60 % on the ebb. Point D located further from the feedback region also showed an increase in the accuracy in relation to the low resolution model without nesting.

Error analysis was also performed on the data generated in the nested domain by calculating the tidally averaged relative error from snapshot data of the nested domain model simulations. Figure 5.25 shows an illustration of a comparison between the  $RE_T$  in the BTWNM\_IV nested domain current velocities to that for the low resolution model.

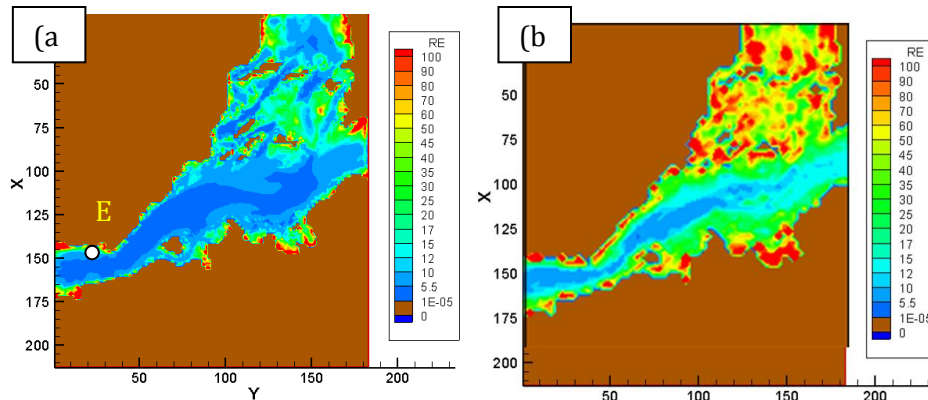


Figure 5: 25  $RE_T$  for velocities in nested domain for (a) BTWNM\_IV and (b) non-nested low resolution coarse model.

Results suggest the nested domain generates a solution of a higher accuracy in comparison to the low resolution model in an area of interest. The tendencies observed in the relative error plot were further exhibited with the time history analysis of point E shown in Figure 5.25(a).

Figure 5.26 shows a comparison of the original coarse domain without nesting (LR), nested domain (BTWNM) and the high resolution single grid domain (HR). Table 5.18 tabulates the results for the percentage difference in the peak ebb and peak flood for the LR and the BTWNM relative to the HR model. Results generated show the nested model solution exhibits an increase in accuracy in comparison to the low resolution model without nesting, with an increase of approximated 47% on the flood and 23% on the ebb.

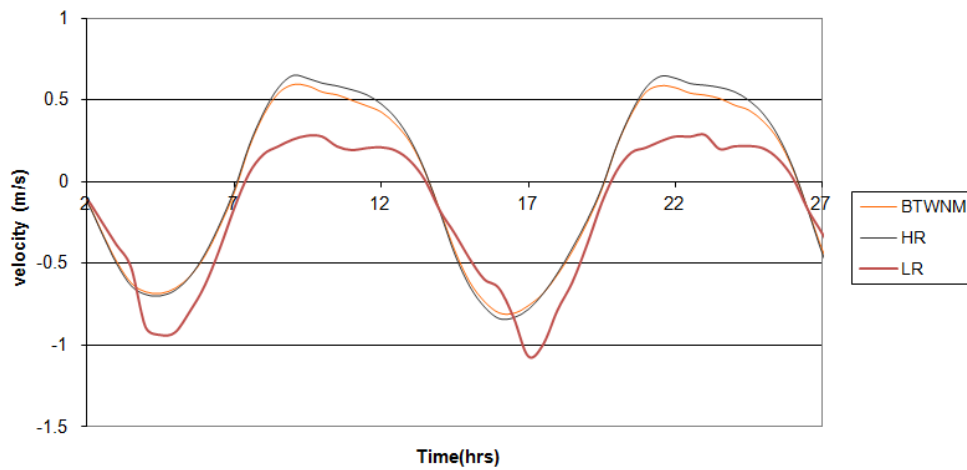


Figure 5: 26 Time history analysis of Point E for BTWNM\_IV model

Table 5: 18 Results of the time history analysis for point E

Point E	Peak ebb velocity (m/s)	% difference	Peak flood velocity (m/s)	% difference
High resolution (HR)	-0.8379	-	0.6444	-
Low resolution (LR)	-1.0675	+27.4%	0.2848	-55.8%
BTWNM	-0.8007	-4.4%	0.5884	-8.6%

## 5.7 SUMMARY AND CONCLUSION

The initial version of the BTWNM was developed in Phase I of the BTWNM development. This consisted of a high resolution grid embedded in a lower resolution grid of the entire domain, and the grids interact with each other. The open boundaries of the nested domain were formulated in the same manner as the one-way nesting technique in DIVAST, which incorporated ghost cells to enable the nested boundary to be formulated as an internal boundary. A boundary operator was used to interpolate and assign boundary data from the coarse domain to force the simulation of the higher resolution nested domain. The operator employed a linear interpolated technique and a Dirichlet boundary condition. The second form of interaction between the domains occurs by using data formulated in the high resolution nested domain to update the coarse domain solution. A feedback operator was used to interpolate and assign high resolution data from nested domain to the coarse domain. The operator employed in Phase I was an averaging interpolation technique and a Dirichlet feedback condition.

The prescription of variables at the feedback interface was the main focus in the first phase of the development process. The results showed that the accuracy of the model varies de-

pending on the variables used in the feedback prescription. The use of a variable prescription containing velocities and elevations generated the best model solution.

The feedback prescription was tested with the use of a model of the Shannon Estuary. Initially, the conservation of momentum across the nested domain boundary were analysed by the calculation of momentum fluxes in the area of the nested boundary for the updated coarse domain, nested domain and the high resolution single grid domain. The propagation of the momentum into the nested domain was also analysed by comparing the nested domain boundary fluxes with the adjacent interior grid cells fluxes.

Four different types of BTWNM were generated to identify the optimum feedback prescription. The initial model BTWNM\_I involved the use of water elevations data, volumetric flux data and water depth data from the nested domain and from these interpolated data U and V were calculated. This large amount of feedback prescription data was initially used to enable the maximum data to be transferred into the coarse domain. Results generated showed poor levels of momentum conservation, and also wave reflection occurring at the boundary. These large inconsistencies between the domains were deemed inadequate and no further investigation was undertaken with this variable prescription.

The removal of prescribed variables was required to improve momentum conservation. The prescription of water elevations and volumetric fluxes in the BTWNM\_II model, gave a minor increase of momentum conservation on the flood tide, but the noise between the two domains was still considerable large. The BTWNM\_III was assigned a flow feedback interface and specification of volumetric fluxes alone gave similar results in comparison to the BTWNM\_II model for the conservation of momentum.

The BTWNM\_IV model achieved the best model performance, with the prescription of water elevations and velocities at the feedback interface. A high level of momentum conservation was achieved, with a difference of 0.7% between the nested domain and the coarse domains momentum fluxes across the boundary at peak ebb and 3% at peak flood. This feedback prescription was assumed adequate and further investigation into the performance of the model was undertaken. The tidally-averaged relative error was generated across the full model domain and results generated exhibited a significant increase in accuracy in the coarse model solution, resulting from the feedback of data from the nested domain. Time history analysis also showed considerable improvements in the model solution, with an in-

crease in accuracy reaching approximately 75% at some points. Error analysis and time history analysis were also performed on the data generated by the nested domain. Results generated showed the nested model solution exhibits an increase in accuracy in comparison to the low resolution model without nesting, with an increase of approximated 47% on the flood and 23% on the ebb.

Therefore, it was assumed the optimum feedback prescription for the existing model was the assignment of velocities and water elevations. However, further investigation was required into the interpolation technique used along with the feedback operator to determine the best two-way nesting model technique.

# **CHAPTER 6: TWO-WAY NESTED MODEL DESIGN AND DEVELOPMENT, PHASE II**

## **6.1 INTRODUCTION**

One of the requirements for a suitable two-way nesting technique is the employment of an effective feedback operator to conserve momentum during data transmission between domains. Phase I of the BTWNM development revealed the type of variable prescription at the feedback interface is a factor in the conservation of momentum between the two grids. The use of water elevations and velocities produced the most accurate model solution. However, the simplest form of feedback condition was employed due to its ease of implementation, and also it has been commonly used as an effective condition in nested models. The results generated with this condition gave quite promising results, however, literature has shown that wave reflection is most common in this type of scheme (Kantha 2000), therefore, research was required to identify a suitable feedback condition. The use of two different types of feedback conditions were implemented and tested to determine the feedback condition that most effectively conserved momentum and transferred the maximum data to the coarse domain.

Secondly, investigation was required into suitable interpolation procedures to be used in the feedback operator. The interpolation technique employed in Phase I was a simple averaging technique. To determine the most appropriate technique three other types of interpolation techniques were tested: 1) direct copy, 2) Shapiro and 3) fully weighted.

## **6.2 FEEDBACK CONDITIONS**

The flow relaxation scheme was one of the methods identified during the literature review as one of the better methods for feedback specification in relation to model performance and accuracy (Debreu 2008). The aim of the scheme is to reduce the error that may be generated due to the difference in resolution between the nested grid and the coarse grid,

through the absorption of boundary disturbances and prevent them propagating out of the nested domain.

The implementation of a flow relaxation scheme involves the application of a varying relaxation factor to the coarse grid updating data in the following way.

$$\phi_c|^{n+\frac{1}{2}} = (1-\alpha)\phi_c|^{n+\frac{1}{2}} + \alpha \phi_n|^{n+\frac{1}{2}} \quad (6.1)$$

with  $\phi_c$  representing the coarse grid variable,  $\phi_n$  the nested grid variable and  $\alpha$  being the varying relaxation factor. This scheme involves the incorporation of an area adjacent to the nested boundary ( $\Gamma_{orig}$ ) called the sponge layer (see Figure 6.1).

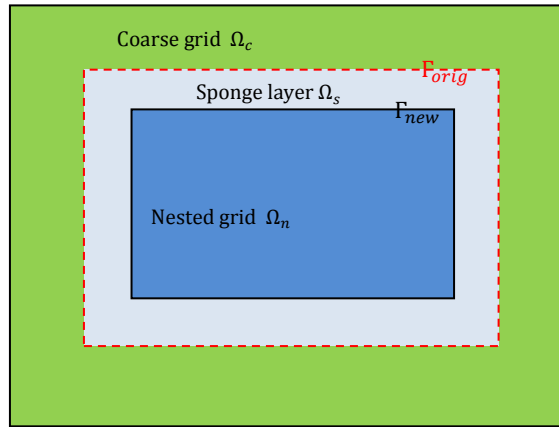


Figure 6: 1 Sponge layer

The scheme was implemented into the model by updating the coarse domain solution in the area of the sponge layer with the use of equation 6.1. The sponge layer consisted of three coarse domain grid cells adjacent to the nested boundary. Two new forms of the varying relaxation factor were used in the sponge layer and calculated relative to momentum and kinetic energy.

The momentum at the nested points in the area of the sponge layer is calculated before data is fed back to the coarse domain as follows:

$$Px_{I,J}^n = u_{I,J}^n{}^2 \times Hx_{I,J}^n \times \rho \times \Delta x^n \quad (6.2)$$

where the density of water is  $\rho$ , the grid spacing is  $\Delta x$ , I,J are the coarse grid coordinates. To obtain values for  $u_{I,J}^n$  (velocity in the x-direction) and  $Hx_{I,J}^n$  (depth in the x-direction) the

nested grid solution was interpolated in space to the resolution of the coarse grid. The momentum at each coarse domain point in the region of the sponge layer is also calculated as follows:

$$Px_{i,j}^c = u_{i,j}^c{}^2 \times Hx_{i,j}^c \times \rho \times \Delta x^c \quad (6.3)$$

These values are then compared with each other in relation to the same point in the domain and a correction factor is generated.

The relaxation coefficient was also manipulated to reflect the variation in kinetic energy in relation to the two domains in the area of the sponge layer. The method used is similar to the momentum variation method, but the kinetic energy is calculated instead of the momentum. The following equation represents the calculation of the kinetic energy:

$$E = \frac{u^3}{2g} \times \rho \times \Delta x \quad (6.4)$$

The implementation of the flow relaxation scheme involved the incorporation of a new subroutine, RELAX, to generate the sponge layer and relaxation factor. A schematic of the model with the introduction of the relaxation scheme is shown in Figure 5.6 in the previous chapter. Four different models were used to test the abilities of the two different forms of the boundary operators. Table 6.1 shows a list of the models used and their feedback conditions.

Table 6: 1 Feedback condition models

<b>Model</b>	<b>Feedback conditions</b>	<b>Variable prescription</b>
BTWNM_MOM(V+E)	Momentum relaxation scheme	$\zeta$ , U, V-interpolated
BTWNM_MOM(ALL)	Momentum relaxation scheme	$\zeta$ , qx, qy -interpolated Hx, Hy, U, V - calculated
BTWNM_KIN(V+E)	Kinetic relaxation scheme	$\zeta$ , U, V-interpolated
BTWNM_KIN(ALL)	Kinetic relaxation scheme	$\zeta$ , qx, qy -interpolated Hx, Hy, U, V - calculated

### 6.2.1 MOMENTUM RELAXATION SCHEME

The momentum flow relaxation scheme was initially implemented into the BTWNM\_MOM (V+E) model, which involved a feedback prescription of velocities and elevations alone, with an average interpolation procedure.

The conservation of momentum was initially investigated by calculating the momentum fluxes in the area of the nested boundary. Figure 6.2 shows a comparison of the nested/child domain's momentum flux across the boundary (NB), with the corresponding fluxes in the updated coarse/parent domain (UC) and the high resolutions model fluxes (HR). Table 6.2 tabulates the percentage difference in peak ebb and peak flood momentum fluxes across the nested boundary for the nested/child domain and the updated coarse/parent domain relative to the high resolution single grid model.

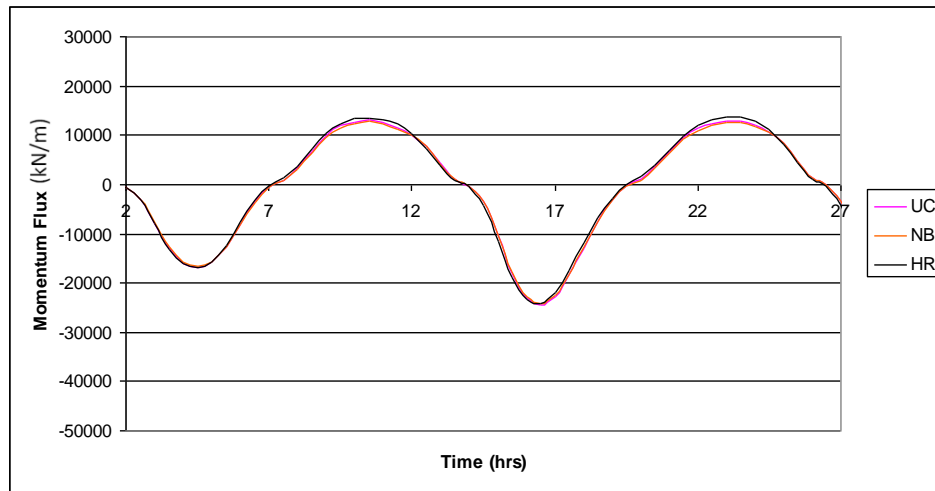


Figure 6: 2 Momentum fluxes across the boundary for BTWNM\_MOM (V+E).

Table 6: 2 Peak ebb and peak flood momentum flux across the nested boundary for BTWNM\_MOM (V+E)

	Peak ebb momentum flux (kN/m)	% difference	Peak flood momentum flux (kN/m)	% difference
High resolution (HR)	-24277.2	-	13724.28	-
Nested boundary (NB)	-24150.9	-0.5%	12653.51	-7.8%
Updates Coarse (UC)	-24432.8	+0.64%	12968.83	-5.5%

The conservation of momentum at the boundary was shown to be of a high standard. Results showed an average percentage difference at peak ebb for NB of 0.5% and UC of 0.64%, relative to the single high resolution model (HR). This is a difference of approximately 0.14% between UC and NB. In comparison to the BTWNM\_IV model, which uses a Dirichet feedback condition, a decrease in the conservation of momentum between the nested grid and the coarse grid is generated; however, there is an increase in accuracy in relation to the single high resolution model. The propagation of the momentum from the nested boundary into the nested domain was also tested by comparing the momentum fluxes along the next column of interior nested cells adjacent to the boundary to momentum fluxes across the boundary (Figure 6.3).

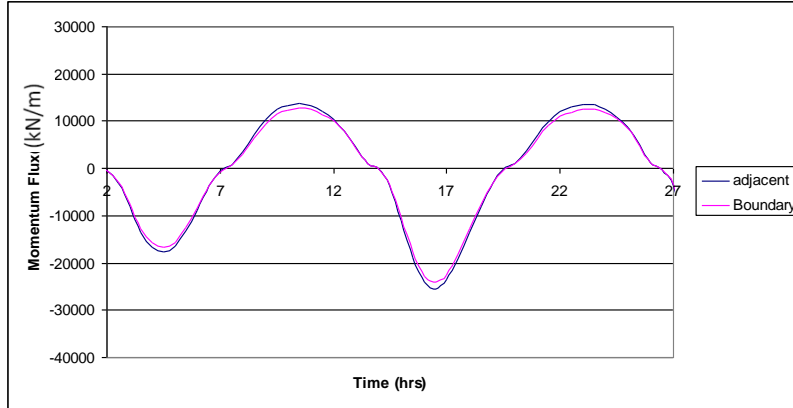


Figure 6: 3 Nested grid momentum fluxes across the boundary cells and cells adjacent to the boundary for BTWNM\_MOM (V+E)

Table 6: 3 Peak ebb and peak flood momentum for the propagation into the nested domain for BTWNM\_MOM (V+E)

	Peak ebb momentum flux (kN/m)	Peak flood momentum flux (kN/m)
Boundary	-24150.9	12653.51
Adjacent	-25476.3	13559.54

Results showed no generation of noise with the propagation of momentum into the nested domain. This high level of conservation of momentum enabled further investigation to be performed on the model to investigate its performance to transfer information into the coarse domain.

Time history analysis of the updated coarse domain was performed at points A-D shown in Figure 6.4. Figures 6.5-6.6 show a comparison of the velocities at point A and B located inside the feedback area, highlighted in Figure 6.4 with a black square. The graphs compare the original coarse domain without nesting (LR), the updated coarse domain with two-way nesting (BTWNM) and the high resolution single grid domain (HR). Results for the percent-

age difference at peak ebb and peak flood for LR and BTWNM relative to HR are tabulated in Tables 6.4-6.5.

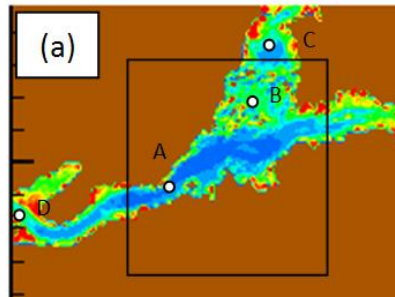


Figure 6: 4 Illustration showing time history points A-D

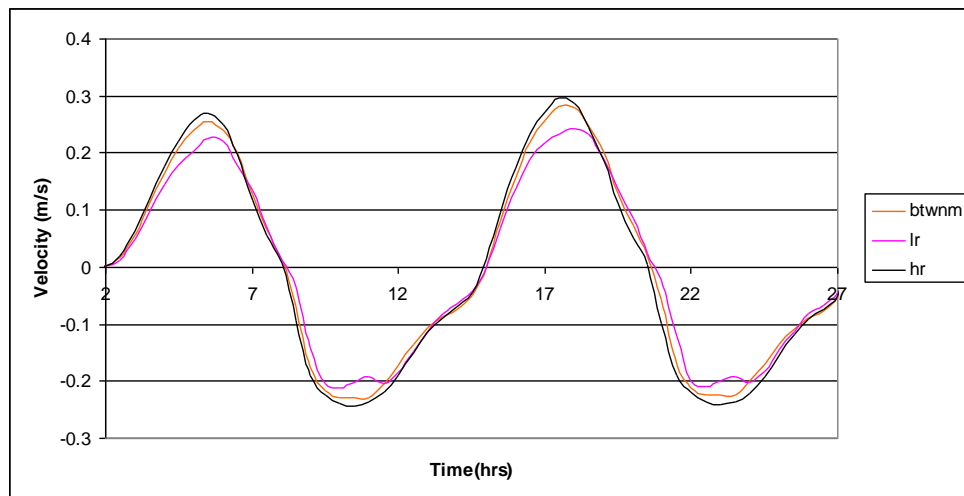


Figure 6: 5 Time history analysis of point A

Table 6: 4 Peak flood and peak ebb velocities of point A

Point A	Peak flood velocity (m/s)	% difference	Peak ebb velocity (m/s)	% difference
High resolution (HR)	0.297	-	-0.241	-
Low resolution (LR)	0.2338	-21.27%	-0.2017	-16.3%
BTWNM	0.2815	-5.2%	-0.2244	-6.88%

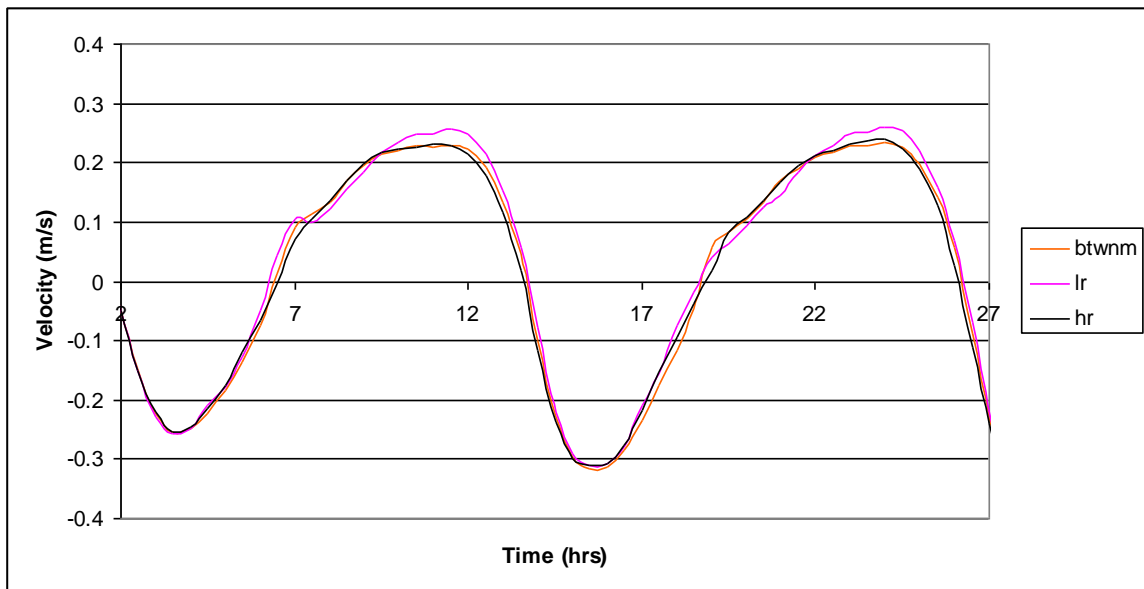


Figure 6: 6 Time history analysis of point B

Table 6: 5 Peak flood and peak ebb velocities of point B

Point B	Peak ebb velocity (m/s)	% difference	Peak flood velocity (m/s)	% difference
High resolution (HR)	-0.3101	-	0.2306	-
Low resolution (LR)	-0.3111	+0.32%	0.2563	+11.1%
BTWNM	-0.3154	+1.7%	0.2332	+1.12%

Results generated show the models differ by 5.2 % at A and 1.12 % at B to the high resolution model at peak flood, which is an increase in accuracy of 1% and 4% respectively in relation to the BTWNM\_IV model, with the Dirichlet feedback condition. Figures 6.7-6.8 show time history analysis of velocities at point C and D, located outside the feedback area. The results are presented in a tabular form in Tables 6.6-6.7 for the percentage difference in peak ebb and peak flood for LR and BTWNM relative to HR.

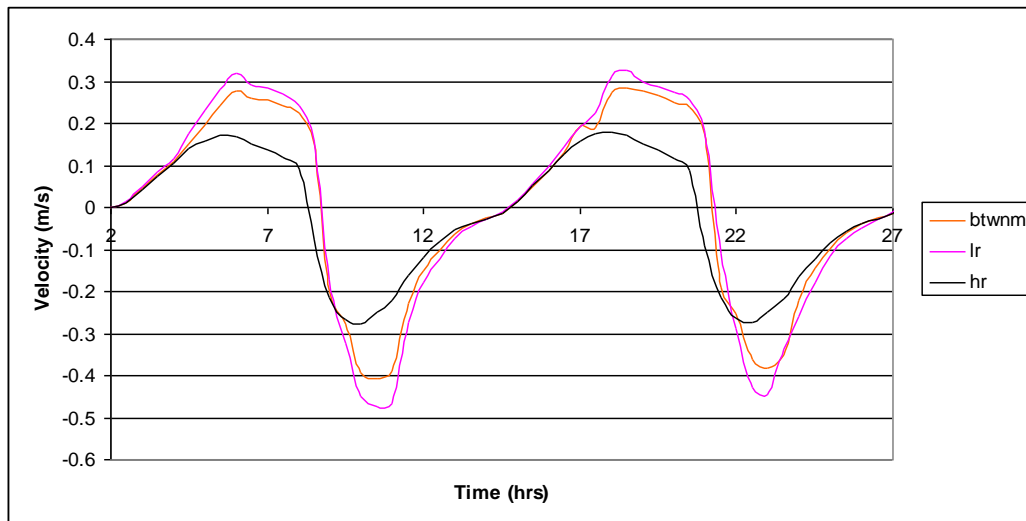


Figure 6: 7 Time history analysis of point C

Table 6: 6 Peak flood and peak ebb velocities of point C

Point C	Peak ebb velocity (m/s)	% difference	Peak flood velocity (m/s)	% difference
High resolution (HR)	-0.2786	-	0.1804	-
Low resolution (LR)	-0.4486	+61%	0.3263	+80.8%
BTWNM	-0.3821	+37%	0.2857	+58.3%

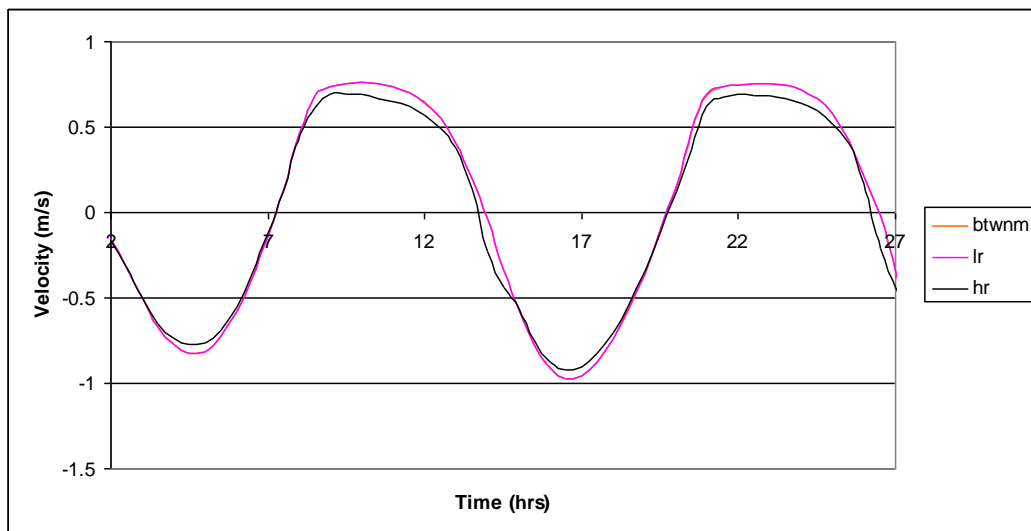


Figure 6: 8 Time history analysis of point D

Table 6: 7 Peak flood and peak ebb velocities of point D

Point D	Peak ebb velocity (m/s)	% difference	Peak flood velocity (m/s)	% difference
High resolution	-0.9172	-	0.6944	-

(HR)				
Low resolution (LR)	-0.9694	+5.69%	0.7578	+9.13%
BTWNNM	-0.9693	+5.68%	0.755	+8.7%

The performance of the model suffered with the introduction of the momentum feedback condition for the points located outside the feedback region. Point C showed an increase in error of 36% and 53.7% at peak flood and ebb respectively, relative to the BTWNNM\_IV model. Point D located further from the feedback region also showed a decrease in the accuracy in relation to BTWNNM\_IV model.

Time history analysis was also performed on the data generated in the nested region. Figure 6.10 shows a comparison of velocities at point E in the nested region for the low resolution model without nesting (LR), the nested domain in the BTWNNM\_MOM (V+E) model (BTWNNM) and the high resolution single grid model (HR). The performance of the model is tabulated in the Table 6.8.

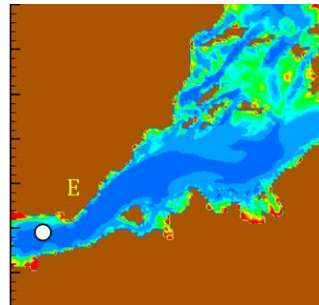


Figure 6: 9 Illustration of nested domain with point E used in the time history analysis

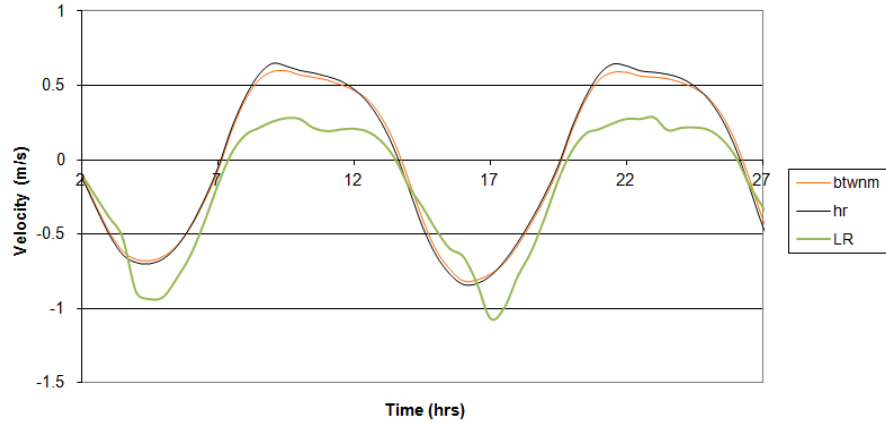


Figure 6: 10 Time history analysis of point E

Table 6: 8 Peak flood and peak ebb velocities of point E

Point E	Peak ebb velocity (m/s)	% difference	Peak flood velocity (m/s)	% difference
High resolution (HR)	-0.8379	-	0.6444	-
Low resolution (LR)	-1.0675	+27.4%	0.2848	-55.8%
BTWNM	-0.8175	-2.4%	0.5862	-9.03%

Results generated show the nested model solution exhibits a high level of accuracy in relation to the low resolution model without nesting. The level of accuracy reached is of a similar form to the BTWNM\_IV.

It was assumed if more data was transmitted from the nested domain using the momentum flow relaxation scheme the accuracy of the model outside the feedback region would increase. Therefore, a model similar to the BTWNM\_I was used with the incorporation of the momentum feedback condition. Analysis was performed to identify the models ability to conserve momentum and results are shown in Figures 6.11. A tabulated form of the re-

sults are shown in tables 6.9. The propagation of momentum into the nested domain was also analysed and results presented in Figure 6.12 and tabulated in Table 6.10.

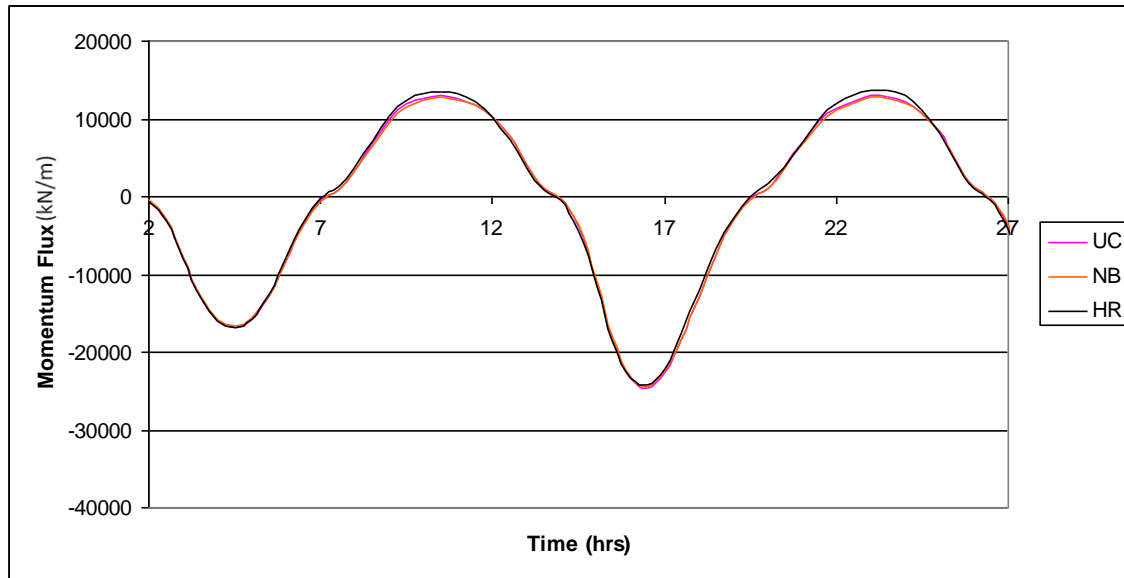


Figure 6: 11 Momentum fluxes across the boundary for BTWNM\_MOM (Q (ALL)).

Table 6: 9 Peak ebb and peak flood momentum fluxes across the nested boundary for BTWNM\_MOM Q (ALL).

	Peak ebb momentum flux (kN/m)	% difference	Peak flood momentum flux (kN/m)	% difference
High resolution (HR)	-24277.2	-	13724.28	-
Nested boundary (NB)	-24454.5	+0.73%	12829.21	-6.5%
Updates Coarse (UC)	-24687	+1.68%	13076.35	-4.7%

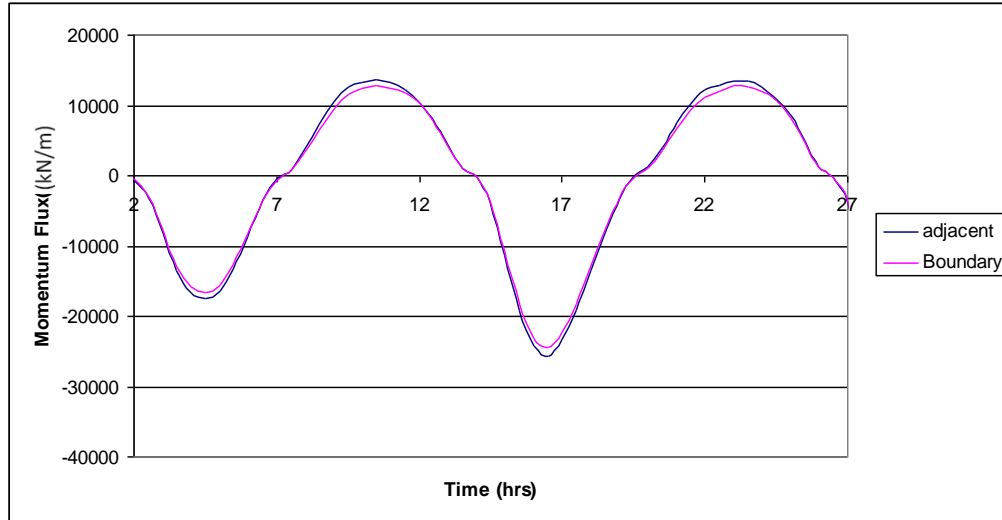


Figure 6: 12 Nested grid momentum fluxes across the boundary cells and cells adjacent to the boundary for BTWNM\_MOM (Q (ALL)).

Table 6: 10 Peak ebb and peak flood momentum for the propagation into the nested domain for BTWNM\_MOM (Q (ALL)).

	Peak ebb momentum flux (kN/m)	Peak flood momentum flux (kN/m)
Boundary	-24454.5	12829.21
Adjacent	-25641.9	13555.3

Results generated a moderately higher level of conservation between the domains in comparison to the previous model. Time history analyses for velocities were performed at points A-D (see Figure 6.4) and are shown in Figures 6.13-6.16. The graphs compare the original coarse domain without nesting (LR), the updated coarse domain with two-way nesting (BTWNM) and the high resolution single grid domain (HR). Results for the percentage difference at peak ebb and peak flood for LR and BTWNM relative to HR are tabulated in Tables 6.11-6.14.

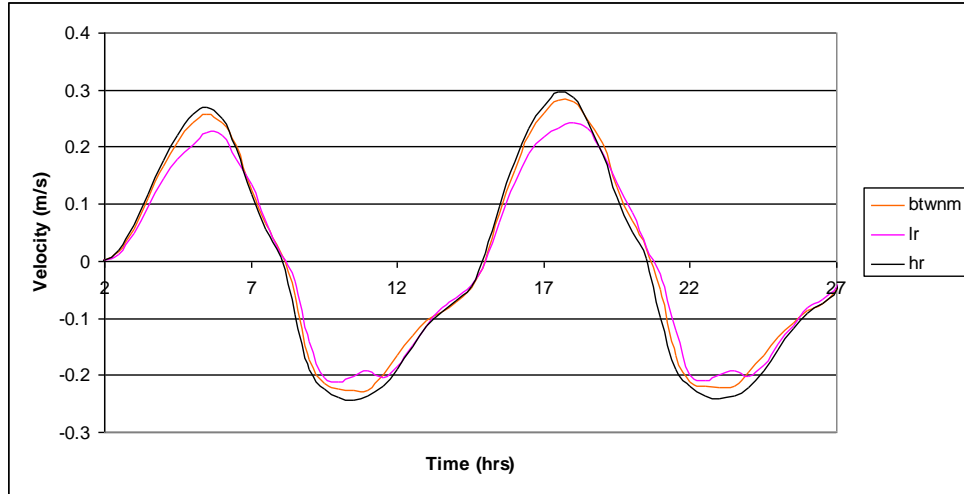


Figure 6: 13 Time history analysis of point A for BTWNM\_MOM (Q (ALL)).

Table 6: 11 Peak flood and peak ebb velocities of point A for BTWNM\_MOM (Q (ALL)).

Point A	Peak flood velocity (m/s)	% difference	Peak ebb velocity (m/s)	% difference
High resolution (HR)	0.297	-	-0.241	-
Low resolution (LR)	0.2338	21.2%	-0.2017	16.3%
BTWNM	0.2818	5.1%	-0.2223	7.7%



Figure 6: 14 Time history analysis of point B for BTWNM\_MOM (Q (ALL)).

Table 6: 12 Peak flood and peak ebb velocities of point B for BTWNM\_MOM (Q (ALL)).

Point B	Peak ebb velocity (m/s)	% difference	Peak flood velocity (m/s)	% difference
High resolution (HR)	-0.3101	-	0.2306	-
Low resolution (LR)	-0.3111	0.32%	0.2563	11.14%
BTWNM	-0.3173	2.32%	0.2367	2.6%

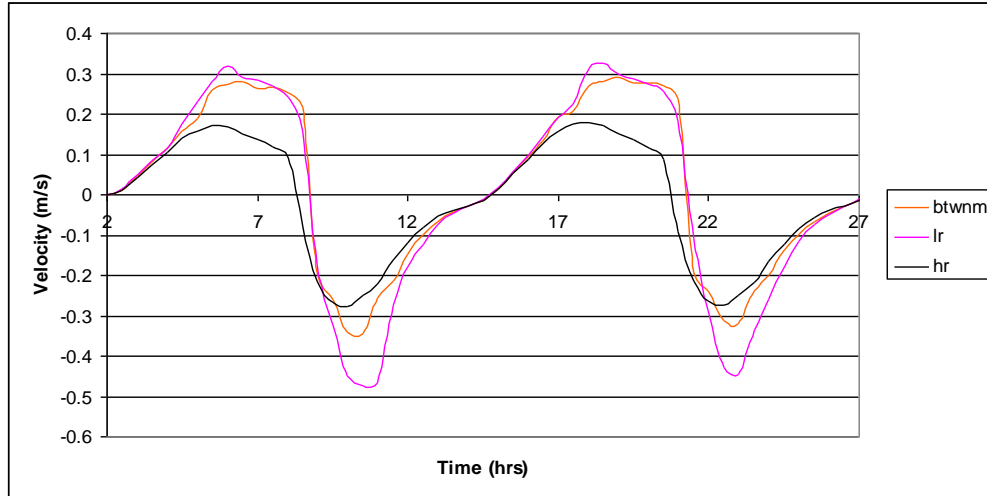


Figure 6: 15 Time history analysis of point C for BTWNM\_MOM (Q (ALL)).

Table 6: 13 Peak flood and peak ebb velocities of point C for BTWNM\_MOM (Q (ALL)).

Point C	Peak ebb velocity (m/s)	% difference	Peak flood velocity (m/s)	% difference
High resolution (HR)	-0.2786	-	0.1804	-
Low resolution (LR)	-0.4486	+61%	0.3263	+80.87%
BTWNM	-0.3207	+15.1%	0.2899	+60.6%

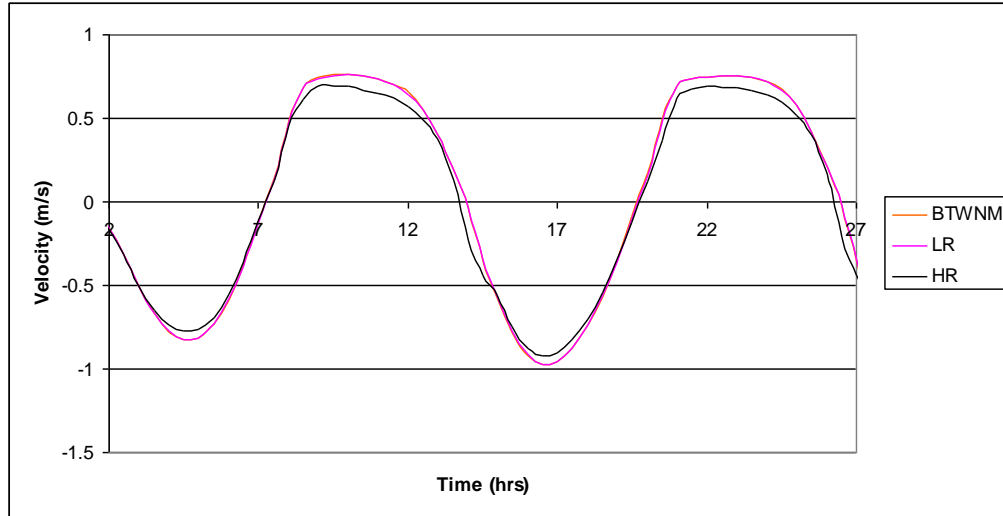


Figure 6: 16 Time history analysis of point D for BTWNNM\_MOM (Q (ALL)).

Table 6: 14 Peak flood and peak ebb velocities of point D for BTWNNM\_MOM (Q (ALL)).

Point D	Peak ebb velocity (m/s)	% difference	Peak flood velocity (m/s)	% difference
High resolution (HR)	-0.9172	-	0.6944	-
Low resolution (LR)	-0.9694	+5.6%	0.7578	+9.12%
BTWNNM	-0.9722	+6.5%	0.7505	+8.07%

Results generated showed no significant improvement to the model performance at points A and B. The performance of the model outside the feedback location at points C and D, also did not show any considerable improvement. The results showed the momentum feedback condition does not perform to the same level as the BTWNNM\_IV model with the Dirichlet feedback condition. Time history analysis was also performed on the solution generated in the nested domain (BTWNNM) and results shown in Figure 6.17 for point E (see Figure 6.9).

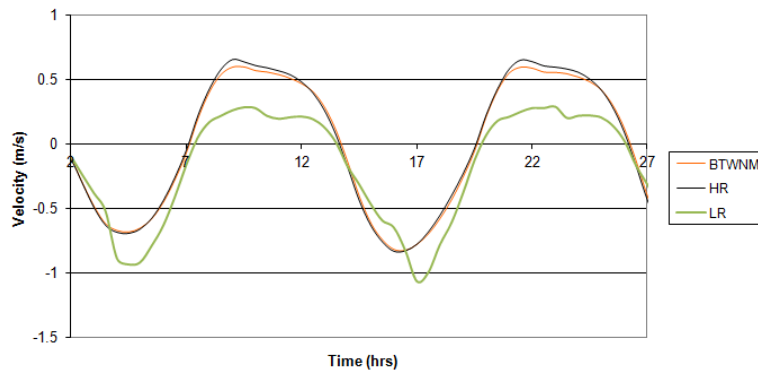


Figure 6: 17 Time history analysis of point E for BTWNM\_MOM (Q (ALL)).

Table 6: 15 Peak flood and peak ebb velocities of point E for BTWNM\_MOM (Q (ALL)).

Point E	Peak ebb velocity (m/s)	% difference	Peak flood velocity (m/s)	% difference
High resolution (HR)	-0.8379	-	0.6444	-
Low resolution (LR)	-1.0675	+27.4%	0.2848	-55.8%
BTWNM	-0.8241	-1.64%	0.5929	-7.9%

Results showed to be of a greater accuracy in relation to the previous model and the BTWNM\_IV model. If a greater degree of accuracy was required in the nested domain in comparison to the coarse domain this model would outweigh the BTWNM\_IV model, therefore the model consists of a flag that allows the user to specify which condition they deem appropriate to use depending on the type of domain being modelled.

## 6.2.2 KINETIC RELAXATION SCHEME

The kinetic feedback condition was introduced into the BTWNM\_IV model similar to the previous BTWNM\_MOM (V+E) model, containing a feedback prescription of velocities and elevations alone, with an average interpolation technique. The performance of the model to conserve momentum was analysed and results are shown in Figures 6-18 and tabulated in Tables 6.16.

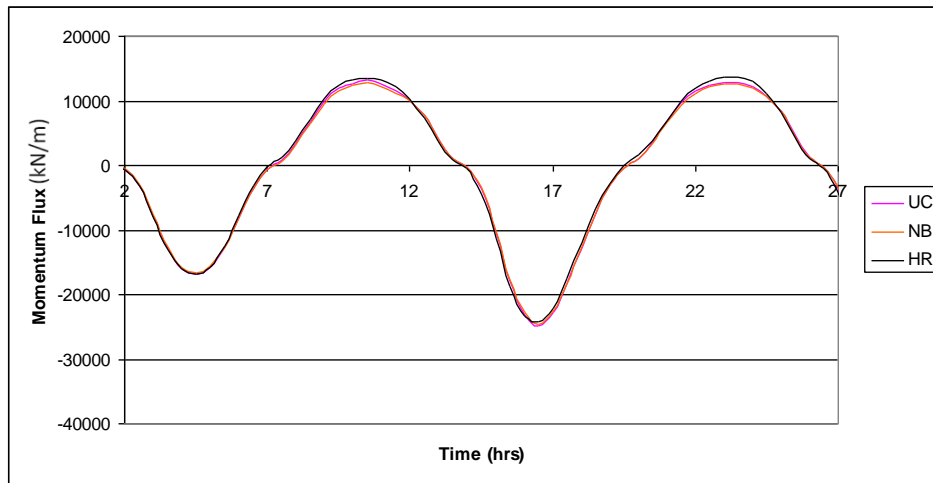


Figure 6: 18 Momentum fluxes across the boundary for BTWNM\_KIN (V+E).

Table 6: 16 Peak ebb and peak flood momentum fluxes across the nested boundary for BTWNM\_KIN (V+E)

	Peak ebb momentum flux (kN/m)	% difference	Peak flood momentum flux (kN/m)	% difference
High resolution (HR)	-24277.2	-	13724.28	-
Nested boundary (NB)	-24581.7	-1.25%	12553.35	-8.5%
Updates Coarse (UC)	-24819.4	-2.2%	12919.76	-5.8%

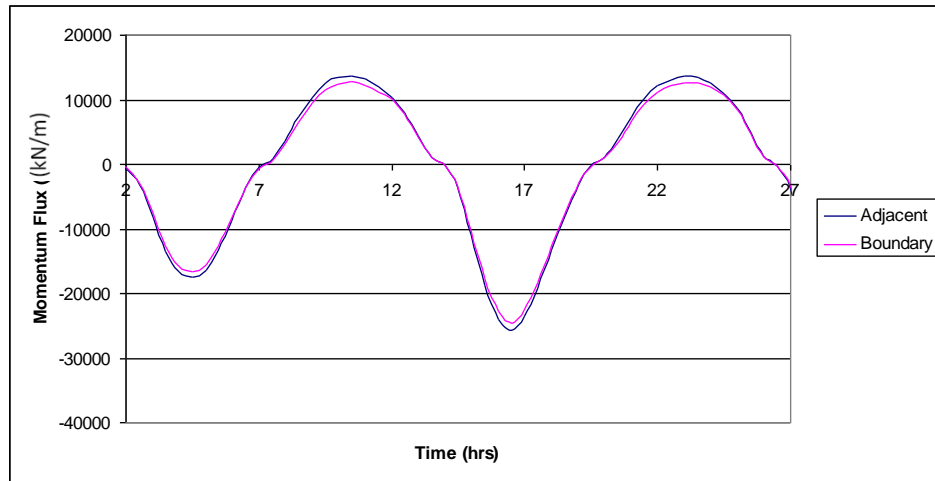


Figure 6: 19 Nested grid momentum fluxes across the boundary cells and cells adjacent to the boundary for BTWNM\_KIN (V+E).

Table 6: 17 Peak ebb and peak flood momentum fluxes across the nested boundary cells and cells adjacent to the boundary for BTWNM\_KIN (V+E)

	Peak ebb momentum flux (kN/m)	Peak flood momentum flux (kN/m)
Boundary	-24581.7	12553.35
Adjacent	-25776.3	13624.08

The results showed the level of conservation deteriorated from the BTWNM\_MOM (V+E) by approximately 0.4% and also the accuracy of the solution has decreased by 0.7%. However, momentum propagation still performed correctly as shown by the small difference between the nested boundary cell and adjacent boundary cell fluxes in Figure 6.19.

Figures 6.20-6.23 show the time history analysis of the models performance in the updated coarse/parent domain (UC) at points A-D shown in Figure 6.4. Table 6.18-6.21 show the percentage difference at peak ebb and peak flood for the low resolution model without nest-

ing (LR) and the updated coarse/parent solution in the BTWNM\_KIN(V+E) (BTWNM) relative to the high resolution single grid solution (HR). The results generated show that the models performance still does not reach the level of accuracy produced in the BTWNM\_IV model.

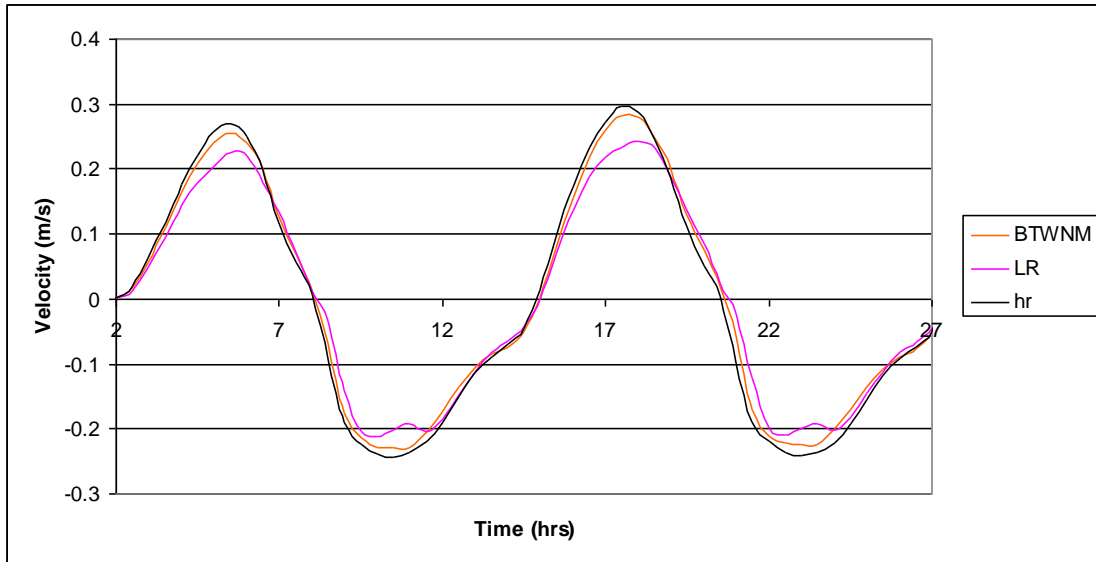


Figure 6: 20 Time history analysis of point A for BTWNM\_KIN (V+E).

Table 6: 18 Peak flood and peak ebb velocities of point A for BTWNM\_KIN (V+E).

Point A	Peak flood velocity (m/s)	% difference	Peak ebb velocity (m/s)	% difference
High resolution (HR)	0.297	-	-0.241	-
Low resolution (LR)	0.2338	-21.2%	-0.2017	-16.3%
BTWNM	0.2816	-5.1%	-0.2244	-6.8%

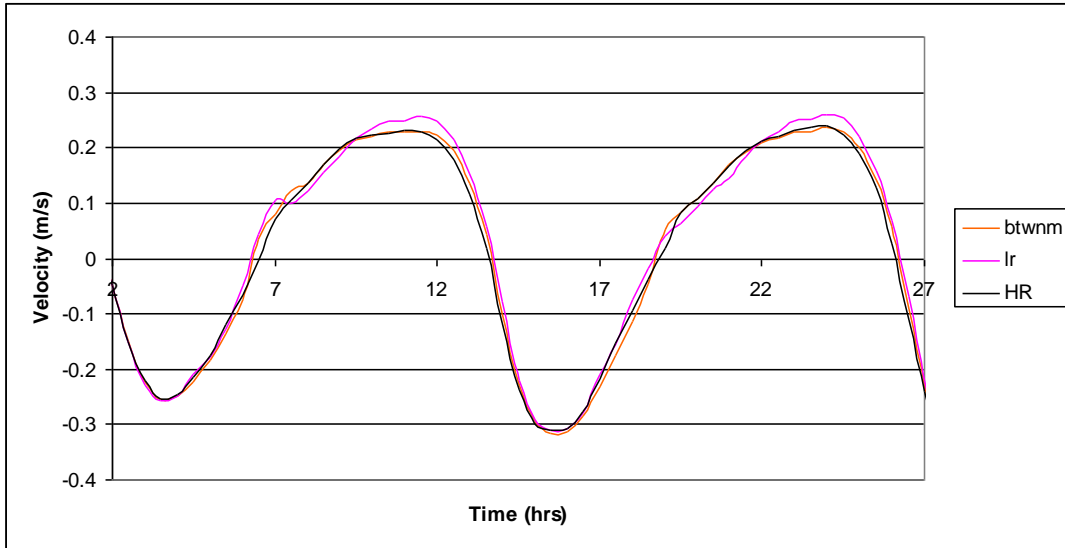


Figure 6: 21 Time history analysis of point B for BTWNM\_KIN (V+E).

Table 6: 19 Peak flood and peak ebb velocities of point B for BTWNM\_KIN (V+E).

Point B	Peak ebb velocity (m/s)	% difference	Peak flood velocity (m/s)	% difference
High resolution (HR)	-0.3101	-	0.2306	-
Low resolution (LR)	-0.3111	+0.32%	0.2563	+11.1%
BTWNM	-0.3153	+1.6%	0.2359	+2.2%

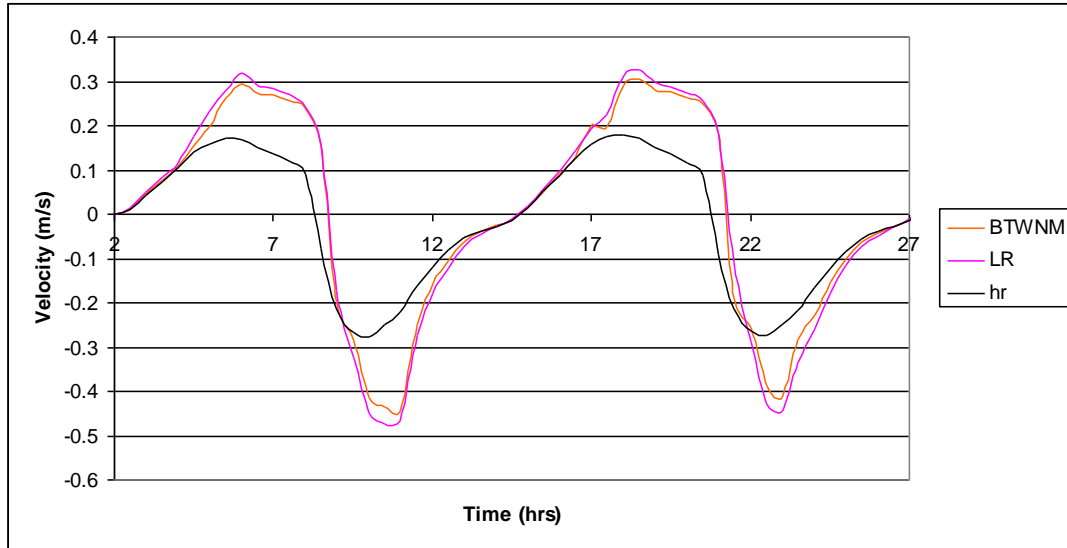


Figure 6: 22 Time history analysis of point C for BTWNNM\_KIN (V+E).

Table 6: 20 Peak flood and peak ebb velocities of point C for BTWNNM\_KIN (V+E).

Point C	Peak ebb velocity (m/s)	% difference	Peak flood velocity (m/s)	% difference
High resolution (HR)	-0.2786	-	0.1804	-
Low resolution (LR)	-0.4486	+61.01%	0.3263	+80.8%
BTWNNM	-0.4147	+48.8%	0.304	+68.51%

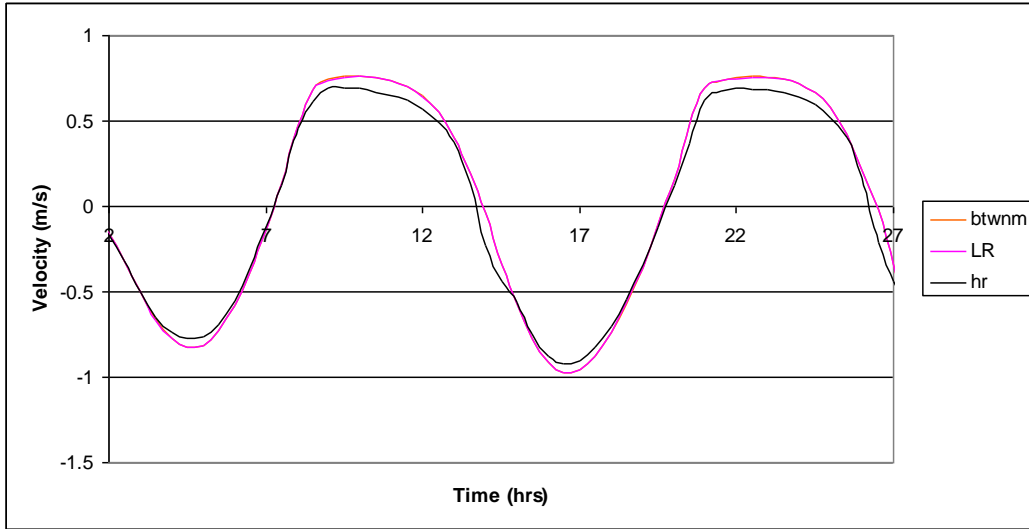


Figure 6: 23 Time history analysis of point D for BTWNM\_KIN (V+E).

Table 6: 21 Peak flood and peak ebb velocities of point D for BTWNM\_KIN (V+E).

Point D	Peak ebb velocity (m/s)	% difference	Peak flood velocity (m/s)	% difference
High resolution (HR)	-0.9172	-	0.6944	-
Low resolution (LR)	-0.9694	+13.9%	0.7578	+9.1%
BTWNM	-0.9717	+5.9%	0.759	+9.3%

Results generated show the models performance in the updated coarse domain (UC) does not reach the level of accuracy produced in the BTWNM\_IV model, with the Dirichlet feedback condition. The results showed areas outside of the feedback interface, points C-D, have considerably decreased in accuracy in comparison to the previous model BTWNM\_MOM (Q (ALL)) and the BTWN\_IV model. In relation to the nested domain solution, the level of accuracy deteriorated in relation to the BTWNM\_MOM (Q (ALL)) model. This is clear from the results generated in Figure 6.24 for the time history analysis of point E shown in Figure 6.4.

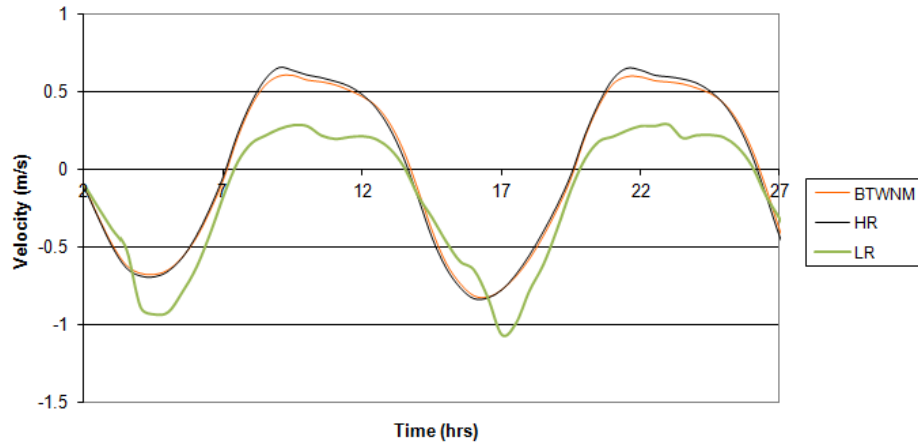


Figure 6: 24 Time history analysis of point E for BTWNM\_KIN (V+E).

Table 6: 22 Peak flood and peak ebb velocities of point E for BTWNM\_KIN (V+E).

Point E	Peak ebb velocity (m/s)	% difference	Peak flood velocity (m/s)	% difference
High resolution (HR)	-0.8379	-	0.6444	-
Low resolution (LR)	-1.0675	+27.4%	0.2848	55.8%
BTWNM	-0.8249	-1.5%	0.5905	-8.3%

The kinetic relaxation scheme was implemented into a model similar to the BTWNM\_I model, which involves using a variable feedback prescription of interpolated water elevation data and volumetric flux data, with water depths and velocities calculated using the interpolated data. This was performed to increase the consistency between the nested/child domain and the coarse/parent domain. The ability of the model to conserve momentum is shown in Figure 6.25 and results tabulated in Table 6.23 for percentage difference in peak ebb and peak flood momentum fluxes across the nested domain boundary (NB) and fluxes

in the equivalent updated coarse domain (UC) relative to the high resolution model (HR). The ability of momentum to propagate into the nested domain is demonstrated in Figure 6.26.

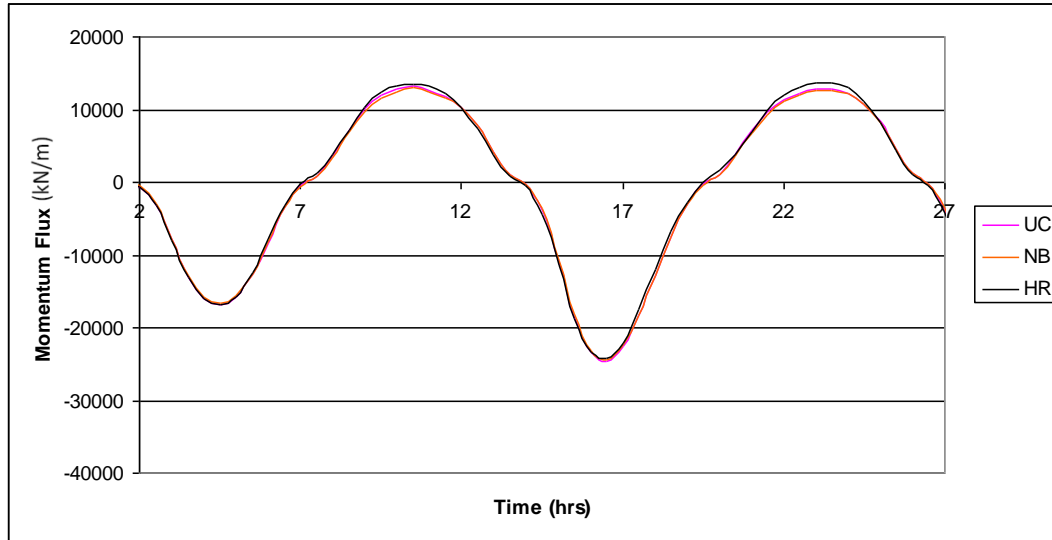


Figure 6: 25 Momentum fluxes across the boundary for BTWNM\_KIN (Q (ALL)).

Table 6: 23 Peak ebb and peak flood momentum flux across the nested boundary for BTWNM\_KIN Q (ALL)).

	Peak ebb momentum flux (kN/m)	% difference	Peak flood momentum flux (kN/m)	% difference
High resolution (HR)	-24277.2	-	13724.28	-
Nested boundary (NB)	-24435.5	+0.65%	12653.8	-7.7%
Updates Coarse (UC)	-24672.5	+1.6%	12932.07	-5.7%

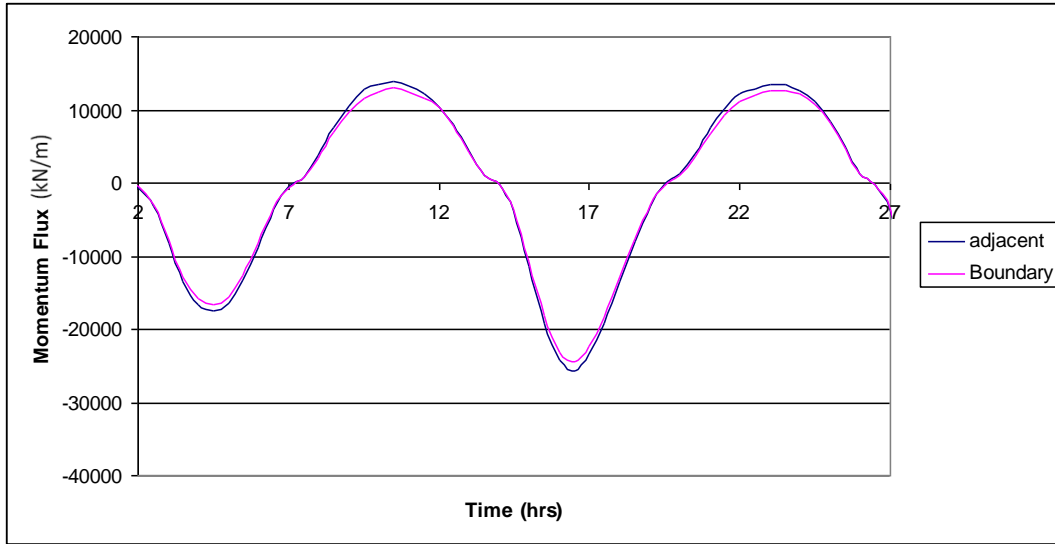


Figure 6: 26 Nested grid momentum fluxes across the boundary cells and cells adjacent to the boundary for BTWNM\_KIN (Q (ALL)).

Table 6: 24 Peak ebb and peak flood momentum for the propagation into the nested domain for BTWNM\_KIN (Q (ALL)).

	Peak ebb momentum flux (kN/m)	Peak flood momentum flux (kN/m)
Boundary	-24435.5	12653.8
Adjacent	-25619.3	13484.59

Results generated showed a high level of conservation, with the propagation of momentum functioning correctly demonstrated by the small difference in the boundary cells and the adjacent cells momentum fluxes.

Figures 6.27-6.30 show the results for the models performance at points A-D (Figure 6.4) in the updated coarse/parent domain. The model solution in the nested domain at point E, shown in Figure 6.9, are analysed by time history analysis and results shown in Figure 6.31.

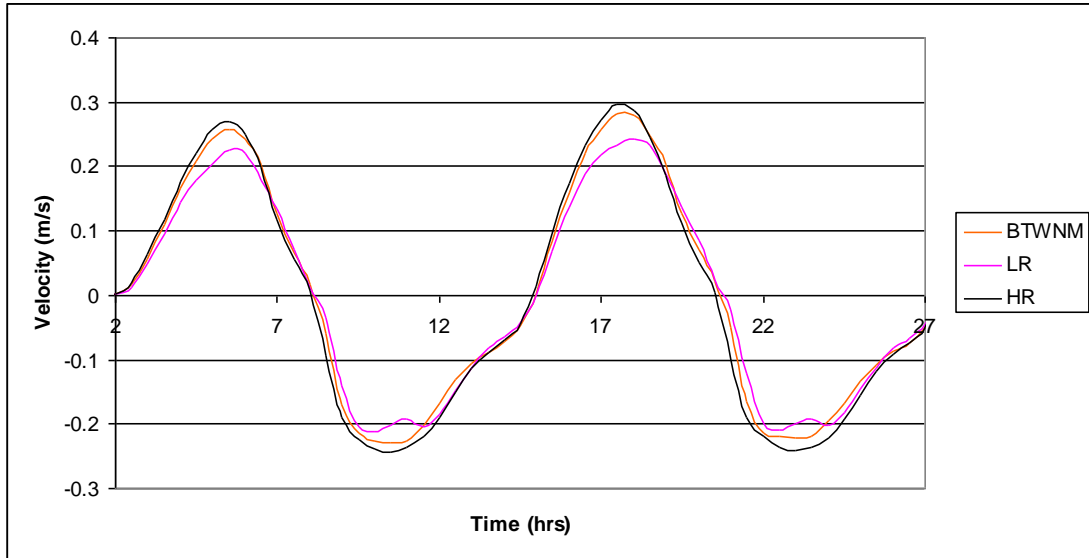


Figure 6: 27 Time history analysis of point A for BTWNM\_KIN (Q (ALL)).

Table 6: 25 Peak flood and peak ebb velocities of point A for BTWNM\_KIN (Q (ALL)).

Point A	Peak flood velocity (m/s)	% difference	Peak ebb velocity (m/s)	% difference
High resolution (HR)	0.297	-	-0.241	-
Low resolution (LR)	0.2338	-21.2%	-0.2017	-16.3%
BTWNM	0.2816	-5.18%	-0.2222	-7.8%

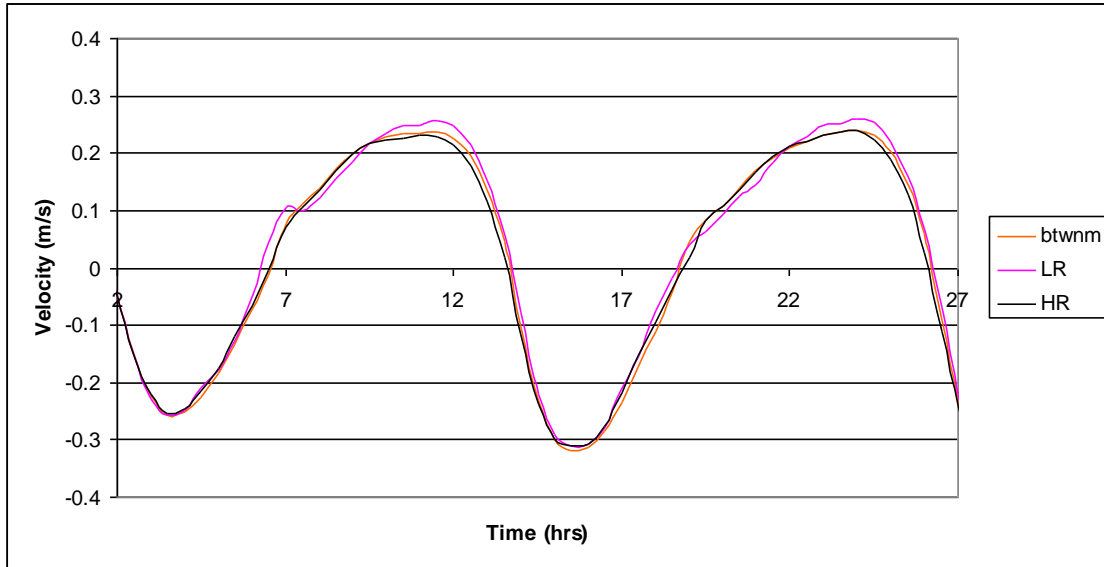


Figure 6: 28 Time history analysis of point B for BTWNM\_KIN (Q (ALL)).

Table 6: 26 Peak flood and peak ebb velocities of point B for BTWNM\_KIN (Q (ALL)).

Point B	Peak ebb velocity (m/s)	% difference	Peak flood velocity (m/s)	% difference
High resolution (HR)	-0.3101	-	0.2306	-
Low resolution (LR)	-0.3111	+0.32%	0.2563	+11.14%
BTWNM	-0.3174	+2.3%	0.2412	+4.5%

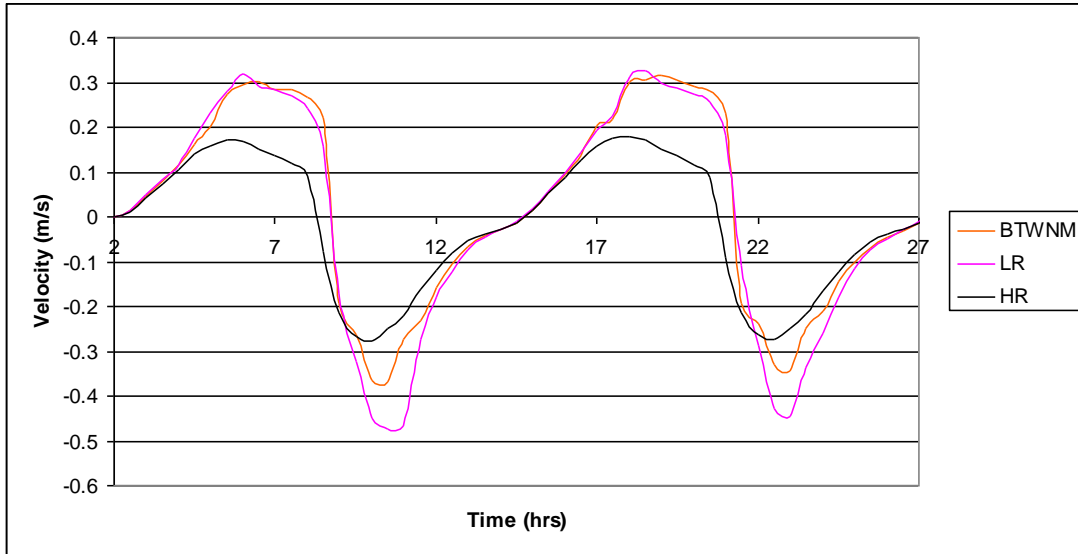


Figure 6: 29 Time history analysis of point C for BTWNM\_KIN (Q (ALL)).

Table 6: 27 Peak flood and peak ebb velocities of point C for BTWNM\_KIN (Q (ALL)).

Point C	Peak ebb velocity (m/s)	% difference	Peak flood velocity (m/s)	% difference
High resolution (HR)	-0.2786	-	0.1804	-
Low resolution (LR)	-0.4486	+61%	0.3263	+80.8%
BTWNM	-0.3429	+23%	0.315	74.6%

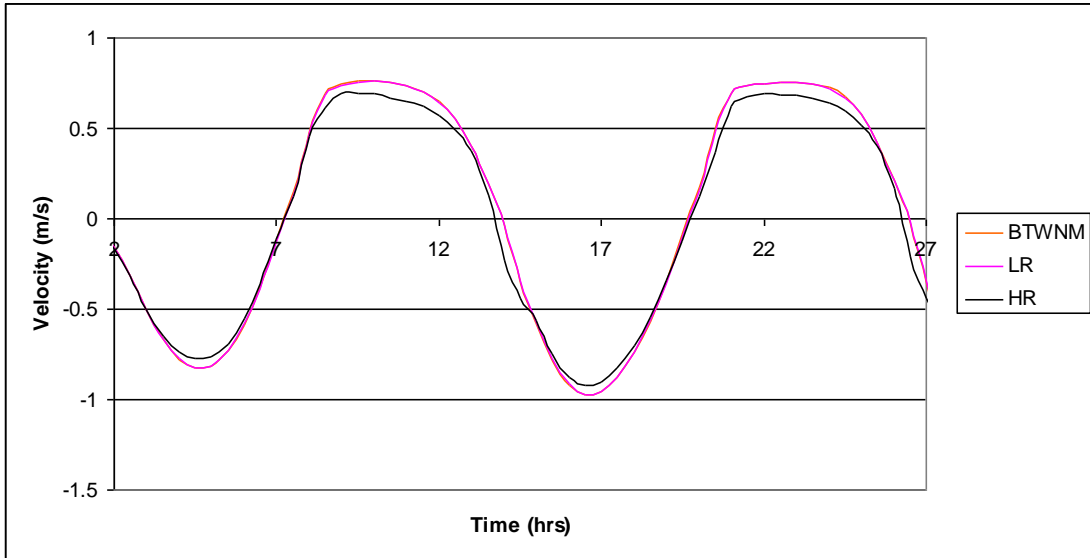


Figure 6: 30 Time history analysis of point D for BTWNM\_KIN (Q (ALL)).

Table 6: 28 Peak flood and peak ebb velocities of point D for BTWNM\_KIN ((Q (ALL)).

Point D	Peak ebb velocity (m/s)	% difference	Peak flood velocity (m/s)	% difference
High resolution (HR)	-0.9172	-	0.6944	-
Low resolution (LR)	-0.9694	+5.69%	0.7578	+9.13%
BTWNM	-0.9717	+5.9%	0.7537	+8.5%

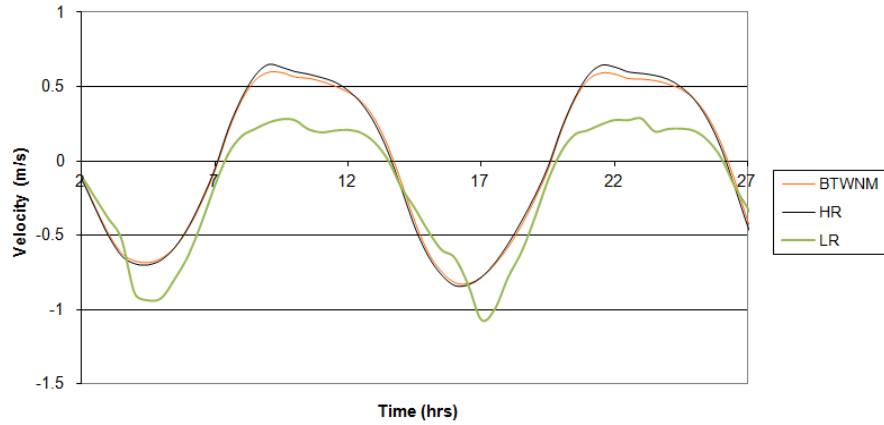


Figure 6: 31 Time history analysis of point E for BTWNM\_KIN (Q (ALL)).

Table 6: 29 Peak flood and peak ebb velocities of point E for BTWNM\_KIN ((Q (ALL)).

Point E	Peak ebb velocity (m/s)	% difference	Peak flood velocity (m/s)	% difference
High resolution (HR)	-0.8379	-	0.6444	-
Low resolution (LR)	-1.0675	+27.4%	0.2848	-55.8%
BTWNM	-0.8238	-1.6%	0.5932	-7.9%

Upon analysis of the BTWNM\_KIN (Q (ALL)) model performance, it was found the accuracy of the model solution in the area outside the feedback area did not reach the same level as the BTWNM\_IV model, with a Dirichlet feedback condition. The performance of the model in the nested domain did not reach the same level of accuracy as the BTWNM\_MOM (Q (ALL)) model.

### 6.3 INTERPOLATION/ UPDATE SCHEMES

The initial interpolation scheme used in the model incorporated an average operating procedure. This was incorporated as literature showed it was a common technique in nesting procedures. The scheme was also one of the most basic schemes and easy to implement. Equation 6.11 shows the formulation of the average interpolation scheme:

$$\sum_{k=1}^N \phi_k^n \Delta x^n \Delta y^n = \phi^c \Delta x^c \Delta y^c \quad (6.11)$$

with N representing the number of grid cells within the coarse grid cell I.

Other interpolation techniques have been shown to give similar if not better solutions, such as work carried out by Debreu (2008), therefore other forms of interpolation techniques required investigation. A number of different versions of the BTWNM\_IV model were developed, each having a different form of interpolation. Table 6.30 shows a list of the models developed to investigate the best interpolation scheme. Chapter 2 gives an in depth description of these interpolation processes.

Table 6: 30 Interpolation models

Model	Interpolation scheme
BTWNM_IV	Average operator
BTWNM_COPY	Direct copy
BTWNM_SHAP	Shapiro scheme
BTWNM_FULLLW	Fully weighted scheme

The performance of the model with different interpolation schemes were determined by calculating the momentum fluxes across the nested boundary, the propagation of momentum into the nested domain, and also with the use of time history analysis to determine the performance of the model in the updated coarse domain and the nested domain.

### 6.3.1 BTWNM\_COPY

The direct copy model was run and the performance of the model in relation to conservation of momentum is shown in Figures 6.32-6.33. The results show the percentage difference between the coarse domain and the nested domain has increased on the ebb tide in relation to the BTWNM\_IV model, which had a difference of just 0.7% between the two domains. The propagation of momentum into the nested domain performed correctly with a slight difference in boundary cell and adjacent cell fluxes. Time history analysis of points A-D (see Figure 6.4) are represented in Figures 6.34-6.37.

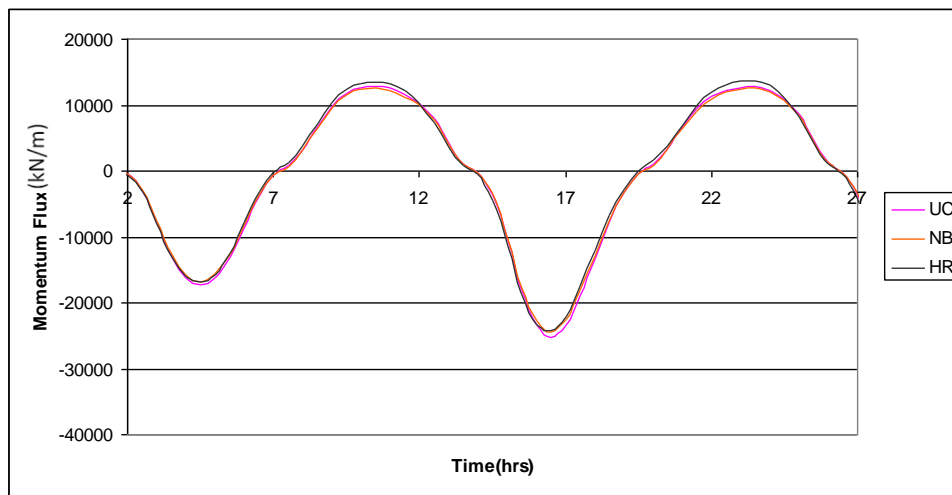


Figure 6: 32 Momentum fluxes across the boundary for BTWNM\_COPY

Table 6: 31 Peak ebb and peak flood momentum flux across the nested boundary for BTWNM\_COPY

	Peak ebb momentum flux (kN/m)	% difference	Peak flood momentum flux (kN/m)	% difference
High resolution	-24277.2	-	13724.28	-
Nested boundary	-24516.6	+0.9%	12588.78	-8.27%
Updates Coarse	-25311.6	+4.2%	12901.91	-5.9%

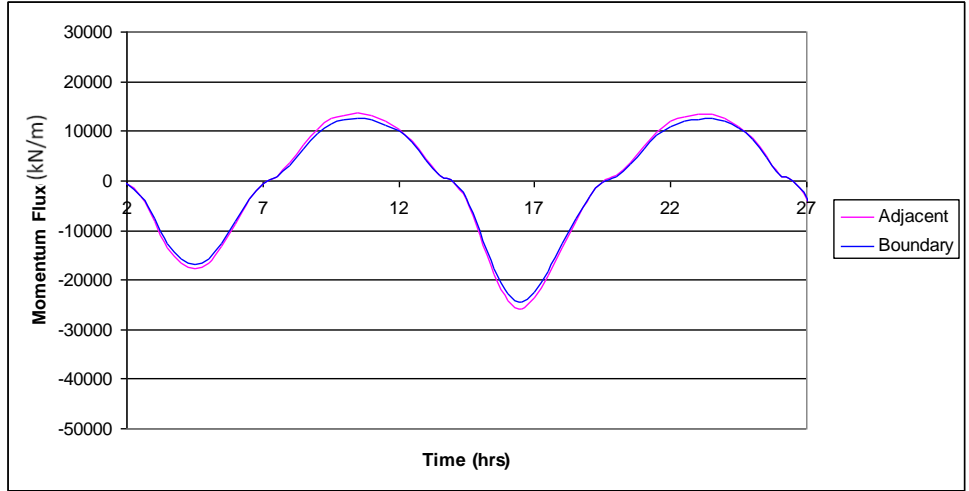


Figure 6: 33 Nested grid momentum fluxes across the boundary cells and cells adjacent to the boundary for BTWNM\_COPY

Table 6: 32 Peak ebb and peak flood momentum fluxes across the boundary cells and cells adjacent to the boundary for BTWNM\_COPY

	Peak ebb momentum flux (kN/m)	Peak flood momentum flux (kN/m)
Boundary	-24516.6	12588.78
Adjacent	-25764	13655.39

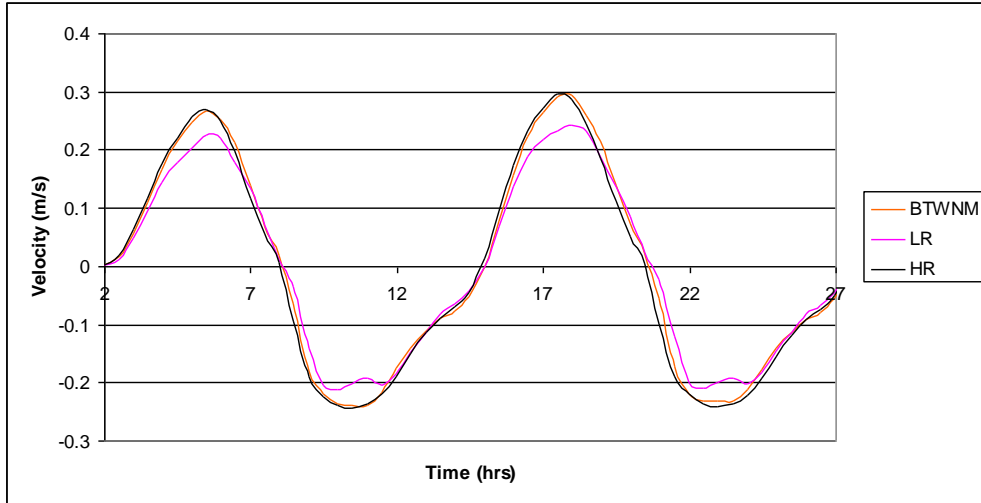


Figure 6: 34 Time history analysis of point A for BTWNM\_COPY.

Table 6: 33 Peak flood and peak ebb velocities of point A for BTWNM\_COPY.

Point A	Peak flood velocity (m/s)	% difference	Peak ebb velocity (m/s)	% difference
High resolution (HR)	0.297	-	-0.241	-
Low resolution (LR)	0.2338	-21.2%	-0.2017	-16.3%
BTWNM	0.2944	-0.87%	-0.2316	-3.9%

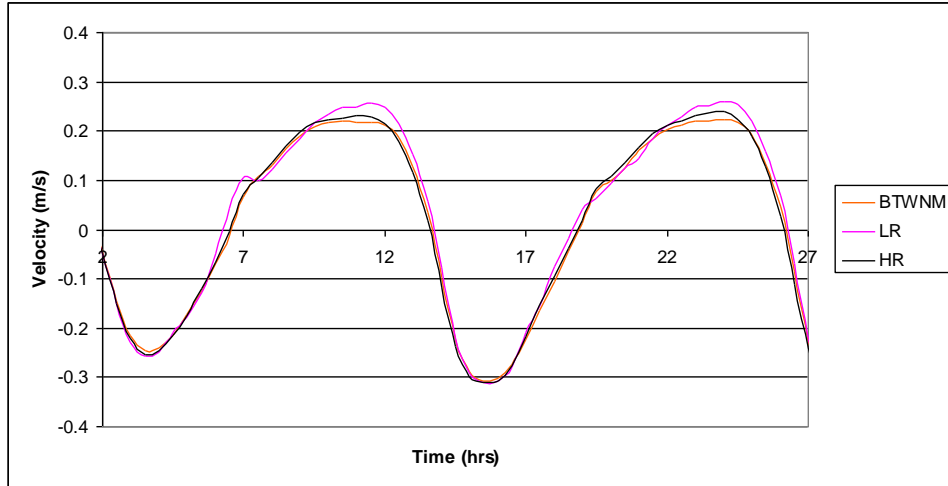


Figure 6: 35 Time history analysis of point B for BTWNM\_COPY.

Table 6: 34 Peak flood and peak ebb velocities of point B for BTWNM\_COPY.

Point B	Peak ebb velocity (m/s)	% difference	Peak flood velocity (m/s)	% difference
High resolution (HR)	-0.3101	-	0.2306	-
Low resolution (LR)	-0.3111	+0.32%	0.2563	+11.14%
BTWNM	-0.3027	-2.3%	0.2238	-2.94%

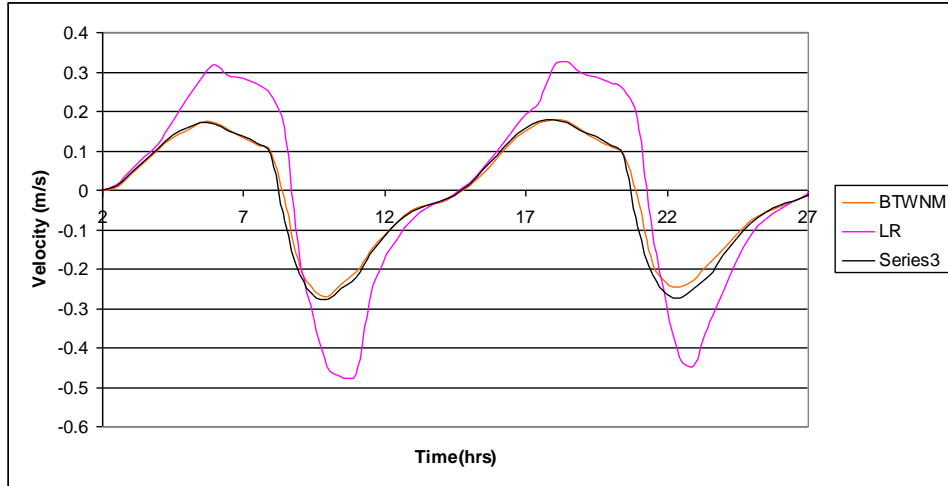


Figure 6: 36 Time history analysis of point C for BTWNM\_COPY.

Table 6: 35 Peak flood and peak ebb velocities of point C for BTWNM\_COPY.

Point C	Peak ebb velocity (m/s)	% difference	Peak flood velocity (m/s)	% difference
High resolution (HR)	-0.2786	-	0.1804	-
Low resolution (LR)	-0.4486	+61.01%	0.3263	+80.87%
BTWNM	-0.2455	-11.88%	0.1782	-1.2%

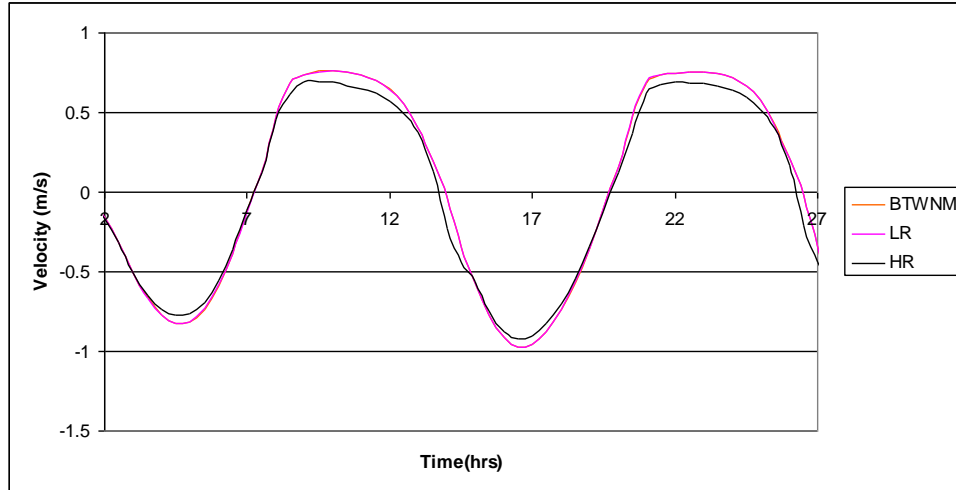


Figure 6: 37 Time history analysis of point D for BTWNNM\_COPY.

Table 6: 36 Peak flood and peak ebb velocities of point D for BTWNNM\_COPY.

Point D	Peak ebb velocity (m/s)	% difference	Peak flood velocity (m/s)	% difference
High resolution (HR)	-0.9172	-	0.6944	-
Low resolution (LR)	-0.9694	+5.6%	0.7578	+9.1%
BTWNNM	-0.9709	+5.8%	0.7537	+8.5%

Results showed the error at the feedback interface was reduced at point A in comparison to the BTWNNM\_IV model with an average interpolation procedure, however, Figure 6.36-6.37 showed that the accuracy of the model outside the feedback interface (points C and D) did not reach the same level of accuracy in relation to the average interpolation model BTWNNM\_IV.

The performance of the nested domain was also investigated and results shown in Figure 6.38. Results generated showed a slight increase in the accuracy on the ebb tide of approximately 2%.

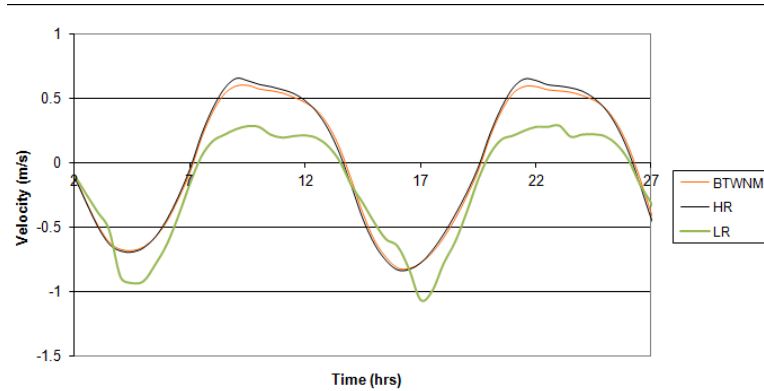


Figure 6: 38 Time history analysis of point E for BTWNM\_COPY.

Table 6: 37 Peak flood and peak ebb velocities of point E for BTWNM\_COPY.

Point E	Peak ebb velocity (m/s)	% difference	Peak flood velocity (m/s)	% difference
High resolution (HR)	-0.8379	-	0.6444	-
Low resolution (LR)	-1.0675	+27.4%	0.2848	-55.8%
BTWNM	-0.8206	-2.06%	0.5894	-8.5%

### 6.3.2 BTWNM\_SHAP

The Shapiro method was introduced into the two-way nested model and results for the conservation of momentum at the boundary of the nested domain are shown in Figures 6.39-6.40. The consistency between the nested domain and the updated coarse domain did not reach the same level as the average interpolation technique in the BTWNM\_IV model, which showed a difference of just 0.7 % on the ebb tide.

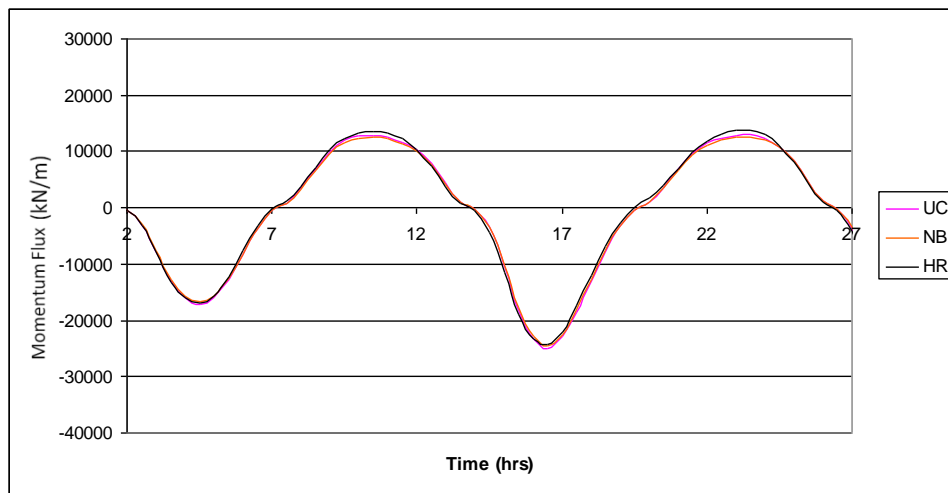


Figure 6: 39 Momentum fluxes across the boundary for BTWNM\_SHAP

Table 6: 38 Peak ebb and peak flood momentum flux across the nested boundary for BTWNM\_SHAP

	Peak ebb momentum flux (kN/m)	% difference	Peak flood momentum flux (kN/m)	% difference
High resolution (HR)	-24277.2	-	13724.28	-
Nested boundary (NB)	-24519.4	+0.9%	12651.07	-7.8%
Updates Coarse (UC)	-24979.2	+2.8%	12957.22	-5.58%

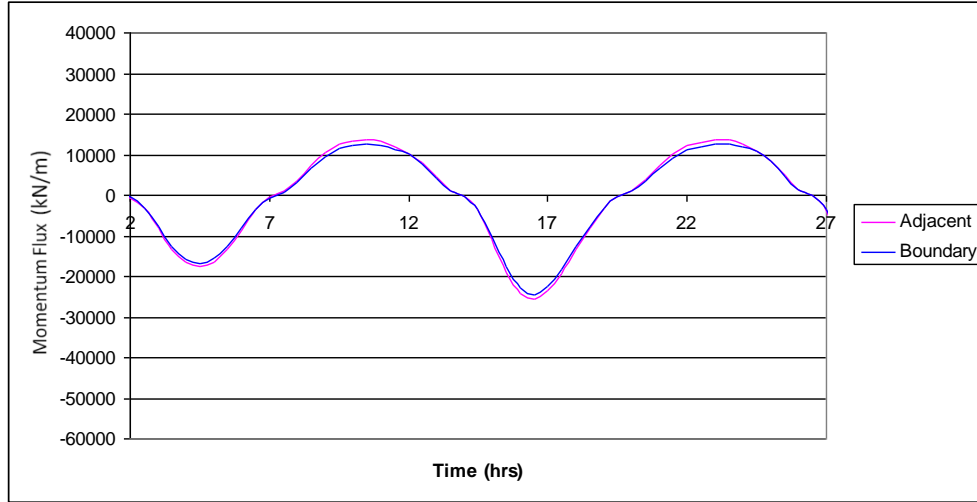


Figure 6: 40 Nested grid momentum fluxes across the boundary cells and cells adjacent to the boundary for BTWNM\_SHAP

Table 6: 39 Peak ebb and peak flood momentum for the propagation into the nested domain for BTWNM\_SHAP

	Peak ebb momentum flux (kN/m)	Peak flood momentum flux (kN/m)
Boundary	-24519.4	12651.07
Adjacent	-25750.3	13612.8

Figures 6.41-6.44 show the performance of the model in the updated coarse domain at points A-D (see Figure 6.4) and results generated show the accuracy of the model with this interpolation technique does not reach the level of accuracy achieved by the average interpolation technique.

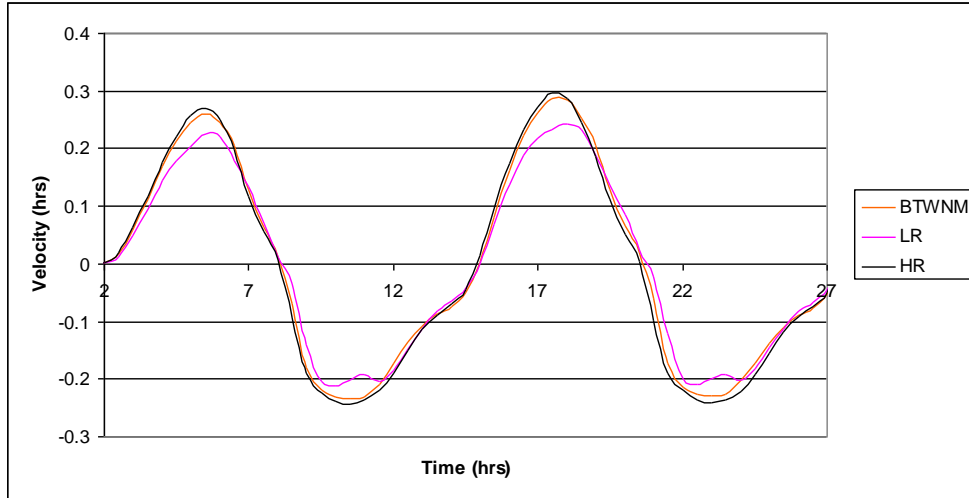


Figure 6: 41 Time history analysis of point A for BTWNM\_SHAP.

Table 6: 40 Peak flood and peak ebb velocities of point A for BTWNM\_SHAP.

Point A	Peak flood velocity (m/s)	% difference	Peak ebb velocity (m/s)	% difference
High resolution (HR)	0.297	-	-0.241	-
Low resolution (LR)	0.2338	-21.27%	-0.2017	-16.3%
BTWNM	0.2863	-3.6%	-0.228	-5.39%



Figure 6: 42 Time history analysis of point B for BTWNM\_SHAP.

Table 6: 41 Peak flood and peak ebb velocities of point B for BTWNM\_SHAP.

Point B	Peak ebb velocity (m/s)	% difference	Peak flood velocity (m/s)	% difference
High resolution (HR)	-0.3101	-	0.2306	-
Low resolution (LR)	-0.3111	+0.32%	0.2563	+11.14%
BTWNM	-0.311	+0.29%	0.2251	--2.3%

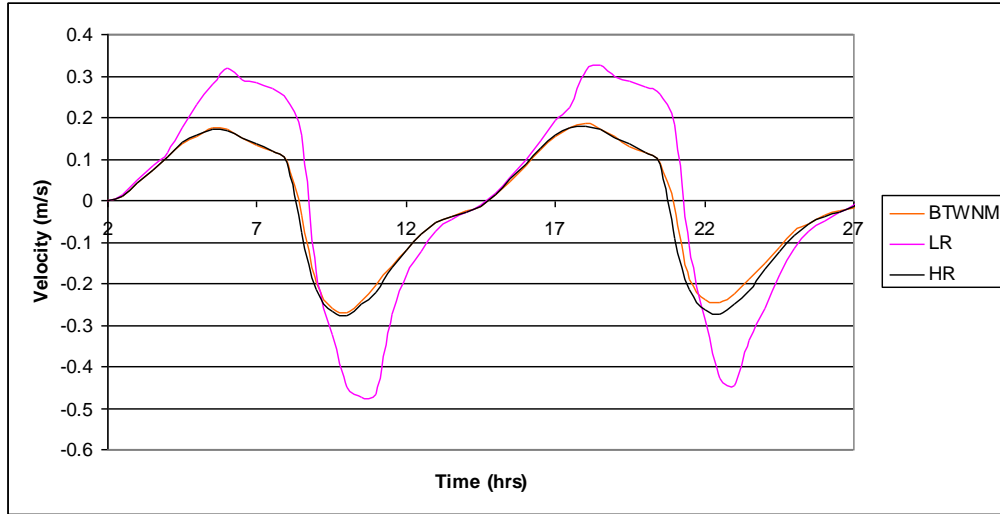


Figure 6: 43 Time history analysis of point C for BTWNM\_SHAP.

Table 6: 42 Peak flood and peak ebb velocities of point C for BTWNM\_SHAP.

Point C	Peak ebb velocity (m/s)	% difference	Peak flood velocity (m/s)	% difference
High resolution (HR)	-0.2786	-	0.1804	-
Low resolution (LR)	-0.4486	+61.0%	0.3263	+80.87%
BTWNM	-0.2453	-11.95%	0.1845	+2.27%

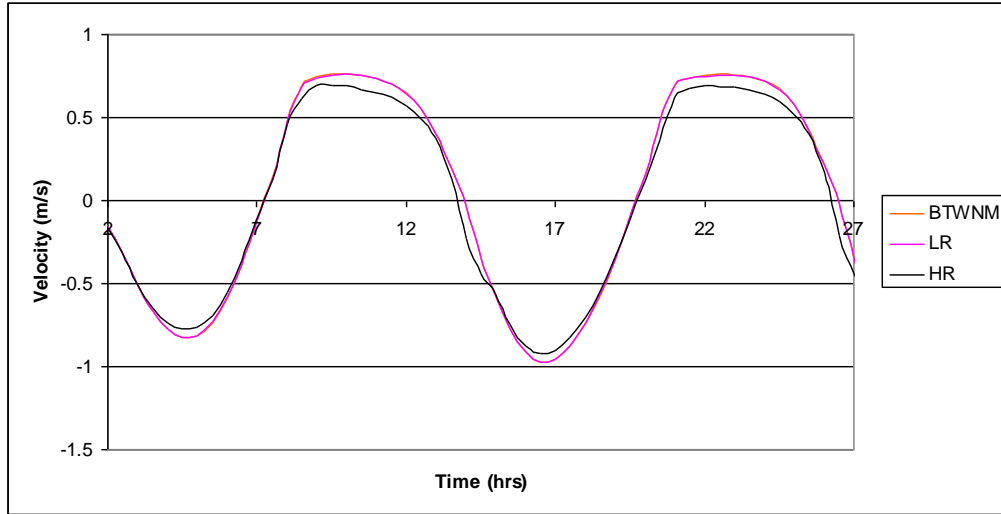


Figure 6: 44 Time history analysis of point D for BTWNM\_SHAP.

Table 6: 43 Peak flood and peak ebb velocities of point D for BTWNM\_SHAP.

Point D	Peak ebb velocity (m/s)	% difference	Peak flood velocity (m/s)	% difference
High resolution (HR)	-0.9172	-	0.6944	-
Low resolution (LR)	-0.9694	+5.7%	0.7578	+9.13%
BTWNM	-0.9711	+5.8%	0.7588	+9.27%

The accuracy of model in the nested domain was also analysed and results shown in Figure 6.45. Time history analysis showed an increase in the performance of the model on the ebb tide, with an increase in accuracy of 3% in relation to the average interpolation model BTWNM\_IV.

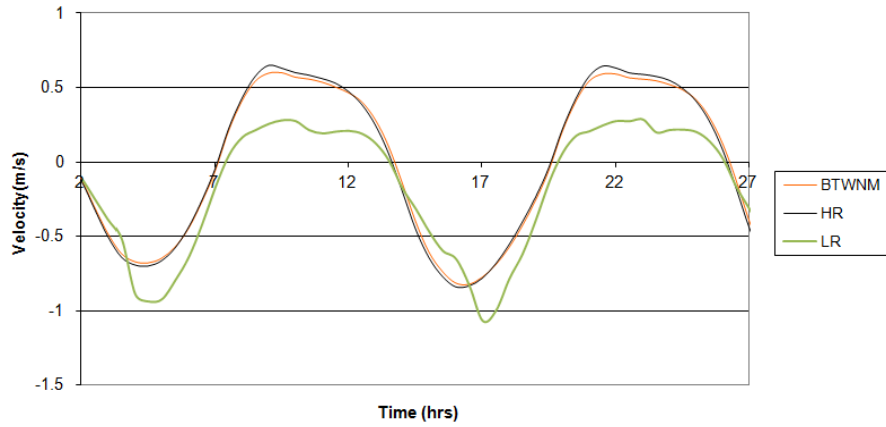


Figure 6: 45 Time history analysis of point E for BTWNM\_SHAP.

Table 6: 44 Peak flood and peak ebb velocities of point E for BTWNM\_SHAP.

Point E	Peak ebb velocity (m/s)	% difference	Peak flood velocity (m/s)	% difference
High resolution (HR)	-0.8379	-	0.6444	-
Low resolution (LR)	-1.0675	+27.4%	0.2848	-55.8%
BTWNM	-0.8256	-1.4%	0.5899	-8.45

### 6.3.3 BTWNM\_FULLLW

Figure 6.46-6.47 illustrates the results for the BTWNM\_FULLLW model containing the fully weighted interpolation technique for the conservation of momentum, and results generated show the conservation between the nested domain and updated coarse domain is of a higher standard in relation to the Shapiro and copy interpolation technique but did not reach the accuracy of the average technique with a reduction in consistency of 0.3%.

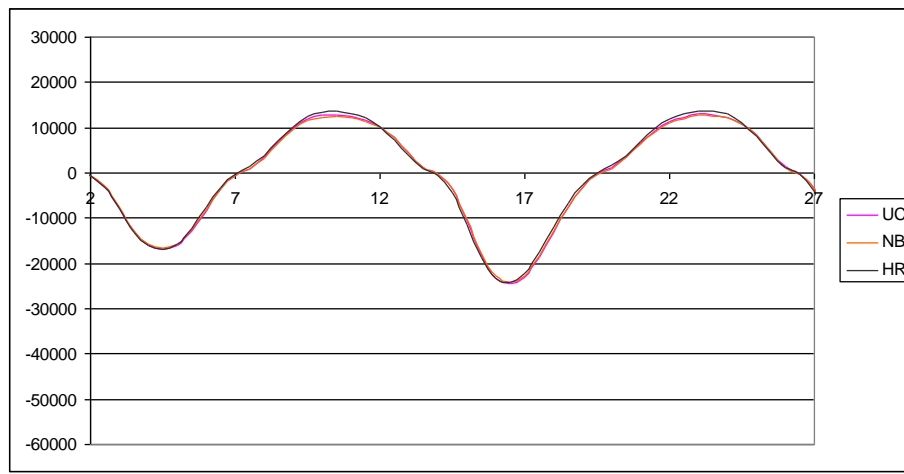


Figure 6: 46 Momentum fluxes across the boundary for BTWNM\_FULLLW

Table 6: 45 Peak ebb and peak flood momentum flux across the nested boundary for BTWNM\_FULLLW

	Peak ebb momentum flux (kN/m)	% difference	Peak flood momentum flux (kN/m)	% difference
High resolution (HR)	-24277.2	-	13724.28	-
Nested boundary (NB)	-24189.2	-0.36%	12707.43	-7.4%
Updates Coarse (UC)	-24608.4	-1.36%	13020.97	-5.12%

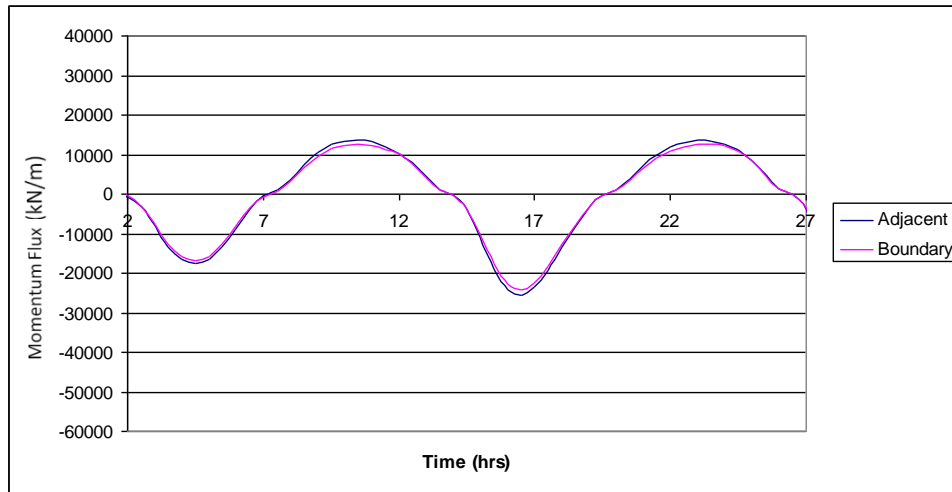


Figure 6: 47 Nested grid momentum fluxes across the boundary cells and cells adjacent to the boundary for BTWNM\_FULLW

Table 6: 46 Peak ebb and peak flood momentum for the propagation into the nested domain for BTWNM\_FULLW

	Peak ebb momentum flux (kN/m)	Peak flood momentum flux (kN/m)
Boundary	-24189.2	12707.43
Adjacent	-25560.7	13624.43

Figure 6.48-6.51 illustrates the results for the BTWNM\_FULLW model for the updated coarse domain. The results indicate the accuracy of the model reached approximately the same level of accuracy in relation to the BTWNM\_IV model in the feedback interface at points A and B (see Figure 6.4), however, the model does not reach the same level of accuracy outside the feedback interface at points C-D.

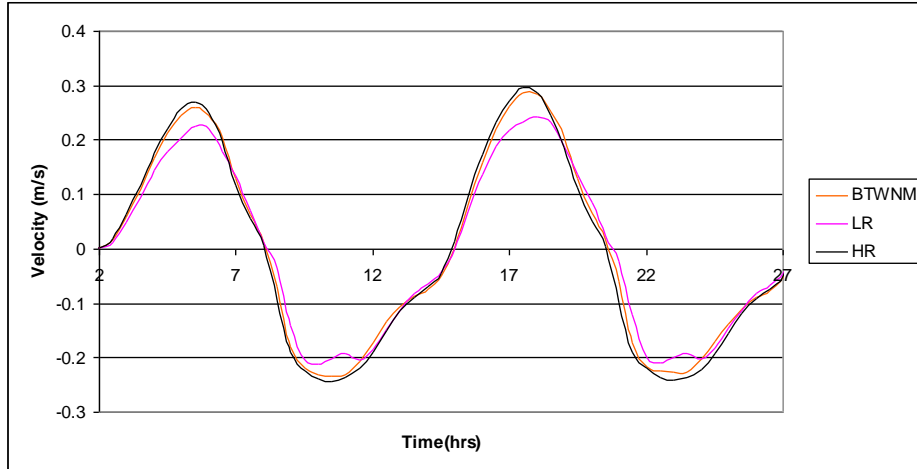


Figure 6: 48 Time history analysis of point A for BTWNM\_FULLW.

Table 6: 47 Peak flood and peak ebb velocities of point A for BTWNM\_FULLW.

Point A	Peak flood velocity (m/s)	% difference	Peak ebb velocity (m/s)	% difference
High resolution (HR)	0.297	-	-0.241	-
Low resolution (LR)	0.2338	-21.2%	-0.2017	-16.3%
BTWNM	0.2858	-3.77%	-0.2261	-6.18%

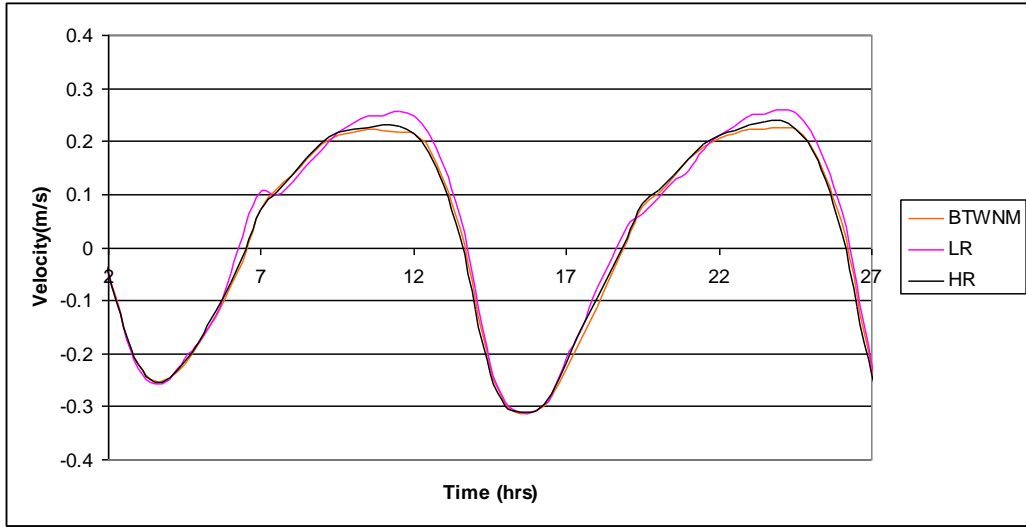


Figure 6: 49 Time history analysis of point B for BTWNM\_FULLW.

Table 6: 48 Peak flood and peak ebb velocities of point B for BTWNM\_FULLW.

Point B	Peak ebb velocity (m/s)	% difference	Peak flood velocity (m/s)	% difference
High resolution (HR)	-0.3101	-	0.2391	-
Low resolution (LR)	-0.3111	+0.32%	0.261	+9.1%
BTWNM	-0.3116	+0.48%	0.2273	-4.9%

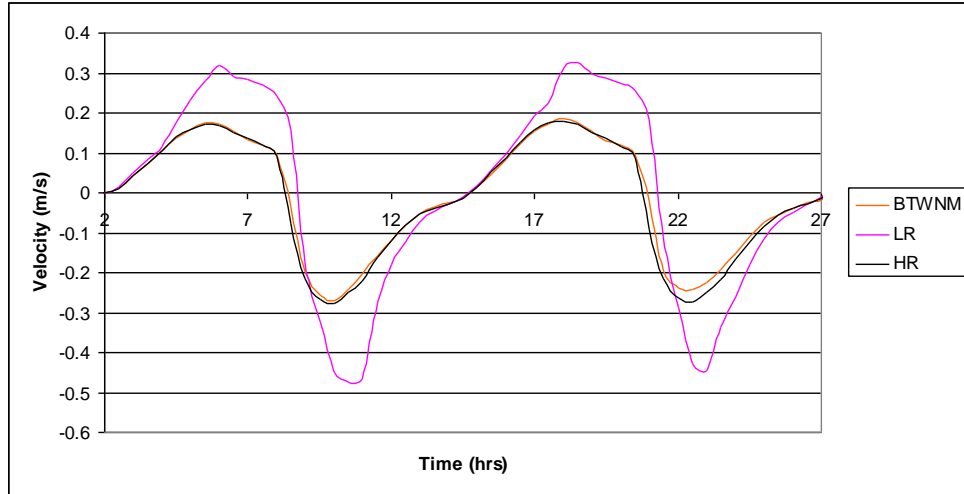


Figure 6: 50 Time history analysis of point C for BTWNM\_ FULLW.

Table 6: 49 Peak flood and peak ebb velocities of point C for BTWNM\_ FULLW.

Point C	Peak ebb velocity (m/s)	% difference	Peak flood velocity (m/s)	% difference
High resolution (HR)	-0.2786	-	0.1804	-
Low resolution (LR)	-0.4486	+61.01%	0.3263	+80.8%
BTWNM	-0.2424	+12.9%	0.1845	+2.27%

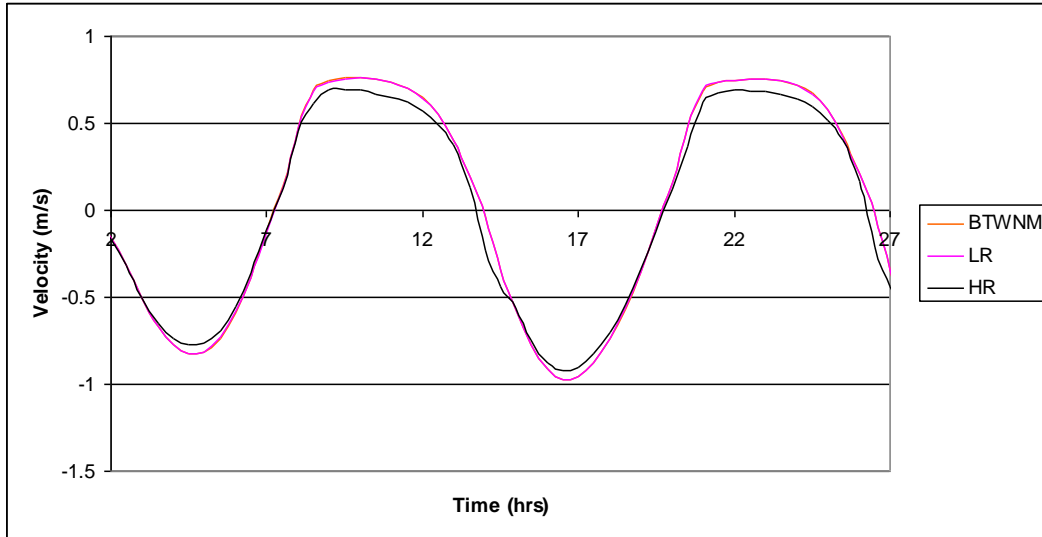


Figure 6: 51 Time history analysis of point D for BTWNM\_FULLW.

Table 6: 50 Peak flood and peak ebb velocities of point D for BTWNM\_FULLW.

Point D	Peak ebb velocity (m/s)	% difference	Peak flood velocity (m/s)	% difference
High resolution (HR)	-0.9172	-	0.6944	-
Low resolution (LR)	-0.9694	+5.69%	0.7578	+9.12%
BTWNM	-0.9698	+5.73%	0.7557	+8.8%

Figure 6.52 shows the result generated in the nested domain at point E (see Figure 6.9) and illustrates a minimal increase in accuracy on the ebb tide and a decrease on the flood tide in relation to the BTWNM\_IV model.

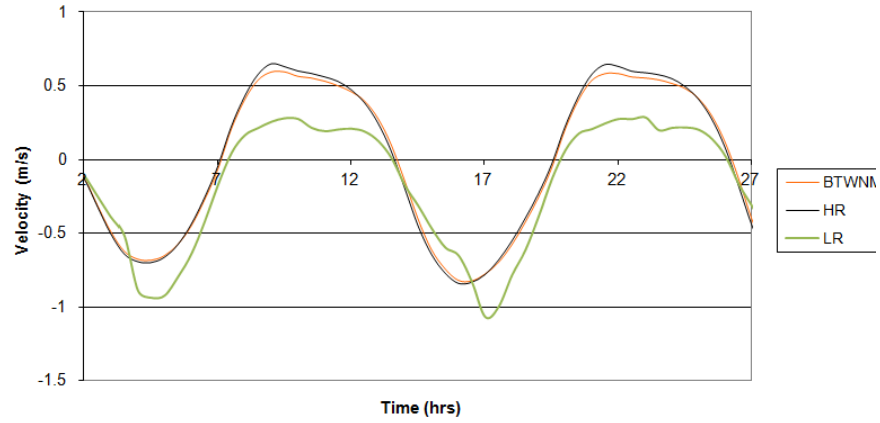


Figure 6: 52 Time history analysis of point E for BTWNM\_ FULLW.

Table 6: 51 Peak flood and peak ebb velocities of point E for BTWNM\_ FULLW.

Point E	Peak ebb velocity (m/s)	% difference	Peak flood velocity (m/s)	% difference
High resolution (HR)	-0.8379	-	0.6444	-
Low resolution (LR)	-1.0675	+27.4%	0.2848	-55.8%
BTWNM	-0.8228	-1.8%	0.5859	-9.07%

## 6.4 SUMMARY AND CONCLUSIONS

During the second stage of development of the BTWNM, investigations were undertaken to determine a suitable feedback operator, which contains an appropriate feedback condition and interpolation technique. The optimum feedback operator was identified as one that contained a Dirichlet feedback condition with an average interpolation procedure.

Phase I of the model development incorporated the simplest form of the feedback condition, due to its ease of implementation. Results generated were of a high standard; however, literature has shown that wave reflection can be produced with this form for feedback condition. An average interpolation technique was also employed due to its common appearance in nesting modelling techniques.

Alternative feedback conditions and interpolation techniques were implemented into the two-way nested model and assessed for their effect on the models performance to conserve momentum and the ability of the nested domain and the coarse domain to interact with each other.

The feedback conditions were initially investigated. Three different types of feedback conditions were assessed for accuracy: 1) Dirichlet, 2) momentum flow relaxation scheme and 3) kinetic energy flow relaxation scheme. It was found the momentum flow relaxation scheme with a variable feedback prescription of velocities and elevations alone and an average interpolation technique reduced the accuracy of the models performance. The conservation of momentum between NB and UC decreased by 0.14% in this model, relative to the BTWNM\_IV model containing a Dirichlet condition. Analysing the performance of the model in the updated coarse domain it was found that the effects of the momentum relaxation scheme on model performance were significant, with a reduction in accuracy at some points of 54%. This decrease in performance in the updated coarse domain resulted from a lack of data being passed from the nested domain, therefore, a variable feedback prescription similar to the BTWNM\_I model was introduced. Results generated showed an increase in the model's performance in the updated coarse domain, however, this increase did not meet the level of accuracy generated with the BTWNM\_IV model containing the Dirichlet feedback condition. However, the performance of the model in the nested domain showed an in-

crease in accuracy of 4% in relation to the BTWNM\_IV model containing the Dirichlet feedback condition.

Similar analysis was performed with the kinetic flow relaxation scheme. The scheme was initially implemented into a model containing a variable feedback prescription similar to the BTWNM\_IV model. The performance of the model to conserve momentum was analysed and showed to function adequately with a small difference in momentum fluxes between NB and UC. However, the performance of the model in the updated coarse domain did not reach the level of accuracy generated by the model containing the Dirichlet condition or the momentum flow relaxation condition. This scheme was also introduced into a model containing a variable feedback prescription similar to the BTWNM\_I model. The performance of the model increased but did not reach the same level of accuracy generated with the momentum relaxation scheme or the Dirichlet condition.

Interpolation techniques were also investigated to assess their effects on the performance of the model. Four different interpolation techniques were assessed: 1) average, 2) direct copy, 3) Shapiro and 4) fully weighted. It was found the average interpolation scheme gave the highest level of model performance. The performance of the model containing the direct copy interpolation technique in the updated coarse domain was considerably high in the area directly overlaid with the nested domain (feedback area), however, outside the feedback interface model accuracy did not reach the same level achieved by the average interpolation scheme. Momentum fluxes at the boundary of the nested domain also showed a reduction in consistency between NB and UC.

The introduction of the Shapiro interpolation technique generated a reduction in the level of momentum conservation between NB and UC across the nested boundary interface. The performance of the model in the updated coarse domain outside the feedback interface increased in accuracy in relation to the direct copy technique, however did not reach the same level as the average interpolation technique. The fully weighted interpolation scheme produced results that indicated the accuracy of the model reached approximately the same level of accuracy in relation to the BTWNM\_IV model in the overlapping nested region; however, it did not reach the same level of accuracy outside the nested region.

The findings from this chapter showed that the two-way nested model containing a variable prescription of velocities and elevation at the feedback interface, with an average interpolation technique and a Dirichlet feedback condition simulated the most accurate model solution. This approach had the advantage of enabling the conservation of momentum and the effective transmission of data to the coarse domain from the nested domain to insure the highest level of model performance.

# CHAPTER 7: DEVELOPMENT OF TTWNM

## 7.1 INTRODUCTION

The development of the BTWNM was the first of two stages in the generation of a two-way nested model with the incorporation of tidal turbine farms (TTWNM). The second stage of the development was the incorporation of advanced features into the existing BTWNM to enable the simulation of tidal turbine farms. This chapter outlines the development undertaken to incorporate the effects of energy extraction by tidal turbine farms into the BTWNM with the use of the Linear Momentum Actuator Disc Theory (LMADT) (Houlsby 2008).

The TTWNM was applied to the Shannon Estuary and tidal turbine farms of different densities were applied to a suitable site. The model was initially run to show the hydrodynamics of the estuary without the incorporation of tidal turbines. The model was then run with different density turbine fields and the results obtained were then compared to identify possible environmental impacts that could be generated from the inclusion of tidal turbine farms. Results generated from the TTWNM were tested against a high resolution single grid model to assess the models performance and identify changes in the tidal regime with the extraction of energy by tidal turbines.

## 7.2 TURBINE REPRESENTATION

Research undertaken by Houlsby (2008) in relation to the Linear Momentum Actuator Disc Theory (LMADT) was used as the basis for incorporating the tidal turbines into the BTWNM (Houlsby 2008). This theory involves using an actuator disc to represent a turbine rotor, which is enclosed in a stream tube, to extract energy and momentum from an open channel (Burton 2001). Figure 7.1 represents the LMADT in an open channel flow, which contains five zones: (1) far upstream of turbine, (2) immediately upstream of the turbine, (3) immediately downstream of the turbine, (4) zone where the turbine wake merges with the by-pass flow and (5) zone where pressure becomes uniform.

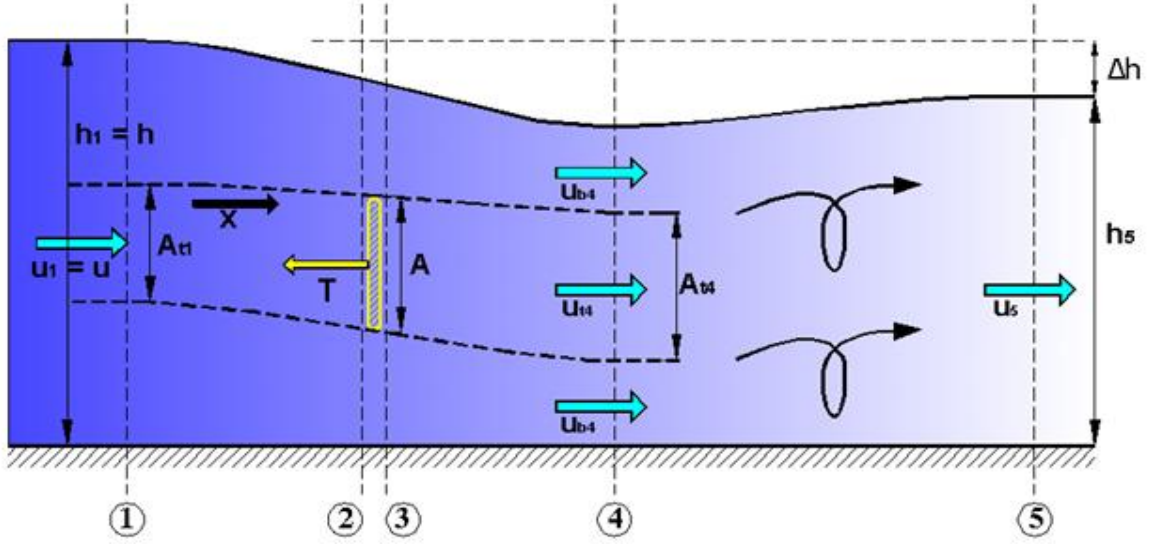


Figure 7: 1 Linear Momentum Actuator Disc Theory in an open channel flow

The area enclosed by lines 2 and 3 experiences a loss of velocity in accordance with work performed by Myers (2012). The merging of this flow with the bypass velocity results in the generation of a wake in an area downstream of the turbine (3 to 4), which is generated to satisfy the conservation of momentum. The extraction of energy also has an effect on the water depth across the turbine of  $\Delta h$  similar to a hydraulic jump.

A turbine induces an equal but opposite thrust force ( $T$ ) on the initially undisturbed flow to comply with Newton's third law. The following equation is used to express the thrust force ( $T$ ):

$$T = \frac{1}{2} \rho u^2 A C_T \quad (7.1)$$

where  $\rho$  represents the fluid density,  $u$  the current velocity,  $A$  the area of the turbine (represented by an actuator disc) and  $C_T$  is the coefficient of thrust that is calculated as follows:

$$C_T = (\beta_4^2 - \alpha_4^2) \quad (7.2)$$

with  $\beta_4$  being the bypass flow velocity coefficient (usually  $>1$ ) and the turbine wake coefficient is  $\alpha_4$  (usually  $<1$ ).

The turbine thrust force was incorporated into the momentum equation as a sink term, to simulate flow through turbines. Equation 7.3 shows the amended x-direction momentum

equation with the inclusion of the sink term highlighted in yellow for the incorporation of tidal turbines (a similar modification is performed on the y-direction momentum equation).

$$\frac{\partial q_x}{\partial t} + \beta \frac{\partial U q_x}{\partial x} + \frac{\partial U q_y}{\partial y} = f q_y + gH \frac{\partial \zeta}{\partial x} + \frac{\tau_{xw}}{\rho} + \frac{\tau_{xb}}{\rho} + 2 \frac{\partial}{\partial x} \varepsilon H \frac{\partial U}{\partial x} + \frac{\partial}{\partial y} \varepsilon H \frac{\partial U}{\partial y} + \frac{\partial v}{\partial x} + \frac{F_{Tx}}{\rho}$$

(7.3)

with the axial thrust per unit area in the x-direction generated by the turbine represented with  $F_{Tx}$ . The following equation represents the total magnitude of the axial thrust induced by the turbines on the flow per unit area of a grid cell:

$$F_T = \frac{T}{\Delta x \Delta y} = \frac{1}{2} \frac{1}{\Delta x \Delta y} C_T \rho A U_{tot}^2$$

(7.4)

where  $U_{tot}$  is the magnitude of the total velocity perpendicular to the sweep area of the turbine. The coefficient of thrust is a function that is generated in relation to the turbine design. It is dependent on the number and geometry of the turbine blades. Research undertaken by Bahaj (2007) and Ahmadian (2012) have assumed a constant value of 0.8 and 1 respectively. The turbine design used for this research is a hypothetical design for which test data was not available, therefore a value of 0.9 was used for  $C_T$ .

The model assumes that the turbines used have the ability to rotate and align themselves in an orientation that is always perpendicular to the flow to enable the maximum energy extraction to be obtained. The following equations represent the axial thrust force generated by the turbine on the flow in the x and y direction, with  $\theta$  representing the angle the turbine axis makes in the positive y-direction:

$$F_{Tx} = F_T \times |\sin(\theta)| \times \text{sign}(U)$$

(7.5)

$$F_{Ty} = F_T \times |\cos(\theta)| \times \text{sign}(V)$$

(7.6)

with  $\text{sign}(u)$  and  $\text{sign}(v)$  being sign convections that take into account the change in tidal flow, which take the value of +1 in the positive x and y direction and -1 in the negative direction.

### 7.3 IMPLEMENTATION

The development of the TTWNM required the modification of the existing BTWNM code and the introduction of new code. New code was added to read input data pertaining to the tidal farm specifications. Modification of the existing code was required to enable the computational solution to take into account the presence of a tidal turbine farm.

The TTWNM was developed so that it could run as a BTWNM in the absence of tidal turbine farms. Figure 7.2 shows a flowchart of the TTWNM and Table 7.1 lists the sections of code that were introduced into the BTWNM for the representation of a turbine farm.

Table 7. 1 Sections of code added to BTWNM to enable the introduction of tidal turbines

Program section	Modifications and functions
FILINP	Read turbine farm input data
MARTURBINIT	Identify Turbine farm and calculate the area of the turbine, in coarse domain.
MARTURB	Calculation of the parameters required for the sink term in the momentum equation, for the coarse domain.
HYDMODX	Introduction of sink term into x-direction momentum equation, for the coarse domain.
HYDMODY	Introduction of sink term into y-direction momentum equation, for the coarse domain.
MARTURBINIT_F	Identify Turbine farm and calculate the area of the turbine, in fine domain.
MARTURB_F	Calculation of the parameters required for the sink term in the momentum equation, for the fine domain
HYDMODX_F	Introduction of sink term into x-direction momentum equation, for the fine domain.
HYDMODY_F	Introduction of sink term into y-direction momentum equation, for the fine domain.

Subroutines MARTURBINIT and MARTURBINIT\_F were introduced into the model to: identify the density of turbines per grid cell and calculate the cumulative area of the turbines per grid cell. The following equations represent these calculations:

$$NT = \frac{\Delta X^2}{\Delta T S^2} \quad (7.7)$$

$$TA = NT \times \frac{D^2 \pi}{4} \quad (7.8)$$

where  $NT$  represents the number of turbines in a grid cell,  $\Delta TS$  is the spacing between turbines and  $\Delta x$  is the grid spacing. The cumulative area of the turbine per grid cell is  $TA$  and the diameter of the turbine is  $D$ .

Subroutines MARTURB and MARTURB\_F are used in the model to calculate the projected area of the turbine in the x-direction ( $TA_x$ ) and y-direction ( $TA_y$ ). The following equations represent these calculations:

$$\phi = \tan^{-1} \frac{|U|}{|V|} \quad (7.9)$$

$$\alpha = \frac{\pi}{2} - \phi \quad (7.10)$$

$$TA_x = TA \times \sin \alpha \quad (7.11)$$

$$TA_y = TA \times \cos \alpha \quad (7.12)$$

These values are incorporated into the momentum equation to enable a sink term to be generated. This is performed in the coarse model in the HYDMODX and HYDMODY subroutines and in the nested domain in the HYDMODX\_F and HYDMODY\_F subroutines. Equation 7.13 represents the turbine thrust sink term added to the x-direction momentum equation.

$$F_{Tx} = \frac{\frac{\Delta T}{2} \times C_T \times TA_x \times |Q| \times \cos \phi}{4\Delta x \Delta y} \quad (7.13)$$

where  $\Delta t$  is the model time step and  $C_T$  is the thrust coefficient.



Figure 7: 2 Flow chart of TTWNM with new and modified subroutine highlighted in yellow

## 7.4 RESULTS

The Shannon Estuary was identified in a study performed by Sustainable Energy Ireland (SEI 2009) as one of the most suitable sites for tidal energy extraction. The selection of a suitable site for the deployment of the tidal turbine farm was generated by analysing the theoretical power available in the Shannon. The following equation was used to calculate the mean power available (MW) in the estuary (SEI 2009). Assuming the tidal cycle is approximately sinusoidal in nature, the following Fraenkel formula was used for the establishment of the mean power available (MW) in the estuary (Wilson 2007; Denot 2012).

$$P_{mean} = 0.5\rho K_s K_n A V_{(peak)}^3 \quad (7.14)$$

where  $K_s$  is the velocity shape factor,  $K_n$  is the neap/spring factor,  $A (= \Delta x H)$  is the cross sectional area of a grid cell and  $V_{peak}$  is the maximum spring velocity. The Fraenkel formulation allocates a value of 0.424 to  $K_s$  and a value of 0.57 to  $K_n$ . Figure 7.3 shows the resource assessment map for the estuary

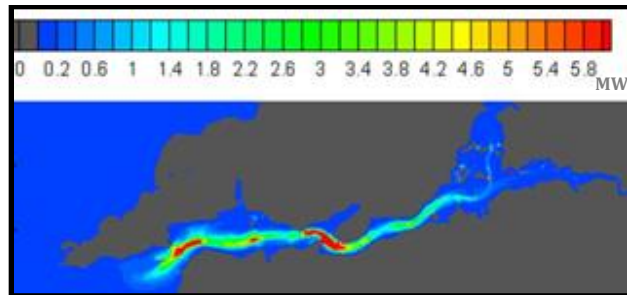


Figure 7: 3 Maximum available power (MW per grid cell) for the Shannon Estuary

The tidal turbines used in the analysis were based on the SeaGen turbine device, which is the first commercially deployed tidal turbine and has a rotor diameter of 16m (Fraenkel 2007). A minimum depth of 20m at low spring water was required for the installation of SeaGen turbines. In practice other factors need to be considered such as proximity to the navigational channel, military zones, sub-marine pipelines and cables. Figure 7.4 shows the area used for the deployment of the turbine farm.

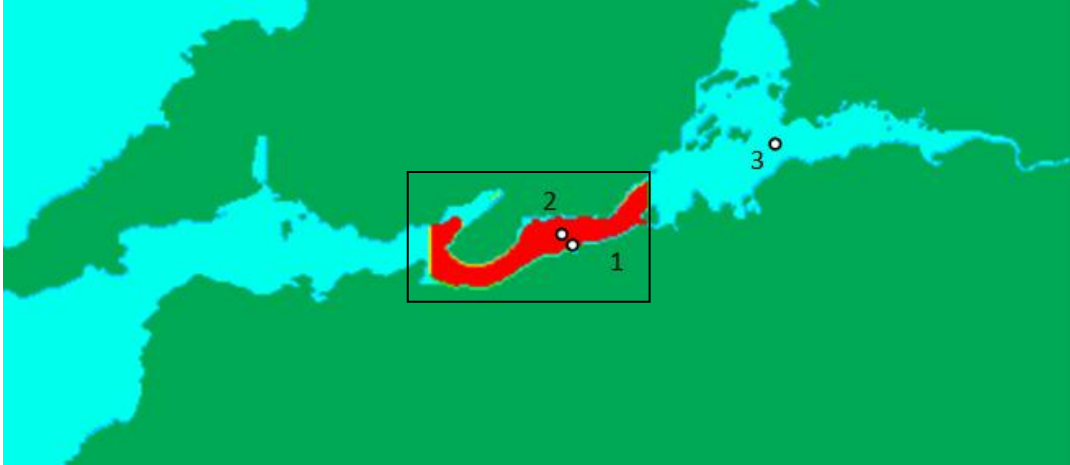


Figure 7: 4 The Shannon Estuary with the extent of the turbine farm highlighted in red and the nested grid position highlighted by the black square.

The spacing between turbines in a turbine farm can have a major effect on the extent of possible changes in the hydrodynamics due to the extraction of energy. Tidal farms of different array configurations were simulated, each containing turbines at different turbine spacing (measured tip to tip) to show the possible impacts. Three fields were generated that contained turbines spaced at 0.5, 2 and 5 rotor diameter spacing.

Time history analysis of velocities at three points (see Figure 7.4) were used to determine the effects of different array configurations, and to also show the ability of the nested model to identify changes in the hydrodynamics with the extraction of energy. A low resolution model was initially run without the inclusion of tidal turbines (SDM); this low resolution model was then run with the inclusion of turbine farms of different densities (LR). Results generated were compared with results from an equivalent high resolution single grid model (HR) and the TTWNM with a high resolution nested region highlighted in Figure 7.4, both containing tidal farms of different configurations.

Results generated for the high density turbine farm containing turbines of 0.5 diameter spacing are shown in Figures 7.5-7.7, with point 1 located outside the turbine farm, point 2 located inside the turbine farm and point 3 located far upstream of the turbine farm. The percentage change in peak ebb and peak flood of the LR model, the HR model and the TTWNM relative to the SDM model are tabulated in Tables 7.2-7.4.

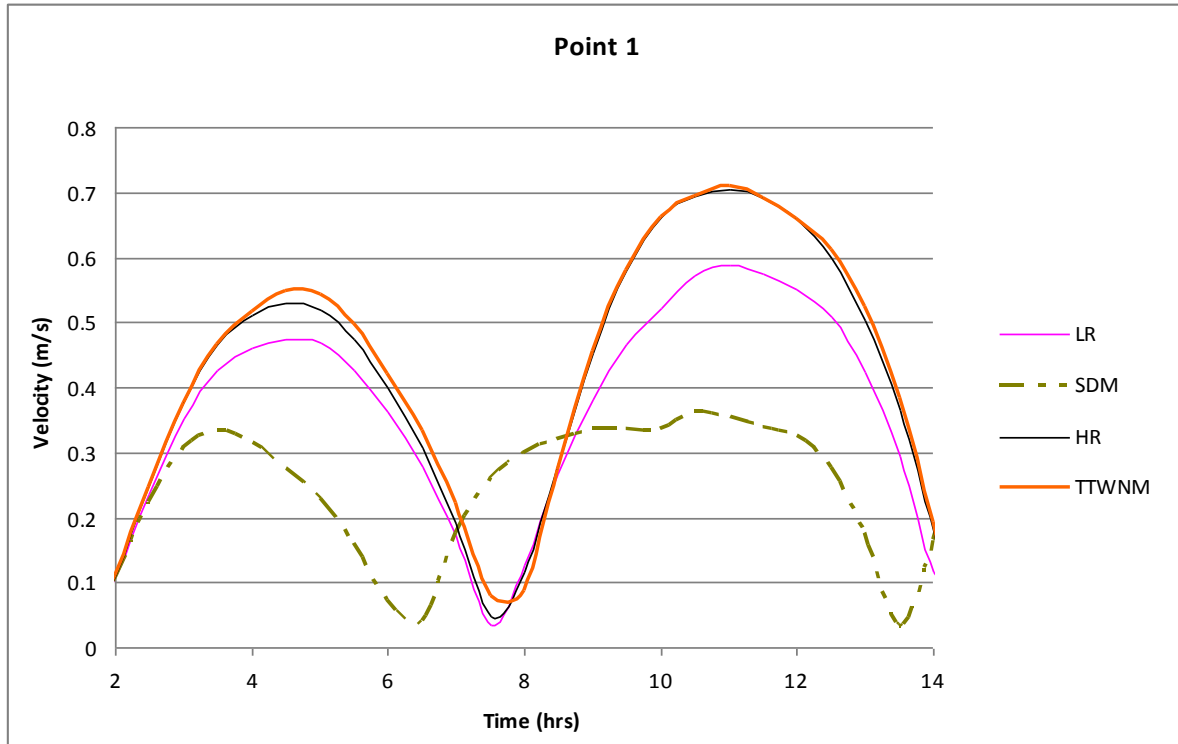


Figure 7: 5 Comparisons of velocities at point 1 outside the turbine farm for 0.5 rotor spacing

Table 7. 2 Percentage change in peak ebb and peak flood velocities at point 1 for 0.5 rotor spacing.

	Peak ebb velocity (m/s)	% change	Peak flood velocity (m/s)	% change
SDM	0.334	-	0.362	-
LR	0.475	+42.23%	0.588	+62.51%
TTWNM	0.548	+64%	0.708	+95.8%
HR	0.530	+59%	0.703	+94.39%

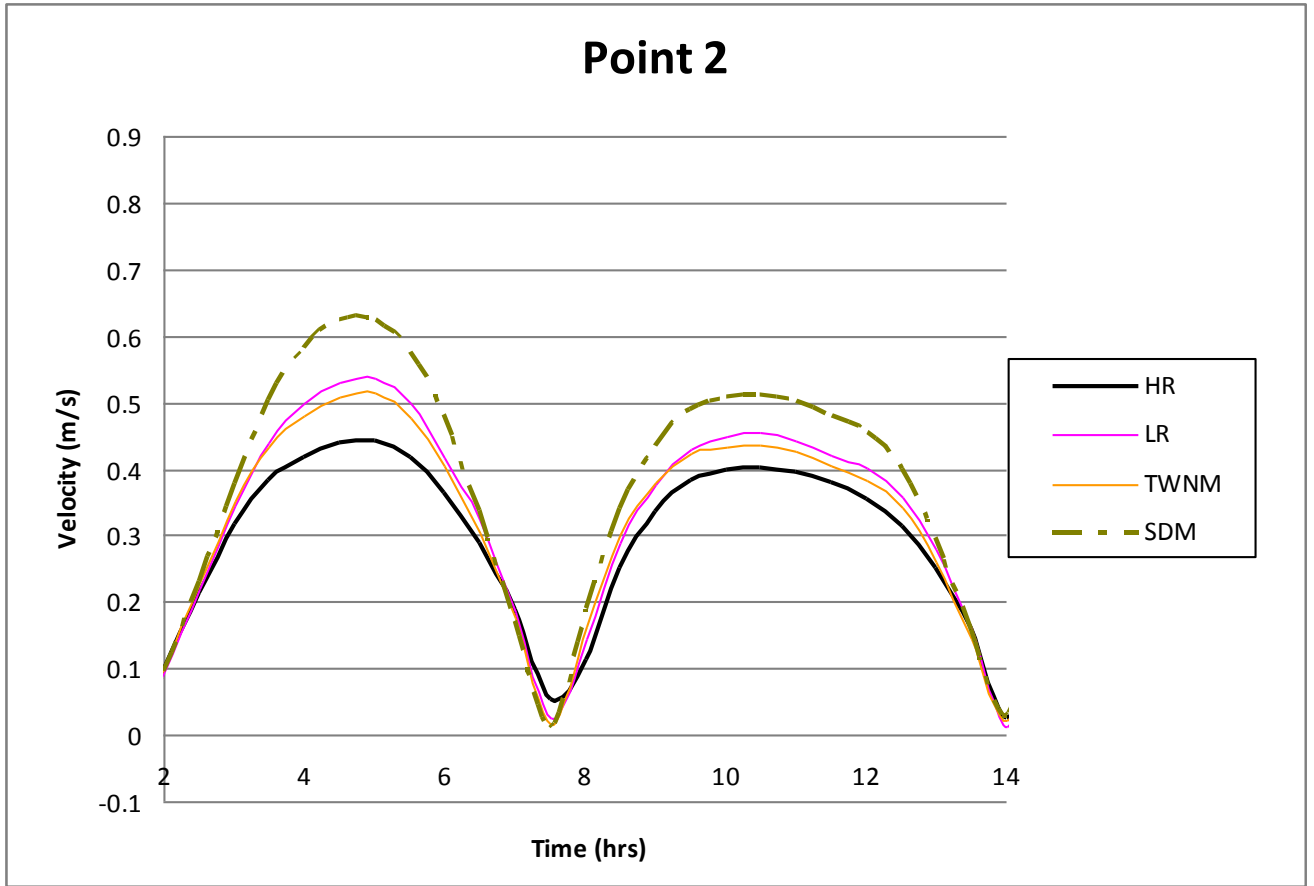


Figure 7: 6 Comparisons of velocities at point 2 inside the turbine farm for 0.5 rotor spacing

Table 7. 3: Percentage change in peak ebb and peak flood velocities at point 2 for 0.5 rotor spacing.

	Peak ebb velocity (m/s)	% change	Peak flood velocity (m/s)	% change
SDM	0.624	-	0.512	-
LR	0.535	-14.26%	0.455	-11.13%
TTWNM	0.514	-17.62%	0.430	-16.01%
HR	0.443	-29%	0.410	-19.92%

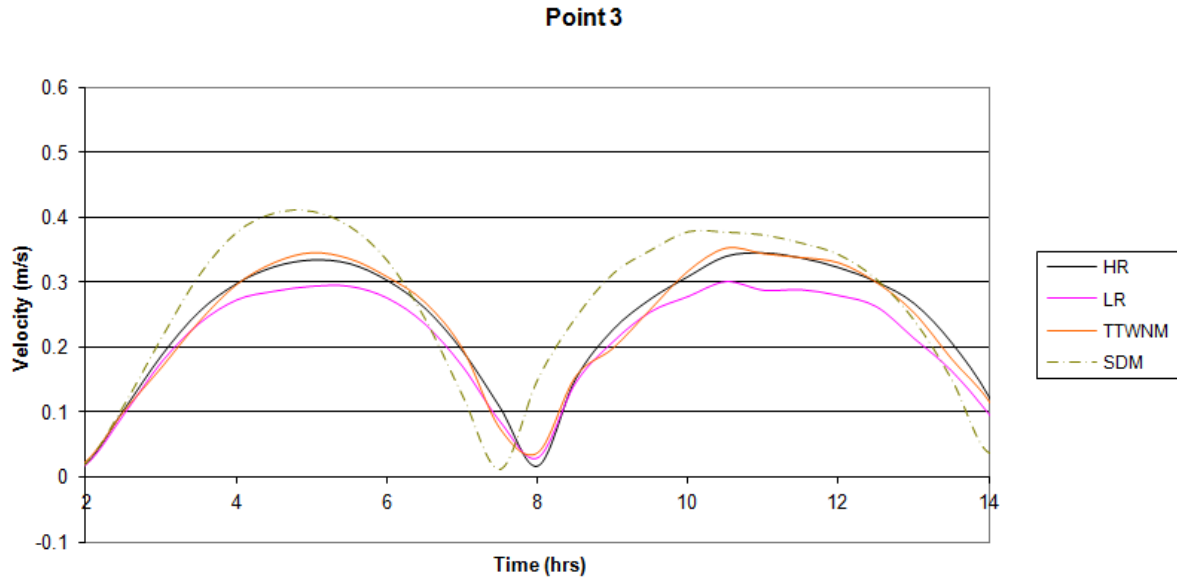


Figure 7: 7 Comparisons of velocities at point 3 upstream of the turbine farm for 0.5 rotor spacing

Table 7. 4 : Percentage change in peak ebb and peak flood velocities at point 3 for 0.5 rotor spacing.

	Peak ebb velocity (m/s)	% change	Peak flood velocity (m/s)	% change
SDM	0.410	-	0.377	-
LR	0.290	-29.26%	0.299	-30.75%
TTWNM	0.340	-17.07%	0.343	-7.8%
HR	0.335	-18.2%	0.345	-7.8%

The presence of the high density turbine farm had an acceleration effect on the currents at point 1 located outside the turbine farm. The high resolution model and the TTWNM both simulated a more significant velocity change in comparison to the low resolution model. Results generated from TTWNM were shown to be of a high level of accuracy with a 5% dif-

ference at peak ebb and a 1.4% difference at peak flood to the 'correct' high resolution model.

Point 2, located inside the turbine farm, shows a reduction in the velocity with the inclusion of the 0.5 spaced turbine farm. Again, the TTWNM simulated results with a higher level of accuracy in comparison to the LR model.

Upstream of the turbine farm the low resolution model incorrectly identifies a larger reduction in the velocities in comparison to the TTWNM and the high resolution model. The TTWNM results showed a higher level of accuracy, in comparison to the LR model, of approximately 10% at peak ebb and 22% at peak flood.

Figure 7.8 shows a plot of the relative percentage change in velocities in the two-way nested model over a full tidal cycle with the inclusion of a tidal turbine farm with 0.5 rotor spaced turbines. The plot shows there is a significant change in the velocities in the area of the turbine farm, however, changes were also exhibited upstream of the turbine farm especially in the River Fergus area, which contains large expanse of environmentally protected inter-tidal zones.

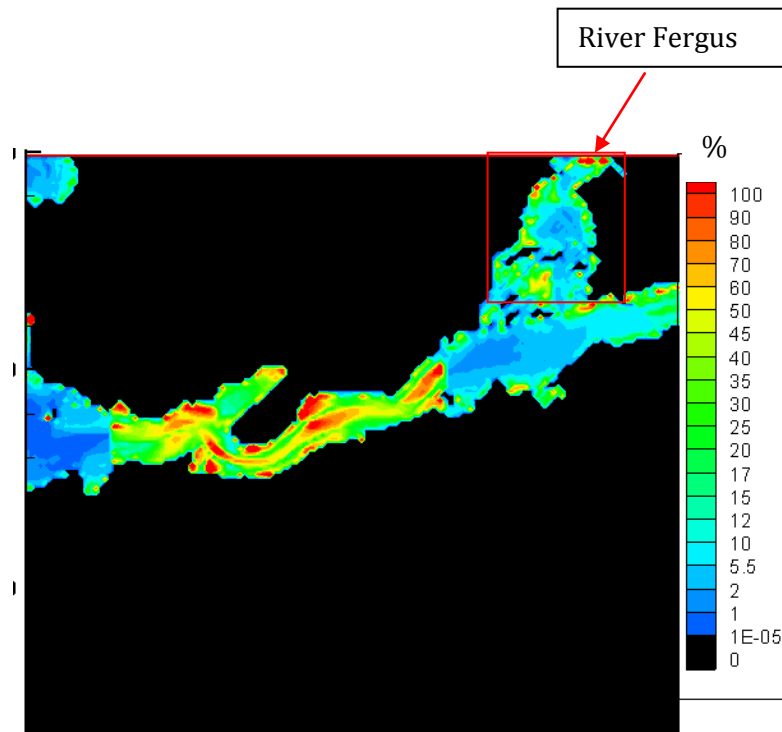


Figure 7: 8 Relative percentage changes in velocities with the inclusion of 0.5 rotor spaced turbine farm.

The four models were run again with the inclusion of a less dense turbine farm with turbine spacing of 2 rotor diameters. Figures 7.9-7.11 show the time history analysis for points 1-3 and the percentage changes are tabulated in Table 7.5-7.7.

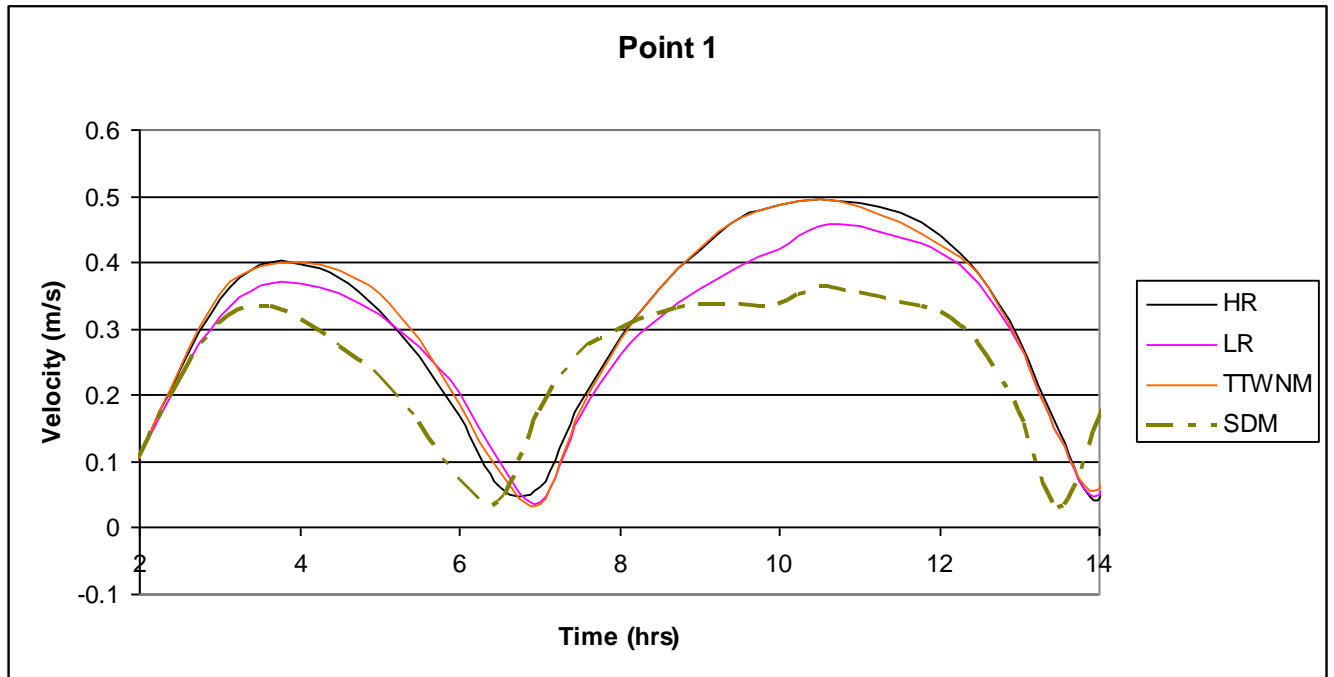


Figure 7: 9 Comparisons of velocities at point 1 outside the turbine farm for 2 rotor spacing

Table 7.5 : Percentage change in peak ebb and peak flood velocities at point 1 for 2 rotor spacing.

	Peak ebb velocity (m/s)	% change	Peak flood velocity (m/s)	% change
SDM	0.334	-	0.362	-
LR	0.360	+7.78%	0.450	+24.3%
TTWNM	0.400	+19.7%	0.494	+36.5%
HR	0.397	+18.8%	0.495	+36.7%

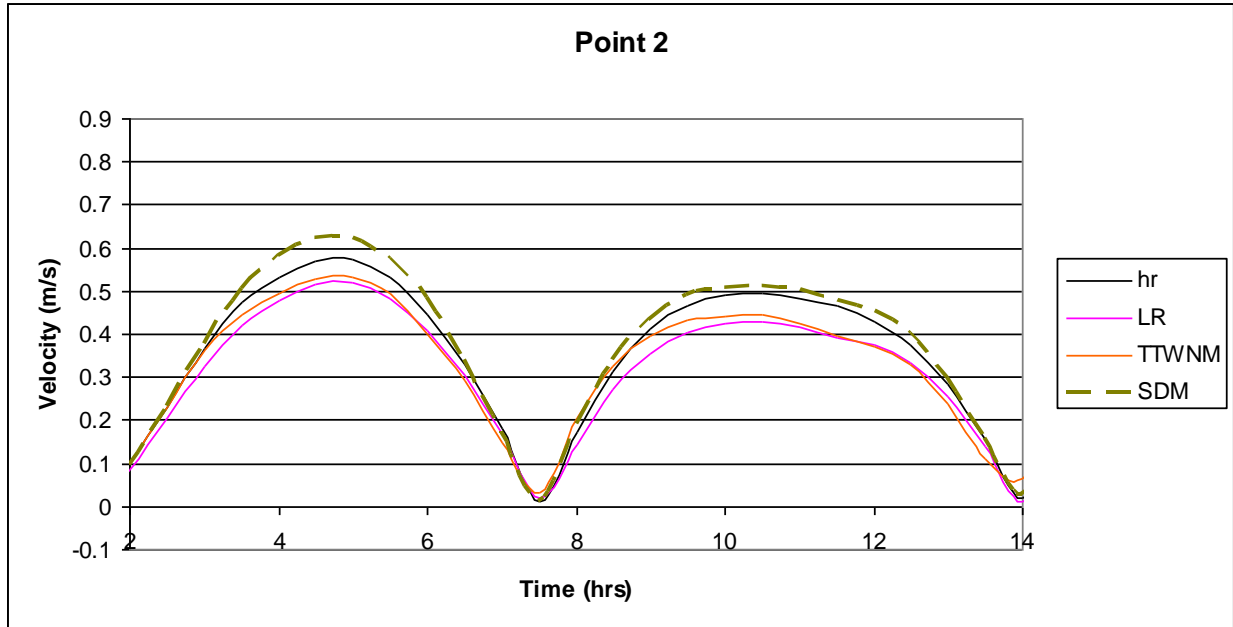


Figure 7: 10 Comparisons of velocities at point 2 inside the turbine farm for 2 rotor spacing

Table 7. 6 Percentage change in peak ebb and peak flood velocities at point 2 for 2 rotor spacing.

	Peak ebb velocity (m/s)	% change	Peak flood velocity (m/s)	% change
SDM	0.624	-	0.512	-
LR	0.520	-16.6%	0.420	-18%
TTWNM	0.540	-13.46%	0.450	-12%
HR	0.570	-8.7%	0.490	-4.3%

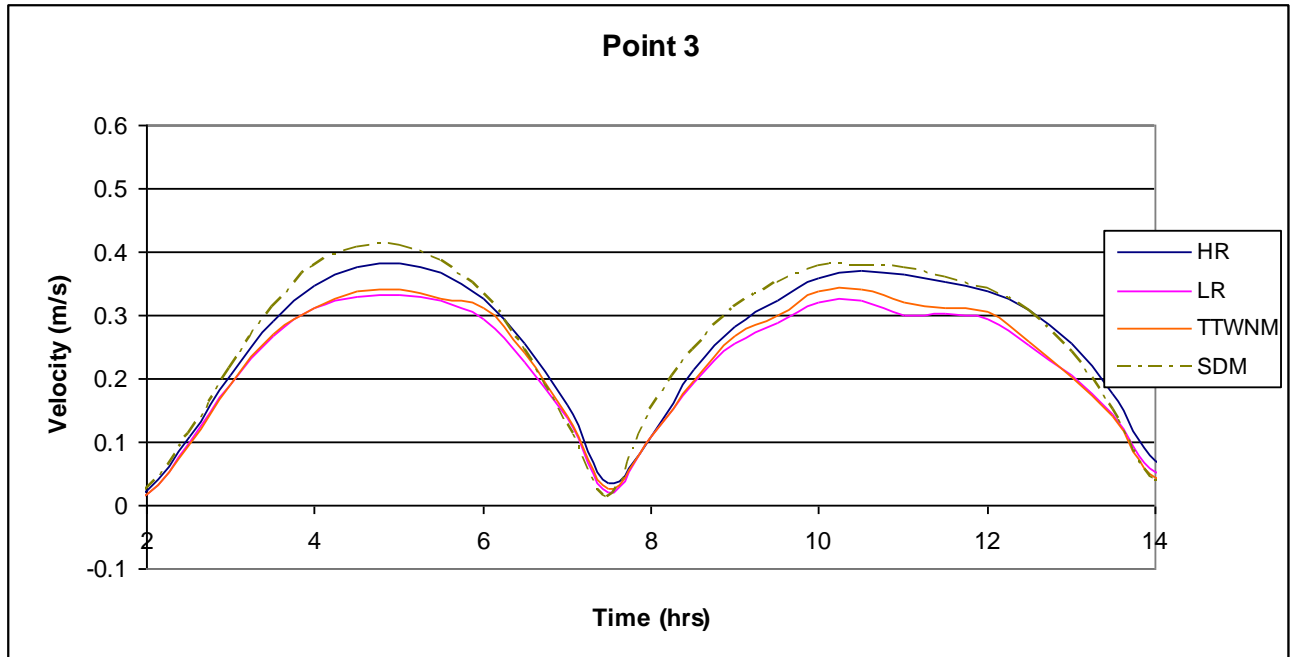


Figure 7: 11 Comparison of velocities at point 3 upstream of the turbine farm for 2 rotor spacing

Table 7. 7 Percentage change in peak ebb and peak flood velocities at point 3 for 2 rotor spacing.

	Peak ebb velocity (m/s)	% change	Peak flood velocity (m/s)	% change
SDM	0.41	-	0.38	-
LR	0.33	-19.51%	0.32	-15.78%
TTWNM	0.35	-14.63%	0.35	-7.89%
HR	0.38	-7.31%	0.37	-3%

Results generated show the changes in the velocities are less significant in comparison to the previous turbine farm. The TTWNM generated a solution with a higher level of accuracy in comparison to the LR model at all points.

Figure 7.12 shows the relative percentage change in the velocities of the two-way nested model with the inclusion of a 2 rotor spaced turbine farm. The illustration shows the changes in velocities inside and outside of the turbine farm are less significant in comparison to the changes with a turbine farm containing 0.5 rotor spaced turbines.

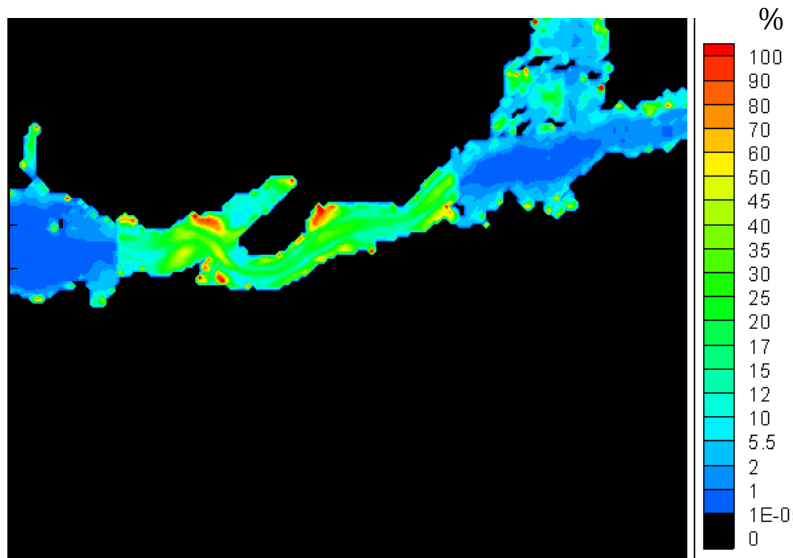


Figure 7: 12 Relative change in velocities in the two-way nested model with the inclusion of turbine farm with 2 rotor spaced turbines

Finally, the four models were run again with the inclusion of a turbine farm with a 5 diameter turbine spacing. Figures 7.13-7.15 show the time history analysis for points 1-3 and tabulated in Table 7.8-7.10. The percentage relative change in velocities in the two-way nested model with the inclusion of a 5 rotor spaced tidal turbine farm are shown in Figure 7.16.

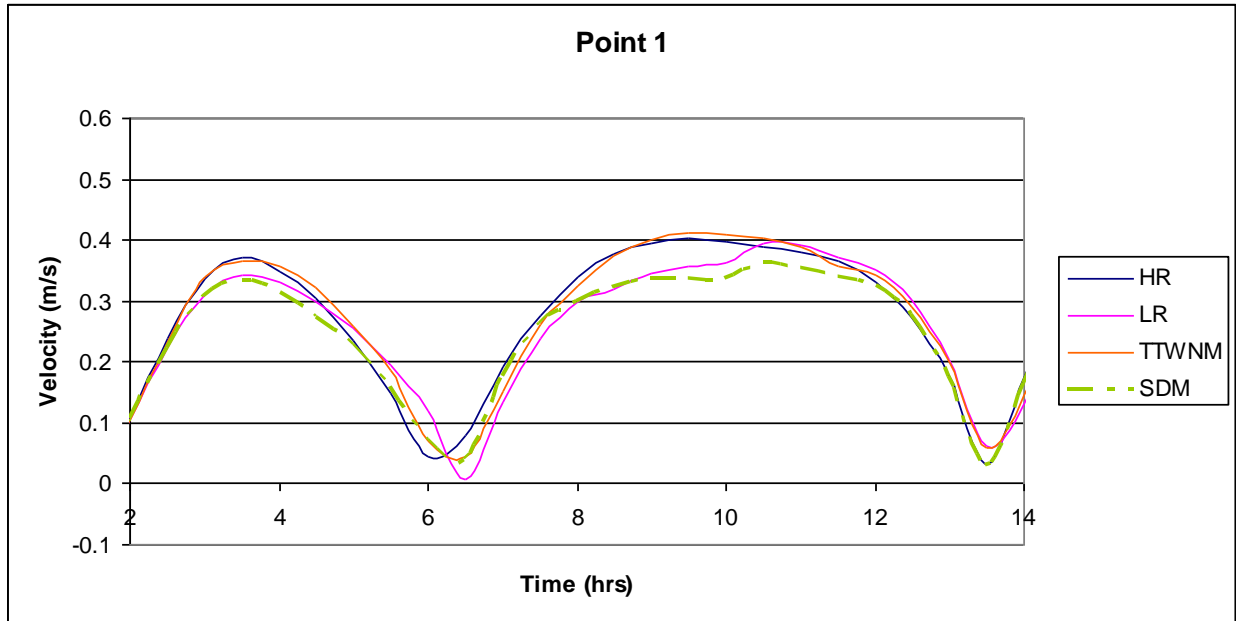


Figure 7: 13 Comparison of velocities at point 1 outside the turbine farm for 5 rotor spacing

Table 7. 8 Percentage change in peak ebb and peak flood velocities at point 1 for 5 rotor spacing.

	Peak ebb velocity (m/s)	% change	Peak flood velocity (m/s)	% change
SDM	0.334	-	0.362	-
LR	0.340	+2.9%	0.390	+7.7%
TTWNM	0.360	+9.5%	0.410	+13.4%
HR	0.370	+11%	0.405	+11.9%

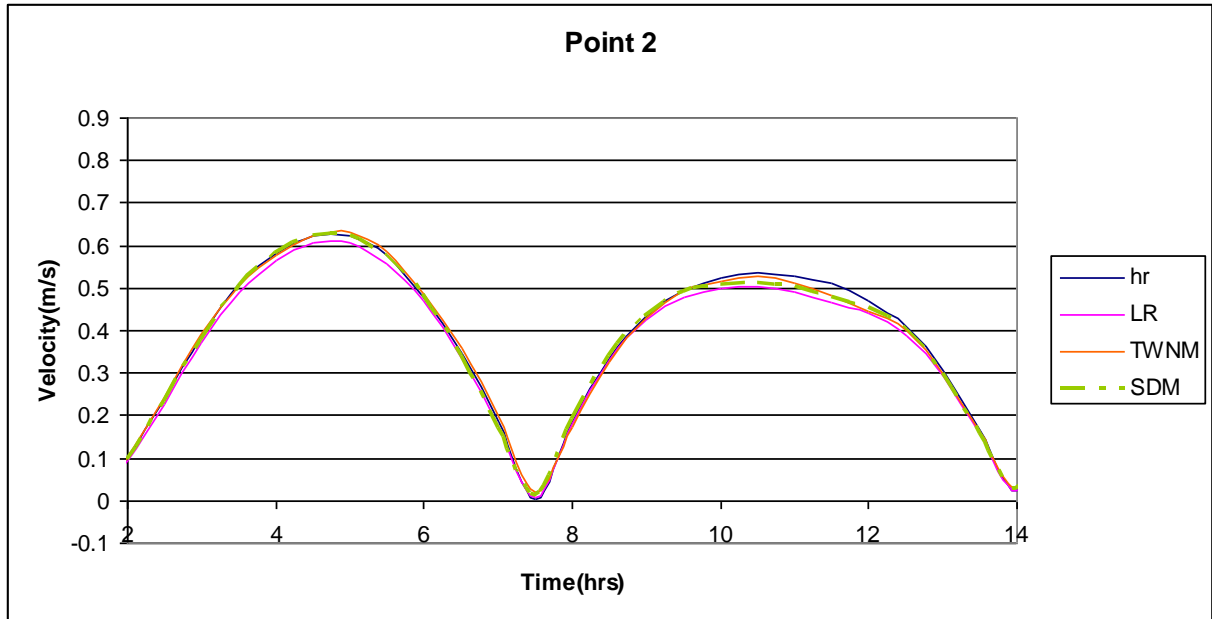


Figure 7: 14 Comparison of velocities at point 2 inside the turbine farm for 5 rotor spacing

Table 7.9 Percentage change in peak ebb and peak flood velocities at point 2 for 5 rotor spacing.

	Peak ebb velocity (m/s)	% change	Peak flood velocity (m/s)	% change
SDM	0.624	-	0.512	-
LR	0.610	-2.24%	0.501	-2.14%
TTWNM	0.629	+0.8%	0.530	+3.5%
HR	0.625	+0.2%	0.534	+4.2%

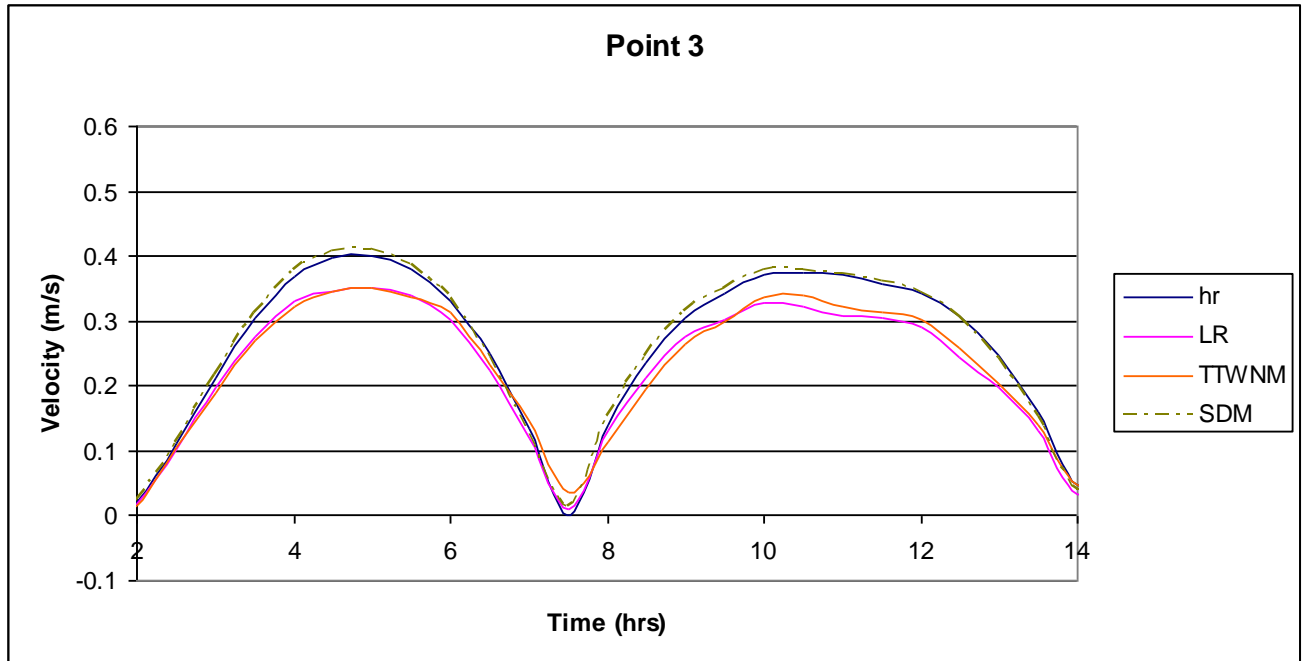


Figure 7: 15 Comparison of velocities at point 3 upstream of the turbine farm for 5 rotor spacing

Table 7. 10 Percentage change in peak ebb and peak flood velocities at point 3 for 5 rotor spacing.

	Peak ebb velocity (m/s)	% change	Peak flood velocity (m/s)	% change
SDM	-0.4089	-	0.3776	-
LR	0.3500	-14.26%	0.3200	-15.3%
TTWNM	0.3519	-13.9%	0.3403	-9.8%
HR	-0.4000	-1.85%	0.3700	-2.1%

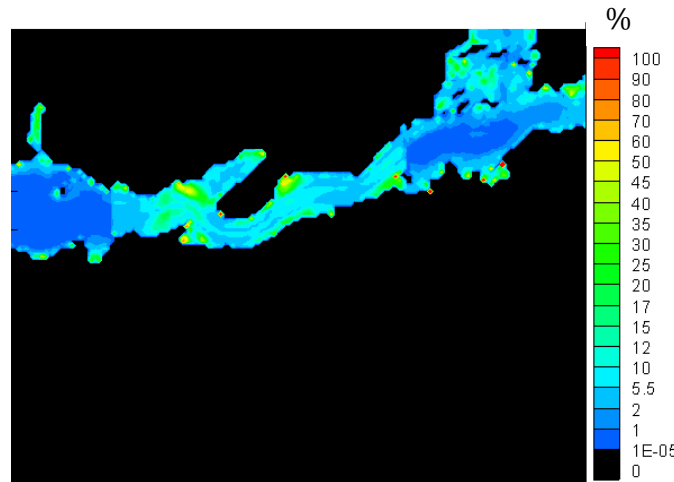


Figure 7: 16 Relative change in velocities in the two-way nested model with the inclusion of turbine farm with 2 rotor diameter spaced turbines

The low density turbine farm with turbines spaced at 5 rotor diameters showed the magnitude of change is less significant in comparison to the higher density farms. The results showed the TTWNM generated a solution that has a higher level of accuracy in comparison to the LR model.

## 7.5 SUMMARY AND CONCLUSION

The deployment of tidal turbine farms in an estuary were shown to effect the hydrodynamics of the estuary in the area of deployment and also upstream of the turbine farm. High density farms were shown to generate the highest distortion in the hydrodynamics. Results showed the two-way nested model can identify hydro-environmental impacts to a greater level of accuracy in comparison to a low resolution model without a high computational cost.

Tidal turbines were introduced into the two-way nested model to get a better understanding of the possible environmental impacts that could be generated from the extraction of energy due to the deployment of tidal turbine farms in the Shannon Estuary. The effects of turbine farms were incorporated into the BTWNM with the use of the Linear Momentum Actuator Disc Theory to calculate the thrust force induced by the turbines and introduce it in the form of a sink term in the momentum equation.

Analysis was performed on the estuary to identify an appropriate deployment site for the turbine farms. This was performed by calculating the mean available power in the estuary. Tidal farms of different densities were deployed with turbines based on the SeaGen tidal turbine.

The model was initially run without the inclusion of tidal turbines to assess the hydrodynamics in the tidal regime. Turbine farms with varying turbine densities were then included in a low resolution model, a high resolution single grid model and the TTWNM.

The high density turbine farm with turbines spaced at 0.5 rotor diameters generated an acceleration effect on the currents outside the turbine farm. The LR model simulated a less significant distortion of velocities in comparison to the TTWNM and the HR model. A high level of accuracy was generated with the TTWNM, with a difference at peak ebb of 5% and at peak flood of 1.4% in comparison to the 'correct' high resolution single grid model. This is an increase in accuracy of 10% on the ebb and 30% on the flood, to the LR model without two-way nesting.

The presence of the high density farm had an attenuation effect on the velocities inside the turbine farm. Again, the TTWNM results showed to be of a higher level of accuracy in comparison to the LR model. Upstream of the farm the LR model identified a large decrease in the velocity in comparison to the HR and TTWNM. The results showed the LR model with the inclusion of nesting (TTWNM) increased the accuracy of the model by 10% on the ebb and 22% on the flood.

The introduction of less dense tidal turbine farms, with turbines spaced at 2 rotor diameters and 5 rotor diameters, showed the magnitude of change decreased. The TTWNM showed to generate a solution with a higher level of accuracy in comparison to the LR model at all points, showing the TTWNM improves the ability of the low resolution model to identify possible hydro-environmental impacts.

## CHAPTER 8: SUMMARY AND CONCLUSIONS

### 8.1 SUMMARY

In order to accurately represent hydrodynamic processes in coastal zones it is necessary to use high spatial resolution modelling. This high level of spatial resolution is computationally expensive which can, in some cases, be quite restrictive. Numerical models with a high computational cost can be problematic if one wishes to use them in a management scenario. One solution to this computational problem is nesting, which embeds a high resolution nested grid into a lower resolution coarse grid and interact occurs between the grids. The objective of this thesis was twofold: firstly, to expand the one-way nesting technique in the numerical model DIVAST to further reduce its computational needs and to increase flexibility and applicability, and secondly, to develop a two-way nested model where the high resolution nested grid solution can be used to update and improve their coarse/parent grid solution. These nesting techniques were introduced into the two-dimensional, depth integrated, finite difference model DIVAST.

The development of an advanced one-way nested model was carried out in two stages. The development of a nested domain with the ability to be orientated at different angles was the first advanced feature incorporated into the one-way nesting technique (RNM). This technique involved the transformation of the physical nested domain onto a computational rotated domain. Transformations of the boundary conditions generated in the coarse domain were performed to force the model simulation in the rotated nested domain. The variable values computed in the nested domain were also transformed back to the original orientation after the nested domain solution scheme was performed to enable the variable to be described with respect to the non-rotated domain. The performance of the model was assessed through its application to a gently sloped harbour of a low resolution embedded with a rotated nested grid with four open boundaries. Results showed that the RNM generated a solution with a level of accuracy equivalent to a high resolution single grid solution of the harbour domain with a reduction in the number of grid points.

The second advanced feature incorporated into the one-way nested model was irregular geometry boundaries (IGB). This feature enables non-rectangular nested grids to be incor-

porated into a low resolution grid. The IGB method was incorporated by the reconstruction of the matrices that identify the characteristics of the nested grid to allow integration of the model solution to be performed with respect to the IGB nested domain. The performance of the model was tested and results generated showed the accuracy of the model solution was equivalent to the original nested domain containing a much greater number of grid points.

The development of the two-way nested model was carried out in two stages. A BTWNM was initially developed and used to test various elements of the feedback/update operator, the interpolation technique used on the nested domains data, the feedback conditions and the type and number of variables to be prescribed at the feedback interface. The final version of the BTWNM was used in the second stage of the model development to incorporate tidal turbine farms to identify changes in the hydrodynamics of the model due to energy extraction (TTWNM). The final version of the model is a two-way nested model, which is used to simulate the interaction between tidal hydraulics and tidal turbine farms. Boundary conditions for the nested domain are linearly interpolated from the coarse domain using a Dirichlet condition and the incorporation of ghost cells in the boundary formulation scheme. Water elevations and velocities are specified at the feedback interface. This data is interpolated using the averaging technique from the high resolution nested grid solution and are assigned to overlapping coarse grid points using a Dirichlet feedback condition.

The performance of the BTWNM was extensively tested before the development of the TTWNM. It was applied to the Shannon Estuary and the accuracy of the BTWNM solution in the updated coarse domain and the nested domain were determined by comparison with a high resolution single grid model solution for the entire domain. The Shannon Estuary presented a rigorous test of the models performance as the estuary contains complex bathymetry and hydrodynamic processes. The test results showed that the BTWNM successively enables the interaction between the nested domain and the coarse domain, resulting in a model with a higher level of accuracy.

The final version of the BTWNM was adapted during the second stage of the two-way nested model development, to incorporate the mechanics of energy extraction by tidal turbines. The Linear Momentum Actuator Disc approach was used to compute the turbine thrust on the water and was included in the momentum equation as a sink term. The TTWNM was applied to the Shannon Estuary, with the nested tidal turbine farm positioned

in an area identified as a possible location for the deployment of tidal turbines. The model investigated the hydro-environmental impacts of tidal turbine arrays, the effects of different array configurations and the performance of the TTWNM.

Model results showed energy extraction by tidal turbines reduced tidal currents inside the turbine farm and upstream of the turbine farm. An acceleration of flow was shown around the turbine arrays. Regarding the effects of array configurations on the hydrodynamic impacts, the impacts were most severe with higher density turbine farms. Results generated with the TTWNM showed the two-way nesting technique increased the accuracy of the model and enabled a better identification of possible environmental impacts without a large increase in the computational needs.

## **8.2 CONCLUSION**

The research carried out by the Author has led to the following main conclusions:

- An effective function was developed and incorporated into the one-way nesting technique in DIVAST to enable the specification of a rotated nested domain. Results showed that the rotated nested grid produced the same level of accuracy as the non-rotated domain but with an increase in flexibility and applicability of the nested domain. To the Author's knowledge, the RNM is the first rotational finite difference nesting procedure to be used to model hydrodynamic processes.
- A methodology was developed to enable the incorporation of a nested domain with irregular geometry boundaries into a coarse hydrodynamic model and resulted in a reduction in the size of a nested domain without reducing the accuracy of the model solution. This, also, to the Author's knowledge is the first such functionality to be incorporated into a nested model.
- An effective two-way nested model for modelling tidal hydraulics in a coastal zone was developed. Results generated showed the two-way nested model can provide an accurate high resolution solution for an area of interest and allow high resolution data to update the lower resolution coarse domain resulting in an increase in accu-

racy of the model. Positive results were demonstrated in the Shannon Estuary showing the model is applicable to real coastal zones.

- Results showed that the two-way nested model can provide an accurate high resolution solution with fifteen times lower computational effort to a standard single grid high resolution model.
- Variable prescription at the feedback interface was found to be of high importance in the conservation of mass between the nested domain and the coarse domain. The use of a variable prescription containing velocities and elevations generated the best model solution.
- The use of a Dirichlet feedback condition was found to work the best. Two other forms of feedback conditions were also tested: momentum flow relaxation method and kinetic flow relaxation method. The momentum and kinetic flow relaxation schemes produced an inferior model solution. The generation of noise with the Dirichlet condition is a recognised problem due to wave reflection, however, this was not found to be a problem.
- Four types of interpolation schemes were tested: 1) copy 2) average 3) Shapiro and 4) fully weighted. It was shown that the type of interpolation scheme was not a large factor in the performance of the model, but the best interpolation scheme was identified as the average method.
- Tidal turbines were introduced into the two-way nested model to allow an effective simulation of a tidal turbine farm without large computational needs. The deployment of tidal turbine farms in an estuary were shown to effect the hydrodynamics of the estuary in the area of deployment and also upstream of the turbine farm. High density farms were shown to generate the highest distortion in the hydrodynamics. Results showed the two-way nested model can identify hydro-environmental impacts to a greater level of accuracy in comparison to a low resolution model without a high computational cost. To the Author's knowledge this is the first two-way nested model that simulates the energy extraction by tidal turbine farms.

### 8.3 FUTURE WORK

The advanced one-way nested model and the two-way nested model are effective modelling systems that generate a high resolution solution at a low computational cost and have many uses in research and industry. The following are recommendations for future work that, in the Author's opinion, could enhance the ability of the nested models:

- Application of all nesting procedures into a three-dimensional model to enable both horizontal and vertical nesting.
- Incorporation of solute transport into the TTWNM to identify the effects of energy extraction by tidal turbines on the flushing characteristics of the model.
- Development of a seamlessly embedded two-way nested model and to compare it with the existing modelling procedure.
- Incorporation of a parallel programming technique into the nested models, to further reduce the running time of the model.
- Incorporation of advanced features of the Linear Momentum Actuator Disc theory for the representation of tidal turbines.
- Incorporation of a high resolution adaptive two-way nested domain into a three dimensional model to simulate the effects of a moving tidal turbine on the far-field hydrodynamics.

## **REFERENCES**

Adcroft, A., (2004). Implementation of an Atmosphere–Ocean General Circulation Model on the Expanded Spherical Cube, *Monthly weather review*, 132, pp. 2845-2863.

Ahmadian, R., Falconer, R. A., (2012). Assessment of array shape of tidal stream turbines on hydro-environmental impacts and available power, *Renewable Energy*, 44, pp. 318-327.

Anthes, R. A., (1974). Data Assimilation and Initialization of Hurricane Prediction Models, *Journal of Atmospheric Science*, 31, pp. 702-719.

Bahaj, A., Molland, AF., Chaplin, JR., Batten, WMJ., (2007). Power and thrust measurements of marine current turbines under various hydrodynamic flow conditions in a cavitation tunnel and a towing tank, *Renewable energy*, 32, pp. 407-426.

Bakker, A., (2008). *Applied Computational Fluid Dynamics*. URL: <http://www.bakker.org/dartmouth0605>. Accessed: June 2012

Barth, A., Alvera-Azca'rate, A., Rixen, M., BeckerS, J-M., (2005). Two- way nested model of mesoscale circulation features in the Ligurian Sea, *Progress in Oceanography* 66, pp. 171-189.

Beevers, L., Durán, R., (2009). Hydrodynamic model report Alexandria Lake Mariout Integrated Management, UNESCO-IHE Institute of Water Education.

Bender, M. A., Ginis, I., Tuleya, R., Thomas, B. and Marchok, T., (2007). The operational GFDL coupled hurricane-ocean prediction system and summary of its performance, *Monthly Weather Review* (135)12, pp. 3965–3989.

Berger, M., and Olinger, J., (1984). Adaptive mesh refinement for hyperbolic partial differential equations, *Journal of Computational Physics* (53), pp. 484–512.

Berkhahn, V., Kaapke, K., Sebastian, R., Pasche, E., (2005). A Hybrid Meshing Scheme Based on Terrain Feature Identification. Proceedings in: 14th International Meshing Roundtable, San Diego, pp. 129-146.

Birchfield, G.E., (1960). Numerical prediction of hurricane movement with the use of fine grid, *Journal of Meteorology*, 17, pp. 406-414.

Blayo, E., Debreu, L., (2006). Nesting ocean models. In: Chassignet, P. and Verron, J. (Eds.), (2006), *Ocean weather forecasting: an integrated view of oceanography*, Springer Netherlands, pp.127-146.

Blayo, E., Debreu, L., (2005). Revisiting open boundary conditions from the point of view of characteristic variables, *Ocean Modelling* (9), pp. 231-252.

Blayo, E., Debreu, L., (1999). Adaptive mesh refinement for finite-difference ocean models: first experiments, *Journal of Physical Oceanography* 29, pp. 1239–1250.

Bleck, R., (2002). An oceanic general circulation model framed in hybrid isopycnic-cartesian coordinates, *Ocean Modelling* 4, pp. 55-88.

Borthwick, A.G.L., Kaar, E.T., (1993). Shallow flow modelling using curvilinear depth-averaged stream function and vorticity transport equations, *International Journal for Numerical methods in Fluids* (27), pp. 417-445.

Borthwick, A.G.L., Cruz Leon, S., Jozsa, J., (2001). The shallow flow equations solved on adaptive quadtree grids, *International Journal for Numerical Methods in Fluids* (37), pp. 691-719.

Borthwick, A.G.L., Marchant, R.D., Copeland, G.J.M., (2000). Adaptive hierarchical grid model of water-borne pollutant dispersion, *Advances in Water Resources* 23(8), pp. 849-865.

Burton, T., Sharpe, D., Jenkins, N., Bossanyi, E. (2001). *Wind Energy Handbook*. Chichester, UK.

Chen, B., (2012). Round off and Truncation Errors. URL:  
<http://berlin.csie.ntnu.edu.tw/Courses/Numerical%20Methods/Lectures2012S> Accessed: November 2011

Clark, T.L., Farley, D., (1984). Severe down slope windstorm calculation in two and three spatial dimension using an elastic interactive grid nesting: a possible mechanism for gustiness, *Journal of Atmospheric Science*, 41, pp. 329-350.

Clough, R.W., (1960). The Finite Element method in plane stress analysis, *Proceedings in: 2<sup>nd</sup> ASCE Conference on Electric Computation*, Pittsburgh.

Colle, B., Wolfe, J., Steenburgh, W.J, Kingsmill, D., Cox, J.A.W, Shafer, J.C., (2005). High-resolution simulations and microphysical validation of an orographic precipitation event over the Wasatch Mountains during IPEX IOP3, *Monthly Weather Review* 133, pp. 2947-2971.

Courant, R., Friedrichs, K.O., Lewy, H., (1928). Über die partiellen Differenzgleichungen der Mathematischen Physik. Math. Ann. 100, pp. 32–74 (English translation, with commentaries by Lax, P.B., Widlund, O.B., Parter, S.V., in IBM J. Res. Develop. 11 (1967)).

Dabrowski, T., (2005). A flushing study analysis of selected Irish water bodies, PhD Dissertation, Department of Civil Engineering, National University of Ireland, Galway.

Dacre, S. L., (2007). The environmental impacts and developmental constraints of tidal current energy extraction, PhD Dissertation, The Robert Gordon University.

Daoud, A. H., Rakha, K.A., Abul-azm, A.G., (2008). A two-dimensional finite volume hydrodynamic model for coastal areas: Model development and validation, Ocean Engineering **35**(1), pp.150-164.

Global River Discharge Database., (2011). URL: <http://www.sage.wisc.edu/riverdata/> Accessed: 10 August 2011.

Davies, H. C., (1976). A lateral boundary formulation for multi-level prediction models, Quarterly Journal of the Royal Meteorological Society, 102(432), pp. 405-418.

Debreu, L., Blayo, E. and Barnier, B., (2005). A general adaptive multi-resolution approach to ocean modelling: experiments in a primitive equation model of the North Atlantic. In: Plewa, T., Linde, T., Weirs, G.V., (Eds.), Adaptive mesh refinement - theory and applications, Springer.

Debreu, L., Blayo, E., (2008). Two-way embedding algorithms: a review, Ocean dynamics, pp.1-21

Demirdzic, I., Peric, M., (1990). Finite Element method for prediction of fluid flow in arbitrarily shaped domains with moving boundaries, *International Journal of Numerical Methods in Fluids* 10, pp. 771-790.

Denot, T., Lang, P., (2012). "Apports de la modélisation numérique à l'étude de la dynamique hydro-sédimentaire de l'estuaire de la Rance." URL: <http://www.opentelemac.org/index.php/publications>

DHI (2013). MIKE 21 & MIKE 3 Flow model: Hydrodynamic Module user guide, DHI Water and Environment.

Drazin, P.G., (2002). *Introduction to Hydrodynamic Stability*, Cambridge University Press.

Falconer, R. A., (1986). Water quality simulation of a natural harbour, *Journal of waterways, port, coastal and ocean engineering - ASCE* (112), pp. 15-34.

Falconer, R. A., (1988). A short course on flow and water quality modelling of coastal waters, estuaries, rivers, lakes and reservoirs: Lecture 7-Solution Procedure, 20-22.

Falconer, R. A., (1994). An introduction to nearly-horizontal flows, *Coastal, Estuarial and Harbour Engineer's Reference Book*, Chapman & Hall.

Falconer, R. A., Lin, B., Win, Y., Harris, E., (2001). *DIVAST model reference manual*, Environmental Water Management Research Centre, Cardiff University.

Fowler, M., (2012). *Calculating Viscous Flow: Velocity Profiles in Rivers and Pipes*, *Physics* 152, URL: <http://galileo.phys.virginia.edu/classes/152.mf1i.spring02/GravityIndex.htm>.

Fox, A., (1995 ). Two way interactive nesting of primitive equation ocean model with topography, *Journal of Physical Oceanography* 25, pp. 2977-2996.

Fraenkel, P. L., (2007). Marine current turbines: pioneering the development of marine kinetic energy converters. *Journal of Power and Energy* 221(2), pp. 159-169.

Ginis, I., Richardson, R.A., Rothstein, L.M., (1998). Design of a multiply nested primitive equation ocean model, *Monthly Weather Review* 126. pp.1054-1079.

Group, S. S. (2013). Surface Water Modelling System V 8.0, URL: [http://www.scisoft-gms.com/sms\\_details](http://www.scisoft-gms.com/sms_details), Accessed: January 2013.

Harrison, E. J., Jr (1973). Three-dimensional numerical simulations of tropical systems utilizing nested finite grids, *Journal of Atmospheric Science* 30, pp. 1528-1543.

Hartnett, M., Nash, S., (2004). Modelling nutrients and chlorophyll dynamics in an Irish brackish water body, *Environmental Modelling and Software*, Vol. 19, pp. 47-56.

Hemker, P. W., (2001). On the order of prolongations and restrictions in multigrid procedures, *Journal of Computational and Applied Mathematics* 32, pp. 423-429.

Holland, W. R., and Vallis, G., (1990). A high resolution model of the California Current embedded into a basin-scale North Pacific circulation model.

Hong, HE., Jian-ren, F., Ke-fa, C., (2000). A numerical method for orthogonal grid generation by Laplace system, *Journal of Zhejiang University SCIENCE*, pp. 125-128.

Houlsby, G. T., Draper, S., Oldfield, M.L.G., (2008). Application of Linear momentum actuator disc theory to open channel flow (No. OUEL 2296/08), University of Oxford.

Kantha, L.H., Clayson, C.A., (2000). Numerical Models of Oceans and Oceanic Processes, Academic Press.

Kim, K. W., McAdory, R., Pratt, T., (2004). Verification of a 2D Hydrodynamic Model of Florida Bay, Water Circulation and Currents, US Army Engineer Waterways Experiment Station, Vicksburg, MS.

Korres, G., Lascaratoe, A., (2003). A one-way nested eddy resolving model of the Aegean and Levantine basins: implementation and climatologically runs. *Annales Geophysicae*, 21, pp. 205-220.

Koch, S.E., McQueen, J.T., (1987). A survey of nested grid techniques and their potential for use within the MASS weather prediction model. NASA Technical Memorandum 87808. National Aeronautics and Space Administration, USA.

Kurihara, Y., Tripoli, G.J., Bender, M.A., (1979). Design of a movable nested-mesh primitive equation model, *Monthly Weather Review*, 107, pp. 239-249.

Kuzmin, D., (2010). A Guide to Numerical Methods for Transport Equations, Fredrich Alexander University, Erlanger-Nurnberg.

Lam, D., Leon, L., Hamilton, S., (2004). Multi-model integration in a decision support system: a technical user interface approach for watershed and lake management scenarios, *Environmental Modelling and Software* 19(3), pp. 317-324.

Laramee, R. S., (2003). FIRST: A flexible and interactive re-sampling tool for CFD simulation data, *Computers & Graphics* 27(6), pp. 905-916.

Layeka, G.C., Midyab, C., (2007). Effect of constriction height on flow separation in a two-dimensional channel, *Communications in Nonlinear Science and Numerical Simulation* 12(5), pp. 745-759.

Ley, G. W., Elsberry, R.L., (1976). Forecasts of Typhoon Irma using a Nested-Grid Model, *Monthly Weather Review*, 104 pp. 1154-1161.

Liang, Q., Du, G., Hall, J.W., Borthwick, A.G.L. (2008). Flood Inundation Modelling with an Adaptive Quadtree Grid Shallow Water Equation Solver, *Journal of Hydraulic Engineering* (134), pp. 1603-1610.

Marchesiello, P., McWilliams, J., Shchepetkin, A. (2001). Open boundary conditions for long term integration of regional oceanic models, *Ocean Modelling* 3, pp. 1-20.

MAREN (2013). MAREN Project, URL: <http://www.marenproject.eu/eng/>.

Martin, J. L., and McCutcheon, S.C., (1999). Hydrodynamics and transport for water quality modelling, Lewis Publishers.

Mcarthur, K.E., (1996). Comparison of finite different and finite element hydrodynamic models applied to the Laguna Madre Estuary, Masters of Science Dissertation, Department of Civil Engineering, Texas A&M University, Texas.

Mingham, C.G., Causon, D.M., (1998). High-Resolution Finite-Volume Method for Shallow Water Flows, *Journal of Hydraulic Engineering* 124(6), pp. 605-614.

Myers, L.E., Bahaj, A.S., (2012). An experimental investigation simulating flow effects in first generation marine current energy converter arrays, *Renewable Energy* 37(1), pp. 28-36.

Nash, S., (2010). A development of an efficient dynamically-nested model for tidal hydraulics and solute transport, PhD Dissertation, Department of Civil Engineering, National University of Ireland, Galway.

Nycander, J., Döös, K., (2003). Open boundary conditions for barotropic waves, *Journal of Geophysical Research*, 108, pp. 3168-3187.

Oddo, P., Pinardi, N., (2008). Lateral open boundary conditions for nested limited area models: a scale selective approach, *Ocean Modelling* 20, pp. 134-156.

Oey, L-Y., Chen, P., (1992). A nested-grid ocean model: with application to the simulation of meanders and eddies in the Norwegian Coastal Current, *Journal of Geophysical Research* 97(20), pp. 063-086.

Olsen, N., Stokseth, S., (1995). Three-Dimensional numerical modelling of water flow in a river with large bed roughness, *Journal of Hydraulic Research* 33(6), pp.571-581.

Ookochi, Y., (1972). A computational scheme for the nesting fine mesh in the primitive equation model, *Journal of meteorology Society of Japan* 50, pp. 37-47.

OPW (2011). Hydro-metric website of the Office of Public Works, URL: <http://opw.ie/hydro>, Accessed: September 2011

Palma, E. D., Matano, R.P., (1998). On the implementation of passive open boundary conditions for a general circulation model: The barotropic mode, *Journal of geographical research* 103, pp. 1319-1341.

Park, K.-Y., Borthwick, A.G.L., Cho, Y-S, (2006). Two-dimensional wave-current interaction with a locally enriched quadtree grid system, *Ocean Engineering* 33(2), pp. 247-263.

Penven, P., Debreu L., Marchesiello, P., McWilliams, J.C., (2006). Evaluation and application of the ROMS 1-way embedding procedure to the central California upwelling system, *Ocean Modelling* 12, pp. 157-187.

Petrila, T., Trif, D., (2005). *Basics of Fluid Mechanics and Introduction to Computational Fluid Dynamics*, Springer.

Pullen, J., Allen, J.S., (2001). Modelling studies of the coastal circulation off the northern coast of California: statistics and patterns of wintertime flow, *Journal of Geophysical Research*, pp. 26,959-26,984.

Rodenhuis, G. S., (1994). Two dimensional nearly horizontal flow models, pp: 129-144, In: Abbot, N.B. and Price, W.A. (Eds), (1994), *Coastal, estuarial, and harbour engineers' reference book*, Routledge, UK.

Røed, L. P., Cooper, C.K., (1987). A Study of Various open Boundary Conditions for Wind-Forced Barotropic Numerical Ocean Models, *Elsevier Oceanography Series* 45, pp. 305-335.

Rowley, C., Ginis, I., (1999). Implementation of a mesh movement scheme in a multiply nested ocean model and its application to air-sea interaction studies, *Monthly Weather Review* (127), pp. 1,879-1,896.

Samet, H., (1990). Applications of Spatial Data Structures, Addison-Wesley.

SEI (2009). Tidal and Current Energy Resources in Ireland, Sustainable Energy Ireland, Dublin, Ireland.

Sheng, J., Greatbach, R.J., Zhai, X., Tang, L., (2005). A new two-way nested technique for ocean modelling based on the smoothed semi-prognostic method, *Ocean dynamics* 55, pp. 162-177.

Sheng, Y.P., Wu, T.S., Wang, P.F., (1988). Coastal and Estuarine Hydrodynamic Modelling in Curvilinear Grids, *Proceeding in: Coastal Engineering IV*, pp. 2655, 2665.

Shore, J. A., (2009). Modelling the circulation and exchange of Kingston Basin and Lake Ontario with FVCOM, *Ocean Modelling* 30, pp. 106-114.

Smith, P.E., (1997). A three-dimensional, finite difference model for estuarine circulation. Doctoral Dissertation, University of California, Davis, CA.

Spall, M.A., Robinson, A.R., (1989). A hybrid coordinate open ocean primitive equation model, *Mathematics and Computers in simulation*, 31, pp. 241-220.

Spall, M., Holland, W.R., (1991). A nested primitive equation model for ocean applications, *Journal of physical oceanography* 21, pp. 205-220.

Staneva, J., Stanev, E.V., Wolff, J.O., Badewien, T.H., Reuter, R., (2009). Hydrodynamics and sediment dynamics in the German Bight. A focus on observations and numerical modelling in the East Frisian Wadden Sea, *Continental Shelf Research* 29, pp. 302-319.

Strikwerda, J.C., (2004). *Finite Difference Schemes and Partial Differential Equations*, SIAM.

Thomé, V., (2001). From finite differences to finite elements: A short history of numerical analysis of partial differential equations, *Journal of Computational and Applied Mathematics* 128(1-2), pp. 1-54.

Thompson, D.B., (1992). *Numerical Methods 101 - Convergence of Numerical Models*, U.S. Geological Survey, Stennis Space Centre.

Treguier, A.M., Barnier, B., De Miranda, A.P., Molines, J.M., Grima, N., Imbard, M., Madec, G., Messenger, C., Reynaud, T., (2001). An eddy-permitting model of the Atlantic circulation: Evaluating open boundary conditions, *Journal of Geophysical Research - Oceans* 106, pp. 22115-22129.

Wang, Y., Murgie, S., (2006). *Hybrid Mesh Generation for Viscous Flow Simulation*, Springer Berlin Heidelberg.

Wanga, M.Y., Wangb, X., (2004). *Computer Methods in Applied Mechanics and Engineering*, *Computer Methods in Applied Mechanics and Engineering* 193, pp. 469-496.

Wilson, B., Batty R.S., Daunt, F., Carter, C., (2007). Collision risk between marine renewable energy devices and mammals, fish and diving birds, *Scottish association for marine science*.

Xinghua, C., Laiping, Z., Xin, H., (2012). Numerical study of the thunniform mode of fish swimming with different Reynolds number and caudal fin shape, *Computers & Fluids* 68, pp. 54-70.

Yu, X., (2013). Grid and mesh generation. URL: <http://aircraftdesign.nuaa.edu.cn/aca>. Accessed: November 2012

Zavatarelli, M., Pinardi, N., (2003). The Adriatic Sea modelling system: a nested approach. *Annales Geophysicae* 21, pp. 345-364.

Zhang, D-L., Chang, H-R., Seaman, N.L., Warner, T.T., Fritsch, J.M., (1986). A two-way interactive nesting procedure with variable terrain resolution, *Monthly Weather Review* 114, pp. 1330-1339.

Zhang, W-Z., Hong, H-S, Shanga, S-P., Chen, D-W., Chaic, F., (2007). A two-way nested coupled tide-surge model for the Taiwan Strait, *Continental Shelf Research* (27), pp. 1548-1567.

## **APPENDIX A**

**Description of terms in the governing equations and  
finite difference methods.**

## A.1 Description of terms in the governing equations.

### Time derivative

This term represents the local change in water elevation and momentum quantities with time, due to tidal action at the boundary.

### Advective terms

Denotes the change of the momentum in the direction of flow. The velocity gradient in the same direction of flow is contained in the non-cross term  $\frac{u\partial u}{\partial x}$  and the velocity gradient in the other co-ordinate direction is contained in the cross term  $\frac{v\partial u}{\partial x}$ . The importance of this term increases the larger the Reynolds number.

### The momentum correction factor

The momentum correction factor can be calculated in the following way, assuming a logarithmic vertical velocity profile:

$$\beta = 1 + \frac{g}{C^2 k^2} \quad (\text{A-1})$$

where  $k$ = von Karman's constant = 0.4. The value of  $\beta$  is 1.016 for an assumed seventh power law velocity profile and for an assumed quadratic velocity profile  $\beta = 1.2$ .

### Coriolis term

This term describes the effect of the earth's rotation on the flow. It acts at a right angle to the flow and is dependent on the velocity of the flow and the latitude. It changes the direction of currents in a channel and can effect sediment transportation and river alignment. It affects tidal currents and amplitudes on the coast; however, in estuaries its influence is minimal in comparison to other effects, unless the model domain is considerable large.

### Surface slope term

Describes the action of gravity, while taking into account water elevation and topographical features. The term contains water elevation and mean depth and the derivative of water elevation, making the term non-linear.

### The effect of wind

As wind blows over the water surface a drag force is induced. The shear force at the interface between air and water is calculated with the assumption that it is proportional to the square of the wind speed at a particular height above the surface of the water. Wilson's value is used in DIVAST, which has a resistance height of  $z=20\text{m}$ . Wind stress in estuaries and rivers is often small in comparison to bottom shear stress.

### Bottom friction

This term has a retarding effect on the flow. The Chezy coefficient is a coefficient of bottom friction that is semi-empirical and was developed originally to describe uniform flow in an open channel. With an assumed logarithmic velocity-depth profile and under turbulent rough flow, the Chezy coefficient of bottom friction varies due to the roughness of the bed and is independent of flow:

$$C = -18.0 * \log_{10} \left( \frac{k}{H * 12.0} \right) \quad (\text{A-2})$$

However, in transitional flow conditions the coefficient varies due to the conditions of flow and is calculated as follows by iteration:

$$C = -18.0 * \log_{10} \left( \frac{k}{H * 12.0} + \frac{5}{Re * 18.0} * C \right) \quad (\text{A-3})$$

where  $k$  is the roughness length,  $Re$  is Reynolds number. This coefficient is calculated in time-steps specified by the user.

### Turbulence

The flow resistance generated from the random fluctuation of water in time and space in represented with this term. The exchange in momentum generated by turbulence causes a more uniform distribution of velocity-depth in comparison to laminar conditions. The DIVAST model takes into account turbulent shear stress near the bed only and is related to Boussinesq's approximation of the mean shear stress  $\tau_e$  in turbulent flow:

$$\tau_e = \varepsilon \frac{dv}{dy} \quad (\text{A-4})$$

with  $\varepsilon$  being the eddy viscosity and is dependent on the characteristics of the turbulence flow. It is calculated in the following manner in DIVAST:

$$\varepsilon = C_e \frac{H}{C} \sqrt{g(U^2 + V^2)} \quad (\text{A-5})$$

where  $C_e$  is the eddy viscosity coefficient and is given a value of  $\approx 1.0$  in DIVAST.

## A.2 Types of finite difference methods

There are three types of finite difference methods: forward difference, backward difference and central difference. The following equations and graph represent these methods:

Forward:

$$\frac{\partial u(x)}{\partial x} \approx \frac{(u_{(x+\Delta x)} - u_{(x)})}{\Delta x} \quad (\text{A-6})$$

Backward:

$$\frac{\partial u(x)}{\partial x} \approx \frac{(u_{(x)} - u_{(x-\Delta x)})}{\Delta x} \quad (\text{A-7})$$

Central:

$$\frac{\partial u(x)}{\partial x} \approx \frac{(u_{(x+\Delta x)} - u_{(x-\Delta x)})}{2\Delta x} \quad (\text{A-8})$$

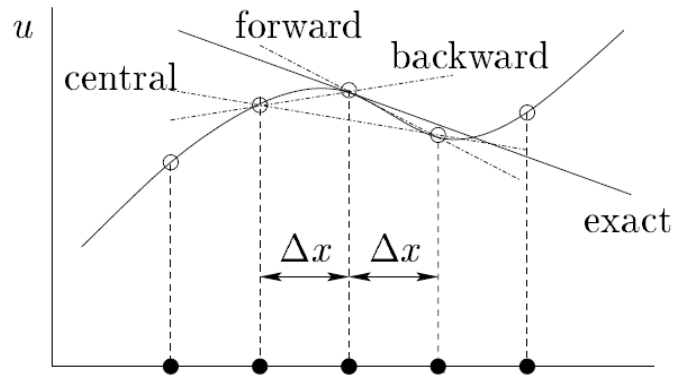


Figure A -1 Finite Difference schemes (Kuzmin 2010)

The central difference method is the most attractive method, due to the size of the truncation error. The equations A-9-A-11 show that the truncation error is half the value of the

forward and backward truncation error. The truncation errors are calculated by using the Taylor series expansion method (Chen 2012).

Forward:

$$\frac{\partial u}{\partial x} = \frac{(u_{i+1}-u_i)}{\Delta x} - \underbrace{\frac{\Delta x}{2} \left(\frac{\partial^2 u}{\partial x^2}\right)_i - \frac{(\Delta x)^2}{6} \left(\frac{\partial^3 u}{\partial x^3}\right)_i}_{\text{Truncation error}} \dots \quad (\text{A-9})$$

Backward:

$$\frac{\partial u}{\partial x} = \frac{(u_i-u_{i-1})}{\Delta x} + \underbrace{\frac{\Delta x}{2} \left(\frac{\partial^2 u}{\partial x^2}\right)_i - \frac{(\Delta x)^2}{6} \left(\frac{\partial^3 u}{\partial x^3}\right)_i}_{\text{Truncation error}} \dots \quad (\text{A-10})$$

Central:

$$\frac{\partial u}{\partial x} = \frac{(u_{i+1}-u_{i-1})}{2\Delta x} - \underbrace{\frac{(\Delta x)^2}{6} \left(\frac{\partial^3 u}{\partial x^3}\right)_i}_{\text{Truncation error}} \quad (\text{A-11})$$

**APPENDIX B**  
**Flow charts**

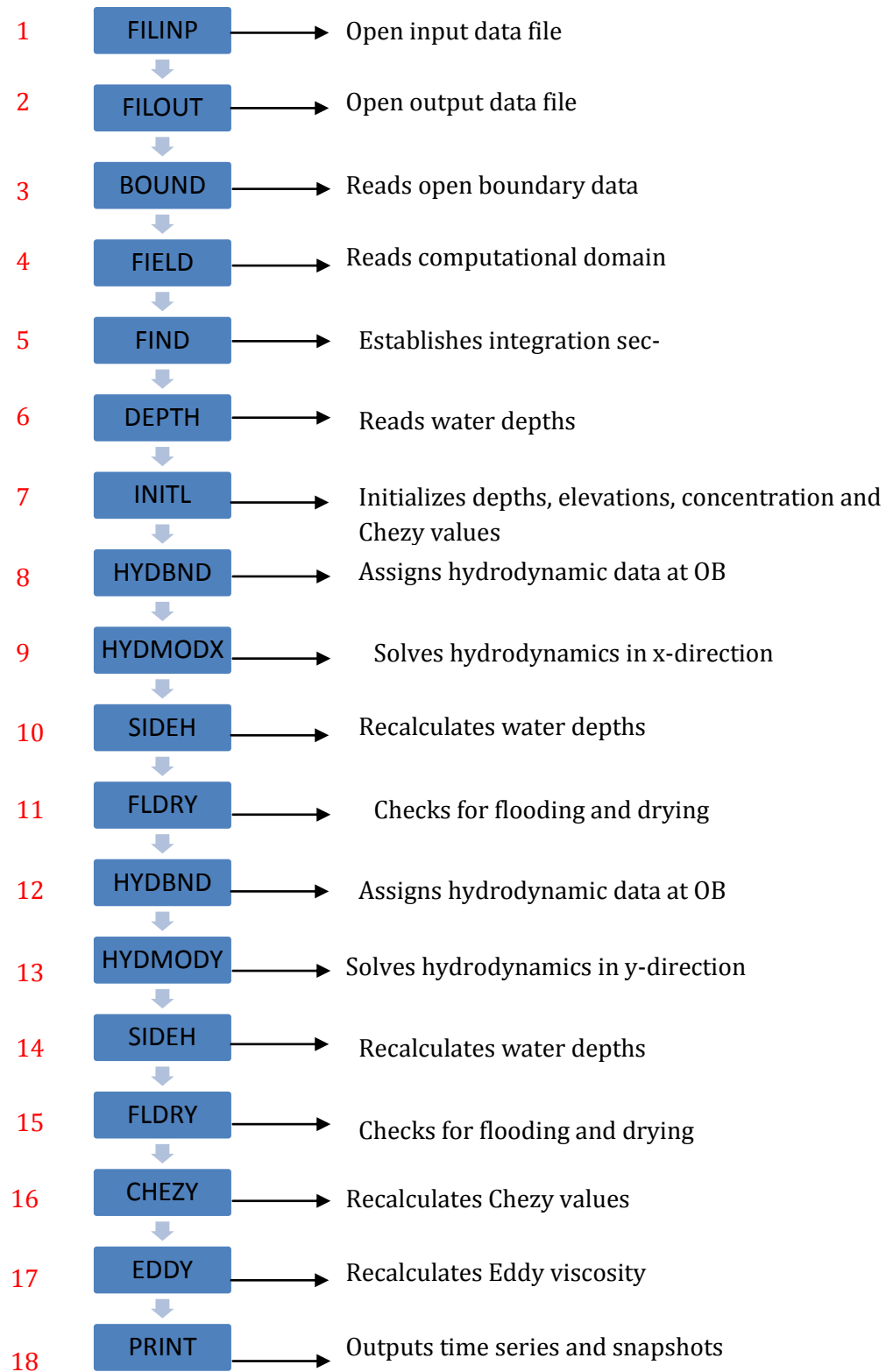


Figure B-1 Flow chart of DIVAST

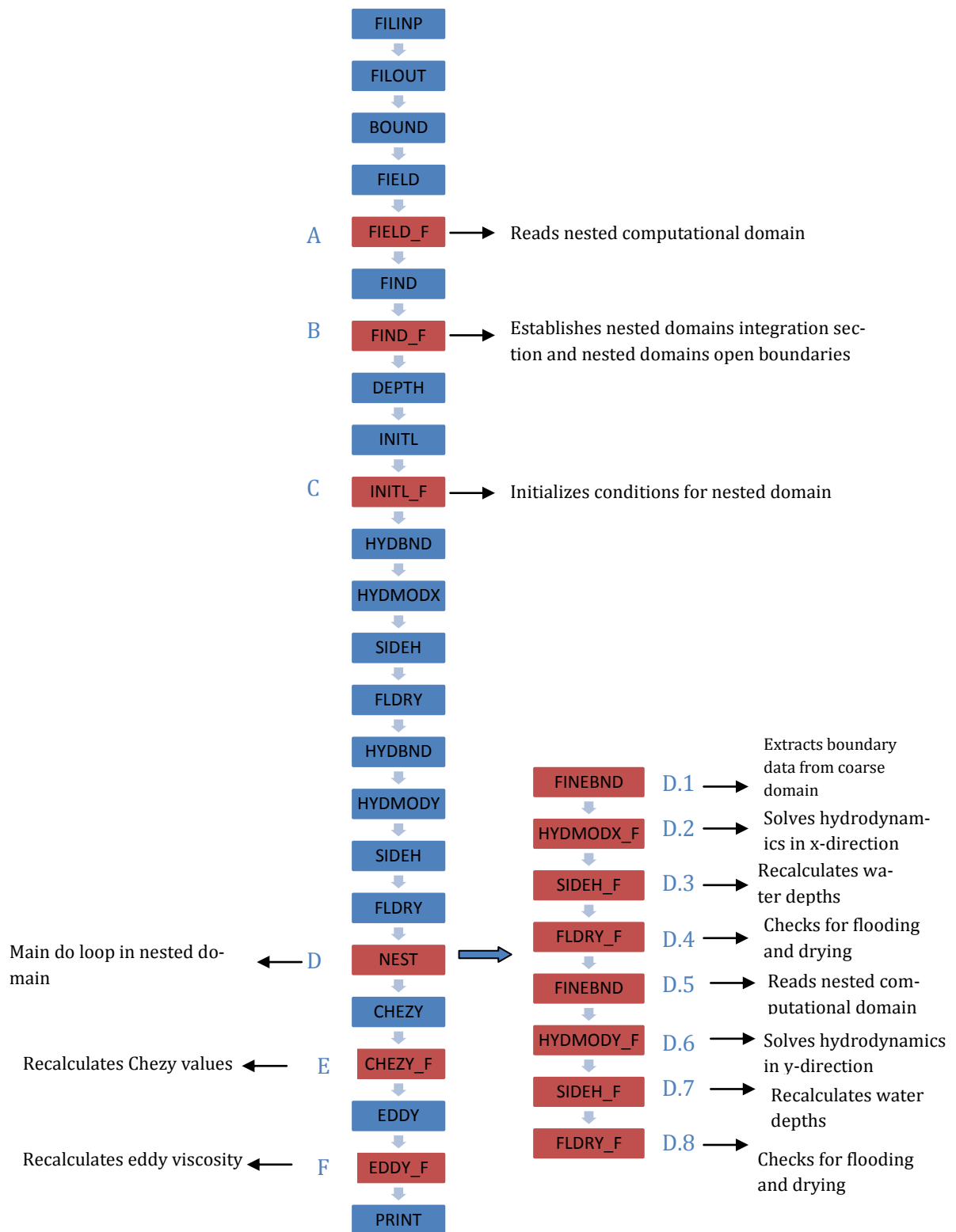


Figure B-2 Flow chart of one-way nested model

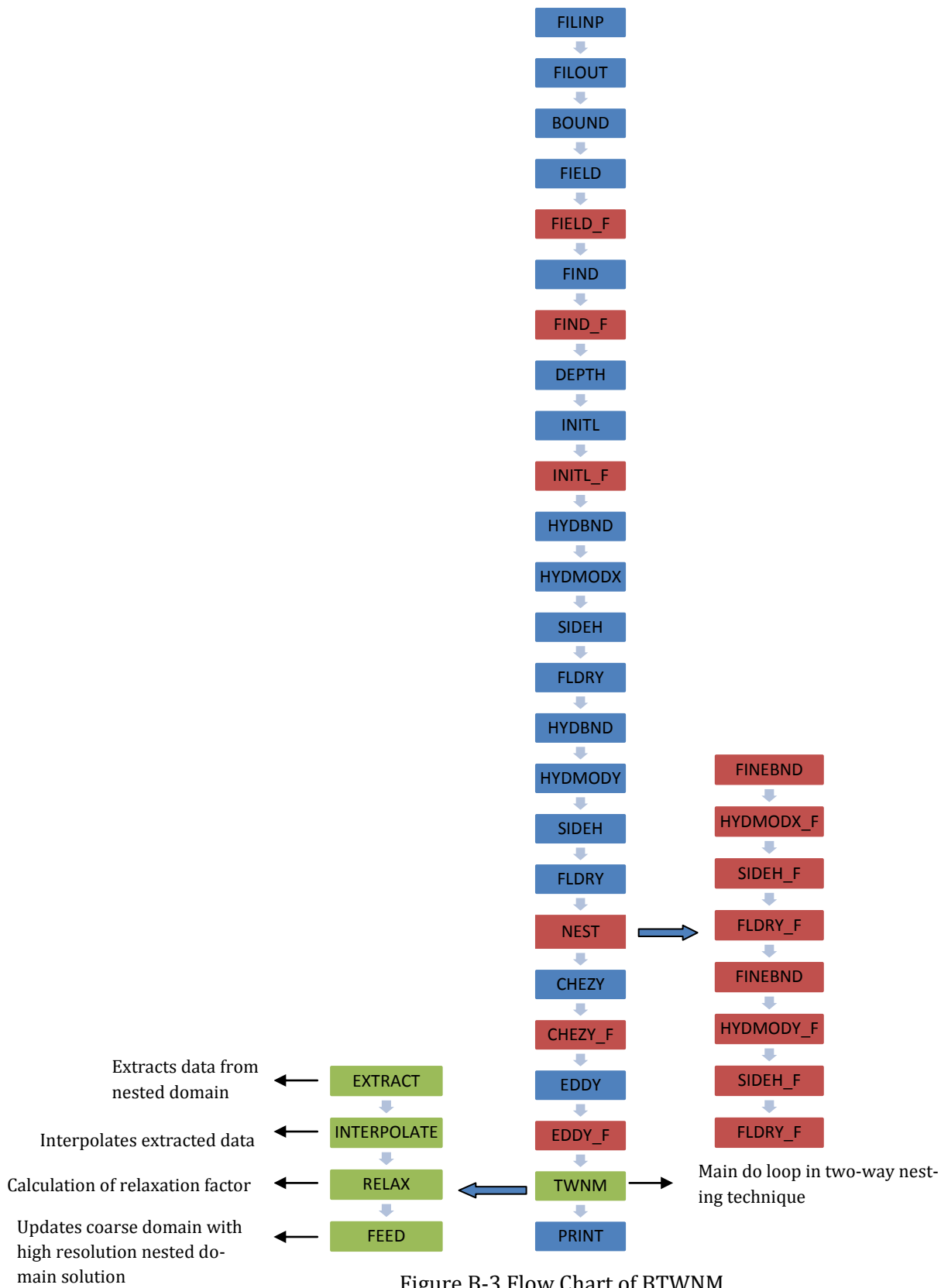


Figure B-3 Flow Chart of BTWNM



Figure B-4 Flow chart of TTWNM